

METABIOTRANS: A 3-D FINITE ELEMENT MODEL FOR THE TRANSPORT AND
BIOTRANSFORMATION OF METALS IN THE SUBSURFACE

By

MOHAMED M. A. MOHAMED

A DISSERTATION PRESENTED TO THE GRADUATE SCHOOL
OF THE UNIVERSITY OF FLORIDA IN PARTIAL FULFILLMENT
OF THE REQUIREMENTS FOR THE DEGREE OF
DOCTOR OF PHILOSOPHY

UNIVERSITY OF FLORIDA

2001

**TO MY BELOVED
MOTHER**
IN THE OCCASION OF HER
FIFTH MEMORIAL

**TO MY BELOVED
FATHER**



ACKNOWLEDGMENTS

I would like to express my deep appreciation and gratitude to Dr. K. Hatfield for his valuable advice and precious guidance during the course of this study. Special thanks and gratitude are due to Dr. L. H. Motz for his support and help during the different phases of this research. I would like to extend my gratitude to Dr. W. D. Graham for her excellent explanation of stochastic hydrology, which constitutes an important part of this research. Many thanks are also directed to Dr. M. Annable for his valuable opinions and suggestions and to Dr. J. Jacobs for her outstanding teaching approaches. Finally, I would like to offer my special gratitude to Dr. A. Hassan, Desert Research Institute, for his valuable technical discussions that enriched the research.

I would like to express my deep appreciation to my father who supported me during the different phases of my life. His continuous prayers were my strong support at difficult times during my studies. I would like to dedicate this work to the soul of my mother, God bless her, in the occasion of her fifth memorial. Her support, care, and love during all stages of my life were and still are the most precious memories I hold. I also would like to thank my brother and his wife for their continuous care, prayers, and endorsement.

TABLE OF CONTENTS

ACKNOWLEDGMENTS	ii
LIST OF TABLES	viii
LIST OF FIGURES	ix
ABSTRACT	xv
CHAPTERS	
1. INTRODUCTION	1
1.1 Background	1
1.2. Objectives and Scope of Study	5
2. LITERATURE REVIEW	8
2.1. Introduction.....	8
2.2. Chromium Reduction.....	8
2.3. Factors affecting microbial reduction of Cr(VI)	18
2.4. Kinetics of Microbial Cr(VI) Reduction.....	20
2.5. Modeling Biodegradation in the Subsurface.....	21
2.5.1. Background	21
2.5.2. Mathematical and Numerical Modeling of Biodegradation in Subsurface	23
2.6. Available Numerical Software Packages for Simulating Biodegradation in the Subsurface.....	26
2.6.1. BIO1D	26
2.6.2. Bioplume I, II, and III:	28

2.6.3. HYDROGEOCHEM.....	29
2.6.4. HYDROGEOCHEM 2:	31
3. MODELING MICROBIAL-MEDIATED REDUCTION IN BATCH REACTORS..	34
3.1. Introduction.....	35
3.2. Governing Equations	37
3.3. Methods of Solution.....	40
3.3.1. Taylor series expansion approximation (TSA)	41
3.3.2. Finite difference method (FDM).....	41
3.3.3. Quasi steady state approximation (QSSA)	42
3.3.4. Fourth order Runge-Kutta method (RKM)	43
3.4. Numerical Examples	43
3.5. Simulation of Cr(VI) Reduction Using QSSA.....	50
4. DEVELOPMENT OF METABIOTRANS.....	57
4.1 Introduction.....	57
4.2 Theoretical Background.....	58
4.2.1 Microbial dynamics	58
4.2.2 Biotransformation kinetics.....	58
4.3. Governing Equations	61
4.3.1. Flow equations.....	61
4.3.2. Transport equations.....	61
4.3.3. Source/sink equations	62
4.3.4. Utilization equations	63
4.3.5. Microbial growth equations	64
4.4. Numerical Implementation	66
4.4.1. Problem discretization	67

4.4.2. Derivation of the approximate equations.....	68
4.4.3. Developing the system of algebraic equation	73
4.4.4. Solving the system of algebraic equation	78
4.5. METABIOTRANS Description.....	80
5. METABIOTRANS VALIDATION	86
5.1. Introduction.....	86
5.2. One-dimensional solute transport validation	86
5.2.1. Test problem 1: Solute transport with zero decay and no retardation	89
5.2.2. Test problem 2: Solute transport with decay and no retardation	91
5.2.3. Test problem 3: Solute transport with retardation and zero decay	93
5.2.4. Test problem 4: Steady state advective solute transport with non-linear biodegradation.....	95
5.3. Two-dimensional solute transport validation.....	96
5.3.1. Test problem 5: Solute transport with zero decay and no retardation	99
5.3.2. Test problem 6: Solute transport with decay and no retardation	100
5.3.3. Test problem 7: Solute transport with retardation and zero decay	102
5.4. Three-dimensional solute transport validation.....	104
5.4.1. Test problem 8: Solute transport with zero decay and no retardation	108
5.4.2. Test problem 9: Solute transport with decay and no retardation	109
5.4.3. Test problem 10: Solute transport with retardation and zero decay	112
5-5. Multi-solutes transport.....	114
6. METABIOTRANS APPLICATION AND SENSITIVITY ANALYSIS	121
6.1 Introduction.....	121
6.2. Example 1	122
6.2.1. Effect of Microbial Growth Rate (μ_{max})	127
6.2.2. Effect of Cr(VI) Half Saturation Coefficient (K_c).....	135

6.2.3. Effect of inhibition factor (K_i)	138
6.2.4. Effect of Bacterial Death Rate (B).....	144
6.2.5. Effect of all Biological Parameters on Mass Flux	148
6.3. Example 2	151
6.3.1 Effect of Microbial Growth Rate (m_{max})	161
6.3.2. Effect of Cr(VI) half Saturation Coefficient (K_c).....	166
6.3.3. Effect of inhibition factor (K_i).....	168
6.3.4. Effect of Bacterial Death Rate (B).....	173
6.3.5. Effect of all Biological Parameters on Mass Flux	173
7. EFFECT OF ELECTRON DONORS AND NUTRIENTS AVAILABILITY ON METALS SOURCE ZONE BIOLOGICAL TREATMENT	178
7.1. Introduction.....	178
7.2. Problem Description	179
7.3. Case 1	186
7.3.1. One Well Treatment.....	186
7.3.2. Three Wells Treatment	197
7.3.3. Line Source Treatment.....	203
7.4. Case 2.....	213
7.4.1. One Well Treatment.....	215
7.4.2. Three Wells Treatment	220
7.4.3. Line Source Treatment.....	228
7.5. Case 3.....	234
7.5.1. One Well Treatment.....	236
7.5.2. Three Wells Treatment	239
7.5.3. Line Source Treatment.....	244

8. MONTE CARLO EVALUATION OF METALS BIOTRANSFORMATION IN TWO-DIMENSIONAL HETEROGENEOUS AQUIFERS	253
8.1. Introduction.....	253
8.2. Monte Carlo Simulations	255
8.3. Physical Variability.....	261
8.4. Biological Variability.....	275
8.5. Physical and Biological Variability	284
8.6. Electron Donor Variability	306
9. SUMMARY AND CONCLUSIONS	314
9.1. Summary and Conclusions	314
9.2. Recommendations for Future Work.....	324
APPENDIX: ANALYTICAL SOLUTION.....	326
LIST OF REFERENCES.....	328
BIOGRAPHICAL SKETCH.....	338

LIST OF TABLES

Table	Page
2-1 Bioremediation of chromium (previous studies)	13
2-2 Kinetic models of Cr(VI) reduction in pure and mixed cultures	21
3-1 Input parameters for the numerical examples 1-4	44
3-2 Average percentage error compared to analytical solution (example 1) and to RKM (examples 2 and 3)	47
3-3 Kinetic parameters for the three laboratory experiments	52
4-1 Subroutines of METABIOTRANS	82
5-1 Input parameters for the eleven test problems	87
6-1 The biological input parameters for the ten runs of Example 1	125
6-2 Percentage of biotransformed mass of Cr(VI) and developed biomass after 60 days for example 1	129
6-3 Biological input parameters for different runs of Example 2	157
6-4 Percentage of biotransformed mass of Cr(VI) after 50 days for example 2	164
7-1 Percentage of Cr(VI) biotransformed mass (bioremediation efficiency) and increase in biomass after 36 days	196
7-2 Percentage change in the bioremediation efficiency from case 2 to 1 and from case 3 to 2	217
8-1 Summary of differences between all Simulations	260
8-2 Bioremediation efficiency of the different simulations	263
8-3 Percentage of mass crossed sections 1 and 2	268

LIST OF FIGURES

Figure	Page
3.1 Comparison between the three methods and RKM for test problem 1.....	45
3.2 Comparison between the three methods and RKM for test problem 2.....	47
3.3 Comparison between the three methods and RKM for test problem 3.....	49
3.4 Comparison between the three methods, RKM, BioKemod and the lab data for test problem 4.	51
3.5 Comparison between QSSA, Shen and Wang 97, and lab data for example 1.....	54
3.6 Comparison between QSSA, Shen and Wang 97, and lab data for example 2.....	55
3.7 Comparison between QSSA, Shen and Wang 97, and lab data for example 3.....	56
4.1 Phases of growth occurring during a closed culture growth cycle in a limited environment, showing the changes in the organism's specific growth rate (Bull, 1974).....	59
4.2 Relationship between specific growth rate and growth limiting substrate concentration (Lynch and Poole, 1979)	59
4.3 Elements used in METABIOTRANS.....	70
5.1 Comparison between METABIOTRANS and analytical solution for test problem 1.....	90
5.2 Comparison between METABIOTRANS and analytical solution for test problem 2.....	91
5.3 Comparison between METABIOTRANS and analytical solution for test problem 3.....	94
5.4 Comparison between METABIOTRANS and analytical solution for test problem 4.....	97
5.5 Comparison between METABIOTRANS and analytical solution for test problem 5.....	101
5.6 Comparison between METABIOTRANS and analytical solution for test problem 6.....	103
5.7 Comparison between METABIOTRANS and analytical solution for test problem 7.....	105
5.8 Comparison between METABIOTRANS and analytical solution for test problem 8.....	110

5.9 Comparison between METABIOTRANS and analytical solution for test problem 9.....	113
5.10 Comparison between METABIOTRANS and analytical solution for problem 10.	115
5.11 comparison between METABIOTRANS, BioMOC, and Chen et al., simulation and lab data for test problem 11.	118
6-1a Layout of example 1.	123
6-1b Cr(VI) concentrations for runs 1 and 2 after 20 and 60 days.....	123
6-1c Biomass concentrations for run 2 after 20 days.	123
6-1d Biomass concentrations for run 2 after 60 days.....	123
6-2a Effect of microbes growth rate (μ_{\max}) on Cr(VI) and biomass concentrations.	128
6-2b Effect of Mmax on the spatial moments of Cr(VI) plume.....	132
6-2c Effect of Mmax on spatial moments of biomass distribution.	136
6-3a Effect of half saturation coefficient (K_c) on Cr(VI) and biomass concentrations.	138
6-3b Effect of K_c on the spatial moments of Cr(VI) plume.	139
6-3c Effect of K_c on spatial moments of biomass distribution.....	141
6-4a Effect of inhibition factor (K_i) on Cr(VI) and biomass concentrations.	142
6-4b Effect of K_i on the spatial moments of Cr(VI) plume.	144
6-4c Effect of K_i on spatial moments of biomass distribution.	145
6-5a Effect of death rate (B) on Cr(VI) and biomass concentrations.....	146
6-5b Effect of B on the spatial moments of Cr(VI) plume.	148
6-5c Effect of B on spatial moments of biomass distribution.....	149
6-6 Effect of the different biological parameters on the mass fluxes.	151
6-7 Layout of the example 2.	152
6-8a Cr(VI) Concentrations for Run 11.	155
6-8b Cr(VI) Concentrations for Run 12.....	156
6-8c biomass concentrations for Run 12 after 15 days.	158
6-8d biomass concentrations for Run 12 after 50 days.....	159

6-9 Effect of the different biological parameters on Cr(VI) concentrations.	160
6-10a Effect of μ_{\max} on biomass concentrations.	162
6-10b Effect of μ_{\max} on spatial moments of Cr(VI) plume.	163
6-11a Effect of K_c on biomass concentrations.	167
6-11b Effect of K_c on spatial moments of Cr(VI) plume.	169
6-12a Effect of K_i on biomass concentration.....	171
6-12b Effect of K_i on spatial moments of Cr(VI) plume.....	172
6-13a Effect of B on biomass concentrations.	174
6-13b Effect of B on spatial moments of Cr(VI) plume.	175
6-14 Mass fluxes at the three sections for Runs of Example 2.....	177
7-1a Layout of the problem.....	180
7-1 b Nutrient and electron donor pump positions for one well.	180
7-1 c Nutrient and electron donor pump positions for three wells.....	180
7-1 d Nutrient and electron donor pump positions for line source.	180
7-2a concentration lines of nutrient and electron donor for case 1.....	184
7-2b concentration lines of nutrient and electron donor for cases 2 and 3.	185
7-3a Effect of one well location on the Cr(VI) concentrations for case 1.	187
7-3b Effect of one well location on biomass concentrations for case 1.....	189
7-3c Effect of 1 well position on Cr(VI) plume's spatial moments for case 1.....	190
7-3d Effect of 1 well position on biomass spatial moments for case 1.....	193
7-4a Effect of three wells location on the Cr(VI) concentrations for case 1.....	198
7-4b Effect of three wells location on biomass concentrations for case 1.....	201
7-4c Effect of 3 well positions on Cr(VI) plume's spatial moments for case 1.	202
7-4d Effect of 3 well positions on biomass spatial moments for case 1.....	204
7-5a Effect of line source location on the Cr(VI) concentrations for case 1.....	206

7-5b Effect of line source location on biomass concentrations for case 1.....	208
7-5c Effect of line source position on Cr(VI) plume's spatial moments for case 1.	209
7-5d Effect of line source position on biomass spatial moments for case 1.	214
7-6a Effect of one well location on the Cr(VI) concentrations for case 2.	215
7-6b Effect of one well location on biomass concentrations for case 2.....	219
7-6c Effect of 1 well position on Cr(VI) plume's spatial moments for case 2.	221
7-6d Effect of 1 well position on biomass spatial moments for case 2.....	223
7-7a Effect of three wells location on the Cr(VI) concentrations for case 2 compared to case 1.....	224
7-7b Effect of three wells location on biomass concentrations for case 2.	226
7-7c Effect of 3 well position on Cr(VI) plume's spatial moments for case 2.	227
7-7d Effect of 3 well positions on biomass spatial moments for case 2.	229
7-8a Effect of line source location on the Cr(VI) concentrations for case 2 compared to case 1.....	230
7-8b Effect of line source location on biomass concentrations for case 2.	232
7-8c Effect of line source position on Cr(VI) plume's spatial moments for case 2.	233
7-8d Effect of line source position on biomass spatial moments for case 2.	235
7-9a Effect of one well location on the Cr(VI) concentrations for case 3 compared to case 2.....	237
7-9b Effect of one well location on biomass concentrations for case 3.....	238
7-9c Effect of 1 well position on Cr(VI) plume's spatial moments for case 3.	240
7-9d Effect of 1 well position on biomass spatial moments for case 3.....	241
7-10a Effect of three wells location on the Cr(VI) concentrations for case 3 compared to case 2.....	243
7-10b Effect of three wells location on biomass concentrations for case 3.	245
7-10c Effect of 3 well position on Cr(VI) plume's spatial moments for case 3.	246
7-10d Effect of 3 well position on biomass spatial moments for case 3.....	247

7-11a Effect of line source location on the Cr(VI) concentrations for case 3 compared to case 2.....	248
7-11b Effect of line source location on biomass concentrations for case 3.....	249
7-11c Effect of line source position on Cr(VI) plume's spatial moments for case 3.	251
7-11d Effect of line source position on biomass spatial moments for case 3.	252
8-1a Problem layout.	257
8-1b Cr(VI) concentration lines of deterministic cases.....	257
8-1c Biomass concentration lines of Simulation 2 at t=10 days.	257
8-1d Biomass concentration lines of Simulation 2 at t=35 days.....	257
8-1e Biomass concentration lines of Simulation 3 at t=10 days.	257
8-1f Biomass concentration lines of Simulation 3 at t=35 days.	257
8-2 Comparison between Cr(VI) and Biomass concentrations mean and variance for simulations 4 and 5.	262
8-3a Spatial moments of Cr(VI) plume for simulations 1, 2, 4, and 5.....	265
8-3b Mass fluxes of simulations 1, 2, 4 and 5.	267
8-4 Comparison between Cr(VI) and Biomass concentrations mean and variance for simulations 4 and 6.	270
8-5a Spatial moments for simulations 1, 3, 4, and 6.....	271
8-5b biomass plume's spatial moments for simulations 3 and 6.....	273
8-5c Mass fluxes of simulations 1, 3, 4 and 6.....	275
8-6 Comparison between Simulation 7 and deterministic cases.....	277
8-7 Comparison between Simulation 8 and deterministic cases (1 and 3).	279
8-8 Comparison between Simulation 3, 8 and 9.....	281
8-9a spatial moments for simulations 1, 2, 3, 7, 8, and 9.	282
8-9b Mass fluxes of simulation 1, 2 , 3, 7, 8, and 9.....	284
8-10a Comparison between concentration's mean and variance of Simulations 10 and 11...	286

8-10b Comparison between biomass mean concentrations of Simulations 10 and 11.....	287
8-10c Comparison between biomass concentration's variance of Simulations 10 and 11.....	288
8-11a Spatial moments for simulations 4, 5, 10, and 11.....	289
8-11b Mass fluxes of simulations 4, 5, 10, and 11.	291
8-12a Comparison between concentration's mean and variance of Simulations 12 and 13...	293
8-12b Comparison between biomass mean concentrations of Simulations 12 and 13.	294
8-12c Comparison between biomass concentration's variance of Simulations 12 and 13.....	295
8-13a Comparison between concentration's mean and variance of Simulations 12 and 14...	297
8-13b Comparison between concentration's mean and variance of Simulations 14 and 15.	298
8-13c Comparison between biomass mean concentrations of Simulations 14 and 15.	299
8-13d Comparison between biomass concentration's variance of Simulations 14 and 15.....	301
8-14a Comparison between the spatial moments of simulations 4, 6, 12, 13, 14, 15.....	302
8-14b comparison between the bacterial spatial moments of simulations 6, 12, 13, 14, 15.....	304
8-14c Mass fluxes of simulations 4, 6, 12, and 13, 14, 15.....	305
8-15(a) Comparison between concentration's mean and variance of Simulations 13 and 16.....	307
8-15(b) Comparison between biomass mean concentrations of Simulations 13 and 16.	308
8-15(c) Comparison between biomass concentration's variance of Simulations 13 and 16.	310
8-16a Comparison between the spatial moments of simulations 4, 6, 13, and 16.....	311
8-16b Comparison between the bacterial spatial moments of simulations 6, 13, and 16.....	312
8-16c Mass fluxes of simulations 4, 6, 13, and 16.....	313

Abstract of Dissertation Presented to the Graduate School
of the University of Florida in Partial Fulfillment of the
Requirements for the Degree of Doctor of Philosophy

METABIOTRANS: A 3-D FINITE ELEMENT MODEL FOR THE TRANSPORT AND
BIOTRANSFORMATION OF METALS IN THE SUBSURFACE

By

Mohamed M. A. Mohamed

August 2001

Chairman: Kirk Hatfield

Major Department: Civil and Coastal Engineering

Bioremediation technologies are increasingly being considered as an effective alternative in remediating contaminated subsurface environments. These technologies have been extensively applied to hydrocarbon-contaminated sites. However, in recent years, the importance of metals as a serious threat to the subsurface environment has created an interest in using in-situ biotechnologies to remediate groundwater contaminated by metals.

In this dissertation, a 3-D finite element model "METABIOTRANS" was developed, tested, and applied to several problems. METABIOTRANS is a multisolute-multispecies model that describes convective-dispersive-reactive transport in heterogeneous/anisotropic saturated porous media. The model uses Michaelis-Menten kinetics relationships to describe the reduction of available electron acceptors, the consumption of electron donors, and the growth of microbial biomass.

METABIOTRANS is used in several applications to simulate microbial-mediated reduction of Cr(VI), as an electron acceptor, in the presence of other electron donors and nutrients. In the first application, the model is used to evaluate the relative importance of different biological parameters that control natural attenuation of a Cr(VI) plume. The investigation involves an analysis of spatial moments of both Cr(VI) and microbial biomass distributions.

The transport model is next used to investigate the active remediation of a Cr(VI) plume. Many factors can affect the remediation efficiency including the number and position of nutrient and electron donor injection wells, the injection rate, and the toxicity of injected solutes on metal reducing bacteria. Several remediation system designs are simulated to assess efficacy of Cr(VI) removal.

In the final application of METABIOTRANS, several Monte Carlo simulations are conducted. The first suite of simulations are performed to assess the effects of both physical (hydraulic conductivity) and biological (biomass initial concentration) spatial heterogeneities on the natural attenuation of Cr(VI). Correlated and uncorrelated realizations of both heterogeneities are used in these simulations with different microbial growth rates. The second and last suite of Monte Carlo simulations are used to explore the effects of spatially variable electron donor availability on Cr(VI) attenuation.

CHAPTER 1

INTRODUCTION

1.1 Background

Groundwater is one of the most important low-cost, high-quality freshwater sources. In many parts of the world, groundwater is the primary source for domestic, industrial, and agricultural uses. In recent years attention has been drawn to the quality of the nation's groundwater resources. Hazardous substances, including radioactive compounds, pesticides, fertilizers, organic compounds, and heavy metals, have contaminated groundwater aquifers from such sources as municipal sanitary landfills and hazardous waste landfills.

The Department of Energy (DOE) has as many as 3000 sites contaminated with complex mixtures of radionuclides (e.g., uranium), metals (e.g., chromium), anions (e.g., nitrate), and chlorinated solvents (e.g., carbon tetrachloride, CT) (Riley and Zachara, 1992). Most of these sites are contaminated with chlorinated hydrocarbons (60%), radionuclides (56%), metals (55%), anions (45%), and fuel hydrocarbons (20%) (Riley and Zachara, 1992).

The most frequent classes of two-compound mixtures in groundwater are metals and chlorinated hydrocarbons (38 sites), metal radionuclide mixtures (36 sites), and metal anion mixtures (33 sites). Palmer et al. (1988) reported that about 50% of the super-fund sites as specified by the EPA between 1982 and 1986 contain inorganic compounds

including acids (18 sites), arsenic (30 sites), asbestos (2 sites), chromium (27 sites), heavy metals (79 sites), and various inorganics (50 sites).

Metals and metal components constitute the second most frequently reported type of subsurface contamination. Ghosh and Bupp (1992) reported that about three billion pounds of were released into the environment in 1987. An extremely toxic and pervasive groundwater metal contaminant, that has the DOE's interest, is chromium (Riley and Zachara, 1992). Metallurgical, chemical, and refractory are the major industries that contribute to chromium consumption and release into the environment. Other sources include the manufacture of pigments, printing inks, photographic films, corrosion inhibitors, fungicides, ferrous and non-ferrous alloys, domestic wastewater, dumping of sewage sludge, and leather tanning and electroplating industries. Hard chrome plating has been used extensively in the manufacturing of components for both commercial and military aircraft (Puls et al., 1994).

Several remediation methods, including physical, chemical, thermal, and biological methods, have been developed to clean-up contaminated groundwaters. The most commonly applied method is pump and treat. This method is expensive and its effectiveness is limited by both the rate of contaminant release to the aqueous phase and by the hydraulic properties of the aquifer. Bioremediation technologies, on the other hand, have become important alternative solutions to contamination problems in the environment. This is particularly true for the subsurface environment where economical and technical reasons play important roles in the selection of suitable remediation techniques.

Bioremediation technology has been extensively applied to organic wastes that are broken down into harmless compounds, ultimately carbon dioxide and water. However, because metals are elements that cannot be biodegraded, they can only be biotransformed from a harmful or toxic state to a less harmful or non-toxic state.

Dissimilatory metal reduction is an important microbial mechanism for removing metals from contaminated environments. This process couples the oxidation of a substrate, the electron donor, to the reduction of a metal, which acts as an electron acceptor (i.e., using the metal as an electron sink). When more than one electron acceptor is available, microorganisms use the one that gives them the most free energy. Lovely (1991) was among the first to recognize that microbially-mediated reduction of Fe(III) and Mn(VI) could be coupled to anaerobic oxidation of aromatic compounds and therefore could operate as a mechanism for the removing such contaminants in the subsurface environment. Later, Shen et al. (1996) reported that microorganisms are capable of using various metals, including Fe(III), Mn(IV), Se(VI), U(VI), Hg(II), As(V), and Cr(VI), as terminal electron acceptors in anaerobic systems.

Metal reduction usually produces an associated change in metal toxicity and solubility. Microbial reduction of Cr(VI), U(VI), As(V), and Se(VI) to their less soluble forms could offer a cost-effective mechanism for controlling the mobility of these metals in groundwater, and thus eliminate or mitigate their impacts on human health and subsurface ecosystems. The concept of using microorganisms to reduce metals to less toxic and/or less mobile forms and remediate metal contaminated groundwaters has captured the interest of the environmental engineering community and has fomented

research to develop models that describe metal transport and microbially-mediated metal reduction.

The focus of this research will be to study and model the physical and biological aspects of remediating aquifers contaminated with Cr(VI). Chromium exists in a variety of oxidation states from 0 to +6 in aqueous systems. However, Cr(VI) and Cr(III) are the principle forms found in the environment. Cr(VI) is highly soluble and toxic, whereas Cr(III) is much less toxic and tends to form insoluble hydroxides. Cr(III) is also quickly immobilized in sediments by adsorption whereas Cr(VI) is not. Several microorganisms have been found to reduce Cr(VI) within a wide range of chromium concentrations. Important factors affecting chromium reduction include the microbial biomass concentration, Cr(VI) concentration, temperature, carbon source, and pH. Therefore, microbial-mediated reduction of Cr(VI) to Cr(III) could be a potentially useful process for the active remediation or natural attenuation of the chromium contaminated aquifers.

1.2. Objectives and Scope of Study

Modeling the transport and biotransformation of metals in groundwater has only recently begun to receive the attention of groundwater modelers. Biologically mediated metal transformations can be described by a system of coupled non-linear partial differential transport equations. These equations include terms that describe physical (transport), chemical (sorption), and biological (biotransformation) processes. Several metal biotransformation studies, on both laboratory and field scales, have been identified in the literature; yet, modeling metal transport and biotransformation in saturated groundwater has only recently been used as a tool to design remediation systems.

The research presented in this dissertation reflects two primary goals, the first of which is to develop the 3-D advective-dispersive-reactive finite element model

(METABIOTRANS) that simulates the transport and biotransformation of metals in saturated groundwater. The second goal is to investigate aspects of remediating Cr(VI) contaminated groundwater in view of remediation system design and aquifer and biological heterogeneities. To achieve both goals, five basic objectives were accomplished. The first objective was to review the literature on recent studies concerning metals biotransformation in the subsurface on both laboratory and field scales. Based on the results from the literature review, the second objective was to derive the governing equations that describe transport and biotransformation of metals in the subsurface. The third objective was to review the numerical techniques that have been used to solve similar equations to the developed governing equations. Based on the results of reviewing the literature on numerical solution methods, the fourth objective was to solve the governing equations with a selected numerical method. Finally, the fifth objective was to use the numerical model as a tool for investigating the bioreduction of Cr(VI) in contaminated aquifers.

Once the model was developed, it was used to study three important aspects of remediating sites contaminated with Cr(VI). The first aspect was the relative sensitivity of single-valued biological parameters on Cr(VI) distribution in the subsurface. Results from this study are of value to those who are working in the field of groundwater bioremediation and to those interested in modeling metal biotransformations. The second aspect was the effects of nutrients and electron donor availability in the aquifer on remediating a Cr(VI) plume. The performance of several remediation scenarios was examined using METABIOTRANS. The final aspect of interest was to investigate effects of both physical and biological heterogeneities on Cr(VI) fate and transport. Several

Monte Carlo simulations, using METABIOTRANS, were used to evaluate fate and transport effects of both heterogeneities as well as the correlation between them. Finally, the Cr(VI) related fate and transport effects of a heterogeneous electron donor distribution are examined.

This dissertation is divided into nine chapters. This first chapter presents a brief introduction about bioremediation techniques that have been used to remediate groundwater and soils. Research goals and objectives are also included in this chapter.

The first part of the second chapter provides the biological and chemical background on chromium reduction and the different factors that affect this process. The second part provides a literature review of the mathematical methods, numerical techniques, and software used to describe the biodegradation process. The priorities of chapter three are 1) to provide simple numerical tools to predict metals concentrations in bioreactors and 2) to identify an accurate method for solving biological ODEs in METABIOTRANS.

The development of METABIOTRANS is presented in the fourth chapter. First, the mathematical background pertinent to describing biological reactions in the subsurface is presented. Then, the governing equations that quantify the physical (transport), chemical (sorption) and biological (biotransformation) processes in the subsurface are discussed. Next, the governing equations that characterize transport and biotransformation of metals in the subsurface are proposed. Finally, a description of METABIOTRANS' features, subroutines, and numerical techniques is presented.

Chapter five is devoted to validating METABIOTRANS. Eleven validation problems were employed to evaluate METABIOTRANS performance under different

groundwater flow, transport, and boundary conditions for one, two, and three-dimensional problems.

Chapters six, seven, and eight present three specific applications of METABIOTRANS. In chapter six, a sensitivity study is performed to assess the relative impacts of the different biological parameters on the Cr(VI) reduction process in both two- and three-dimensional transport scenarios. Chapter seven examines remediation design issues pertinent to treating Cr(VI) plumes. Next, in chapter eight, an evaluation is conducted to assess the sensitivity of model results to the impact of both physical and biological heterogeneities in the subsurface. Finally, chapter nine provides a summary, conclusions of the work presented, and recommendations for future work.

CHAPTER 2

LITERATURE REVIEW

2.1. Introduction

The widespread use of chromium and the frequent inadequate disposal of chromium based byproducts and wastes from industrial processes have created serious subsurface pollution problems. To address this problem, it has been suggested that Cr(VI), the most toxic and soluble form, may be reduced through microbial processes to Cr(III), the less toxic and less soluble form. The first part of this chapter provides a literature review on the process of reducing Cr(VI) to Cr(III) and the factors affecting this process while the second part examines mathematical models and numerical methods historically used to describe biodegradation in the subsurface.

2.2. Chromium Reduction

Chromium is present in subsurface systems and natural waters in the +3 and +6 oxidation states. In the more reduced +3 state, chromium is cationic and exists primarily as CrOH^{2+} and Cr(OH)_3^0 ; however, it may also complex with other inorganic and organic ligands. Cr(VI) exists primarily as CrO_4^{2-} and HCrO_4^- in natural systems. The latter two species are much more toxic, more soluble, and more mobile in environmental systems than the former ones (Pulse et al. 1994). Therefore, it is important to accurately characterize chromium speciation at hazardous waste sites.

Chromium reduction from Cr(VI) to Cr(III) occurs when another redox couple provides the three required electrons for reduction. In natural subsurface systems, the

typical redox couples are $\text{H}_2\text{O}/\text{O}_2$, $\text{Mn}^{2+}/\text{Mn}^{4+}$, NO_2/NO_3 , $\text{Fe}^{2+}/\text{Fe}^{3+}$, S^{2-} , SO_4^{2-} , and CH_4/CO_2 (Puls et al. 1994). Mineral phases capable of providing ferrous iron through dissolution or through surface-mediated reactions include magnetite, iron sulfides, and chlorite (Puls et al. 1994). Soil organic matter may also reduce Cr(VI). Several studies have indicated that chromium reduction is favored under acidic conditions regardless of the presence or absence of significant quantities of soil organic matter. Chromium oxidation appears to be largely governed by manganese oxides in subsurface systems that occur mainly as surface coatings, crack deposits, or finely disseminated grains. The proposed reaction involves the sequential adsorption of Cr(III) onto MnO_2 surface sites followed by oxidation by surface Mn^{4+} and subsequent release or desorption of Cr(VI) (Puls et al. 1994). Eary and Rai (1987) found that oxygen does not oxidize Cr(III) to any significant extent, and that the rate of Cr(III) oxidation by MnO_2 decreases with increasing pH and decreasing ratio of surface area to solution volume.

Adsorption reactions can play a significant role in the attenuation of chromium in natural subsurface systems. Cr(III) is strongly and specifically adsorbed, and as with most cationic species, its adsorption increases with increasing pH. For Cr(VI), adsorption is also strongly pH dependant, but increasing with decreasing pH. Zachara et al. (1989) have also shown decreased chromate adsorption with increasing dissolved inorganic carbon and sulfate. James and Bartlett (1983) showed decreased adsorption of chromate with increased phosphate and sulfate. Increases in ionic strength have also shown decreased chromate adsorption (James and Bartlett, 1983).

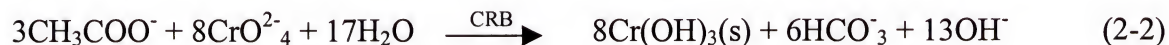
There is considerable evidence that Cr(VI) can be reduced by different microbes under both aerobic and anaerobic conditions. For example, Horitsu et al. (1987) reported

that *P. ambigua* G-1 reduced Cr(VI) rapidly from 150 to 60 mg/l after only 6 hrs of cultivation, but no further significant reduction occurred after 36 hrs. *E. cloacae* HO1 and *P. dechromaticans* were used by Wang et al. (1989) and Romanenko and Koren'kov (1977) to reduce Cr(VI). They reported that Cr(VI) reduction occurred only under anaerobic conditions. In addition to the above, Lovely and Phillips (1994) reported that *Desulfovibrio vulgaris*, a sulfate-reducing bacterium that is capable of reducing Fe(III) and U(VI), could also reduce Cr(VI) in the presence of H₂ as electron donor. Chen and Hao (1996) reported the reduction of Cr(VI) by mixed cultures; they also studied the effect of the different environmental factors, including pH, temperature, and other electron acceptors, on the reduction process.

The biotransformation or the microbial reduction of Cr(VI) and the consequent precipitation of Cr(III) can be illustrated by the following equation:



where CRB indicates Cr(VI)-reducing bacteria. It is clear from this equation that three electrons are needed to reduce Cr(VI) to Cr(III). An electron donor compound that provides these electrons must be present during the reduction process. If the electron donor is the acetate, the reduction equation could be written as:



Lovely (1993) concluded that the Cr(VI) reduction process does not produce enough energy to support bacterial growth. Therefore, nutrients should be present for the purpose of bacterial growth.

Bacteria must be able to tolerate the toxicity of Cr(VI) for reduction to occur. Chromium-reducing bacteria have a finite tolerance for Cr(VI). Bacterial resistance to

Cr(VI) has been found in *P. ambigua*, *P. fluorescence*, *P. aeruginosa*, *Alcaligenes eutrophus*, *Streptococcus lactis*, *Escherichia coli*, and *Entrobacter cloacae* (Ohtake and Silver, 1994). Cr(VI) reduction may be a process by which organisms decrease local levels of Cr(VI) to tolerable levels or it may also be a fortuitous reaction that is catalyzed by enzymes that have other physiological functions.

Traditional techniques for remediating Cr(VI)-contaminated water involve reduction of Cr(VI) to Cr(III) by chemical or electrochemical means at pH greater than 5 followed by precipitation and finally filtration or sedimentation (Eary and Rai, 1988). The discovery of microorganisms that reduce Cr(VI) to Cr(III) has led to applications in the bioremediation field which are potentially more cost effective techniques than traditional ones. Currently, there are two strategies for immobilizing Cr through microbial transformation, namely biosorption/reduction and gaseous bioreduction. Bioreduction of Cr(VI) can occur as a direct result of microbial metabolism. It takes place under both aerobic and anaerobic conditions, and has been shown to be enzymatic in nature (Bopp et al. 1983; Horitsu et al. 1987).

Cr(VI) can be the terminal electron acceptor in the oxidation of organic matter, or it can be reduced as a detoxification mechanism (Wood and Wang, 1983). Romanenko et al. (1976) and Romanenko and Koren'kov (1977) first proposed using Cr(VI)-reducing bacterial isolates in removal of Cr(VI) from various industrial effluents. Since then, a wide variety of bacterial strains with accelerated Cr(VI) reducing capabilities have been isolated from Cr(VI)-contaminated water, soils and sediments (Table 2.1). It is evident that these organisms can mediate bioreduction of Cr(VI). On the other hand, gaseous bioreduction involves microbial reduction of Cr(VI) by a metabolic byproduct (in this

case H_2S), which is produced in anaerobic environments by sulfate-reducing bacteria. This technology has shown some promise for both anaerobic bioreactor systems and possibly in situ applications.

Previous studies have revealed the potential of biological detoxification of chromium through microbial reduction of Cr(VI) to Cr(III) (Shen and Wang, 1995). Most of these studies appear to have been conducted with the potential of microbial Cr(VI) reduction as a remediation tool in mind. The applied aspects of this process have been most extensively studied in *E. cloacae* strain HO1.

Initial studies with *E. cloacae* demonstrated that high concentrations of Cr(VI) could be rapidly reduced, but Cr(III) was difficult to remove from the culture (Lovely, 1995). Most of the soluble chromium could be removed from solution with Cr(VI) reduction if the cells of *E. cloacae* were placed on one side of an anion exchange membrane which permitted CrO_4^- but not Cr^{3+} to pass through. With this method *E. cloacae* could reduce an initial concentration of 1 mM Cr(VI) to 0.04 mM dissolved chromium within 55h (Lovely, 1995). However, the successful removal of dissolved chromium during growth in heterotrophic growth medium could not be matched in contaminated waters. Cr(VI) was not reduced when a cell suspension of *E. cloacae* was added directly to the chromate-containing industrial effluent (Lovely, 1995).

It was speculated that heavy metals were responsible for the inhibition of chromium reduction. Further testing of heavy metals toxicity indicated that the following metal ions inhibit Cr(VI) reduction: Hg^{2+} , Ag^+ , Cu^{2+} , Zn^{2+} , Ni^{2+} , Co^{2+} , and Mn^{2+} (Lovely, 1995). Cr(VI) was not reduced in an industrial effluent that contained Cu^{2+} (390 μM),

Table 2-1 Bioremediation of chromium: previous studies.

Mechanism	Organism	Description and effectiveness
Bioreduction	<i>Pseudomonas ambigua</i> G-1	Cr(VI) concentration was lowered from 150 to 35 mg L ⁻¹ over 36 hours in liquid media. Shown to be enzymatic.
Bioreduction	P. K-21	Reduction rates were proportional to the glucose concentration in the medium. Cr(VI) concentration dropped from 200 to 100 mg L ⁻¹ in the presence of 0.2% glucose and to ~0 mg L ⁻¹ with 1% glucose after 40 days.
Bioreduction	<i>P. fluorescens</i> LB300	Reduced about half of Cr(VI) in media spiked with 40 mg L ⁻¹ Cr(VI) over 48 hours.
Biosorption	<i>Oscillatoria</i> sp.	Algal cultures removed 20% of Cr(VI) from water spiked at levels from 1-20 mg L ⁻¹ .
Biosorption	<i>Arthrobacter</i> sp. <i>Agrobacter</i> sp.	Accumulated Cr(VI) with increasing concentration gradient of Cr(VI) up 400 mg L ⁻¹ (<i>Arthrobacter</i> sp.) and 100 mg L ⁻¹ (<i>Agrobacter</i> sp.)
Bioreduction/ biosorption.	<i>P. areuginosa</i> S 128	Removed 15-25% of Cr(VI) from liquid media spiked with 1000 mg L ⁻¹ Cr(VI) over 72 hrs. glucose enhanced the removal rate.
Bioreduction	Sulfate reducing bacteria	Cr(VI) concentration in water was lowered from 11 to 0.21 mg L ⁻¹ with addition of sulfate and acetate in an anaerobic bioreactor which produced H ₂ S, reducing Cr(VI).
Bioreduction	<i>E. cloacae</i> HO1	Cr(VI) at 182 mg L ⁻¹ in wastewater was completely reduced at high cell densities with appropriate nutrient addition.
Bioreduction	<i>E. cloacae</i> HO1	90% of Cr(VI) was removed from water with an initial Cr(VI) concentration of 208 mg L ⁻¹ .

Table 2-1 Bioremediation of chromium: previous studies (cont.)

Mechanism	Organism	Description and effectiveness
Bioreduction/ biosorption	Sulfate reducing bacteria	100% Cr(VI) removal was achieved in water with Cr(VI) concentration up to 150 mg L ⁻¹ .
Bioreduction/ biosorption	Chlamydomonas sp.	An average of 30% Cr(VI) removal from water with initial concentration of 0.2 mg L ⁻¹ in an aerobic bioreactor system.
Bioreduction	P. putida PRS2000	Cr(VI) concentration was reduced from 1.04 to 0.36 mg L ⁻¹ over 90 hrs. reduction was shown to be associated with soluble protein in cells. Process was unaffected by SO_4^{2-} or NO_3^- .
Bioreduction	Chlorella vulgaris; Zoogloea ramigera	Maximum adsorption was seen at pH =2 and at 25-50 °C for both organisms.
Bioreduction	Consortium of bacteria	Reduced all CrO_4^{2-} in liquid media at 30 mg L ⁻¹ after 48 hrs.
Bioreduction	Aeromonas dechromatica	Effective reduction observed with appropriate carbon source, $\text{Cu}(\text{OH})_2$, Zn^0 , and $\text{Zn}(\text{OH})_2$, promoted bioreduction, Cd had no effect, and Ni, Fe(III) and Cu inhibited the transformation.
Bioreduction	Unidentified pure bacterial cultures	Reduced 40-60% of Cr(VI) added to liquid media at 10 and 25 mg L ⁻¹ ; approximately 50% at 60 mg L ⁻¹ , and 10% at 120 mg L ⁻¹ over 18 days with no additional nutrient supplement.
Bioreduction	Indigenous soil organisms.	Removed up to 98% of Cr(VI) added in irrigation water with a Cr(VI) concentration of 1.0 mg L ⁻¹ . Important factors shown to be organic matter loadings, O ₂ status and residence time in bioactive zone.

(Source: Frankenberger and Losi, 1995)

Mn^{2+} (480 ηM), and Zn^{2+} (0.3 ηM) (Lovely, 1995). Even when the heavy metals were removed, only 40% of the Cr(VI) could be reduced. *Desulfovibrio vulgaris* might be more useful than *E. cloacae* for chromate bioremediation because sulfate and a variety of metals had no effect on Cr(VI) reduction by *D. vulgaris* (Lovley, 1995). An additional benefit was that *D. vulgaris* could reduce Cr(VI) in a simple mineral medium with H_2 serving as the electron donor. It did not require the rich heterotrophic medium required by *E. cloacae* (Lovely, 1995).

In another study investigating the potential practical application of microbial Cr(VI) reduction, a mixed microbial community that was established as a biofilm on rotating plastic disks readily reduced Cr(VI) in synthetic waste water (Coleman and Padran, 1991). Cr(VI) concentrations of as high as 200 mg L^{-1} were effectively treated to levels of 2-3 mg L^{-1} in the final effluent. The microorganisms responsible for the reduction were not determined.

Shen et al. (1996) conducted a series of microcosms and enrichments to evaluate the potential for microbially mediated Cr(VI) reduction linked to benzoate catabolism. Bacterial degradation of benzoate with transport of electrons to Cr(VI) was achieved using nitrate or molecular oxygen as an initial stimulator. After depletion of nitrate or oxygen, microcosms and enrichments still retained the capacity for benzoate degradation linked to Cr(VI) reduction. Experiments demonstrated that benzoate degradation occurred concurrently with the reduction of Cr(VI) and was strongly dependent on the presence of Cr(VI). In other words, benzoate degradation proceeded as long as Cr(VI) was present, ceased when Cr(VI) was completely removed, and continued once Cr(VI) was added. Furthermore, the observed benzoate removal was linearly correlated with Cr(VI)

consumed and the stoichiometric ratio was in good agreement with the theoretical ratio for the complete oxidation of benzoate to carbon dioxide coupled to the reduction of Cr(VI) to Cr(III). The addition of nitrate up to a concentration of 5.0 mM did not inhibit Cr(VI) reduction but enhanced benzoate degradation in the enrichments.

In a defined coculture of a Cr(VI) reducer, *E. coli* ATCC 33456, and a phenol degrader, *P. putida* DMP-1, simultaneous reduction of Cr(VI) and degradation of phenol was observed (Shen and Wang, 1995). When Cr(VI) was present in the coculture, quantitative transformation of Cr(VI) into Cr(III) proceeded with simultaneous degradation of phenol. Cr(VI) reduction was correlated to phenol degradation in the coculture as demonstrated by a regression analysis of the cumulative reduction of Cr(VI) and the cumulative phenol degradation. Both the rate and extent of Cr(VI) reduction and phenol degradation were significantly influenced by the population compositions of the coculture. Although Cr(VI) reduction occurred as a result of *E. coli* metabolism, the rate of phenol degradation by *P. putida* may become a rate limiting factor for Cr(VI) reduction at a low population ratio of *P. putida* to *E. coli*. Phenol degradation by *P. putida* was very susceptible to the presence of Cr(VI), whereas Cr(VI) reduction by *E. coli* was significantly influenced by phenol only when phenol was present at high concentrations (Shen and Wang, 1995).

In another study, fermented molasses and sulfate were injected into a shallow aquifer that was contaminated with Cr(VI) and other metals (DeFilippi 1994). The Cr(VI) was almost completely reduced to Cr(III) and other metals were precipitated via sulfate reducing bacteria. Another study (Losi et al. 1994a) indicated that a contaminated water with 1 mg/l of Cr(VI) was treated by irrigating it onto an organic-amended soil. The

concentration of the Cr(VI) in the drainage water was below 50 µg/l. It was shown that more Cr(VI) reduction could occur under lower oxygen concentration conditions (Losi et al. 1994b). The potential for biological reduction of Cr(VI) in a Cr(VI)-contaminated aquifer was evaluated by inoculating aquifer material into an anaerobically prepared mineral salts medium (McInerney et al. 1995). The extent and the rate of the Cr(VI) reduction by aquifer microcosms were not affected by the addition of exogenous electrons donors such as glucose, acetate, formate, or benzoate, indicating that the aquifer material had sufficient levels of endogenous electron donors to support Cr(VI) reduction.

Cr(VI) usually exists in the environment in low levels and thus could be reduced to Cr(III) by organic matter or other reductants (Niebore and Jusys, 1988). However, the presence of Cr(VI) at higher levels could inhibit the reducing capability of the environmental systems, thus allowing Cr(VI) to persist in potentially toxic concentrations. Many bacterial strains have been reported to have resistance to Cr(VI). For example, Luli et al. (1983) reported that of 89 isolates obtained from metal-contaminated river sediment, 47% were resistant to 100 mg/l of Cr(VI), and 20% were resistant to 250 mg/l. Bopp et al. (1983) reported that an isolate of *P. fluorescence* LB300 was able to grow in a minimal salt medium with as high as 270 mg/l of Cr(VI). The growth rate of the strain was not affected at 65 mg/l of Cr(VI). Other Cr(VI)-resistant bacterial strains such as *P. ambigua* G-1 and *E. cloacae* HO1 were also isolated (Horitsu et al. 1978; Wang et al. 1989). *P. ambigua* could tolerate Cr(VI) concentrations as high as 2000 mg/l. Analytical results revealed that *P. ambigua* could uptake a significant amount of Cr(VI) with 87% in the soluble fraction and 13% in the insoluble fraction. A summary of some of the Cr(VI)-resistant bacteria that have been reported is given in Table 2-1.

Gorby et al. (1994) evaluated a biotic approach for remediating subsurface sediments and groundwater contaminated with carbon tetrachloride (CT) and chromium. They added dissimilatory Fe(III)-reducing bacteria strain BrY to sealed, anoxic flasks containing Hanford site groundwater, natural subsurface sediments, and either CT or Cr(VI). Dissimilatory reducing bacteria, such as the anaerobic strain BrY, couple the reduction of a wide range of multivalent metals, including iron, chromium, and uranium, to the oxidation of reduced organic matter or hydrogen (Lovley, 1993). These bacteria gain energy for growth by the enzymatic process under anoxic conditions. With lactate as the electron donor, these microorganisms reduced Cr(VI) to Cr(III). Gorby et al. (1994) reported that Cr(VI) was reduced by a direct enzymatic reactions in the presence or absence of Fe(III)-bearing sediments. This results show that Fe(III) reducing bacteria provide potential for transforming CT and for reducing Cr(VI) to Cr(III).

2.3. Factors affecting microbial reduction of Cr(VI)

1. Biomass density: many studies have indicated that the initial cells density has significant effect on the Cr(VI) reduction rates (Ohtake et al. 1990a,b and c; Shen and Wang 1994a; and Chen and Hao 1996).
2. Initial Cr(VI) concentration: the addition of Cr(VI) to a cell-growing culture led to a transient decrease in cell viability, regardless whether the culture was aerobic or anaerobic (Wang et al. 1989; Komori et al. 1990; Ohtake et al. 1990b).
3. Carbon source: many organic compounds can serve as electron donors for the Cr(VI) reduction process. Ohtake et al. (1990d) reported that acetate, ethanol, malate, succinate, glycerol, and amino acid mixtures are effective electron donors for the reduction of Cr(VI) by *E. cloacae* HO1. They also indicated that glucose, citrate, pyruvate, and lactate supported anaerobic growth, but only limited amounts of

reduction were observed with those organic compounds. Shen and Wang (1994a) indicated that cells of *E. coli* ATCC 33456 were able to reduce Cr(VI) by using a variety of electron donors, including glucose, acetate, propionate, glycerol and glycine. Many other researchers have studied Cr(VI) reduction in the presence of different electron donors (Romanenko and Koren'kov, 1977; Ohtake et al. 1990c; Fujie et al. 1994; and Chen and Hao, 1996).

4. Temperature and pH: Cr(V) reduction by *E. coli* ATCC 33456 occurred within a pH range of 3.0 to 8.0 (Shen and Wang, 1994a), while reduction by *E. cloacae* HO1 was observed only at pH levels of 6.0 to 8.5 (Ohtake et al. 1990b). Both reduction processes by the two bacteria occurred at temperature of 10 to 50°C, and the effect of temperature on the reduction rate was found to follow the Arrhenius equation over the range of 10 to 30°C, with a wide temperature-dependant relationship. The optimum pH was 7.0 and the optimum temperature was 37°C for both bacteria. Different scientists studied the effect of temperature and pH on the Cr(VI) reduction (Komori et al. 1989; Chen and Hao, 1996; and Suzuki et al. 1992).
5. Dissolved Oxygen: Komori et al. (1990b) reported that *E. cloacae* HO1 cells grew much faster under aerobic conditions, but no Cr(VI) decrease was detected with the aerobic cultures. They also concluded that rates of Cr(VI) reduction decreased when increasing the initial concentration of O₂, and that an O₂ concentration above 4.5mg/l strongly inhibits the Cr(VI) reduction. In another study, Shen and Wang (1994b) found that the dissolved oxygen is an uncompetitive inhibitor to the Cr(VI) reduction with *E. coli*. They reported that the inhibitor coefficient was 1.1 mg DO/l.

6. Oxidation-reduction potential (ORP): the introduction of Cr(VI) into the bacterial growth system results a sharp jump of ORP (Gvozdyak et al., 1986). The reduction of the Cr(VI) to Cr(III) is accompanied by a transfer of three electrons, and as a result the ORP gradually decreases. Many other researchers studied the effect of ORP as an environmental factor on the Cr(VI) reduction (Llovera et al. 1993; Ohtake and Hardoyo, 1992; Shen and Wang 1994b; and Fujie et al. 1994).

2.4. Kinetics of Microbial Cr(VI) Reduction

The Michaelis-Menten enzymatic equation has been used to predict Cr(VI) reduction by Cr(VI) reduction bacteria. Ishibashi et al. (1990) determined the apparent Michaelis-Menten constant (K_c) and the maximum specific reduction rate (μ_{max}) to be $40\mu\text{M CrO}_4^{2-}$ and 6 nmol/mg protein/min, respectively, for *P. putida*. The same coefficients were found to be $13\mu\text{M CrO}_4^{2-}$ and 27 nmol/mg protein/min, respectively, for *P. ambigua* (Suzuki et al. 1992).

Ohtake et al. (1990b) employed a substrate inhibition model to fit the experimental data of *E. cloacae* HO1 (Table 3). The best fit parameters were: $\mu_{max} = 2.0$ mg Cr(VI)/mg cell hr, $K_c = 0.057$ mg Cr(VI)/l, and $K_i = 37$ mg Cr(VI) /l. The same model was further investigated by Yamamoto et al. (1993), who considered two types of bacterial cells: induced Cr(VI) resistance cells and uninduced sensitive ones. Only resistance cells were assumed to have the ability to reduce Cr(VI). The death rate of the sensitive cells was proportional to the Cr(VI) concentration, while the death rate of the resistance cells was negligible.

The Haldand-type substrate inhibition model was proposed to characterize the rate and extent of microbial Cr(VI) reduction by *E. coli* ATCC 33456 (Shen and Wang 1994b)

(Table 2.2). The inhibition term C^2/K_i was eliminated at $C \leq 160$ mg Cr(VI)/l for the simplification of the model. Modifications to the Michaelis-Menten enzymatic equation that describe the Cr(VI) reduction were performed to incorporate the availability of electron donors. Models developed in this dissertation will use the modified equations in the reaction term of the governing equations, as discussed in the following section.

Table 2-2 Kinetic models of Cr(VI) reduction in pure and mixed cultures.

Reference	Strain	Kinetic Model
Ohtake et al. 1990b Yamamoto et al. 1993	<i>E. cloacae HO1</i>	$\mu = \frac{\mu_{\max} C}{(K_c + C) \left(1 + \frac{C}{K_i} \right)} \quad (2-3)$
Shen and Wang, 1994b Chen and Hao, 1996	<i>E. coli 33456</i>	$\mu = \frac{\mu_{\max} C}{(K_c + C + \frac{C^2}{K_i})} \quad (2-4)$

Where C is the Cr(VI) concentration (mg/l), μ is the specific Cr(VI) reduction rate (mg Cr(VI)/mg cells .hr), μ_{\max} is the maximum specific Cr(VI) reduction rate (mg Cr(VI)/mg cells), K_c is the half-saturation constant for Cr(VI) (mg/l), and K_i is the inhibition constant of Cr(VI) (mg/l).

2.5. Modeling Biodegradation in the Subsurface

2.5.1. Background

Biodegradation is a manifestation of a host of coupled biochemical reactions mediated by microorganisms. This process couples the oxidation (loss of electrons) of an electron donor (usually hydrocarbons) and the reduction (gain of electrons) of an electron acceptor. When oxygen is available, it often acts as the electron acceptor and this process is called aerobic biodegradation. On the other hand, when oxygen is not present anaerobic biodegradation occurs and microorganisms use other organic or inorganic chemicals as alternative electron acceptors. Fermentative, denitrifying, iron-reducing,

sulfate-reducing, and methanogenic conditions are most common anaerobic biodegradation regimes. In fermentation, microorganisms utilize the substrate as both electron acceptor and electron donor. Denitrifying bacteria use NO_3^- as the electron acceptor, and reduce it into NO_2^- , N_2O , or N_2 . Iron and sulfate-reducing bacteria utilize ferric iron and SO_4^{2-} as electron acceptors respectively, and reduce them to ferrous iron and H_2S respectively. Methanogens are methane-producing bacteria that utilize CO_2 as an electron acceptor.

Bedient et al. (1994) listed six basic requirements of biodegradation as:

1. Existence of the appropriate organisms.
2. Energy source: organic carbon is required as an energy source and is used by the organisms for cell maintenance and growth. The organic carbon is transformed into inorganic carbon, energy, and electrons.
3. Carbon source: about 50% of the dry weight of bacteria is carbon. Organic carbon, as a carbon source, is used with energy to generate new cells.
4. Electron acceptors: some chemicals should accept the electrons released from the energy source. Typical acceptors include O_2 , NO_3^- , SO_4^{2-} , and CO_2 .
5. Nutrients: the required nutrients include nitrogen, phosphorus, calcium, magnesium, iron, and trace metals.
6. Acceptable environmental conditions such as: temperature, pH, salinity, hydrostatic pressure, radiation, and presence of toxic materials.

Microbial investigations of the subsurface have revealed that all aquifers examined thus far support microbes. Typical microbial numbers range from 1×10^5 to 1×10^7 cells per gram dry weight cells/gdw (Ghiorse and Balkwill, 1983; Wilson et al.

1983; Balkwill and Ghiorse, 1985; and Beeman and Suflita, 1987). Relatively high numbers of microorganisms have been detected in contaminated aquifers at different depths and in various geological formations. The microorganisms were found to be small, capable of responding to an influx of nutrients, and primarily attached to solid surfaces (Suflita, 1989).

2.5.2. Mathematical and Numerical Modeling of Biodegradation in the Subsurface

The mathematical modeling of a groundwater process is quite complex, involving three important phenomena that occur simultaneously; namely, groundwater flow, transport of different chemical species, and microbial biodegradation kinetics. The importance of microbial activity in degrading organic substances in both subsurface and deep groundwater has been widely recognized over the last two decades. For instance, Harvey et al. (1984) and Chapelle et al. (1995) have addressed role of the microbial activity in degrading organic substances in the shallow groundwater, while Lovley and Capelle (1995) concentrated in the deep groundwater. In these works, evidence was provided that bacterial activity can be correlated to the plumes of organic substrates.

Many authors have addressed various numerical approaches to solve the flow equation and the transport equation, which includes the bioremediation kinetics. Molz et al. (1986) and Widdowson et al. (1988) used a finite difference technique to solve the system of equations in 1-D, while Kinzelbach et al. (1991) and Frind et al. (1990) used the same technique for the 2-D problem. Chen et al. (1992), Tracy et al. (1993), and Tracy et al. (1994) used finite elements techniques, while Chiang et al. (1989) used finite elements techniques with the modified method of characteristics (MMOC), which was applied by Wood et al. (1994 and 1995). Kindred and Celia (1989) presented a conceptual model of the subsurface contaminant transport with biodegradation, which

incorporate both aerobic and anaerobic reactions. They used Michaelis-Menten kinetics to describe nutrient uptake and included several uptake inhibition factors in the model. One-dimensional numerical experiments were conducted by Celia et al. (1989) using an optimal test function (OTF) method, conceptualized by Kindred and Celia (1989), to solve the nonlinear system of equations that is closely related to the Galerkin method. Chen et al. (1992), Wood et al. (1995), Malone et al. (1993) and Wood et al. (1994) focused on the parameter calibration of biodegradation kinetics.

Bosma et al. (1988) presented a one-dimensional model which can be used to simulate the behavior of xenobiotic chemicals in soil columns, by including terms that describe the biological transformation of xenobiotic in the model. They used Monod-kinetics equations to describe the microbial growth. Bosma et al. concluded that the model was useful as a tool for the investigation of bacterial degrading activities in soil columns.

Borden and Bedient (1986) and Rifai (1989) modified the Konikow-Bredeheoft (1978) code (MOC) to simulate aerobic biodegradation by assuming an instantaneous stoichiometric biochemical oxidation of the soluble organics. Widdowson et al. (1987) employed a first order finite difference Eulerian-Lagrangian scheme for transport and used a Newton Raphson method to treat the nonlinear reaction terms. Their transport scheme is equivalent to a finite difference modified method of characteristics, which was analyzed by Douglas and Russel (1982). Borden and Bedient (1986), Refai (1989), and Widdowson et al. (1987) have compared their numerical results with field data.

Wheeler and Dawson (1988) presented another numerical method for approximating the Borden and Bedient (1986) equations. This work represents extensions

of earlier work of Douglas and Russel (1982), Russel (1985), and Russel et al. (1986). Numerical experiments using this method have been reported in Dawson et al. (1986 and 1987a, b), Wheeler and Dawson (1988), and Wheeler et al. (1987).

De Blanc et al. (1996) developed a 3-D finite difference model that simulates the flow of a non-aqueous phase liquid (NAPL) in a porous medium, the transport of NAPL components from the NAPL phase into the aqueous phase, and the biodegradation of aqueous phase NAPL constituents. The model included biodegradation equations that describe the transport of dissolved substrate and electron acceptors into attached biomass, the loss of substrate and electron acceptor through biodegradation reactions, and the resulting growth of the attached biomass. They included nonlinear Monod kinetic terms in the system of biodegradation equations, which were ordinary differential equations. They tested four different numerical methods to solve that system of equations; namely, (1) a fully explicit (Euler's) method, (2) a Runge-Kutta-Fehlberg (RKF) method, (3) an Adams-Moulton method, and (4) Gear's method. They compared the results of each method based on the accuracy and speed of convergence. They concluded that Gear's method solves the system of equations that include mass transfer more efficiently than RKF method. They also concluded that Gear's method and RKF method perform similarly when solving the system of equations that do not include mass transfer terms.

MacQuarry et al. (1990) employed an iterative principle direction finite-element technique to develop numerical solution for the transport of biodegradable organic solutes in groundwater. They combined Monod equations with the advection-dispersion equation to represent the biological and physical processes affecting the fate and transport of an organic solute and electron acceptor and the growth of a microbial population. By

using this iterative principle, efficiency is achieved by decoupling each of the 2-D transport equations into a series of 1-D equations. They compared the results from the model with column experiment results to calibrate the model. The comparison suggested that the model gave good results.

2.6. Available Numerical Software Packages for Simulating Biodegradation in the Subsurface

Several Numerical models exist to simulate the advection-dispersion-reaction problem in the subsurface; however, none of which are developed for simulating the biotransformation of metals. In addition, predictions for transient microbial distributions in the subsurface were not presented. A brief introduction of the features, capabilities, and limitations of some of these models is provided in the following sections.

2.6.1. BIO1D

BIO1D is a one-dimensional modeling code that simulates biodegradation and sorption in contaminant transport. The objective of BIO1D was to provide an interactive, user-friendly microcomputer software package to serve as an educational tool for understanding the relative importance of various physicochemical and biochemical processes. The BIO1D code is especially useful for analyzing laboratory data from column experiments.

BIO1D includes a preprocessor that enables the user to prepare input data interactively. The preparation includes features such as inputting new data and storing them in a disk file, or reading data from a disk file and editing them. The BIO1D preprocessor has built-in error recovery procedures to forgive most input errors made by a user during interaction.

A run-time monitor is displayed and updated constantly as the simulation progresses. The user may run the simulation for a certain time period, monitoring its behavior, and then choose a different set of run-time options for the rest of the simulation. The options include printing concentrations, cumulative mass balance information, and selecting plotting intervals. Advanced debugging options such as iteration information, nodal mass balance tables, displacement matrices, and matrix solver monitors are also available at run time.

Features

1. Advective and dispersive transport of a hydrocarbon and an electron acceptor (e.g., oxygen).
2. Aerobic biodegradation using modified Monod function.
3. Anaerobic biodegradation for both substances.
4. Linear, Freundlich, and Langmuir adsorption isotherms for both substances.
5. Dirichlet, Neumann, and Cauchy boundary conditions modified to include first-order degradation.
6. Cumulative mass balance report.
7. Output is in a format required by SURFER and other graphics packages.

Limitations

1. Transport is one-dimensional.
2. Flow field is uniform (constant velocity).
3. Material properties of both substances are uniform throughout the medium.
4. Only one reactive substrate is considered per simulation.
5. Microbial density is assumed temporally constant and spatially uniform.

2.6.2. Bioplume I, II, and III:

Borden and Bedient (1986) developed the Bioplume I model. Bioplume I is based on the assumption that aerobic biodegradation of hydrocarbons is often limited by the availability of dissolved oxygen in groundwater aquifers. Borden and Bedient simulated the aerobic biodegradation of hydrocarbons as an instantaneous reaction between the hydrocarbon and oxygen. Rifai et al. (1988) developed the Bioplume II model by incorporating the concepts developed by Borden and Bedient into the U. S. Geologic Survey (USGS) two-dimensional solute-transport model MOC (Konikow and Bredehoeft, 1978). The Bioplume II model tracks two plumes: oxygen and the hydrocarbon. The two plumes are superimposed to determine the resulting concentrations of oxygen and hydrocarbon at each time step. Anaerobic biodegradation in Bioplume II was simulated as a first-order decay in hydrocarbon concentrations.

Bioplume III is a two-dimensional, finite difference model for simulating the biodegradation of hydrocarbons in groundwater. The model simulates both aerobic and anaerobic biodegradation processes in addition to advection, dispersion, sorption and ion exchange. Bioplume III simulates the biodegradation of an organic contaminant using a number of aerobic and anaerobic electron acceptors: oxygen, nitrate, iron (III), sulfate, and carbon dioxide.

Bioplume III is based on the USGS Method of Characteristics Model (MOC) dated July 1989 (Konikow and Bredehoeft). The Bioplume III code was developed primarily to model the natural attenuation of organic contaminants in groundwater due to the processes of advection, dispersion, sorption and biodegradation. Bioplume III solves the transport equation six times to determine the fate and transport of the hydrocarbons and the electron acceptors/reaction byproducts. For the case where iron (III) is used as an

electron acceptor, the model simulates the production and transport of iron (II) or ferrous iron.

Three different kinetic expressions can be used to simulate the aerobic and anaerobic biodegradation reactions. These include first-order decay Monod kinetics. The principle of superposition is used to combine the hydrocarbon plume with the electron acceptor plume(s).

2.6.3. HYDROGEOCHEM

HYDROGEOCHEM is a coupled model of hydrologic transport and geochemical reaction in saturated-unsaturated media. It is designed to simulate transient and/or steady-state transport of N_a , aqueous components and transient and/or steady-state mass balance of N_s adsorbent components and ion-exchange sites. Along the transport path, HYDROGEOCHEM computes the species distribution of N component species, M_x complexed species, M_y adsorbed species, M_z ion-exchanged species, and M_p potentially precipitated species.

Physical, hydrological and chemical settings are as follows:

1. Media: Heterogeneous and Anisotropic.
2. Flow Conditions: Saturated-Unsaturated Flows.
3. Hydrologic Processes: Advection, Dispersion and Diffusion.
4. Chemical Processes: Aqueous Complexation, Adsorption/Desorption (Surface Complexation, Constant Capacitance, and Double Layer Approaches), Ion-Exchange, Precipitation/Dissolution, Redox, and Acid-Base Reactions.
5. Source/Sink: Spatially- and Temporally-Dependent Element and Point Sources/Sinks.
6. Initial Conditions: Prescribed Initial Condition or the Simulated Steady-State Solution as the Initial Condition.

7. Boundary Conditions: Prescribed Total Analytical Concentrations on Dirichlet Boundaries, Prescribed Fluxes on Flow-In Boundaries, Natural Advective Fluxes on Flow-Out Boundaries - All Boundary Values (Concentrations or Fluxes) are Spatially- and Temporally-Dependent.
8. Numerical Discretization: Finite-Element Methods with Quadrilateral Elements, Triangular Elements, or the Mixtures of These Two Types.
9. Approximation Options: Consistent Matrix or Mass Lumping, Nodal Quadrature or Gaussian Quadrature for Surface and Element Integrations.
10. Solvers: Direct Band Matrix Solver, Basic Point Iterations, and 4 PCG Methods (polynomial PCG, Incomplete Cholesky PCG, Modified Incomplete Cholesky PCG, and Symmetric Successive Over-Relaxation PCG).
11. Time Stepping: Implicit Difference, Crank-Nicholson Central Difference, or Mid-Difference.
12. Solution Methods for Geochemical Reactions: Newton-Raphson with Full Pivoting to Solve the Jacobian Matrix Equation and Constraints on Species Concentrations.

Features

1. Treat heterogeneous and anisotropic media.
2. Consider spatially and temporally-distributed as well as point sources/sinks.
3. Accept the prescribed initial conditions or obtain initial conditions by simulating the steady-state version of the system under consideration.
4. Deal with prescribed transient concentrations distributed over a Dirichlet boundary.
5. Handle time-dependent fluxes over variable boundaries.
6. Deal with time-dependent total fluxes over Cauchy boundaries.

7. Include the off-diagonal dispersion coefficient tensor components in the governing equation for dealing with cases when the coordinate system does not coincide with the principal directions of the dispersion coefficient tensor.
8. Provide two options for treating the mass matrix - consistent and lumping.
9. Give three options (exact relaxation, under- and over-relaxation) for estimating the nonlinear matrix.
10. Include two options (direct solution with Gaussian elimination method and successive point iterations) for solving the linearized matrix equations.
11. Include both quadrilateral and triangular elements to facilitate the discretization of the region.
12. Automatically reset time step size when boundary conditions or sources/sinks change abruptly.
13. Include simultaneous chemical processes of aqueous complexation, precipitation/dissolution, adsorption, ion exchange, redox, and acid-base reactions.

Limitations

HYDROGEOCHEM dose not include biogeochemical reactions (biological activities).

2.6.4. HYDROGEOCHEM 2:

HYDROGEOCHEM 2 is a modification of HYDROGEOCHEM 1.0 (Yeh et al. 1991), a general purpose computer program written in FORTRAN 77 which was designed to solve coupled hydrologic transport and geochemical equilibrium problems. The modification includes replacement of the EQMOD chemical equilibrium subroutines by a mixed chemical Kinetic and Equilibrium model (KEMOD) to deal with species whose concentrations are controlled by either thermodynamics or kinetics.

HYDROGEOCHEM 2 is a coupled model of hydrologic transport and geochemical reaction in saturated-unsaturated media. HYDROGEOCHEM 2 comprises two basic modules: the transport module and the geochemical reaction module. The transport module is designed to simulate: (1) transient and/or steady-state transport of N_s aqueous components, (2) transient and/or steady-state mass balance of N_s adsorbent components and NSITE ion-exchange sites. The geochemical reaction module is designed to compute the species distribution of $N = (N_a + N_s)$ component species, M_x - K_x equilibrium-controlled complexed species, $(M_y - K_y)$ equilibrium-controlled adsorbed species, K_y kinetic-controlled adsorbed species, $(M_z - K_z)$ equilibrium-controlled ion-exchanged species, K_z kinetic-controlled ion exchanged species, $(M_p - K_p)$ equilibrium-controlled potentially-precipitated species, and K_p kinetic-controlled precipitated species. The two modules are solved iteratively with three options:

1. A complete iteration,
2. An operator splitting, or
3. A predictor-corrector method.

The transport module includes advection and dispersion/diffusion. In the geochemical reaction module, nine types of reactions are included to generate the aforementioned eight types of product species.

Limitations

1. Inability to simulate co-precipitation (solid solution).
2. Inability to simulate microbiological reactions which may transform pollutants in the subsurface environment.

3. The need to import hydrologic variables of flow velocity, moisture content, and pressure head generated by a subsurface flow model.
4. The assumption of isothermal conditions.
5. Applications limited to two-dimensional problems.
6. Applications limited to single-fluid phase flows.

CHAPTER 3

MODELING MICROBIAL-MEDIATED REDUCTION IN BATCH REACTORS

The governing equations that describe the microbially-mediated reduction of heavy metals in the subsurface include a system of coupled nonlinear partial differential equations (PDE's) that involve physical (transport), chemical (sorption), and microbial (oxidation/reduction) processes. The existence of nonlinear reaction terms makes numerical simulations more challenging. Such PDE's are often solved using a time splitting algorithms, through which the nonlinear reaction terms are solved separately from the convective-dispersive components of the governing transport equations. This reduces reaction modeling to solving a system of non-linear ordinary differential equations (ODE's). Various numerical methods to solve non-linear ODE's have been applied to simulate hydrocarbon biodegradation; however, it has not been the case that these numerical methods have been widely developed and applied to simulate microbially-mediated reduction of heavy metals. In this chapter, a coupled system of nonlinear ODE's that describe microbially-mediated oxidation/reduction processes are first developed and then solved using four separate numerical methods. The numerical methods evaluated are the fourth order Runge-Kutta method (RKM), the forward explicit finite difference approximation (FDA), the Taylor series expansion approximation (TSA), and the quasi-steady-state approximation (QSSA) that is frequently applied in atmospheric chemistry transport modeling. Transient simulations of electron donor

oxidation, electron acceptor reduction, and microbial biomass accumulation are performed using each of the four methods with results compared to those generated from an analytical solution and from another numerical model BIOKEMOD (Salvage and Yeh, 1997). Results indicate that the easily implemented QSSA produces simulations of comparable accuracy to the more complicated fully numerical RKM. Simulation results obtained using QSSA are further compared to experimental results from microbially-mediated chromium reductions in batch cultures.

3.1. Introduction

Bioremediation technologies have become important economic and permanent solutions to the contamination problems in the environment. This is particularly true for the subsurface environment where economical and technical reasons play important role in the selection of suitable remediation techniques. Models that simulate electron donor oxidation, electron acceptor reduction, and microbial biomass accumulation can be applied to evaluate and predict passive remediation (natural attenuation) or they may be used to design and predict the performance of active bioremediation systems. This suggests that research focused on developing, evaluating, and verifying such models could serve to advance the science and engineering of subsurface bioremediation systems.

In recent years the reduction of hydrocarbon and solvent concentrations has been the primary focus of most bioremediation technologies; however, metals constitute the second most frequently reported type of subsurface contamination after organic/volatile organic compounds (VOC's). Lovely (1991), was among the first to recognize the microbially-mediated reduction of Fe(III) and Mn(VI), similar to the reduction of the nitrate and sulfate, may be coupled to anaerobic oxidation of aromatic compounds and

serve as an important mechanism for the removal of those contaminants when oxygen becomes limited in the subsurface environment (Lovely, 1991). Later, Shen et al. (1996) reported that microorganisms are capable of using various metals, including Fe(III), Mn(IV), Se(VI), U(VI), Hg(II), As(V), and Cr(VI), as terminal electron acceptors in anaerobic systems. Reducing a metal usually alters its associated toxicity and solubility. Microbial reduction of Cr(VI), U(VI), As(V), and Se(VI) to their less soluble forms may offer a cost-effective mechanism for controlling the mobility of these contaminants in the subsurface, and thus eliminate or mitigate their impacts on human health and subsurface ecosystems.

Despite the importance of metals as a serious threat to the subsurface environment, limited attention has been given to explore the potential for using resident microorganisms to reduce metals to less toxic and/or less mobile forms. As a result, the development of subsurface models for metals transport and microbially-mediated metals reduction is currently evolving. The purpose of this chapter is to provide the reader with additional information on the computational modeling of coupled nonlinear microbially-mediated processes with examples specifically extended to heavy metal reduction. In this chapter, four numerical methods are presented and used to solve the system of non-linear coupled ODE's specifically developed to describe microbially-mediated heavy metals reduction in batch systems. Results from the four numerical methods are compared against simulations of substrate utilization, metal reduction, and microbial biomass accumulation generated from an analytical solution, and a widely used numerical model (BIOKEMOD). As a final exercise, results from QSSA are compared to data from laboratory studies published in the literature.

3.2. Governing Equations

For a simple system of a single substrate (electron donor), an electron acceptor (i.e., a metal), and a single bacterial species, the system of biotic reaction equations can be written as:

$$\frac{dS}{dt} = -\frac{\beta\kappa\bar{M}}{m_c}(S - \bar{S}) - \frac{\mu_{\max}M}{Y}\left(\frac{S}{K_s + S}\right)\left(\frac{A}{K_a + A}\right) \quad (3-1)$$

$$\frac{d\bar{S}}{dt} = \frac{\beta\kappa}{V_c}(S - \bar{S}) - \frac{\mu_{\max}\rho_c}{Y}\left(\frac{\bar{S}}{K_s + \bar{S}}\right)\left(\frac{\bar{A}}{K_a + \bar{A}}\right) \quad (3-2)$$

$$\frac{dA}{dt} = -\frac{\beta\kappa\bar{M}}{m_c}(A - \bar{A}) - \frac{\mu_{\max}ME}{Y}\left(\frac{S}{K_s + S}\right)\left(\frac{A}{K_a + A}\right) \quad (3-3)$$

$$\frac{d\bar{A}}{dt} = \frac{\beta\kappa}{V_c}(A - \bar{A}) - \frac{\mu_{\max}\rho_c E}{Y}\left(\frac{\bar{S}}{K_s + \bar{S}}\right)\left(\frac{\bar{A}}{K_a + \bar{A}}\right) \quad (3-4)$$

$$\frac{dM}{dt} = \mu_{\max}M\left(\frac{S}{K_s + S}\right)\left(\frac{A}{K_a + A}\right) - BM \quad (3-5)$$

$$\frac{d\bar{M}}{dt} = \mu_{\max}\bar{M}\left(\frac{\bar{S}}{K_s + \bar{S}}\right)\left(\frac{\bar{A}}{K_a + \bar{A}}\right) - B\bar{M} \quad (3-6)$$

where

S = aqueous phase substrate concentration (ML^{-3}).

\bar{S} = substrate concentration in attached biomass (ML^{-3}).

A = aqueous phase electron acceptor concentration (ML^{-3}).

\bar{A} = electron acceptor concentration in attached biomass (ML^{-3}).

M = aqueous phase concentration of unattached biomass (ML^{-3}).

\bar{M} = attached biomass concentration; mass of attached cells per volume of aqueous phase (ML^{-3}).

E = mass of electron acceptor consumed per mass of substrate biodegraded.

β = surface area of a single microcolony (L^2).

κ = mass transfer coefficient (LT^{-1}).

μ_{\max} = maximum specific growth rate (T^{-1}).

ρ_c = biomass density; mass of cells per volume of biomass (ML^{-3}).

V_c = volume of a single microcolony (L^3).

Y = yield coefficient; mass of cells produced per mass of substrate biodegraded.

m_C = mass of cells in a single microcolony; $m_C = \rho_c V_C$ (M).

K_S = substrate half - saturation coefficient (ML^{-3}).

K_a = electron acceptor half - saturation coefficient (ML^{-3}).

B = endogenous decay coefficient (T^{-1}).

k_{abio} = first order abiotic rate constant (T^{-1}).

t = time (T).

Equations (3-1) through (3-6) were solved by Molz et al. (1986) and Chen et al. (1992). The first equation includes two loss mechanisms of the substrate from the aqueous phase, the first of which is the diffusion of the substrate across a stagnant liquid layer into attached biomass; while the second is the biodegradation of the substrate by unattached microorganisms in the aqueous phase. Degradation reactions are limited by both the substrate and electron acceptor concentrations through the Monod terms. Equation (3-2) describes the loss of the substrate within the attached biomass (Molz et al., 1986). This equation incorporates both the diffusion of substrate into attached biomass and degradation of the substrate within the biomass. Similarly, equations (3-3) and (3-4) quantify the same mechanisms for the electron acceptor; however, the Monod terms in each equation are multiplied by the factor E , which equals the mass of electron acceptor consumed per mass of substrate degraded. The fifth and sixth equations describe the growth and decay of unattached and attached biomass, respectively.

Three assumptions are commonly used in biodegradation models to simplify the system of equations in a manner that facilitates solution. The first assumption is that contribution of mobile organisms is minor compared to attached ones. The second assumption is that the time rate of change of the concentrations in the biomass is fast relative to the time rate of change of the bulk phase concentration; thus, the term

$d\bar{S}/dt \cong 0$. This assumption was first employed by Chen et al. (1992) and Molz et al. (1986), which is equivalent to the assumption that steady state conditions exist across the diffusion layer between the attached biomass and the bulk liquid (Molz et al. 1986). The third assumption is that mass transfer into the biomass is sufficiently fast that mass transfer resistance can be neglected; as a result, constituent concentrations available to the microorganisms are the same as the concentrations in the bulk liquid. This assumption was employed by Malone et al. (1993) and Wood et al. (1994). These three assumptions reduce the number of equations by half. If the substrate (electron donor) is not a nutrient, another equation for nutrient N is added to produce the following four final governing equations:

$$\frac{dS}{dt} = -\frac{\mu_{\max} \bar{M}}{Y_s} \left(\frac{S}{K_s + S} \right) \left(\frac{N}{K_n + N} \right) \left(\frac{A}{K_a + A} \right) \quad (3-7)$$

$$\frac{dA}{dt} = -\frac{\mu_{\max} \bar{M}}{Y_a} \left(\frac{S}{K_s + S} \right) \left(\frac{N}{K_n + N} \right) \left(\frac{A}{K_a + A} \right) \quad (3-8)$$

$$\frac{dN}{dt} = -\frac{\mu_{\max} \bar{M}}{Y_n} \left(\frac{S}{K_s + S} \right) \left(\frac{N}{K_n + N} \right) \left(\frac{A}{K_a + A} \right) \quad (3-9)$$

$$\frac{d\bar{M}}{dt} = \mu_{\max} \bar{M} \left(\frac{S}{K_s + S} \right) \left(\frac{N}{K_n + N} \right) \left(\frac{A}{K_a + A} \right) - B \bar{M} \quad (3-10)$$

$$Y_s = Y; \quad Y_a = Y/E; \quad Y_n = Y/E_n \quad (3-11)$$

where E_n is the mass of nutrient consumed per mass of substrate biodegraded. It should be clear that M is the concentration of attached biomass and all other concentrations (S , A and N) are aqueous phase concentrations. For simplicity, M will be used instead of \bar{M} to represent the concentration of attached biomass. These equations can be used to simulate

microbially-mediated heavy metals reduction, in which case the metal is considered to be the electron acceptor that is reduced in the presence of an electron donor and a nutrient.

3.3. Methods of Solution

Several numerical methods can be used to solve stiff systems of ODE's. The most common one is Gear's method (Gear, 1971); however, this method is time consuming because it requires the inversion of large matrices. In the case of simulating subsurface biotic reactions along with constituent transport, the convection-dispersion-reaction PDE's are usually solved for a large number of grid points. Therefore, in order to reduce the computational time of subsurface simulations, simpler methods are required for solving the reaction ODEs.

For the current study, four numerical methods were selected to be examined as potential methods for solving the system of coupled reaction ODE's (3-7 through 3-10). The first was the fourth order Runge-Kutta method (RKM). This method was selected because previous studies have found it to be as accurate as Gear's when mass transfer is not considered (de Blanc et al. 1996). The forward explicit finite difference approximation (FDA) was chosen as the second method due to its simplicity and ease of implementation. Despite the difficulties associated with its implication to solve multi-ODE's, Taylor series expansion approximation (TSA) was chosen as the third method because of its analytical features. Finally, the quasi-steady-state approximation (QSSA) was included because it has the virtue of being analytically based and easy to implement. Though used extensively in atmospheric chemistry transport modeling [Mathur et al. 1998, Odman et al. 1992, and Hertel et al. 1993], QSSA has not been used, to simulate nonlinear biotic reactions and processes in the subsurface. To validate each of the four

methods, a comparison was made to exact results generated from analytical solution to equations (3-7) through (3-10) (Appendix A).

3.3.1. Taylor series expansion approximation (TSA)

The Taylor series expansion of a function $F_i(t)$ about the ordinary point $t = t_0$ is well known to be:

$$F_i(t) = F_i(t_0) + \sum_{n=1}^{\infty} F_i^{(n)}(t_0) \frac{(t - t_0)^n}{n!} \quad (3-12)$$

where $F_i^{(n)}(t)$ is the n^{th} derivative of the function $F_i(t)$.

The development of this expansion requires only the value of the function and its derivatives at a single point. Equation (3-12) is only evaluated for a specific number of terms and the rest of the terms are considered truncation error. By setting F_i equals to S , A , N , and M for $i = 1, 2, 3$ and 4 respectively, approximation expressions for the four variables can be determined. In this investigation, the Taylor expansion was evaluated up to the third derivatives.

3.3.2. Finite difference method (FDM)

The forward explicit finite difference method is also employed in this chapter to solve equations (3-7), (3-8), (3-9), and (3-10). For each time step j the following finite difference expressions can be obtained:

$$S_{j+1} = S_j - \frac{\mu_{\max}}{Y_s} \left(\frac{S_j}{S_j + K_s} \right) \left(\frac{A_j}{A_j + K_a} \right) \left(\frac{N_j}{N_j + K_n} \right) M_j \Delta t \quad (3-13)$$

$$A_{j+1} = A_j - \frac{\mu_{\max}}{Y_a} \left(\frac{S_{j+1}}{S_{j+1} + K_s} \right) \left(\frac{A_j}{A_j + K_a} \right) \left(\frac{N_j}{N_j + K_n} \right) M_j \Delta t \quad (3-14)$$

$$N_{j+1} = N_j - \frac{\mu_{\max}}{Y_n} \left(\frac{S_{j+1}}{S_{j+1} + K_s} \right) \left(\frac{A_{j+1}}{A_{j+1} + K_a} \right) \left(\frac{N_j}{N_j + K_n} \right) M_j \Delta t \quad (3-15)$$

$$M_{j+1} = M_j + (\mu_{\max} \left(\frac{S_{j+1}}{S_{j+1} + K_s} \right) \left(\frac{A_{j+1}}{A_{j+1} + K_a} \right) \left(\frac{N_{j+1}}{N_{j+1} + K_n} \right) M_j - BM_j) \Delta t \quad (3-16)$$

3.3.3. Quasi steady state approximation (QSSA)

A common numerical method for solving systems of ODE's is the Quasi-Steady-State Approximation (QSSA). This method was first presented by Hesstvedt et al. (1978) and has since been used in many atmospheric transport chemistry models (Mathur et al. 1998, Odman et al. 1992, and Hertel et al. 1993). QSSA possesses the advantages of being fast and easy to implement. The four governing equations (3-7 through 3-10) can be written in the following general form:

$$\frac{dC_i}{dt} = P_i \left(\frac{C_i}{C_i + K_{C_i}} \right) \quad (3-17)$$

where C_i is S, A, N, or M for $i = 1, 2, 3$, and 4, respectively. P_i is function of the other variables ($P_i(C_j) \quad j \neq i$). The applied concept behind the QSSA is to consider the function P_i as a constant for each time step; therefore, an analytical solution of equation 3-17 can be obtained for each variable. By applying this method to the equations 3-7, 3-8, 3-9, and 3-10 one can obtain the following expressions.

$$S_{j+1} + K_s \ln S_{j+1} = S_j + K_s \ln S_j - \frac{\mu_{\max} M_j}{Y_s} \left(\frac{A_j}{A_j + K_a} \right) \left(\frac{N_j}{N_j + K_n} \right) \Delta t \quad (3-18)$$

$$A_{j+1} + K_a \ln A_{j+1} = A_j + K_a \ln A_j - \frac{\mu_{\max} M_j}{Y_a} \left(\frac{S_{j+1}}{S_{j+1} + K_s} \right) \left(\frac{N_j}{N_j + K_n} \right) \Delta t \quad (3-19)$$

$$N_{j+1} + K_n \ln N_{j+1} = N_j + K_n \ln N_j - \frac{\mu_{\max} M_j}{Y_n} \left(\frac{A_{j+1}}{A_{j+1} + K_a} \right) \left(\frac{S_{j+1}}{S_{j+1} + K_s} \right) \Delta t \quad (3-20)$$

$$\ln M_{j+1} = \ln M_j + \left[\mu_{\max} \left(\frac{S_{j+1}}{S_{j+1} + K_s} \right) \left(\frac{A_{j+1}}{A_{j+1} + K_a} \right) \left(\frac{N_{j+1}}{N_{j+1} + K_n} \right) - B \right] \Delta t \quad (3-21)$$

where j indicates the time step number, and Δt is the time interval. Equations 3-18, 3-19, 3-20, and 3-21, are solved for each time step using a Newton-Raphson iteration method.

3.3.4. Fourth order Runge-Kutta method (RKM)

For the fourth order Runge-Kutta method the four ODE's (3-7 to 3-10) are assumed to have the following form:

$$\frac{dY}{dt} = f(Y, t) \quad (3-22)$$

The value of each unknown Y (A, S, N, or M) at time step t_{n+1} is given by:

$$Y_{n+1} = Y_n + \frac{\Delta t}{6}(k_1 + 2k_2 + 2k_3 + k_4) \quad (3-23)$$

where

$$k_1 = f(Y_n, t_n) \quad (3-24)$$

$$k_2 = f(Y_n + 0.5 k_1, t_n + 0.5 \Delta t) \quad (3-25)$$

$$k_3 = f(Y_n + 0.5 k_2, t_n + 0.5 \Delta t) \quad (3-26)$$

$$k_4 = f(Y_n + k_3, t_n + \Delta t) \quad (3-27)$$

3.4. Numerical Examples

The four methods presented above were used to solve four different numerical examples. The first three examples are hypothetical, while the fourth one is taken from the literature. The input data for these four examples are presented in table 3-1. A wide range of model parameter values was selected to test the four methods.

In the first example, results of the four methods were compared to those of the analytical solution. Figure 3-1a presents the evolution of substrate S concentration simulated with the four numerical models and the analytical solution.

Table 3-1 Input parameters for the numerical examples 1-4.

Input parameters	Example 1	Example 2	Example 3	Example 4 (Salvage and Yeh, 1997)
μ_{\max} (hr ⁻¹)	0.85	0.05	0.5	0.0378
Y_s (cell/mg)	5000	1E+11	100000	0.13E-3
Y_a (cell/mg)	6000	1.5E+11	200000	-
Y_n (cell/mg)	7000	2E+11	300000	-
K_s (mg/L)	0.5	12	5	7.5
K_a (mg/L)	0.6	15	6	-
K_n (mg/L)	0.7	18	7	-
B (hr ⁻¹)	0	0	0.005	0
S_0 (mg/L)	1.0	100	10	200
A_0 (mg/L)	1.05	105	10.5	-
N_0 (mg/L)	1.1	110	11	-
M_0 (cell/L)	10000	1E+12	100000	0.001
Δt (hr)	0.1	0.1	0.1	0.1

This figure clearly shows that three methods (RKM, QSSA, and FDM) produced accurate solutions compared to those of the analytical solution. The same figure, however, shows that TSA failed to simulate the problem after the first hour. Using only three terms in the Taylor expansion series was clearly the cause of such inaccurate results.

Transient changes in the microbial biomass concentration in the first example are shown in Figure 3-1b. The microbial biomass concentration curve starts with an initial concentration of 10000 cell/L and a linear slope. After 8 hours, there is little change of biomass concentration with time. This occurs because the concentration of substrate S has reached a limiting concentration value. It is also clear from Figure 3-1b that the

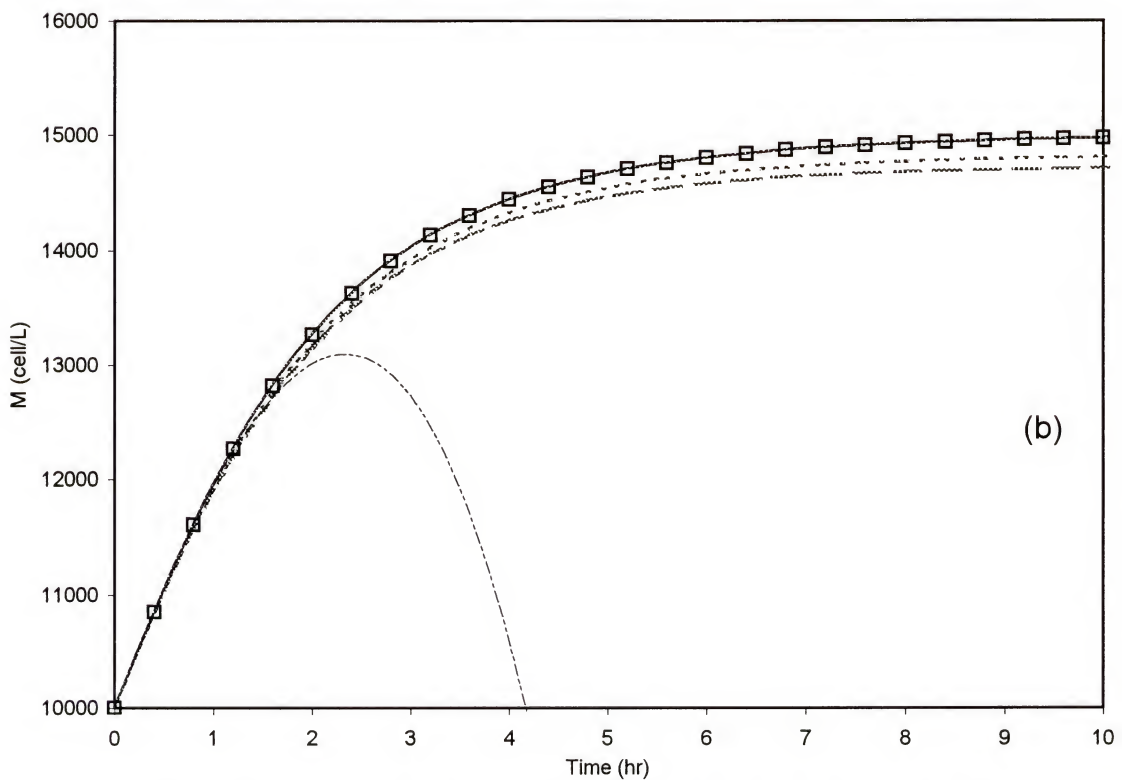
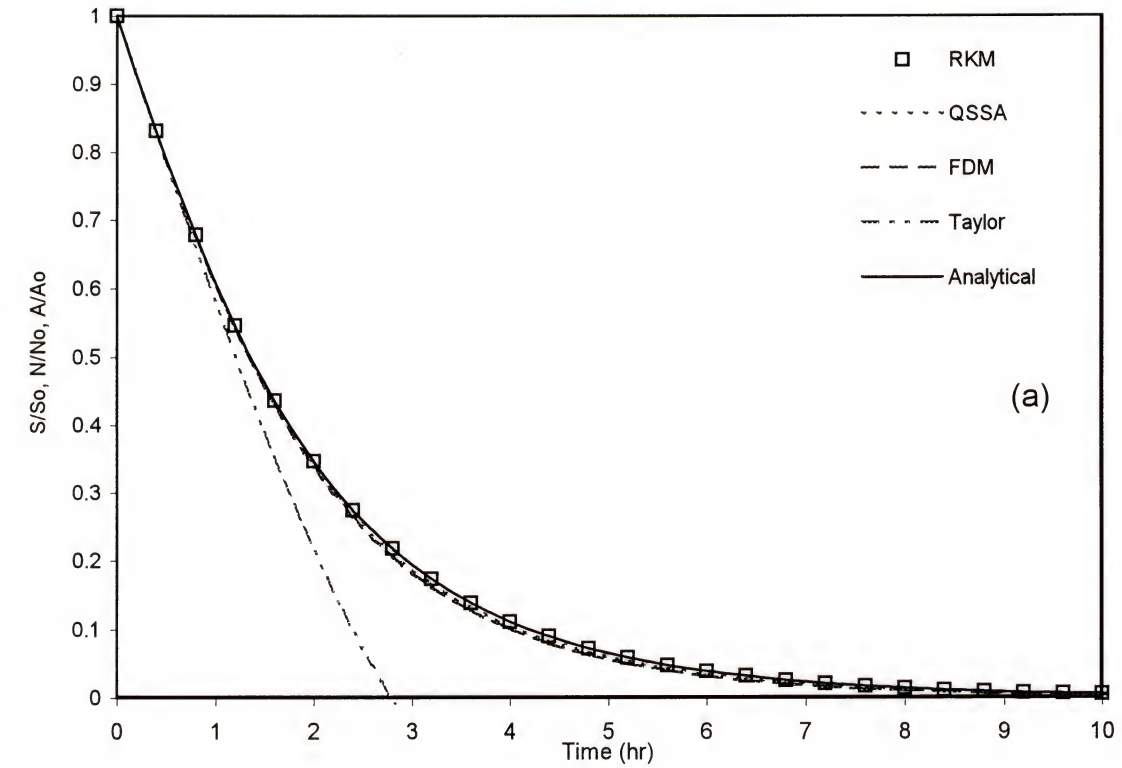


Figure 3-1 comparison between RKM, QSSA, FDM, TSA, and the analytical solution for test problem 1.
 (a) Solutes relative concentrations.
 (b) Microbial concentrations.

results from the three numerical solutions (RKM, QSSA, FDM) are in good agreement with results of the analytical solution. However, a closer look at Figure 3-1b suggests that both RKM and QSSA solutions are closer to the analytical solution than FDM.

The relative prediction errors between the investigated methods and the analytical solution in the first example are shown in the first column of Table 3-2. Having an average error of almost zero, the RKM solution gave an excellent match with the analytical solution. The same table illustrates that QSSA and the FDM methods gave quite good results as well. The average error of the QSSA results was about 1%, whereas the average error was 1.5 % for the FDM results. These errors may be assumed small considering measurement uncertainties that always accompany these experiments.

Table 3-2 Average percentage error compared to analytical solution (example 1) and to RKM (examples 2 and 3).

Method	Example 1	Example 2	Example 3
RKM	0.000035	-	-
QSSA	0.96	0.02	0.17
FDM	1.52	0.22	1.23
TSA	>50	45.91	>50

In the second example, using a different set of model parameters, numerical results of QSSA, FDM and TSA were compared to RKM, the method producing results closest to the analytical solution. Figures 3-2a and 3-2b show the change of the concentration of substrate S and biomass with time, respectively. Both graphs suggest that results of RKM, QSSA, and FDM are in good agreement with each other. On the other hand, for the same reason mentioned above, the same graphs show the Taylor series expansion solution as not accurate.

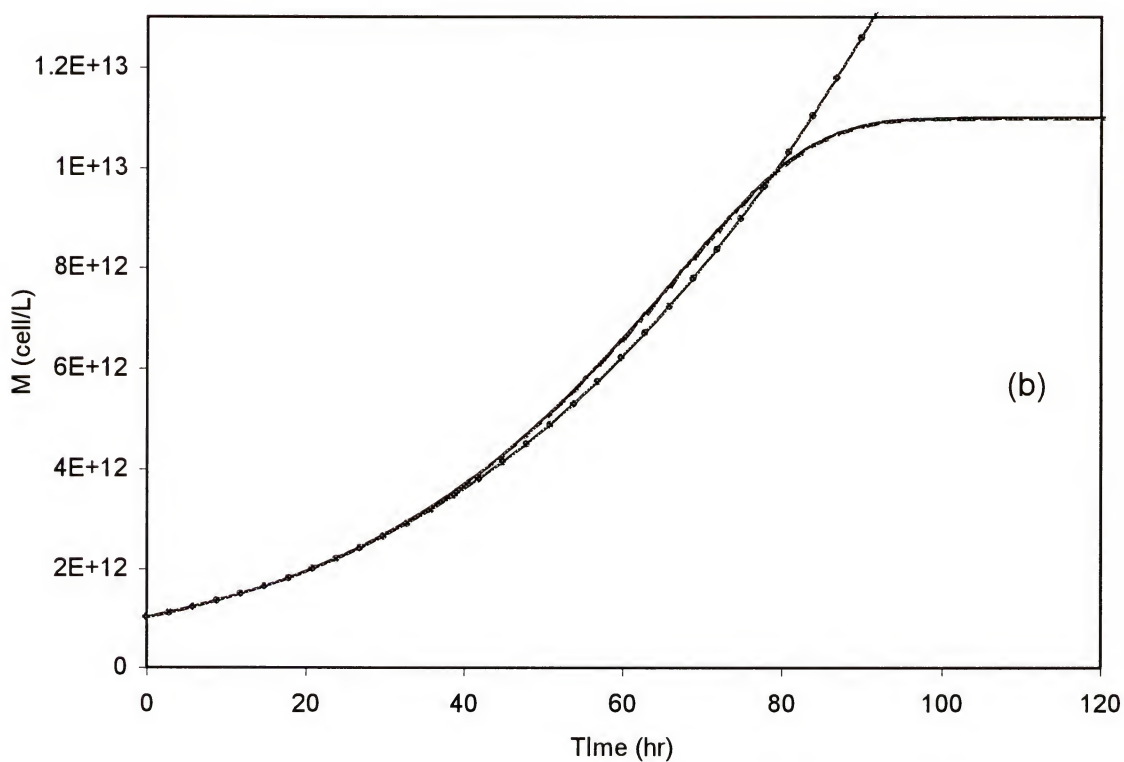
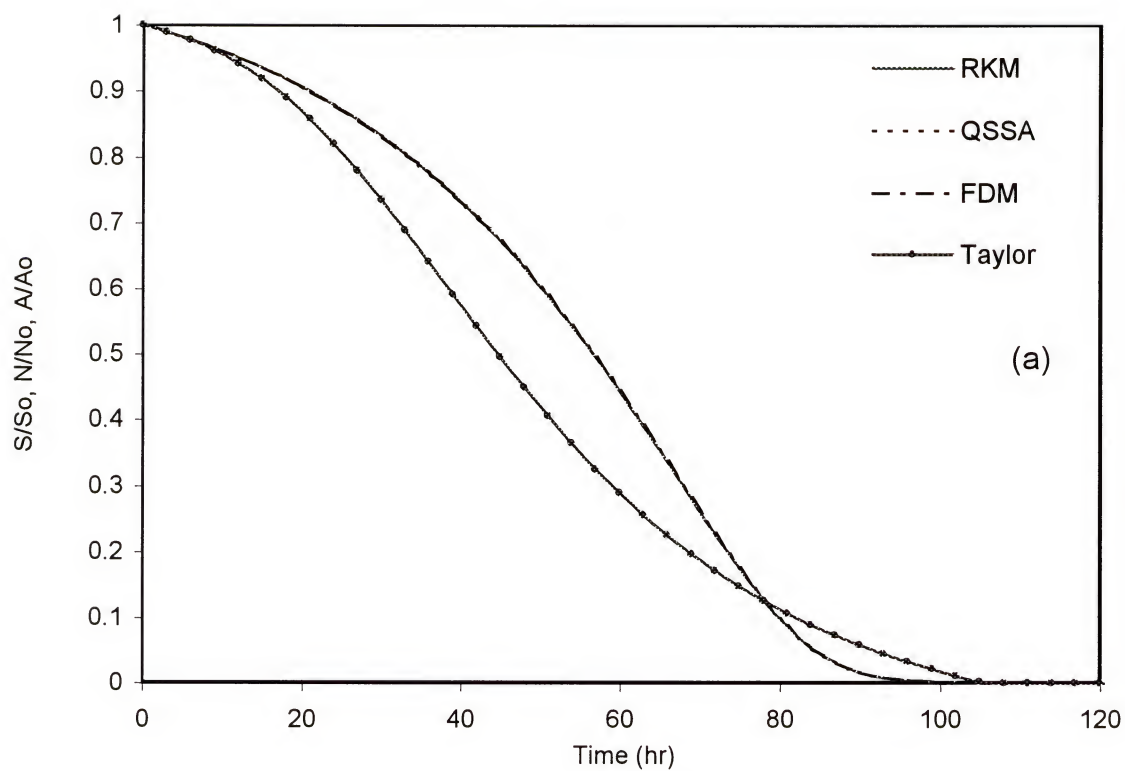


Figure 3-2 Comparison between QSSA, FDM, TSA and RKM for test problem 2.

(a) Solutes relative concentrations.

(b) Microbial concentrations.

The second column in Table 3-2 shows the prediction errors of QSSA, FDM and Taylor predictions as compared to RKM. QSSA model has the lowest average error (0.02%), indicating that it is in excellent agreement with those of RKM. FDM also gave a good solution when compared to RKM solution; however, the error was one order of magnitude higher than that of QSSA. Conversely, Taylor expansion series solution, with 45 % average error, shows inaccurate results. More terms in the Taylor expression are required to have a more accurate solution.

In the third example, another verification of model parameters values was examined. In these simulations, the bacterial death rate (B) was assumed to be 0.005 day⁻¹. The effect of this factor can be clearly observed in Figure 3-3b, as the biomass concentration decreases after it reaches maximum value. That trend was missed in the first two examples because B was given a zero value. Figures 3-3a and 3-3b confirm the same observation obtained from the previous two examples regarding the accuracies of the numerical solutions. Thus, as shown in the third column of Table 3-2, QSSA produced results in closer agreement with RKM solution than FDM solution.

The final validation problem was adopted from Salvage and Yeh (1997). This example represents the consumption of N-NO_2^- by *Nitrobacter winogradski* that was grown in a 200 mg/l NaNO_2 medium by Corman and Pave (1983) who measured concentrations of both substrate and biomass over a period of 93 hours. However, Corman and Pave used substrate concentrations (because of their higher precision), rather than biomass, to estimate the biological parameters of *Nitrobacter winogradski* (Table 1). Salvage and Yeh used values of experimental parameters, generated by Corman and Pave, in a numerical model (BIOKEMOD), which solves batch system biochemical

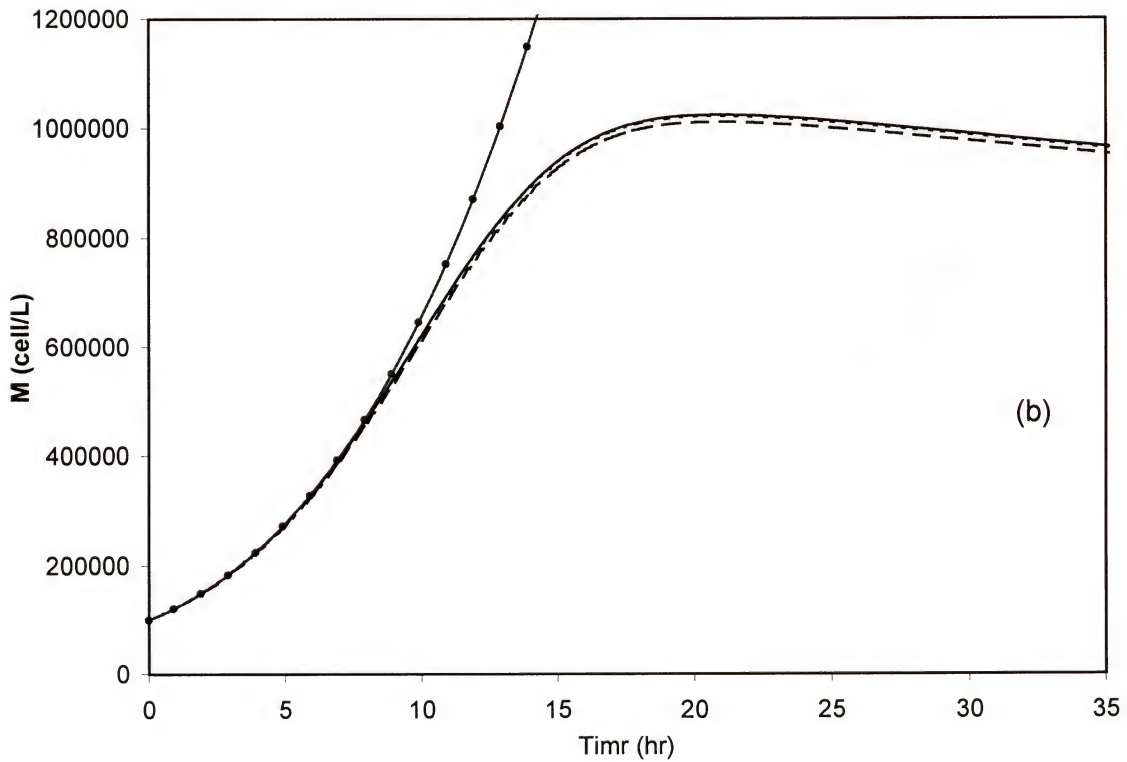
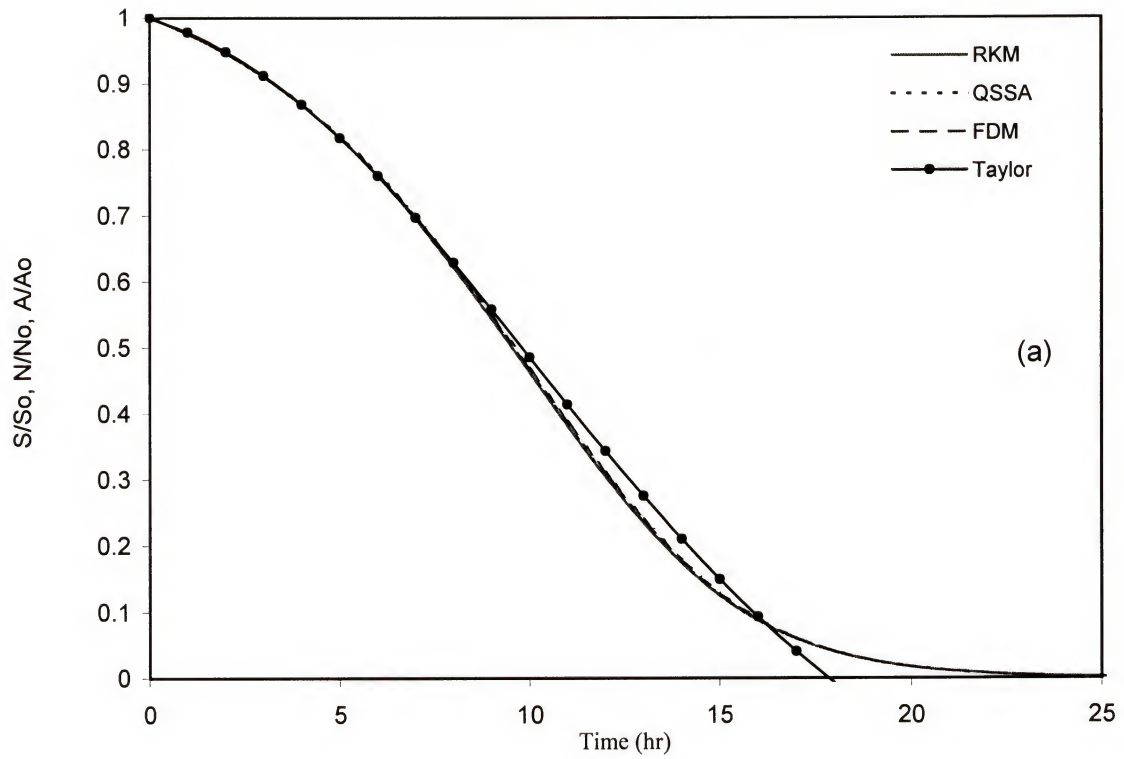


Figure 3-3 Comparison between QSSA, FDM, TSA, and RKM for test problem 3.

(a) Solutes relative concentrations.

(b) Microbial concentrations.

reaction ODEs using the Newton-Raphson method, to predict transient solute and biomass concentrations.

The model parameters used by Salvage and Yeh were used in this chapter to produce additional numerical solutions using RKM, QSSA, FDM, and TSA. Figure 3-4 presents a comparison between the laboratory data of Corman and Pave (1983), and numerical solutions generated from BIOKEMOD, RKM, QSSA, FDM, and TSA. One can easily notice that simulations from BIOKEMOD are as good as RKM, FDM, and QSSA in simulating the evolution of N-NO_2^- concentration with time. However, the biomass concentration curve of BIOKEMOD does not match the results of RKM, QSSA, and FDM.

One can conclude from the previous examples that QSSA gives excellent results compared to both the analytical solution (example 1) and the RKM solution (examples 1-4). However, unlike RKM, QSSA is a simple method that can be used to solve the biological ODEs as it has an analytical basis. For these reasons, QSSA is used in the following section to simulate Cr(VI) reduction in batch cultures.

3.5. Simulation of Cr(VI) Reduction Using QSSA

In this section, QSSA is used to simulate Cr(VI) reduction in batch systems using published laboratory data by Wang and Shen (1997) (Table 3-3). They studied the change of Cr(VI) concentrations in the presence of one microbial species where there was an abundance of an electron donor. In this case, equations (3-7) to (3-9) reduce to one equation as follows:

$$\frac{dA}{dt} = \frac{\mu_{\max} M}{Y_A} \frac{A}{K_A + A} \quad (3-28)$$

where

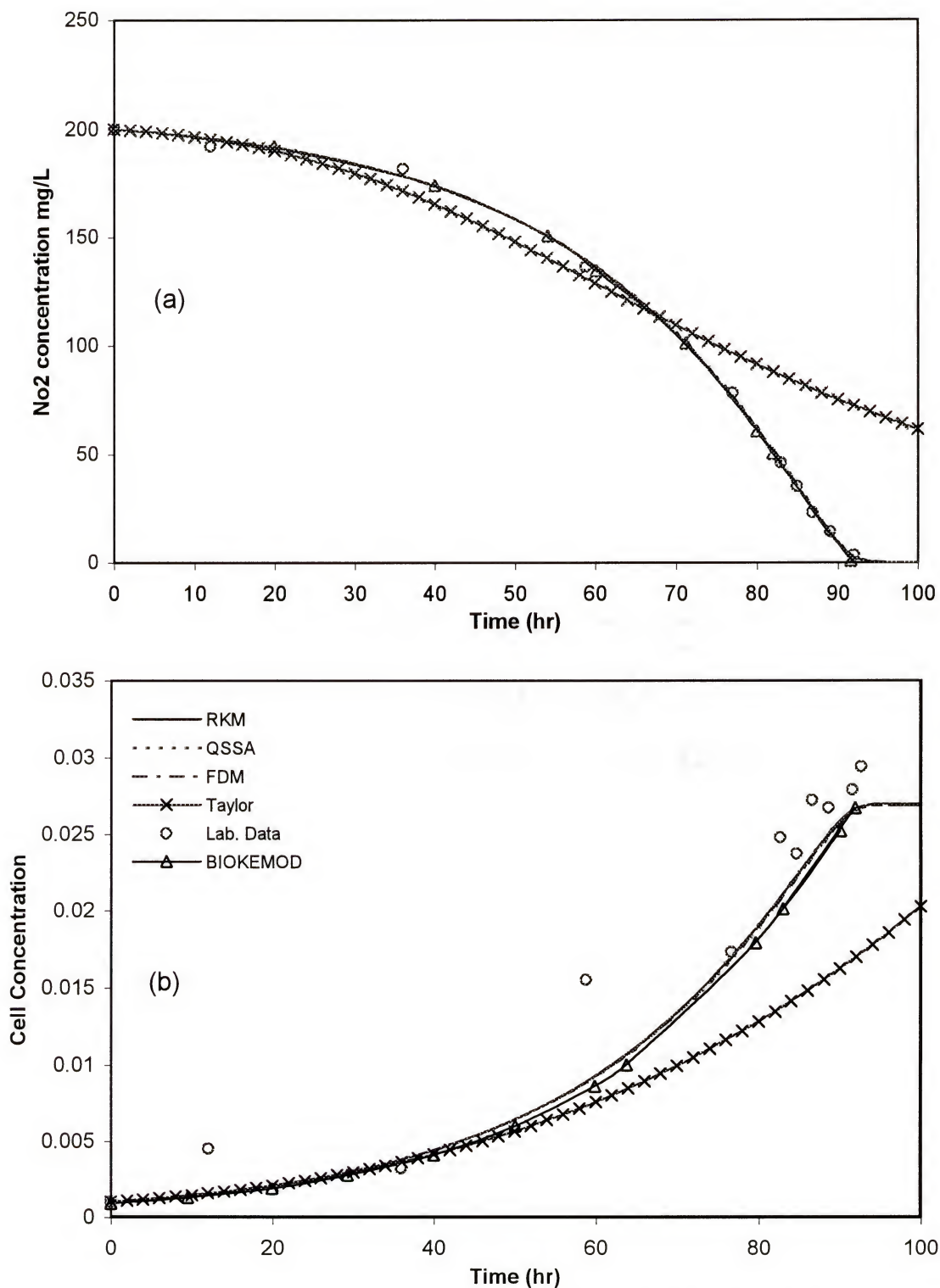


Figure 3-4 Comparison between QSSA, FDM, TSA, RKM, BioKemod and lab data for test problem 4.

(a) Solutes relative concentrations.

(b) Microbial concentrations.

A = Cr(VI) concentration (ML^{-3}).

M = biomass concentration; mass of active cells per volume (ML^{-3}).

Y_A = yield coefficient; mass of cells produced per mass of Cr(VI) reduced.

K_A = Cr(VI) half - saturation coefficient (ML^{-3}).

Table 3-3 Kinetic parameters for the three laboratory experiments.

Parameter	First Example	Second Example	Third Example
Species	<i>Bacillus sp.</i>	E.coli ATCC 33456	<i>P. fluorescens</i> LB 300
μ_{\max} (hr^{-1})	0.04952	0.064345	0.02745
Y_s (cell/mg)	4.80E11	1.39E11	3.2E11
K_s (mg/L)	5.43	8.64	5.55
B(hr^{-1})	0	0	0
So(mg/L)	Varies	Varies	Varies
Mo(cell/L)	1.0E13	9.0E12	1.0E13
Δt (hr)	0.1	0.1	0.1

Wang and Shen assumed that the active cell concentration decreases in proportion to the amount of Cr(VI) reduced due to the toxicity of Cr(VI). The same assumption was employed here by multiplying the first term in the RHS of equation 3-10 by -1, which yields:

$$\frac{dM}{dt} = -\mu_{\max} M \frac{A}{K_A + A} - B M \quad (3-29)$$

For B=0, equation 3-29 is substituted into equation 3-28 and then integrated to yield:

$$t = \frac{K_A Y_A}{\mu_{\max} (A_0 Y_A - M_0)} \ln\left(\frac{A M_0}{A_0 (M_0 - Y_A (A_0 - A))}\right) + \frac{1}{\mu_{\max} Y_A} \ln\left(\frac{M_0}{M_0 - Y_A (A_0 - A)}\right) \quad (3-30)$$

Equation 3-30 is equivalent to the mathematical model used by Wang and Shen, 1997. Model parameters (μ_{\max} , Y_s , K_s) obtained by Wang and Shen (Table 3-3) were used in QSSA simulations. Figures 3-5 to 3-7 represent comparison between QSSA results, the

mathematical model results (Eq. 3-30), and the laboratory data. Four different values of Cr(VI) initial concentration were used in the first set of simulations (Figure 3-5). The reduction rate of Cr(VI) by *Bacillus sp.* decreases with time as the bacterial concentration decreases due to the toxic effect of Cr(VI) the bacteria (Equation 3-30). The agreement between QSSA solution and that of the mathematical model is remarkable (Figure 3-5). Both solutions produced good representation of the range of Cr(VI) concentrations used as initial conditions.

Similarly, in the second and third simulation sets, five runs were performed with five different Cr(VI) initial concentrations. It is notable that QSSA gives an excellent agreement with both laboratory observation and the mathematical simulation (Equation 3-30) of Cr(VI) reduction. These results strongly suggest using QSSA in modeling multi-substrate uptake in batch culture experiments where mathematical solutions are difficult to obtain.

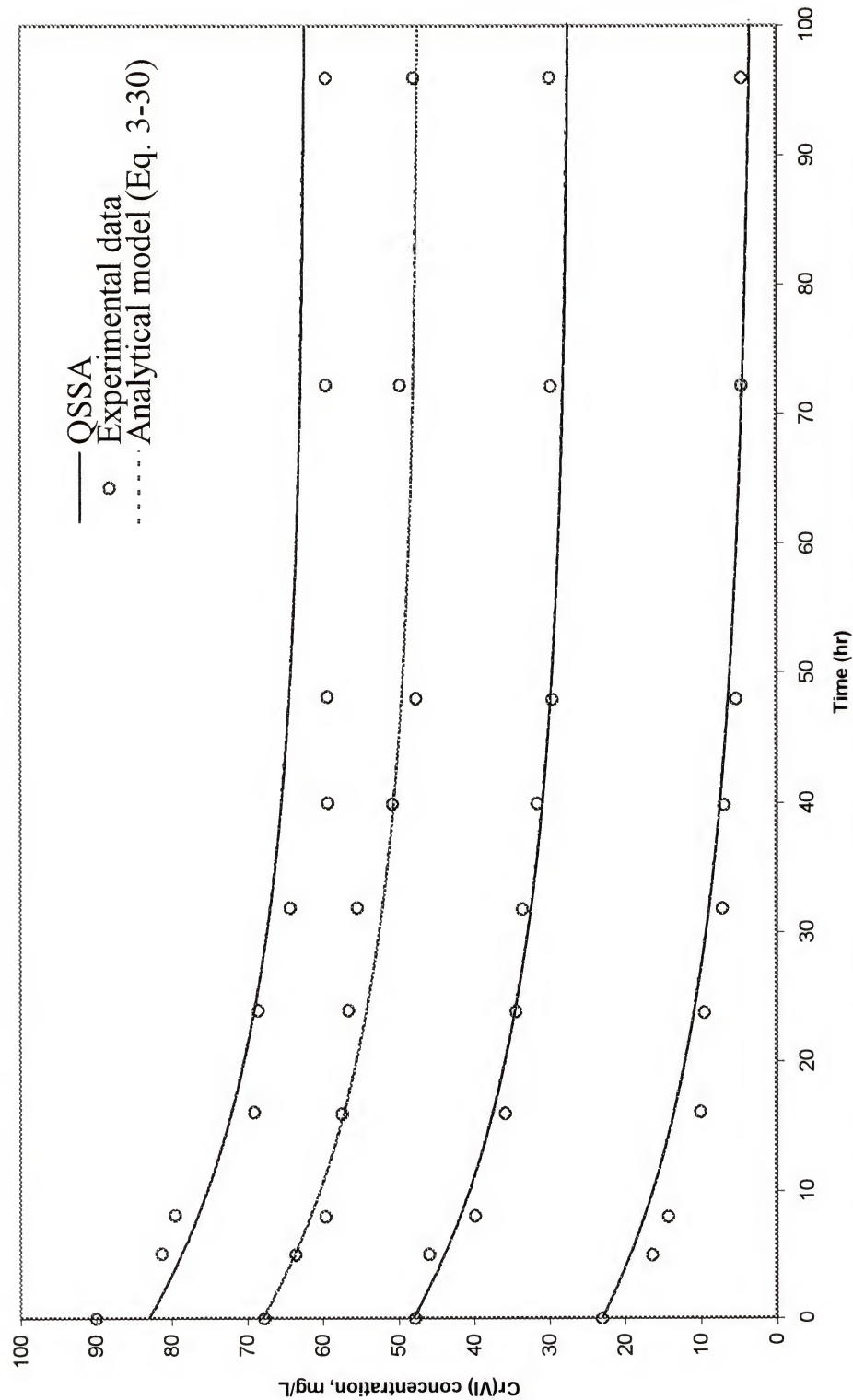


Figure 3-5 comparison between QSSA, analytical model, and experimental data (Wang and Shen) for example 1.

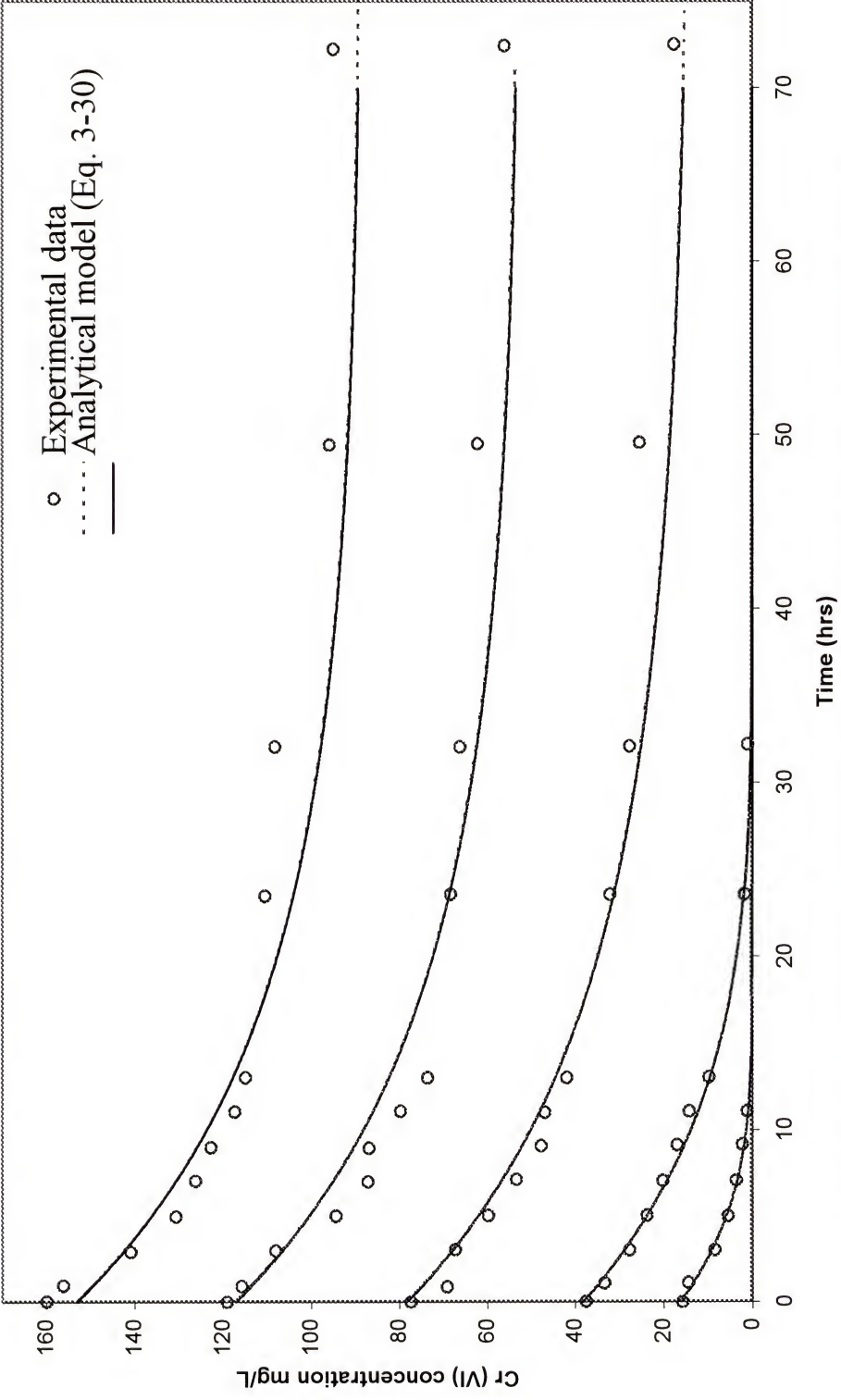


Figure 3-6 comparison between QSSA, analytical model, and experimental data (Wang and Shen) for example 2.

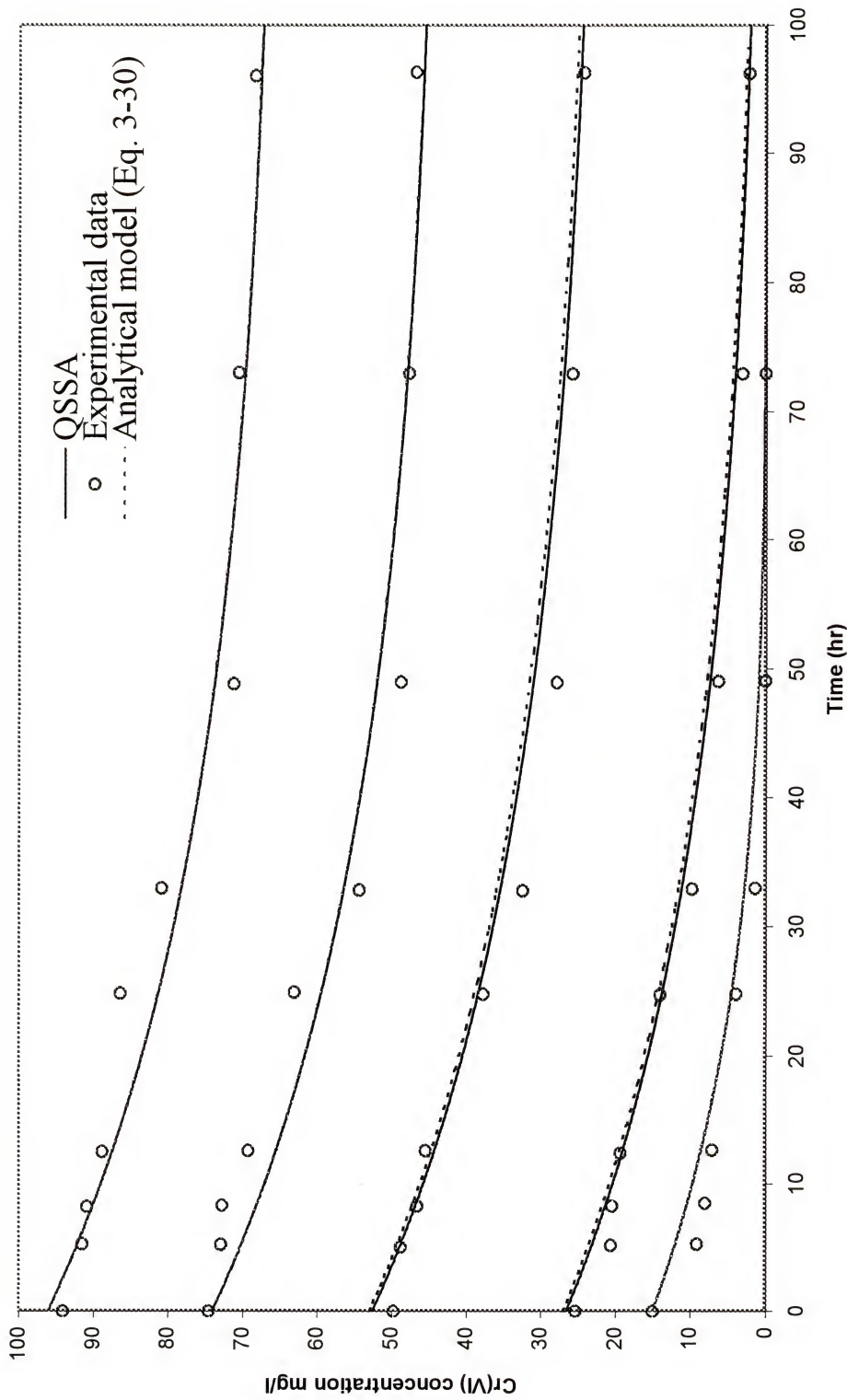


Figure 3-7 comparison between QSSA, analytical model, and experimental data (Wang and Shen 97) for example 3.

CHAPTER 4 DEVELOPMENT OF METABIOTRANS

4.1 Introduction

This chapter presents the computer model, METABIOTRANS, which simulates the transport and biotransformation of metals in saturated groundwater. METABIOTRANS is a three-dimensional finite elements model that simulates the transport of multi-solutes (metals, hydrocarbons, or any other solute) in heterogeneous /anisotropic aquifers and the consequent concentration change in these solutes over time. METABIOTRANS simulates the biological reduction of metals (electron acceptors) by different microbial species in the presence of several electron donors. At each time step, METABIOTRANS solves the advective-dispersive transport equation for each solute then calculates the change of solutes and microbial concentrations due to the biological processes. The model uses Michaelis-Menten kinetics equations to describe the reduction process. These equations are modified to incorporate two different inhibition mechanisms that could affect the reduction process. One of these inhibition factors deals with the existence of others electron acceptors in the aquifer and their effect on the reduction process of the metal under consideration. The other inhibition factor represents the toxic level of the metal itself on the bacterial species. Mathematical background is presented first followed by a detailed description of the model.

4.2 Theoretical Background

4.2.1 Microbial dynamics

Figure 4-1 shows the growth of microorganisms in a limited environment (limited nutrients and carbon sources) such as a groundwater aquifer. This graph could be divided into several phases, including lag phase, acceleration phase, exponential phase, retardation phase, maximum population phase, and death phase. The lag phase shows no change in population size. Growth rate increases in the beginning of the acceleration phase. The exponential phase can be described by the basic growth equations. When the growth rate starts to decline, the retardation phase begins. The maximum population phase marks the maximum population size, when the microorganisms are metabolically active but active growth stops. Finally, the death phase starts when the population size starts to decline. The logistic model, a well-known model often used to describe microbial growth in a closed environment, can be used from the beginning of the exponential phase through the maximum population phase (Lynch and Poole, 1979).

$$\frac{dx}{dt} = \mu_{\max} \times \left(1 - \frac{x}{x_f}\right) \quad (4-1)$$

where x is the population size, μ_{\max} is the maximum growth rate [T^{-1}], x_f is the population size in the maximum population phase.

4.2.2 Biotransformation kinetics

Kinetic expressions are expressions that describe the rate of biotransformation of contaminants. Three main kinetic expressions have been developed to describe the biodegradation process in the groundwater, namely Monod kinetics, first-order decay kinetics, and instantaneous reaction kinetics. The most common of these models is the hyperbolic saturation function presented by Monod (1942) and typically referred to as

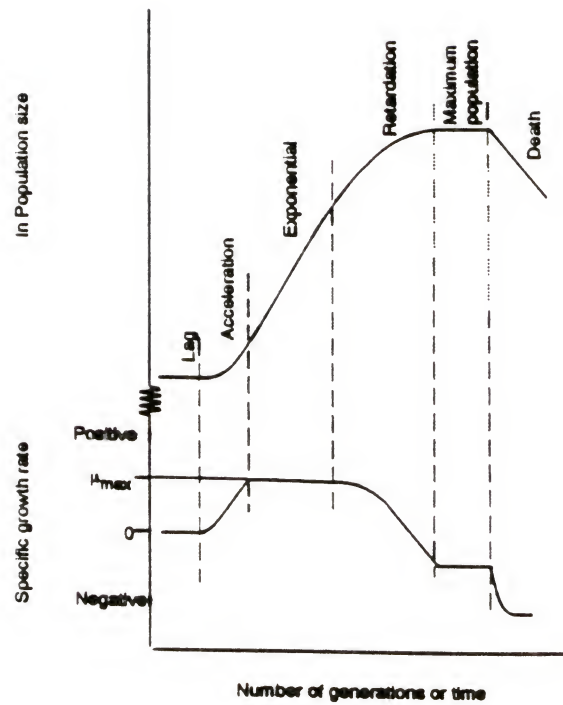


Figure 4-1 Phases of growth occurring during a closed culture growth cycle in a limited environment, showing the changes in the organism's specific growth rate (Bull, 1974).

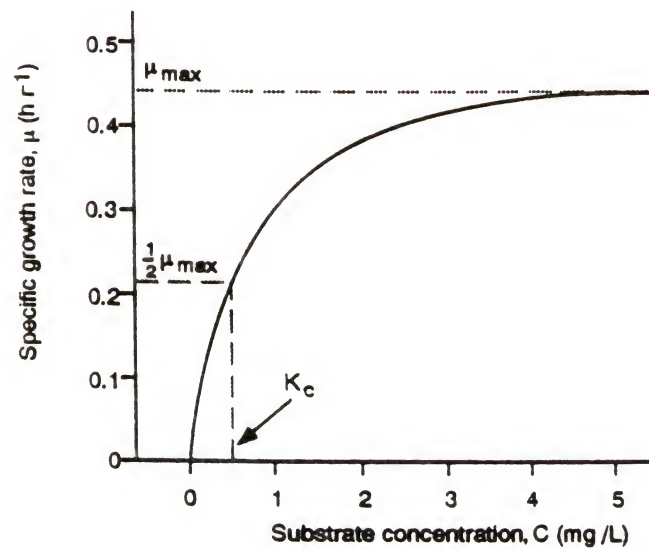


Figure 4-2 Relationship between specific growth rate and growth limiting substrate concentration (Lynch and Poole, 1979).

Monod or Michaelis-Menten kinetic growth function:

$$\mu = \mu_{\max} \frac{C}{K_c + C} \quad (4-2)$$

where μ is the growth rate [T^{-1}], μ_{\max} is the maximum growth rate [T^{-1}], C is the concentration of the growth-limiting substrate [mg/l], and K_c is the half saturation constant, which is defined as the growth limiting substrate concentration that allows microorganisms to grow at half the maximum specific growth rate (Figure 4-2).

The Monod growth function can be related to the rate of contaminant loss through a yield coefficient Y , which is a measure of the microbial mass formed per unit mass of substrate utilized. Thus, the change in substrate concentration can be expressed as:

$$\frac{dC}{dt} = \mu_{\max} \frac{M}{Y} \frac{C}{(K_c + C)} \quad (4-3)$$

where M is the microbial mass in mg/l, which is related to the substrate utilization through an expression of the change in the microbial mass as a function of time:

$$\frac{dM}{dt} = \mu_{\max} M \frac{C}{(K_c + C)} - B M \quad (4-4)$$

where B is the first order decay rate which accounts for cell death.

First-order kinetics are an approximation of Monod kinetics when $K_c \gg C$. The following exponential equation represents an integrated form of equations 4-3 and 4-4:

$$C = C_0 e^{-kt} \quad (4-5)$$

where C is the remaining concentration of the substrate at time t , C_0 is the initial concentration, and k is the 1st order decay coefficient of the substrate. Using equation 4-5, Equation 4-7 provides an estimate of the substrate half-life ($t_{1/2}$):

$$t_{1/2} = \frac{0.693}{k} \quad (4-6)$$

The advantage of using Monod expressions is that the constants K_c and μ_{\max} uniquely define the rate equations for mineralization of specific compounds, and thus incorporate both the activity of the degrading population and the substrate dependency of the reaction. Therefore, this expression takes into consideration the both population and substrate levels.

4.3. Governing Equations

4.3.1. Flow equations

The relationship between the total head and the velocity field in groundwater flow can be expressed as a system of partial differential equations. Assuming that the soil matrix is incompressible, the steady-state saturated flow equation can be written as:

$$\frac{\partial}{\partial x} \left(K_x \frac{\partial h}{\partial x} \right) + \frac{\partial}{\partial y} \left(K_y \frac{\partial h}{\partial y} \right) + \frac{\partial}{\partial z} \left(K_z \frac{\partial h}{\partial z} \right) = 0 \quad (4-7)$$

where K is the hydraulic conductivity tensor [LT^{-1}] and h is the hydraulic head [L].

4.3.2. Transport equations

Aqueous phase transport is described by the advection-dispersion equation for each metal (electron acceptor), substrate (electron donor), nutrient, and endproduct.

These equations are coupled through source/sink terms for biotransformation.

For each substrate k [$k=1, 2, 3, \dots, NS$ (number of substrates)], the transport equation may be written as:

$$R_k \frac{\partial S_k}{\partial t} = \frac{\partial}{\partial x_i} \left(D_{ij} \frac{\partial S_k}{\partial x_j} \right) - V_i \frac{\partial S_k}{\partial x_i} + Q_k^{\text{bio}} \quad (4-8)$$

where S_k is the aqueous phase concentration [$M_k L^{-3}$] for substrate k (electron donor or nutrient), V_i is the average pore water velocity in the i direction [LT^{-1}], x_i is the distance in the i direction ($i = 1, 2, 3$ or $x_i = x, y, z$) [L], D_{ij} is the 2nd order tensor for hydrodynamic dispersion [$L^2 T^{-1}$], Q_k^{bio} is a biotransformation sink term [$M_k L^{-3} T^{-1}$], R_k is the retardation factor for the substrate k [dimensionless], and t is time [T].

For each metal a [$a=1,2,\dots,NA$ (number of metals)], the transport equation can be written as:

$$R_a \frac{\partial A_a}{\partial t} = \frac{\partial}{\partial x_i} \left(D_{ij} \frac{\partial A_a}{\partial x_j} \right) - V_i \frac{\partial A_a}{\partial x_i} + Q_a^{bio} \quad (4-9)$$

where A_a is the aqueous phase concentration [$M_a L^{-3}$] of metal a , Q_a^{bio} is the biotransformation sink term for the metal a [$M_a L^{-3} T^{-1}$], and R_a is the retardation factor for metal a [dimensionless].

For each endproduct p [$p=1,2,\dots,NP$ (number of endproducts)], the transport equation can be written as:

$$R_p \frac{\partial P_p}{\partial t} = \frac{\partial}{\partial x_i} \left(D_{ij} \frac{\partial P_p}{\partial x_j} \right) - V_i \frac{\partial P_p}{\partial x_i} + Q_p^{bio} \quad (4-10)$$

where P_p is the aqueous phase concentration [$M_p L^{-3}$] for endproduct p , Q_p^{bio} is the biotransformation source term [$M_p L^{-3} T^{-1}$], and R_p is the retardation factor for endproduct p [dimensionless].

4.3.3. Source/sink equations

The biotransformation source/sink terms are evaluated by summing the effects of all bacterial species on each metal in the presence of the utilized substrates:

$$\frac{dS_k}{dt} = Q_k^{\text{bio}}(S_k, A_a, M_b) = \frac{-1}{\theta} \sum_{b=1}^{NB} M_b \chi_{b,k} \quad (4-11)$$

$$\frac{dA_a}{dt} = Q_c^{\text{bio}}(S_k, A_a, M_b) = \frac{-1}{\theta} \sum_{b=1}^{NB} M_b \chi_{b,a} \quad (4-12)$$

$$\frac{dP_p}{dt} = Q_p^{\text{bio}}(S_k, A_a, M_b) = \frac{1}{\theta} \sum_{b=1}^{NB} \sum_{k=1}^{NS} \zeta_{p,b,k} M_b \chi_{b,k} \quad (4-13)$$

where M_b is the microbial biomass concentration [$M_b \text{ L}^{-3}$] of bacterial species $b=1,2,\dots,NB$ (number of microbial species), θ is the aquifer porosity [L^0], $\chi_{b,k}$ is the utilization rate of substrate k by the bacterial species b [$M_s M_k^{-1} \text{ T}^{-1}$], $\chi_{b,a}$ is the utilization rate of metal a by the bacterial species b [$M_a M_b^{-1} \text{ T}^{-1}$], and $\zeta_{p,b,k}$ is the endproduct p generation coefficient generated from substrate k by bacterial species b [$M_p M_s^{-1}$]. Equations 4-11 and 4-12 have the same form as equations 3-7 and 3-8.

4.3.4. Utilization equations

As discussed before (equation 4-4), utilization rates may be related to the specific growth rates ($\mu_{b,k}$) for bacterial species b utilizing substrate k [$M_b M_k^{-1} \text{ T}^{-1}$]. Utilization of each substrate k by bacterial species b can be written as:

$$\chi_{b,k} = \frac{\mu_{b,k}}{Y_{b,k}} \quad (4-14)$$

and the utilization of metal a by bacterial species b can be written as:

$$\chi_{b,a} = \sum_{k=1}^{NS} \gamma_{b,a} \mu_{b,k} = \sum_{k=1}^{NS} \frac{\mu_{b,k}}{Y_{b,a}} \quad (4-15)$$

where $Y_{b,k}$ is the yield coefficient [$M_b M_k^{-1}$] representing the mass of bacterial species b produced per unit mass of substrate k , and $\gamma_{b,a}$ is the use coefficient [$M_a M_b^{-1}$] representing the mass of metal a reduced to produce a unit mass of bacterial species b .

4.3.5. Microbial growth equations

The specific growth rate of the microbial species b utilizing substrate k (as electron donor) and metal a (as electron acceptor) can be written as:

$$\mu_{b,k} = \mu_{b,k}^{\max} \left(\frac{A_a}{(K_a + A_a + \frac{A_a^2}{K_i^{a,b}})} \right) \left(\frac{S_k}{K_k + S_k} \right) I_b \quad (4-16)$$

where $\mu_{b,k}^{\max}$ is the maximum specific growth rate [$M_b M_k^{-1} T^{-1}$], K_a is the half saturation coefficient for metal a [$M_a L^{-3}$], K_k is the half saturation coefficient for substrate k [$M_k L^{-3}$], $K_i^{a,b}$ is the metals' inhibition factor representing the concentration of metal a that exerts toxic effect on microbial species b (equation 2-4), and I_b is the electron acceptor inhibition factor, which represents the concept that microbial species b will utilize the electron acceptor that provides more free energy with higher rates rather than those provide less free energy. If there are NE electron acceptors, then I_b can be represented as:

$$I_b = \prod_{e=1}^{NE} \left(\frac{Kc_{b,e}}{Kc_{b,e} + E_e} \right) \quad (4-17)$$

where $Kc_{b,e}$ is the inhibition constant of bacterial species b with the electron acceptor e ($e=1, 2, 3, \dots, NE$) [$M_e L^{-3}$], and E_e is the concentration of electron acceptor e [$M_e L^{-3}$]. In particular, if there are electron acceptors that provide much more free energy to bacterial species b than metal a, then $I_b \cong 0$. On the other hand, if metal a is providing more free energy to bacterial species b ($Kc_{b,e} \gg E_e$) or concentrations of other electron acceptors are very small ($E_e \cong 0$), then $I_b = 1$.

The mass balance equation for growth and death of microbial population b can be written as:

$$\frac{dM_b}{dt} = M_b \sum_{k=1}^{NS} \mu_{b,k} - M_b B \quad (4-18)$$

where B is the first order decay rate which accounts for cell death.

For the simple case of one microbial species, two substrates (an electron donor and a nutrient), and a single metal as an electron acceptor, the number of equations (4-11, 4-12, and 4-18) reduces to the following four equations:

$$R_s \frac{\partial S}{\partial t} = \frac{\partial}{\partial x_i} \left(D_{ij} \frac{\partial S}{\partial x_j} \right) - V_i \frac{\partial S}{\partial x_i} - \frac{\mu_{\max} M}{Y_s} \left(\frac{S}{K_s + S} \right) \left(\frac{N}{K_n + N} \right) \left(\frac{A}{K_a + A + \frac{A^2}{K_i}} \right) I \quad (4-19)$$

$$R_A \frac{\partial A}{\partial t} = \frac{\partial}{\partial x_i} \left(D_{ij} \frac{\partial A}{\partial x_j} \right) - V_i \frac{\partial A}{\partial x_i} - \frac{\mu_{\max} M}{Y_a} \left(\frac{S}{K_s + S} \right) \left(\frac{N}{K_n + N} \right) \left(\frac{A}{K_a + A + \frac{A^2}{K_i}} \right) I \quad (4-20)$$

$$R_n \frac{\partial N}{\partial t} = \frac{\partial}{\partial x_i} \left(D_{ij} \frac{\partial N}{\partial x_j} \right) - V_i \frac{\partial N}{\partial x_i} - \frac{\mu_{\max} M}{Y_n} \left(\frac{S}{K_s + S} \right) \left(\frac{N}{K_n + N} \right) \left(\frac{A}{K_a + A + \frac{A^2}{K_i}} \right) I \quad (4-21)$$

$$\frac{dM}{dt} = \mu_{\max} M \left(\frac{S}{K_s + S} \right) \left(\frac{N}{K_n + N} \right) \left(\frac{A}{K_a + A + \frac{A^2}{K_i}} \right) I - B M \quad (4-22)$$

where S, A, and N are the aqueous phase concentration of the electron donor, electron acceptor (metal), and nutrient, respectively, $[M_{s,a,n} \text{ L}^{-3}]$; Y_s, Y_a , and Y_n are the yield coefficients, representing the mass of bacterial species produced per unit mass of electron donor, electron acceptor, and nutrient, respectively, $[M_b M_{s,a,n}^{-1}]$; K_i is the inhibition constant of the metal ($M_a \text{ L}^{-3}$); and I is the inhibition factor for bacterial species as previously described (Equations 4-16). It should be noted that $Y_a = 1/\gamma$, where γ is the use

coefficient [$M_a M_b^{-1}$] representing the mass reduced of the metal to produce a unit mass of the bacteria.

4.4. Numerical Implementation

The transport equations discussed earlier (4-8 to 4-10) are coupled-nonlinear PDE's that include physical (advection and dispersion), and biological (biotransformation) terms. Biotransformation terms generally need to be approximated on smaller time scales than advection and dispersion terms. Consequently, a solution to the pertinent non-linear system of equations using small time steps is very costly. For this reason, among others, METABIOTRANS uses a time splitting algorithm (TSA), which was applied by Wheeler et al. (1987), Dawson et al. (1987), and Chiang et al. (1991), to solve the transport non-linear coupled PDE's (4-8 to 4-10). Before using the TSA with the transport equations, the steady-state saturated groundwater equation (4-7) is solved, via METABIOTRANS flow module, for the head values at each node in the problem domain. Next, accurate Darcy velocities are generated in each element. Then, TSA can be summarized into the following steps:

1. Separate reaction terms from each constituent transport equation (Equations 4-8 to 4-10); and then, solve each resultant advection-dispersion transport equation using finite element method.

2. Treat the reaction terms (Equations 4-11 to 4-13) along with the microbial growth equation (4-18) as a system of non-linear ordinary differential equations, where the fourth-order Runge Kutta method is employed (Equations 3-22 to 3-27), using smaller time steps (1% of that used in step 1).

3. Steps (1) and (2) are repeated N times where $N \times \Delta t = \text{total time}$.

Using this algorithm, one transport time step is initially performed. The results are used as initial conditions for the reaction equations, which are solved with smaller time steps. After modifying all the solutes and bacterial concentration values, the model moves to the next transport time step. The solution for the last (smaller) reaction time step is used as initial condition for the next transport time step. The model terminates when the specified number of transport time steps is completed. A discussion of finite element solution of the flow and transport governing equations is presented in the following sections.

4.4.1. Problem discretization

The first step in modeling a groundwater flow or transport problem using finite element method is the discretization of the problem domain into a grid of elements and nodes. The continuous variables of the governing equations are replaced with discrete variables that are defined at the grid elements and/or nodes. Therefore, the continuous PDEs, which could represent hydraulic heads or solute concentration over the problem domain, are replaced by a finite number of algebraic equations that define the same variables at specific points in the problem domain. Then, this system of algebraic equations is usually solved using matrix techniques.

In METABIOTRANS, three basic element shapes are used including linear elements (for 1-D problems), linear quadrilateral elements (for 2-D problems), and linear parallelepiped (for 3-D problems) [Figure 4-3]. These elements consist of 2, 4, and 8 nodes, respectively. In general, numerical solutions, which require discretization of space and time, present only an approximate solution to the governing equations. Therefore, the finer the discretization, the closer the numerical solution will be to the

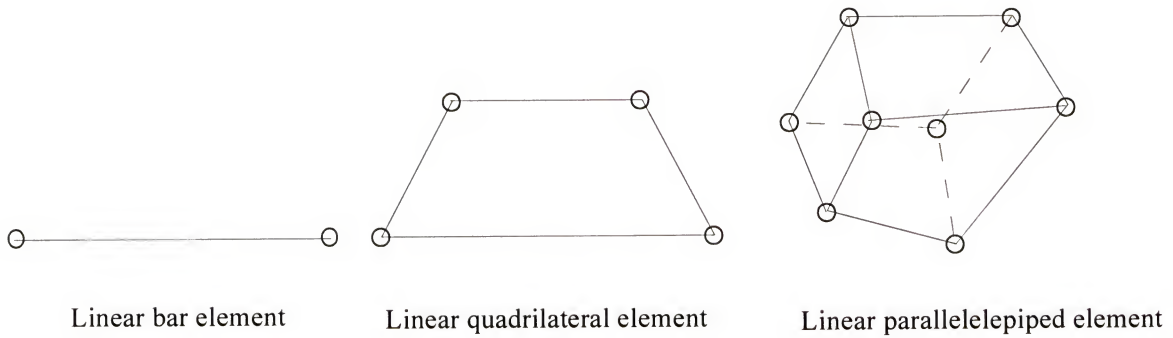


Figure 4-3 Elements used in METABIOTRANS.

analytical solution. It should be mentioned here that the precision of the finite element solution as well as the computational effort required to obtain such solution depends to large extent on the number of nodes and the differences between the highest and lowest number of nodes numbers within any element (bandwidth).

4.4.2. Derivation of the approximate equations

In this second step the integral formulations of the governing groundwater flow or transport equations are derived. These integral formations lead to a system of algebraic equations. By solving these algebraic equations nodal values of hydraulic head or solute concentrations are obtained. Because it is widely applied in solving groundwater flow and transport problems, the method of weighted residuals is used in METABIOTRANS. In this method, an approximate solution to the boundary or initial value problem is defined. Then, by substituting this solution into the governing equation, a residual (error) occurs at each node. When the weighted average of the residuals at each node is forced to be zero, a solution is obtained.

Flow equation

An approximate solution for head (h) in the 3-D steady state saturated groundwater flow equation (4-7) can be written in the form:

$$\hat{h}^{(e)} = \sum_{i=1}^n N_i^{(e)} h_i \quad (4-23)$$

where $\hat{h}^{(e)}$ is the approximate solution for the hydraulic head within element e, $N_i^{(e)}$ are interpolation functions for each node within element e, n is the number of nodes within element e, and h_i are the unknown head values at each node within element e. When equation (4-23) is substituted into equation 4-7, then an error or residual is obtained at every node of the problem domain. The contribution of any element e to the residual at a node i to which the element is joined can be written as:

$$R_i^{(e)} = - \iiint_{V^{(e)}} W_i^{(e)}(x, y, z) \left[\frac{\partial}{\partial x} \left(K_x \frac{\partial \hat{h}^{(e)}}{\partial x} \right) + \frac{\partial}{\partial y} \left(K_y \frac{\partial \hat{h}^{(e)}}{\partial y} \right) + \frac{\partial}{\partial z} \left(K_z \frac{\partial \hat{h}^{(e)}}{\partial z} \right) \right] dx dy dz \quad (4-24)$$

where $W_i^{(e)}$ is the weighting function for node i and the limits of the integration represent the volume of element e. In Galerkin's method the weighted function for each node in the element is chosen to be equal to the interpolation function for that node (i.e. $W_i^{(e)} = N_i^{(e)}$). The value of the saturated hydraulic head is further assumed to be constant within each element (but varies from an element to the other). With this assumption equation 4-24 reduces to:

$$R_i^{(e)} = - \iiint_{V^{(e)}} N_i^{(e)} \left[K_x^{(e)} \frac{\partial^2 \hat{h}^{(e)}}{\partial x^2} + K_y^{(e)} \frac{\partial^2 \hat{h}^{(e)}}{\partial y^2} + K_z^{(e)} \frac{\partial^2 \hat{h}^{(e)}}{\partial z^2} \right] dx dy dz \quad (4-25)$$

where $K_x^{(e)}$, $K_y^{(e)}$, and $K_z^{(e)}$ are the values of the saturated hydraulic conductivity

within element e in x, y, and z directions, respectively. Using the definition of the

approximate value of the hydraulic head (4-23) and integration by parts, equation 4-25 can be reduced to:

$$R_i^{(e)} = - \iiint_{V^{(e)}} N_i^{(e)} \left[K_x^{(e)} \frac{\partial N_i^{(e)}}{\partial x} \frac{\partial \hat{h}^{(e)}}{\partial x} + K_y^{(e)} \frac{\partial N_i^{(e)}}{\partial y} \frac{\partial \hat{h}^{(e)}}{\partial y} + K_z^{(e)} \frac{\partial N_i^{(e)}}{\partial z} \frac{\partial \hat{h}^{(e)}}{\partial z} \right] dx dy dz \quad (4-26)$$

which is the integral formulation for equation 4-7. Using the definition of the interpolation function, the integral equation can be evaluated to obtain the conductance matrix $[K^{(e)}]$ as following:

$$[K^{(e)}]_{nxn} = \iiint_{V^{(e)}} \begin{bmatrix} \frac{\partial N_1^{(e)}}{\partial x} & \frac{\partial N_1^{(e)}}{\partial y} & \frac{\partial N_1^{(e)}}{\partial z} \\ \vdots & \vdots & \vdots \\ \frac{\partial N_n^{(e)}}{\partial x} & \frac{\partial N_n^{(e)}}{\partial y} & \frac{\partial N_n^{(e)}}{\partial z} \end{bmatrix}_{nx3} \begin{bmatrix} K_x^{(e)} & 0 & 0 \\ 0 & K_y^{(e)} & 0 \\ 0 & 0 & K_z^{(e)} \end{bmatrix}_{3x3} \begin{bmatrix} \frac{\partial N_1^{(e)}}{\partial x} & \dots & \frac{\partial N_n^{(e)}}{\partial x} \\ \frac{\partial N_1^{(e)}}{\partial y} & \dots & \frac{\partial N_n^{(e)}}{\partial y} \\ \frac{\partial N_1^{(e)}}{\partial z} & \dots & \frac{\partial N_n^{(e)}}{\partial z} \end{bmatrix}_{3xn} dx dy dz \quad (4-27)$$

If equation (4-27) is then combined with equation (4-24), one can obtain:

$$\begin{Bmatrix} R_1^{(e)} \\ \vdots \\ R_n^{(e)} \end{Bmatrix}_{nx1} = [K^{(e)}]_{nxn} \begin{Bmatrix} h_1 \\ \vdots \\ h_n \end{Bmatrix}_{nx1} \quad (4-28)$$

Equation 4-28 is written for each element. However, they can be combined to obtain:

$$\begin{Bmatrix} R_1 \\ \vdots \\ R_p \end{Bmatrix}_{px1} = [K]_{pxp}^{global} \begin{Bmatrix} h_1 \\ \vdots \\ h_p \end{Bmatrix}_{px1} \quad (4-29)$$

where p is the total number of nodes in the domain. Then, by setting the residuals equal to zero and considering flow from specific nodes in the mesh equation 4-29 becomes

$$\begin{matrix} [K] \\ \text{global} \\ p \times p \end{matrix} \begin{matrix} \{h\} \\ p \times 1 \end{matrix} = \begin{matrix} \{F\} \\ p \times 1 \end{matrix} \quad (4-30)$$

where $\{F\}$ is the global specified flow matrix.

Transport equation

For each transport equation (4-8 to 4-10), an approximation of the concentration is assumed as follows:

$$\hat{C}^{(e)}(x, y, z) = \sum_{i=1}^n N_i^{(e)} C_i \quad (4-31)$$

where $\hat{C}^{(e)}$ is the approximate solution for the solute concentration within element e and C_i are the unknown solute concentrations for each node within element e . When this approximate solution is inserted into the transport equation one obtains:

$$\begin{aligned} R_i^{(e)} = - \iiint_{V^{(e)}} W_i^{(e)}(x, y, z) & \left[\theta^{(e)} D_x \frac{\partial^2 \hat{C}^{(e)}}{\partial x^2} + \theta^{(e)} D_y \frac{\partial^2 \hat{C}^{(e)}}{\partial y^2} + \theta^{(e)} D_z \frac{\partial^2 \hat{C}^{(e)}}{\partial z^2} - \frac{\partial(V_x \hat{C}^{(e)})}{\partial x} \right. \\ & \left. - \frac{\partial(V_y \hat{C}^{(e)})}{\partial y} - \frac{\partial(V_z \hat{C}^{(e)})}{\partial z} - \frac{\partial(\rho_d k_d \hat{C}^{(e)})}{\partial t} - \theta^{(e)} \frac{\partial \hat{C}^{(e)}}{\partial t} \right] dx dy dz \end{aligned} \quad (4-32)$$

Using the same assumption employed before with the flow equation that the interpolation function equals the weighting function and that all material properties (ρ_d and k_d) as well as the apparent groundwater velocity are constants within each element (but can vary from one element to the other), then the integral formulation can be obtained from equation 4-32 as follows:

$$\begin{aligned}
R_i^{(e)} = - \iiint_{V^{(e)}} N_i^{(e)}(x, y, z) & \left[D_x^{(e)} \frac{\partial^2 \hat{C}^{(e)}}{\partial x^2} + D_y^{(e)} \frac{\partial^2 \hat{C}^{(e)}}{\partial y^2} + D_z^{(e)} \frac{\partial^2 \hat{C}^{(e)}}{\partial z^2} - \frac{V_x^{(e)}}{\theta^{(e)}} \frac{\partial(\hat{C}^{(e)})}{\partial x} \right. \\
& \left. - \frac{V_y^{(e)}}{\theta^{(e)}} \frac{\partial(\hat{C}^{(e)})}{\partial y} - \frac{V_z^{(e)}}{\theta^{(e)}} \frac{\partial(\hat{C}^{(e)})}{\partial z} - \left(1 + \frac{\rho_d^{(e)} k_d^{(e)}}{\theta^{(e)}} \right) \frac{\partial \hat{C}^{(e)}}{\partial t} \right] dx dy dz
\end{aligned}
\tag{4-33}$$

Because METABIOTRANS solves the steady state saturated groundwater flow equation, apparent groundwater velocity is constant with time. By combining the integral expressions for each node in element e, equation 4-33 can be written in matrix form as following:

$$\begin{Bmatrix} R_1^{(e)} \\ \vdots \\ R_n^{(e)} \end{Bmatrix} = [D^{(e)}] \begin{Bmatrix} C_1 \\ \vdots \\ C_n \end{Bmatrix} + [A^{(e)}] \begin{Bmatrix} \frac{\partial C_1}{\partial t} \\ \vdots \\ \frac{\partial C_n}{\partial t} \end{Bmatrix}
\tag{4-34}$$

where $[D^{(e)}]$ is the element advection-dispersion matrix and $[A^{(e)}]$ is the element sorption matrix which can be written as:

$$\begin{aligned}
[D^{(e)}] = & \iiint_{V^{(e)}} \begin{bmatrix} \frac{\partial N_1^{(e)}}{\partial x} & \frac{\partial N_1^{(e)}}{\partial y} & \frac{\partial N_1^{(e)}}{\partial z} \\ \vdots & \vdots & \vdots \\ \frac{\partial N_n^{(e)}}{\partial x} & \frac{\partial N_n^{(e)}}{\partial y} & \frac{\partial N_n^{(e)}}{\partial z} \end{bmatrix} \begin{bmatrix} D_{xx}^{(e)} & D_{xy}^{(e)} & D_{xz}^{(e)} \\ D_{yx}^{(e)} & D_{yy}^{(e)} & D_{yz}^{(e)} \\ D_{zx}^{(e)} & D_{zy}^{(e)} & D_{zz}^{(e)} \end{bmatrix} \begin{bmatrix} \frac{\partial N_1^{(e)}}{\partial x} & \dots & \frac{\partial N_n^{(e)}}{\partial x} \\ \frac{\partial N_1^{(e)}}{\partial y} & \dots & \frac{\partial N_n^{(e)}}{\partial y} \\ \frac{\partial N_1^{(e)}}{\partial z} & \dots & \frac{\partial N_n^{(e)}}{\partial z} \end{bmatrix} dx dy dz \\
& + \iiint_{V^{(e)}} \begin{bmatrix} N_1^{(e)} N_1^{(e)} N_1^{(e)} \\ \vdots & \vdots & \vdots \\ N_n^{(e)} N_n^{(e)} N_n^{(e)} \end{bmatrix} \begin{bmatrix} \frac{V_x^{(e)}}{\theta^{(e)}} & 0 & 0 \\ 0 & \frac{V_y^{(e)}}{\theta^{(e)}} & 0 \\ 0 & 0 & \frac{V_z^{(e)}}{\theta^{(e)}} \end{bmatrix} \begin{bmatrix} \frac{\partial N_1^{(e)}}{\partial x} & \dots & \frac{\partial N_n^{(e)}}{\partial x} \\ \frac{\partial N_1^{(e)}}{\partial y} & \dots & \frac{\partial N_n^{(e)}}{\partial y} \\ \frac{\partial N_1^{(e)}}{\partial z} & \dots & \frac{\partial N_n^{(e)}}{\partial z} \end{bmatrix} dx dy dz
\end{aligned}
\tag{4-35}$$

and

$$[A^{(e)}] = \iiint_{V^{(e)}} \begin{bmatrix} N_1^{(e)} \\ \vdots \\ N_n^{(e)} \end{bmatrix} \left[1 + \frac{\rho_d^{(e)} k_d^{(e)}}{\theta^e} \right] [N_1^{(e)} \dots N_n^{(e)}] dx dy dz \quad (4-36)$$

Similar to the global conductance matrix [K], the global advection-dispersion matrix [D] and sorption matrix [A] can be obtained by the summation of the advection-dispersion and sorption matrices of all elements, respectively. Then, by forcing the weighted residual (equation 4-34) to be zero and considering concentration flux from specific nodes one can obtain:

$$\begin{matrix} [D] & \{C\} & + & [A] & \{C'\} & = & \{F\} \\ p \times p & p \times 1 & & p \times p & p \times 1 & & p \times 1 \end{matrix} \quad (4-37)$$

where {F} is the global specified concentration flux and

$$\{C'\} = \begin{Bmatrix} \frac{\partial C_1}{\partial t} \\ \vdots \\ \frac{\partial C_p}{\partial t} \end{Bmatrix} \quad (4-38)$$

Equation (4-37) is a system of ODE's, the solution of which provides values for C and $\frac{\partial C}{\partial t}$ at each node of the domain and at each time step. This equation is solved using

finite difference method as follows:

$$([A] + w\Delta t[D])\{C\}_{t+\Delta t} = ([A] - (1-w)\Delta t[D])\{C\}_t + \Delta t((1-w)\{F\}_t + w\{F\}_{t+\Delta t}) \quad (4-39)$$

where w is a weighting constant. $w=0, 0.5$, or 1.0 when forward, central, or backward difference method is used, respectively.

4.4.3. Developing the system of algebraic equation

In order to evaluate the integral formulation obtained in the last step, an interpolation function and its derivatives should be defined for each element. Gauss

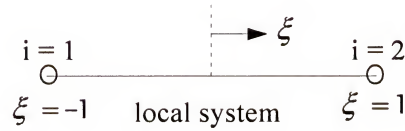
quadrature numerical integration method was used to solve the integral formulations obtained before. In this method an approximation of the integration over an interval is obtained by computing the weighted sum of values of the function for specific points on the interval as following:

$$\int_{-1}^1 \int_{-1}^1 \int_{-1}^1 f(\xi, \psi, \zeta) d\xi d\psi d\zeta = \sum_{i=1}^{N_\xi} \sum_{j=1}^{N_\psi} \sum_{k=1}^{N_\zeta} \tau_i(\xi_i) \tau_j(\psi_j) \tau_k(\zeta_k) f(\xi_i, \psi_j, \zeta_k) \quad (4-40)$$

where $\tau_i(\xi_i)$, $\tau_j(\psi_j)$, and $\tau_k(\zeta_k)$ are the weights assigned to the value of function f at the Gauss point ($\xi = \xi_i$, $\psi = \psi_j$, and $\zeta = \zeta_k$) and N_ξ , N_ψ , and N_ζ are the numbers of Gauss points in intervals $-1 \leq \xi \leq 1$, $-1 \leq \psi_j \leq 1$, and $-1 \leq \zeta_k \leq 1$, respectively.

In the development of METABIOTRANS, two Gauss points are used located at $(\frac{1}{\sqrt{3}}, \frac{-1}{\sqrt{3}})$ of each interval with weights of (1, 1) for the two points. The numerical integration is significantly simplified when the interpolation function and its derivatives at each node are defined using a local coordination system.

Linear bar element (1-D)

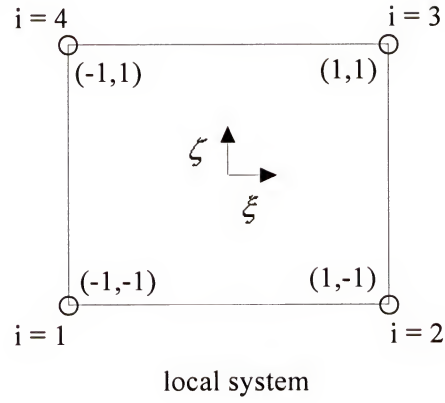


$$N_i = \frac{1}{2}(1 + \xi_i \xi) \quad (4-41)$$

$$\frac{\partial N_i}{\partial \xi} = \frac{\xi_i}{2} \quad (4-42)$$

where i is the local node number.

Linear quadrilateral element (2-D)

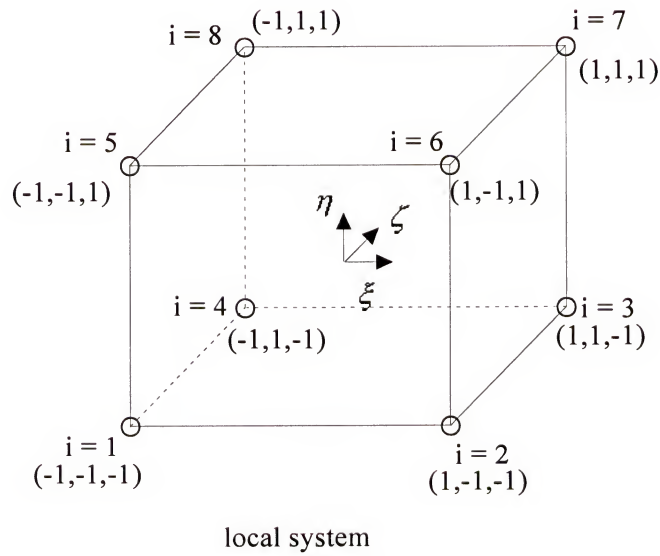


$$N_i = \frac{1}{4}(1 + \xi_i \xi)(1 + \zeta_i \zeta) \quad (4-43)$$

$$\frac{\partial N_i}{\partial \xi} = \frac{1}{4} \xi_i (1 + \zeta_i \zeta) \quad (4-44)$$

$$\frac{\partial N_i}{\partial \zeta} = \frac{1}{4} \zeta_i (1 + \xi_i \xi) \quad (4-45)$$

Linear parallelepiped element (3-D)



$$N_i = \frac{1}{8}(1 + \xi_i \xi)(1 + \zeta_i \zeta)(1 + \eta_i \eta) \quad (4-46)$$

$$\frac{\partial N_i}{\partial \xi} = \frac{\xi_i}{8} (1 + \zeta_i \zeta) (1 + \eta_i \eta) \quad (4-47)$$

$$\frac{\partial N_i}{\partial \zeta} = \frac{\zeta_i}{8} (1 + \xi_i \xi) (1 + \eta_i \eta) \quad (4-48)$$

$$\frac{\partial N_i}{\partial \eta} = \frac{\eta_i}{8} (1 + \xi_i \xi) (1 + \zeta_i \zeta) \quad (4-49)$$

Substituting these relations into the element conductance, advection-dispersion, and sorption matrices (equations 4-27, 4-35, and 4-36) one obtains:

$$[K^{(e)}]_{nxn} = \int_{-1}^1 \int_{-1}^1 \int_{-1}^1 \begin{bmatrix} \frac{\partial N_1^{(e)}}{\partial \xi} & \frac{\partial N_1^{(e)}}{\partial \zeta} & \frac{\partial N_1^{(e)}}{\partial \eta} \\ \vdots & \vdots & \vdots \\ \frac{\partial N_n^{(e)}}{\partial \xi} & \frac{\partial N_n^{(e)}}{\partial \zeta} & \frac{\partial N_n^{(e)}}{\partial \eta} \end{bmatrix}_{nx3} [J^{-1}]_{3 \times 3}^T \begin{bmatrix} K_x^{(e)} & 0 & 0 \\ 0 & K_y^{(e)} & 0 \\ 0 & 0 & K_z^{(e)} \end{bmatrix}_{3 \times 3} [J^{-1}]_{3 \times 3} \begin{bmatrix} \frac{\partial N_1^{(e)}}{\partial \xi} & \dots & \frac{\partial N_n^{(e)}}{\partial \xi} \\ \frac{\partial N_1^{(e)}}{\partial \zeta} & \dots & \frac{\partial N_n^{(e)}}{\partial \zeta} \\ \frac{\partial N_1^{(e)}}{\partial \eta} & \dots & \frac{\partial N_n^{(e)}}{\partial \eta} \end{bmatrix}_{3 \times n} |J| d\xi d\zeta d\eta \quad (4-50)$$

$$[D^{(e)}] = \int_{-1}^1 \int_{-1}^1 \int_{-1}^1 \begin{bmatrix} \frac{\partial N_1^{(e)}}{\partial \xi} & \frac{\partial N_1^{(e)}}{\partial \zeta} & \frac{\partial N_1^{(e)}}{\partial \eta} \\ \vdots & \vdots & \vdots \\ \frac{\partial N_n^{(e)}}{\partial \xi} & \frac{\partial N_n^{(e)}}{\partial \zeta} & \frac{\partial N_n^{(e)}}{\partial \eta} \end{bmatrix} [J^{-1}]^T \begin{bmatrix} D_{xx}^{(e)} & D_{xy}^{(e)} & D_{xz}^{(e)} \\ D_{yx}^{(e)} & D_{yy}^{(e)} & D_{yz}^{(e)} \\ D_{zx}^{(e)} & D_{zy}^{(e)} & D_{zz}^{(e)} \end{bmatrix} [J^{-1}] \begin{bmatrix} \frac{\partial N_1^{(e)}}{\partial \xi} & \dots & \frac{\partial N_n^{(e)}}{\partial \xi} \\ \frac{\partial N_1^{(e)}}{\partial \zeta} & \dots & \frac{\partial N_n^{(e)}}{\partial \zeta} \\ \frac{\partial N_1^{(e)}}{\partial \eta} & \dots & \frac{\partial N_n^{(e)}}{\partial \eta} \end{bmatrix} |J| d\xi d\zeta d\eta$$

$$+ \int_{-1}^1 \int_{-1}^1 \int_{-1}^1 \begin{bmatrix} N_1^{(e)} & N_1^{(e)} & N_1^{(e)} \\ \vdots & \vdots & \vdots \\ N_n^{(e)} & N_n^{(e)} & N_n^{(e)} \end{bmatrix} \begin{bmatrix} \frac{V_x^{(e)}}{\theta^{(e)}} & 0 & 0 \\ 0 & \frac{V_y^{(e)}}{\theta^{(e)}} & 0 \\ 0 & 0 & \frac{V_z^{(e)}}{\theta^{(e)}} \end{bmatrix} [J^{-1}] \begin{bmatrix} \frac{\partial N_1^{(e)}}{\partial \xi} & \dots & \frac{\partial N_n^{(e)}}{\partial \xi} \\ \frac{\partial N_1^{(e)}}{\partial \zeta} & \dots & \frac{\partial N_n^{(e)}}{\partial \zeta} \\ \frac{\partial N_1^{(e)}}{\partial \eta} & \dots & \frac{\partial N_n^{(e)}}{\partial \eta} \end{bmatrix} |J| d\xi d\zeta d\eta$$

(4-51)

$$[A^{(e)}] = \int_{-1}^1 \int_{-1}^1 \int_{-1}^1 \begin{bmatrix} N_1^{(e)} \\ \vdots \\ N_n^{(e)} \end{bmatrix} \left[1 + \frac{\rho_d^{(e)} k_d^{(e)}}{\theta^e} \right] [N_1^{(e)} \dots N_n^{(e)}] |J| d\xi d\zeta d\eta \quad (4-52)$$

where $[J]$ is the Jacobian matrix for the coordination transformation, which can be written as:

$$[J] = \begin{bmatrix} \frac{\partial N_1}{\partial \xi} & \dots & \frac{\partial N_n}{\partial \xi} \\ \frac{\partial N_1}{\partial \zeta} & \dots & \frac{\partial N_n}{\partial \zeta} \\ \frac{\partial N_1}{\partial \eta} & \dots & \frac{\partial N_n}{\partial \eta} \end{bmatrix} \begin{bmatrix} x_1 y_1 z_1 \\ \vdots \\ x_n y_n z_n \end{bmatrix} \quad (4-53)$$

Equations 4-50, 5-51, and 4-52 are the element conductance, advection-dispersion, and sorption matrices in the local coordination system. These matrices are calculated for each element using the Gauss quadrature numerical integration method (equation 4-40). Then, all element matrices are combined to obtain the global matrices needed to solve for the unknowns (hydraulic head or concentration). This process is called ‘assembling’ the global system of equations. The assembly process can be written as:

$$[K]_{global} = \sum_{e=1}^m [K^{(e)}] \quad (4-54)$$

$$[F]_{global} = \sum_{e=1}^m [F^{(e)}] \quad (4-55)$$

$$[D]_{global} = \sum_{e=1}^m [D^{(e)}] \quad (4-56)$$

$$[A]_{global} = \sum_{e=1}^m [A^{(e)}] \quad (4-57)$$

Boundary conditions

At this stage, modifications to the global matrices are performed to incorporate the flow and transport boundary conditions of the problem. There are two types of boundary conditions including Dirichlet and Neumann boundary conditions. In the first condition, values of the unknowns (hydraulic head or concentration) are specified at some nodes in the domain. These values are, in most cases, needed to solve the flow or transport governing equation. By specifying these values, the global system of the equations must be modified before solving the equations. These modifications cause reduction in the global system of equations by the number of nodal specified values. Then values of [F] are modified accordingly. In the second type of boundary conditions, rates of groundwater flow or solute flux are specified at one or more nodes. If a flux is specified at a node, then this specified flux entry is introduced in the local flux matrix ($[F^{(e)}]$) of the element which contains that node. Accordingly, this value appears in the global [F] matrix in the assembling step. The flux value at any node should not be included in the local flux matrix of all elements surround this node; instead, it should be represented by one element only.

4.4.4. Solving the system of algebraic equation

Choleski method is used to solve the system of linear algebraic equations obtained in the previous step. This method uses the fact that any square matrix [M] can be expressed as the product of a lower triangular matrix [L] and an upper triangular matrix [U].

$$[M] = [L][U] \quad (5-58)$$

Therefore, one can rewrite equations 3-30 as follows (equation 3-39 can be solved similarly):

$$[K]\{h\}=[L][U]\{h\}=[F] \quad (5-59)$$

Define vector $\{B\}$ as:

$$[U]\{h\}=\{B\} \quad (5-60)$$

then

$$[L]\{B\}=\{F\} \quad (5-61)$$

Values of the vector $\{B\}$ can be obtained directly using the following equation:

$$b_i = \frac{f_i - \sum_{j=1}^{i-1} l_{ij} b_j}{l_{ii}}, \quad i = 1 \text{ to } p \quad (5-62)$$

After obtaining all values of $\{B\}$, values of $\{h\}$ can be obtained by solving equation 4-60 as following:

$$h_{p+1-i} = b_{p+1-i} - \sum_{j=1}^{i-1} u_{p+1-i, p+1-j} h_{p+1-j}, \quad i = 1 \text{ to } p \quad (5-63)$$

The algebraic equations obtained using the finite element method are banded. For that reason, vector storage is used to assemble and solve all systems of equations to save computer storage. In vector storage only the entries within the band are stored; while those outside the band, which are all zero, are discarded. For non-symmetric equations (when solving the transport equation) the vector size G can be defined as:

$$G = (\text{DOF})^2 - (\text{DOF} - \text{SBW})(1 + \text{DOF} - \text{SBW}) \quad (5-64)$$

where DOF is the degree of freedom of the square matrix and SBW is the semi-band width. However, if the square matrix is symmetric (when solving the flow equation) the vector size is even reduced to:

$$G = \text{SBW}(\text{DOF} - \text{SBW} + 1) + 0.5 \text{ SBW} (\text{SBW} - 1) \quad (5-65)$$

4.5. METABIOTRANS Description

METABIOTRANS is a 3-D metals transport and biotransformation finite element model. METABIOTRANS models subsurface transport of multiple solutes in anisotropic, heterogeneous saturated aquifers, as influenced by advection, dispersion, adsorption, and biodegradation/biotransformation. The solutes may be biodegradable and/or non-biodegradable substrates (electron donors and nutrient) and metals (electron acceptors). Metals biotransformation follows the Michaelis-Menten kinetics equation modified to include two inhibition factors, which were used by Chen and Hao (1996) (Table 2-2), and the effect of electron donor availability. The first inhibition factor takes place when there is any other electron acceptor(s) that provides more free Gibbs energy than the metal being reduced. The existence of such an electron acceptor(s) will inhibit the reduction process. The second mechanism, on the other hand, works when the considered metal exists at sufficiently high concentrations such that it inhibits the ability of the bacteria to bring about reduction. This mechanism was considered in the kinetic equation itself (Table 2-2). Solute dissolved in the aqueous phase may adsorb to the solid phase following a linear isotherm, or they may diffuse into microbial phase where biotransformation occurs.

METABIOTRANS has the following features:

1. Multi-component aqueous advective and dispersive transport in saturated groundwater aquifers.
2. Simulates 1-D, 2-D, and 3-D problems.
3. Linear adsorption isotherm for all the solutes (electron donors and acceptors)
4. Anaerobic biodegradation/biotransformation using Michaelis-Menten kinetics.

5. Spatial variation in recharge/injection.
6. Multiple pumping and/or injecting wells.
7. Simulation of heterogeneous and/or anisotropic porous media.
8. Biotransformation by multi-bacterial-species that can reduce the considered metal.
9. Two inhibition factors that affect the behavior of the bacterial species.

The model consists of many subroutines that perform different tasks. Table 4-1 presents these subroutines and the main purpose of each one.

The main subroutine controls the program execution. Subroutine UTLPAR reads all the utilization and biological parameters from the input data file. These data include problem dimension, number of solutes, number of bacterial species, utilization parameters for each solute, and biological parameters for each bacterial species. Subroutines NODES and ELEMENTS are responsible for reading the input data for nodes numbers and their Cartesian coordination, element numbers and node numbers within each element, respectively. Subroutine MATPRO reads the different material properties of each element such as hydraulic conductivity in all directions, dispersivity coefficients in all directions, first order decay rate, solid particles density, sorption coefficients, and porosity. Meanwhile, subroutines BCF and BCT obtain boundary conditions data for the flow equations and solute transport equations, respectively. Subroutine IC calls two other subroutines, ICS and ICB, which read initial conditions of all solutes and bacterial species, respectively.

Both ASMF and ASMT subroutines assemble the global matrices for flow and transport equations, respectively, while, subroutines DCMPF and DCMPT decompose

the same two global matrices. Subroutines SOLVEF and SOLVET are accountable for solving the algebraic system of equations for both flow and transport governing equations, respectively. VELOCITY subroutine calculates the nodal values of the groundwater velocity in all directions. It calls three other subroutines V1D, V2D, and V3D for 1, 2, and 3-D problems, respectively. Finally, RKM subroutine uses fourth order Runge-Kutta Method to modify all solutes and bacterial species concentrations due to biotransformation by solving all biological equations (Monod-type kinetics equations). This subroutine uses a much smaller time step than the time step used to solve the transport equation.

Table 4-1 Subroutines of METABIOTRANS

Subroutine	Purpose
Main	Controls execution
UTLPAR	Biological data input
NODES	Nodes data input
ELEMENTS	Elements data input
MATPRO	Elements' properties data input
BCF	Boundary conditions for flow equation
BCT	Boundary conditions for transport equation
ASMF	Assembles the global conductance matrix
IC	Initial Conditions
ASMT	Assembles the global dispersion and sorption matrix
DCMPF	Matrix decomposition for flow equation
DCMPT	Matrix decomposition for transport equation
SOLVEF	Solves flow equation
SOLVET	Solves transport equation
VELOCITY	Calculates velocity
RKM	Modifies concentration due to biological reactions

In METABIOTRANS, any number of solutes NS can be used. In addition, the microbial phase is assumed to consist of NM independent bacteria, which have the ability to reduce the considered metals. These bacteria are assumed to exist as scattered microcolonies attached to the porous media. Although transport of microbes within the porous media has been reported (Harvey et al., 1987; and Kim and Corapcioglu, 1996), METABIOTRANS assumes that mobile organisms have a negligible effect compared to the attached microbes. Microbial growth is assumed to depend on the availability of substrates (electron donors), nutrients (if they are not the electron donor), and the metal being reduced (electron acceptor).

In preparation for using METABIOTRANS, the user should prepare a data file containing the following:

1. Problem dimensions: 1, 2 or 3-D.
2. Nodes data: node number and its corresponding Cartesian coordination.
3. Elements data: number of each element and the corresponding nodal numbers.
4. Materials data: the different aquifer material properties at each element.
5. Boundary conditions:
 - a. Flow boundary conditions
 - b. Specified head.
 - c. Specified flow.
6. Transport boundary conditions:
 - a. Specified solute concentration.
 - b. Specified solute flux.
7. Initial conditions for transport equation.
8. Injection/discharge data:

- a. Number if injection/discharge wells.
- b. Time functions

9. Solutes data:

- a. Number of solutes.
- b. Chemical properties for each solute.

10. Bacterial species data:

- a. Number of bacterial species.
- b. Solutes that are being utilized by each bacterial species.
- c. Growth parameters for each bacterial species.

METABIOTRANS uses time splitting algorithm to solve the system of non-linear partial differential governing equations. First, the model solves the steady-state saturated groundwater equations (4-1 and 4-2) for the head values at each node in the problem domain. Secondly, the flow velocity is calculated in each element. Then, for each time step, the transport equations (4-3 and 4-4) are solved (without the biological terms), for each solute, using the velocity values obtained previously. For each bacterial species, solutes and bacterial concentration values are then modified by solving the biological equations (4-23, 24, and 32) using the fourth-order Runge Kutta method with smaller time steps (1% of the original time step). After modifying all the solutes and bacterial concentration values, the model moves to the next time step. The model terminates when the specified number of time steps is completed. An output file is then created, which includes the nodal values of:

- 1. Initial and boundary condition values of hydraulic head and solute concentration.
- 2. Hydraulic head.

3. Flow velocity.
4. Solute concentration for each solute at the specified time steps.
5. Microbial concentrations for each microbial species at the specified time steps.
6. Moment results and mass fluxes through specified sections.

CHAPTER 5 METABIOTRANS VALIDATION

5.1. Introduction

Several test problems are performed and presented in this chapter to validate METABIOTRANS. These examples are designed for the purpose of assessing the performance of METABIOTRANS in solving each term of the governing equations. Results of eleven different test problems (Table 5-1) are compared to either analytical solutions or other numerical solutions. Three simulations are conducted to test the advection and dispersion components of the governing equations. The purpose of other three problems is to examine the model in simulating solutes transport with first order decay. Results obtained via METABIOTRANS of three more test problems that include linear sorption are compared to the analytical solution results. Finally, two test problems are considered to investigate the model performance in solving the biological terms of the governing equations.

5.2. One-dimensional solute transport validation

The first four validation problems are chosen to test METABIOTRANS in simulating 1-D solute transport. Test problem 1 is designed to investigate model performance when simulating convection and dispersion, while the purpose of the second test problem is to examine the effectiveness of METABIOTRANS as a tool for simulating solute transport with first order decay.

Table 5-1 Input parameters for the eleven test problems.

Parameter	1	2	3	4	5	6	7	8	9	10	11
Dimension	1-D	1-D	1-D	1-D	2-D	2-D	2-D	3-D	3-D	3-D	1-D
Purpose	C&D ^a	FOD ^b	Ret. ^c	Bio. ^d	C&D	FOD	Ret.	C&D	FOD	Ret.	Bio.
L_x^e	30.0	12.0	12.0	400	4500	4500	4500	1000	1000	1000	0.56
L_y	-	-	-	-	3000	3000	3000	500	500	500	-
L_z	-	-	-	-	-	-	-	500	500	500	-
N_x	40	40	40	100	180	180	180	40	40	40	56
N_y	-	-	-	-	120	120	120	20	20	20	-
N_z	-	-	-	-	-	-	-	20	20	20	-
V_x^f	1.5	1.5	3.0	1.0	1.0	1.5	2.0	1.0	1.5	2.0	0.33
D_x^g	3.75	3.75	7.5	0	200	200	400	100	100	200	0.0074
D_y	-	-	-	-	20	20	40	10	10	20	-
D_z	-	-	-	-	-	-	-	10	10	20	-
λ^h	0	0.1	0	0	0	0.001	0	0	0.001	0	0
R	1.0	1.0	2.0	1.0	1.0	1.0	2.0	1.0	1.0	2.0	1.0
μ_{max}ⁱ	-	-	-	0.01	-	-	-	-	-	-	9.9,8.3
K_s^j	-	-	-	0.5	-	-	-	-	-	-	17.4,12.2
Time^k	20	20	20	500	2000	2000	2000	300	300	300	10
Δt^k	0.5	0.5	0.5	2	20	20	20	6	6	6	0.01

^a Convection and Dispersion^b First order decay^c Retardation^d Biodegradation^e Problem domain: cm for 1-D problems, meters for 2, 3-D problems, and examples 4 and 11^f Velocity: cm/hr for 1-D, m/d for 2, 3-D, and examples 10 and 11^g Dispersion coefficient: cm²/hr for 1-D, m²/d for 2, 3-D, and example 11^h First order decay rate coefficient: hr⁻¹ for 1-D and d⁻¹ for 2 and 3-Dⁱ Max specific growth rate d⁻¹^j Half saturation coefficient mg/l^k hours for examples 1,4,7 and days for examples 2,3,5,6,8,9,10,11

The main goal of the third problem is to validate the model solutions for solute transport with linear sorption (retardation). Finally, the last one-dimensional test is designed to study model performance with non-linear biodegradation.

METABIOTRANS solutions to the four test problems are compared against those of analytical or other numerical models. The one-dimensional transport model with linear sorption and biotransformation is obtained from equation (4-19) when one substrate is modeled as following:

$$R \frac{\partial S}{\partial t} = D \frac{\partial^2 S}{\partial x^2} - V \frac{\partial S}{\partial x} - \lambda S - \mu_{\max} \left(\frac{S}{K_s + S} \right) \quad (5-1)$$

If K_s is assumed to be much larger than the dissolved substrate concentration S , then the equation collapse to the 1-D transport equation with first order decay coefficient $\lambda =$

$\frac{\mu_{\max}}{K_s}$ and the remaining terms are as defined before in chapter 4. Only the dissolved

solute in equation (5-1) is assumed to undergo first order decay or biodegradation. By applying the following boundary and initial conditions to equation (5-1):

$$S = S_0 \quad \text{at } x = 0, \quad (5-2)$$

$$S, \frac{\partial S}{\partial t} = 0 \quad \text{at } x = \infty, \quad (5-3)$$

and

$$S = 0 \quad \text{for } 0 < x < \infty \quad \text{at } t = 0 \quad (5-4)$$

the following analytical solution is obtained:

$$S(x, t) = \frac{S_0}{2} \left\{ \exp \left[\frac{x}{2D} (V - U) \right] \operatorname{erfc} \left[\frac{Rx - Ut}{2\sqrt{RDt}} \right] + \exp \left[\frac{x}{2D} (V + U) \right] \operatorname{erfc} \left[\frac{Rx + Vt}{2\sqrt{RDt}} \right] \right\} \quad (5-5)$$

where erfc is the complimentary error function and

$$U = \sqrt{V^2 + 4\lambda D} \quad (5-6)$$

5.2.1. Test problem 1: Solute transport with zero decay and no retardation

For the case of solute that is not subjected to first order decay ($\lambda=0$) and retardation, equation (5-5) reduces to:

$$S(x, t) = \frac{S_0}{2} \left\{ \operatorname{erfc} \left[\frac{x - Vt}{2\sqrt{Dt}} \right] + \exp \left[\frac{x V}{D} \right] \operatorname{erfc} \left[\frac{x + Vt}{2\sqrt{Dt}} \right] \right\} \quad (5-7)$$

A hypothetical test problem is adopted from USGS. (1989) for the case of 1-D advection-dispersion transport in saturated groundwater that is represented by equation (5-7). Model parameter values for this test problem are as follows:

Velocity (V)	= 1.50 cm/h
Longitudinal dispersion (D)	= 3.75 cm ² /h
Solute concentration at inflow boundary (S ₀)	= 1.0 mg/l
Maximum distance along x-axis (L)	= 30.0 cm

The same problem is solved via METABIOTRANS using 40 linear elements and a time step of 0.5 hr. Comparisons between METABIOTRANS results and those of the analytical solution for $t = 2.5, 5, 10$, and 20 hrs are presented in Figure 5-1, which clearly shows that both solutions are in good agreement with each other. Because METABIOTRANS solves the flow equation before the transport equation, values for the hydraulic conductivity, porosity, and flow boundary conditions are assumed to maintain a constant velocity of 1.5 cm/h. Test problem 1 illustrates that METABIOTRANS effectively simulates 1-D advection-dispersion transport.

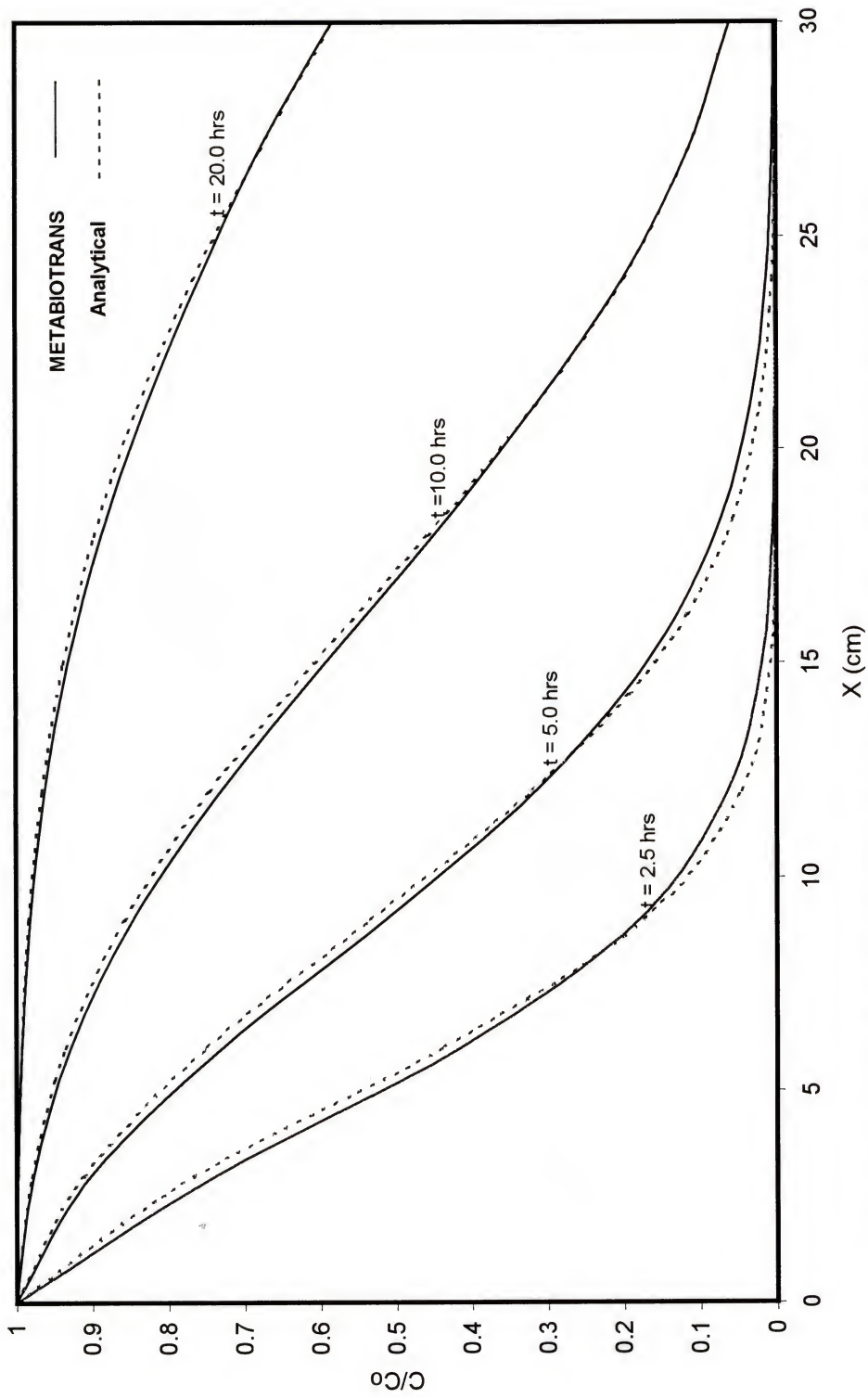


Figure 5-1. Comparisons between METABIOTRANS and the analytical solution for test problem 1.

5.2.2. Test problem 2: Solute transport with decay and no retardation

The main goal of this test problem is to test METABIOTRANS in simulating 1-D solute transport with first order decay. Equation 5-8 presents the analytical solution for such case of solute transport, which is equivalent to equation 5-5 with $R=1.0$.

$$S(x, t) = \frac{S_o}{2} \left\{ \exp \left[\frac{x}{2D} (V - U) \right] \operatorname{erfc} \left[\frac{x - Ut}{2\sqrt{Dt}} \right] + \exp \left[\frac{x}{2D} (V + U) \right] \operatorname{erfc} \left[\frac{x + Ut}{2\sqrt{Dt}} \right] \right\} \quad (5-8)$$

The input parameters for this test problem are similar to those of test problem 1 except that the first order decay rate (λ) is given a value of 0.1 hr^{-1} . Another input data file for METABIOTRANS was prepared for this problem with 40 linear elements and 0.5 hr time step. Figure 5-2 represents METABIOTRANS results for test problem 2 against those of the analytical solution (equation 5-8). METABIOTRANS produced excellent approximations for test problem 2 as compared to the analytical solution for all the considered time values.

As steady state is approached, both solutions converge to one another. By comparing Figure 5-1 with Figure 5-2, one can see the difference between the transport of the solute with first order decay and that of solute with no decay. Clearly, there are small differences between the two cases for $t = 2.5$ hrs; however, as time increases, the distinction between solutions of the two problems becomes more clear. At $t = 20$ hrs, the relative concentration (C/C_o) of solute with first order decay rate of 0.1 reaches a value of 0.15 at $X=30$ cm, whereas the dimensionless concentration is 0.6 for non-decaying solute transport. Beyond 2.5 hrs, it becomes evident that more contaminant moves further into the problem domain in the first test problem than the second. Because of solute decay, contaminant fluxes are lower in the problem domain for the second test problem.

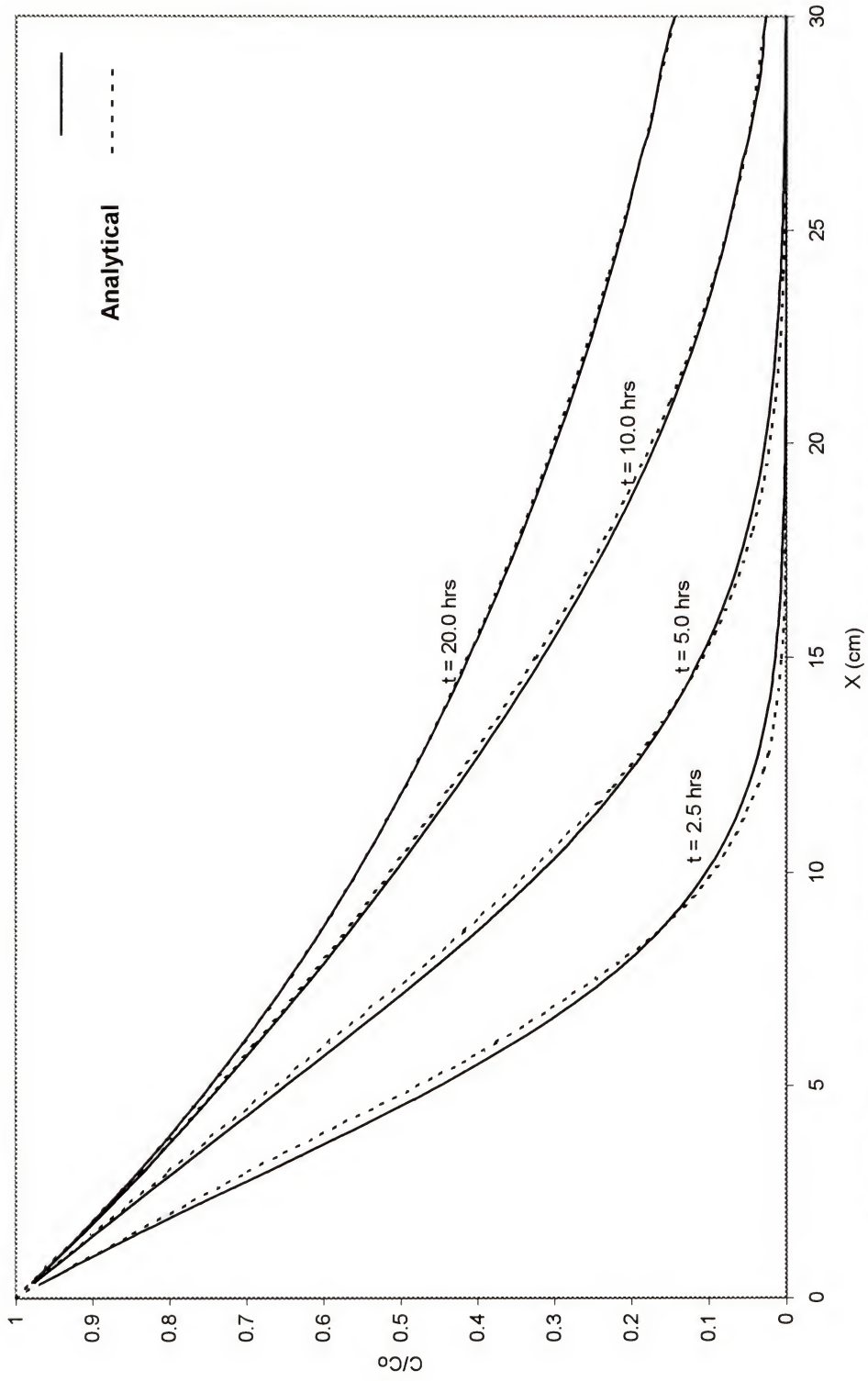


Figure 5-2. Comparison between METABIOTRANS and the analytical solution for test problem 2.

Test problem 2 shows that METABIOTRANS is quite accurate in solving 1-D first order solute decay and transport in saturated groundwater.

5.2.3. Test problem 3: Solute transport with retardation and zero decay

Test problem 3 is designed to test METABIOTRANS as a tool for simulating solute transport problems with solute sorption that is linear, reversible, and instantaneous. For the case of a solute not subjected to first order chemical transformation ($\lambda=0$), equation (5-5) reduces to:

$$S(x, t) = \frac{S_o}{2} \left\{ \operatorname{erfc} \left[\frac{Rx - Vt}{2\sqrt{RDt}} \right] + \exp \left[\frac{xV}{D} \right] \operatorname{erfc} \left[\frac{Rx + Vt}{2\sqrt{RDt}} \right] \right\} \quad (5-9)$$

The following model parameter values were chosen for this problem:

Velocity (V)	= 3.0 cm/h
Longitudinal dispersion coefficient (D)	= 7.5 cm ² /h
Solute concentration at inflow boundary (S _o)	= 1.0 mg/l
Maximum distance along x-axis (L)	= 30.0 cm
Retardation factor (R)	= 2.0

METABIOTRANS solution to this test problem is exactly the same as the solution to test problem number 1. The velocity (V), longitudinal dispersion coefficient (D), and the retardation factor (R) for test problem 3 are chosen to be twice as large as those for test problem 1; thus, the apparent velocity (V/R) and the longitudinal dispersivity (D/R) are the same for both test problems. Accordingly, both problems yield the same solution (Figures 5-1 and 5-3). Thus, it may be concluded that METABIOTRANS simulates 1-D solute transport problems with linear sorption.

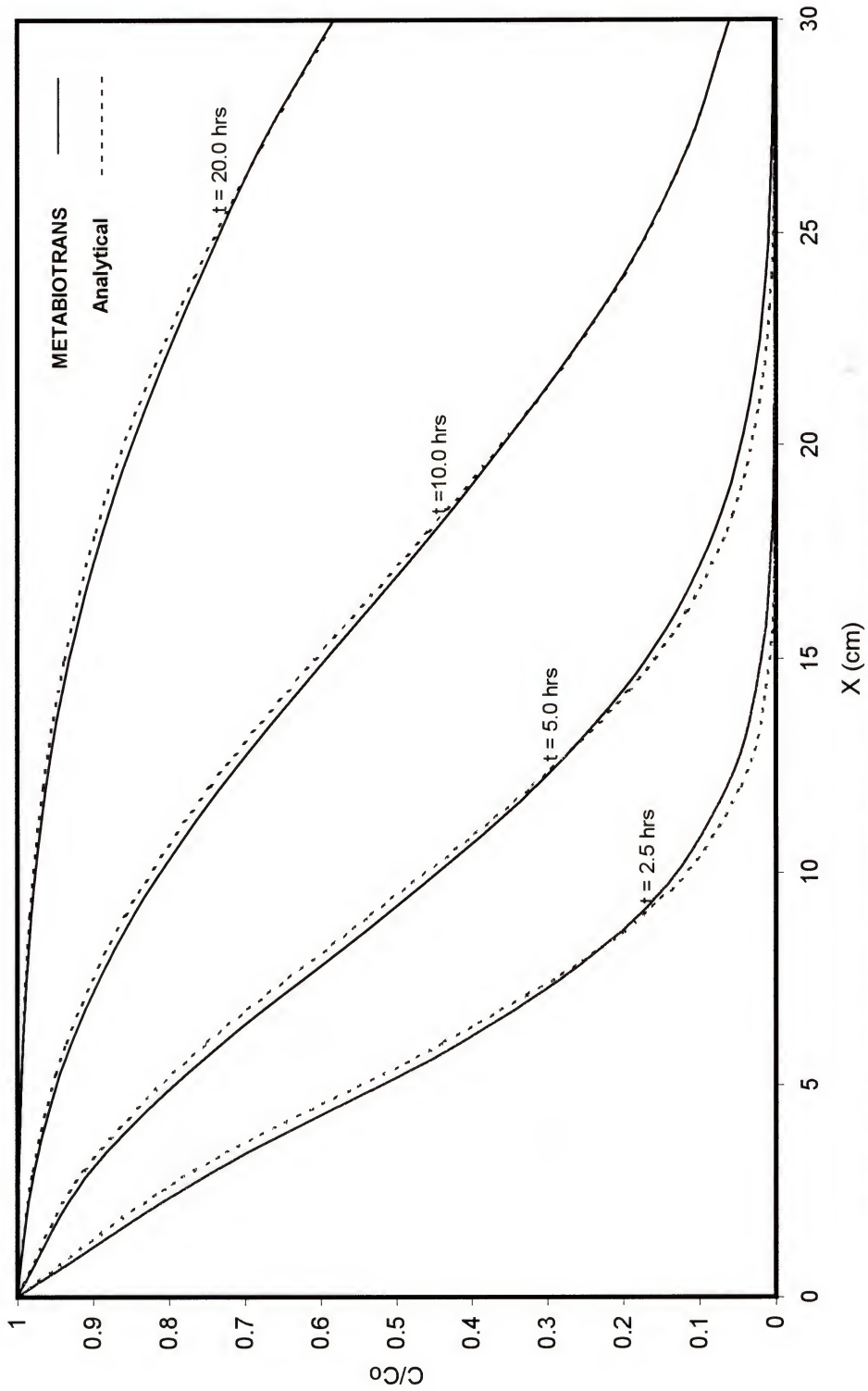


Figure 5-3. Comparisons between METABIOTRANS and the analytical solution for test problem 3.

5.2.4. Test problem 4: Steady state advective solute transport with non-linear biodegradation

The last three test problems examined METABIOTRANS performance with the first three terms of the governing equation (equation 5-1). The fourth validation problem is formulated to test the fourth term of the governing equations. For the case of steady state advective solute transport and non-linear biodegradation, equation 5-1 reduces to:

$$V \frac{\partial S}{\partial x} + \mu_{\max} \left(\frac{S}{K_s + S} \right) = 0 \quad (5-10)$$

Assembling the following boundary conditions:

$$S = S_o \quad \text{at } x = 0.0 \quad (5-11)$$

$$\text{and } \frac{\partial S}{\partial x} = 0 \quad \text{at } x = L. \quad (5-12)$$

Parlange et al. (1984) presented equation 5-13 as the analytical solution for equation 5-10. This equation (5-13) may be used to calculate the distance X corresponding to a given concentration $S(X)$.

$$x = \frac{V}{\mu_{\max}} \left[K_s \ln \left(\frac{S}{S_o} \right) + S_o - S \right] \quad (5-13)$$

This analytical solution was used to compare its results with METABIOTRANS results for test problem 4. The model parameter values specified for this validation test are chosen as follows:

Velocity (V)	= 1.0 m/d
Solute concentration at inflow boundary (S_o)	= 1.0 mg/l
Maximum distance along x-axis (L)	= 400 m
Half saturation constant (K_s)	= 0.5 mg/l
Maximum specific growth rate (μ_{\max})	= 0.01 d ⁻¹

Element length (Δx)	= 4.0 m
Time interval (Δt)	= 2 d
Total time (t_t)	= 500 d

As equation 5-13 represents a steady state solution, and in order to compare METABIOTRANS solution of test problem 4 to that of the analytical solution, many time steps were simulated until steady state condition was achieved at approximately $t = 500$ days.

Figure 5-4 represents METABIOTRANS results at $t = 50, 100, 200$, and 500 days. In addition, the same figure shows the steady state analytical solution (equation 5-13) of test problem 4. Clearly, both the analytical and the METABIOTRANS solutions ($t = 500$ days) are in good agreement. The explicit agreement between the two solutions suggests that METABIOTRANS successfully simulates the transport equation that includes Monod kinetics.

5-3. Two-dimensional solute transport validation

As a continuation of model evaluation, this section deals with 2-D groundwater solute transport problems. Three validation problems are presented in this section with the purpose of testing METABIOTRANS performance in solving each term of the 2-D solute transport governing equations. Test problem 5 investigates the advection-dispersion transport of a non-decaying non-sorbed solute in saturated groundwater, while test problems 6 and 7 examine METABIOTRANS in modeling solute transport with first order decay and linear sorption, respectively. METABIOTRANS results from these three test problems are compared against those of analytical solutions. Assuming $K_s \gg S$ in equation 4-19, then the reaction term reduces to a first order function with decay rate $\lambda =$

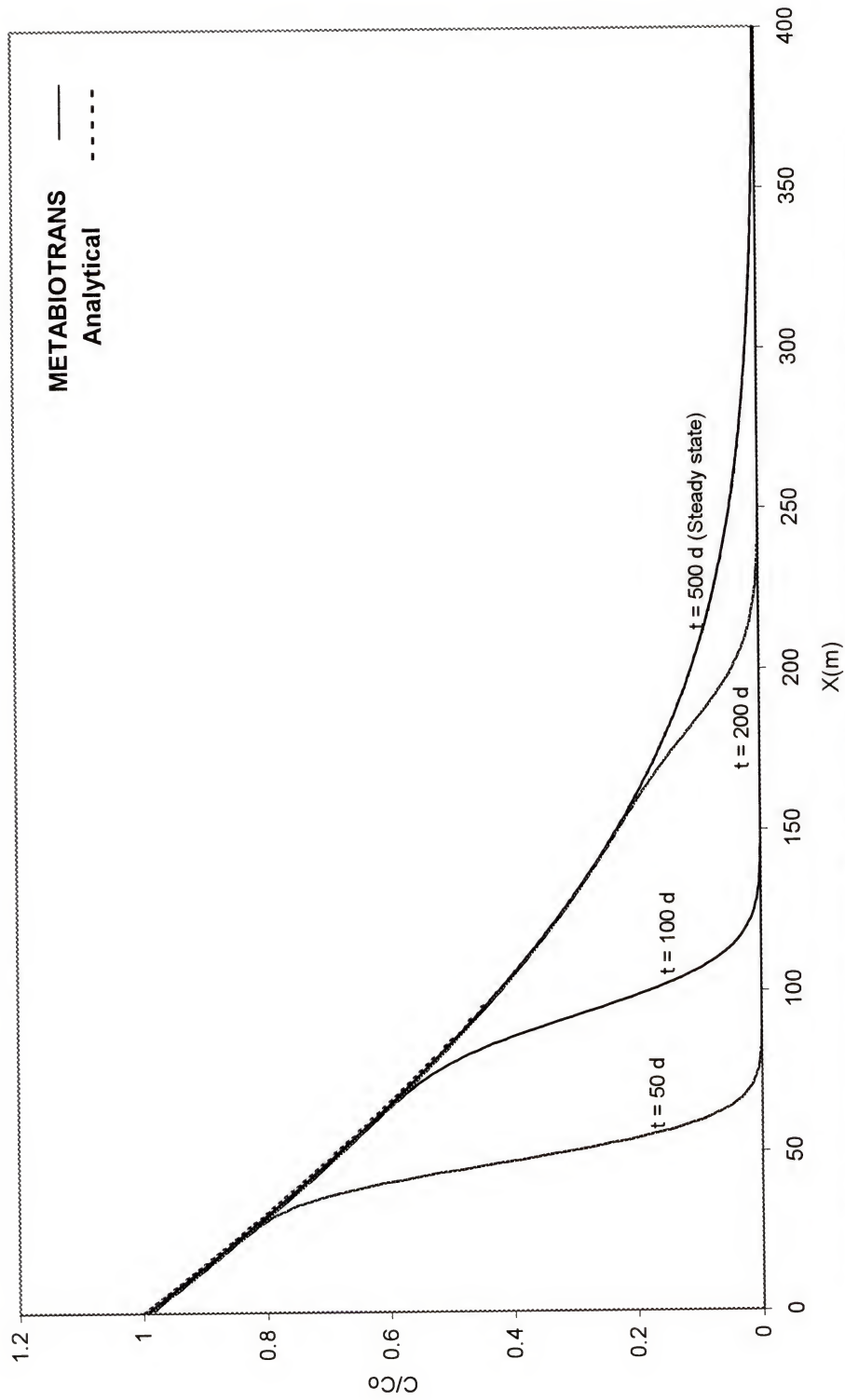


Figure 5-4. Comparison between METABIOTRANS and the analytical solution for test problem 4.

$\frac{\mu_{\max}}{K_s}$. In addition, if the equation is limited to a two-dimensional domain, equation 4-19

becomes:

$$R \frac{\partial S}{\partial t} = D_x \frac{\partial^2 S}{\partial x^2} + D_y \frac{\partial^2 S}{\partial y^2} - V \frac{\partial S}{\partial x} - \lambda S \quad (5-14)$$

For a 2-D horizontal flow domain of finite width containing a continuous source of contamination that is a plane of a finite width located at the longitudinal origin ($x=0$), the following boundary and initial conditions may be used:

$$S = S_0 \quad \text{at } x = 0, \quad (5-15)$$

$$S = S_0 \quad \text{at } Y_c - W_s/2 < y < Y_c + W_s/2, \quad (5-16)$$

$$S, \frac{\partial S}{\partial y} = 0 \quad \text{at } y = 0, \quad (5-17)$$

$$S, \frac{\partial S}{\partial y} = 0 \quad \text{at } y = W, \quad (5-18)$$

$$S, \frac{\partial S}{\partial x} = 0 \quad \text{at } x = \infty \quad (5-19)$$

$$\text{and } S = 0 \quad \text{for } 0 < x < \infty \text{ and } 0 < y < W \quad \text{at } t = 0 \quad (5-20)$$

where D_x and D_y are dispersion coefficients in x and y directions, respectively [L^2T^{-1}], V is the velocity in the x -direction [LT^{-1}], W is the aquifer width [L], W_s is the solute source width [L], and Y_c is the transverse (y -coordinate) of the center of the solute source. The analytical solution to equation 5-14, with the above described boundary and initial conditions (equations 5-15 to 5-20), was presented by Hewson (1976) as follows:

$$S(x, y, t) = S_0 \sum_{n=0}^{\infty} L_n P_n \cos(\eta y) \left\{ \exp \left[\frac{x(V - \beta R)}{2D_x} \right] \operatorname{erfc} \left[\frac{x - \beta t}{2\sqrt{D_x t/R}} \right] + \exp \left[\frac{x(V + \beta R)}{2D_x} \right] \operatorname{erfc} \left[\frac{x + \beta t}{2\sqrt{D_x t/R}} \right] \right\} \quad (5-21)$$

where
$$L_n = \begin{cases} 0.5 & n = 0 \\ 1 & n > 0 \end{cases} \quad (5-22)$$

$$P_n = \begin{cases} \frac{Y_2 - Y_1}{W} & n = 0 \\ \frac{[\sin(\eta Y_2) - \sin(\eta Y_1)]}{n\pi} & n > 0 \end{cases} \quad (5-23)$$

$$Y_1 = Y_c - W_s/2, \quad (5-24)$$

$$Y_2 = Y_c + W_s/2, \quad (5-25)$$

$$\eta = n\pi/W, \quad (5-26)$$

and
$$\beta = \frac{1}{R} \sqrt{V^2 + 4D_x (\eta^2 D_y + R \lambda)} \quad (5-27)$$

5.3.1. Test problem 5: Solute transport with zero decay and no retardation

This test problem was selected to investigate METABIOTRANS performance in modeling 2-D advection- dispersion solute transport. The analytical solution of this case is equivalent to equations 5-21 to 27 with $R = 1.0$ and $\lambda = 0$:

$$S(x, y, t) = S_o \sum_{n=0}^{\infty} L_n P_n \cos(\eta y) \left\{ \exp \left[\frac{x(V - \beta)}{2D_x} \right] \operatorname{erfc} \left[\frac{x - \beta t}{2\sqrt{D_x t}} \right] + \exp \left[\frac{x(V + \beta)}{2D_x} \right] \operatorname{erfc} \left[\frac{x + \beta t}{2\sqrt{D_x t}} \right] \right\} \quad (5-28)$$

$$\beta = \sqrt{V^2 + 4D_x \eta^2 D_y} \quad (5-29)$$

The parameters values chosen for this validation test are:

Velocity (V)	= 1.0 m/d
Longitudinal dispersion coefficient (D_x)	= 200 m ² /d
Transverse dispersion coefficient (D_y)	= 20 m ² /d

Solute concentration at inflow boundary (S_o)	= 1.0 mg/l
Maximum distance along x-axis	= 4500 m
Maximum distance along y-axis (aquifer width) (W)	= 3000 m
Element size in x-direction (Δx)	= 25.0 m
Element size in y-direction (Δy)	= 25.0 m
Time interval (Δt)	= 20 d
Total time (t_t)	= 2000 d
Solute source width (W_s)	= 2200 m
Y-coordination of solute source (Y_c)	= 1500 m

Using the above model parameter values, a data file is prepared for test problem 5 with 21600 square elements. Comparisons between the METABIOTRANS and the analytical solutions for $t = 1000$ and 2000 days are shown in Figures 5-5a and 5-5b, respectively. These figures show that the two solutions are in good agreement with each other. This test problem clearly shows that METABIOTRANS simulates 2-D advection-dispersion transport problems with high accuracy.

5.3.2. Test problem 6: Solute transport with decay and no retardation

Similar to test 2 for 1-D validation, test problem 6 is used to demonstrate the ability of METABIOTRANS to simulate 2-D transport of solutes subject to first order decay. The analytical solution in this case can be produced from equations (5-21 to 27) setting $R=1.0$. As a result, equations 5-21 and 5-27 become the following:

$$S(x, y, t) = S_o \sum_{n=0}^{\infty} L_n P_n \cos(\eta y) \left\{ \exp \left[\frac{x(V - \beta)}{2D_x} \right] \operatorname{erfc} \left[\frac{x - \beta t}{2\sqrt{D_x t}} \right] + \exp \left[\frac{x(V + \beta)}{2D_x} \right] \operatorname{erfc} \left[\frac{x + \beta t}{2\sqrt{D_x t}} \right] \right\} \quad (5-30)$$

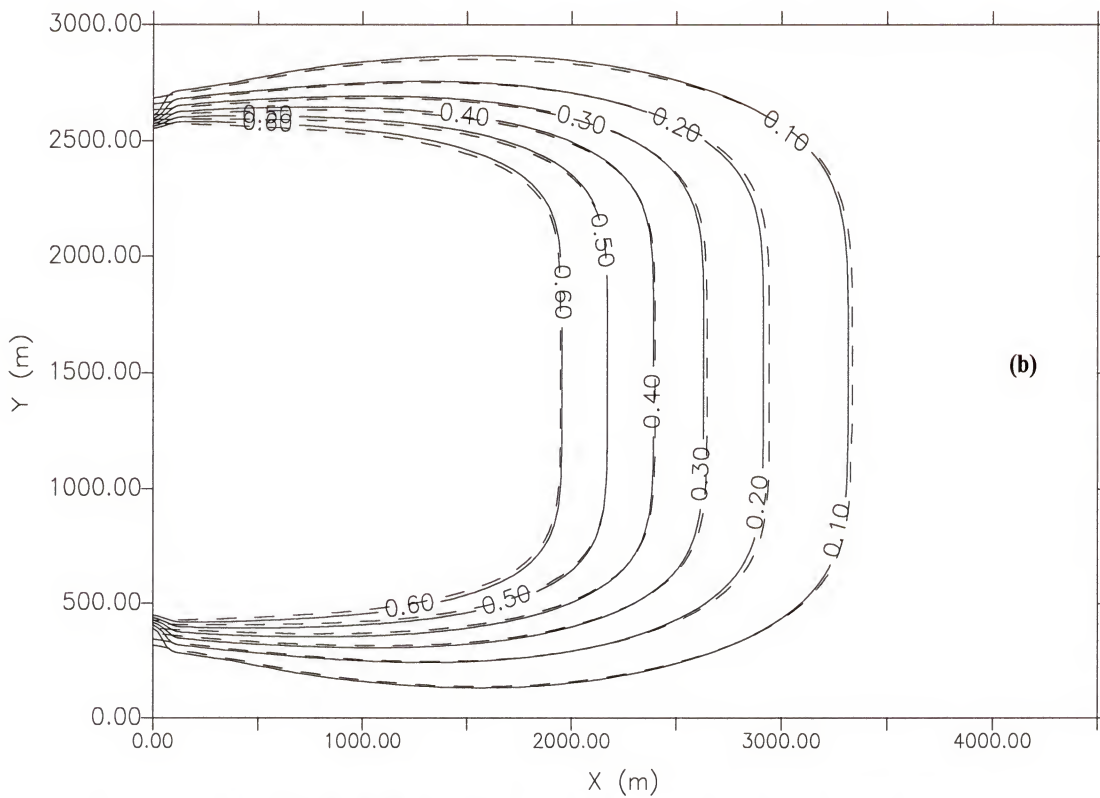
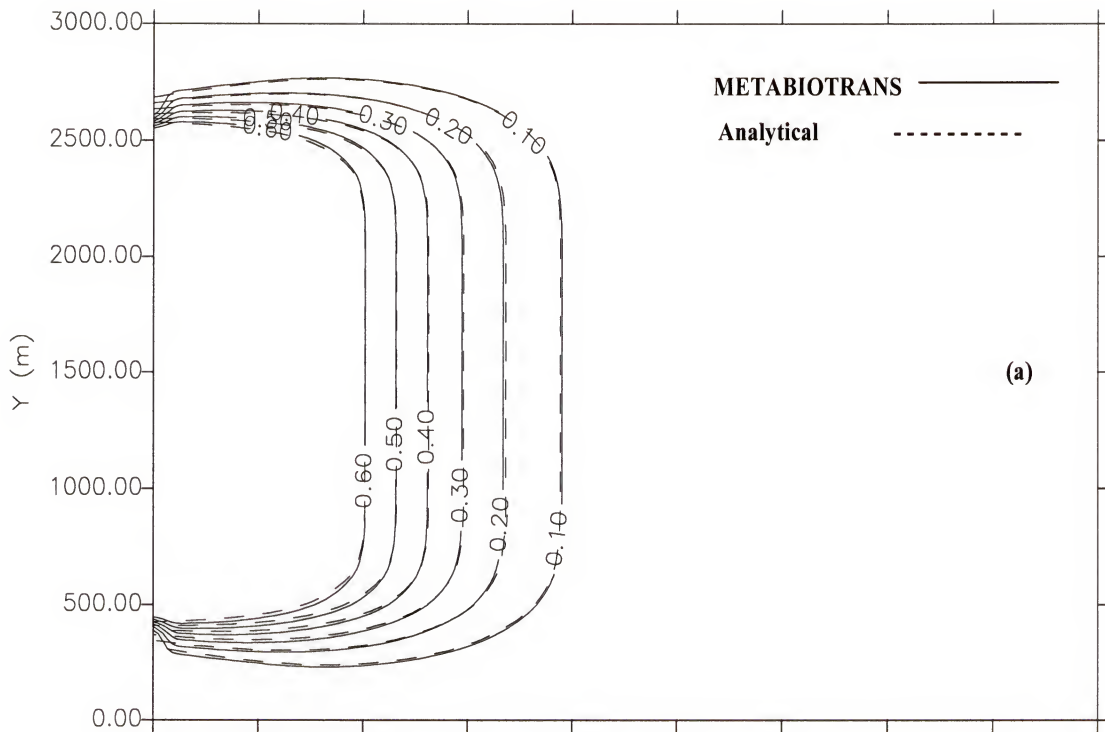


**Figure 5-5 Comparison between METABIOTRANS and analytical solution
for test problem 5. (a) $t = 1000$ days and (b) $t = 2000$ days**

$$\beta = \sqrt{V^2 + 4D_x(\eta^2 D_y + \lambda)} \quad (5-31)$$

Model parameters values specified for this validation test are:

Velocity (V)	= 1.5 m/d
Longitudinal dispersion coefficient (D_x)	= 200 m ² /d
Transverse dispersion coefficient (D_y)	= 20 m ² /d
Solute concentration at inflow boundary (S_o)	= 1.0 mg/l
First order decay rate (λ)	= 0.001
Maximum distance along x-axis	= 4500 m
Maximum distance along y-axis (aquifer width) (W)	= 3000 m
Element size in x-direction (Δx)	= 25.0 m
Element size in y-direction (Δy)	= 25.0 m
Time interval (Δt)	= 20 d
Total time (t_t)	= 2000 d
Solute source width (W_s)	= 2200 m
Y-coordination of solute source (Y_c)	= 1500 m

Comparisons between the model results and the analytical solution results for $t = 1000$ and 2000 days are provided in Figure 5-6. This Figure shows a significant agreement between both solutions.

5.3.3. Test problem 7: Solute transport with retardation and zero decay

In this test problem, simulation results of METABIOTRANS for 2-D transport of solutes with linear sorption (which is linear, reversible and instantaneous) are compared to those of analytical solution. After setting the first order decay factor (λ) to a value of

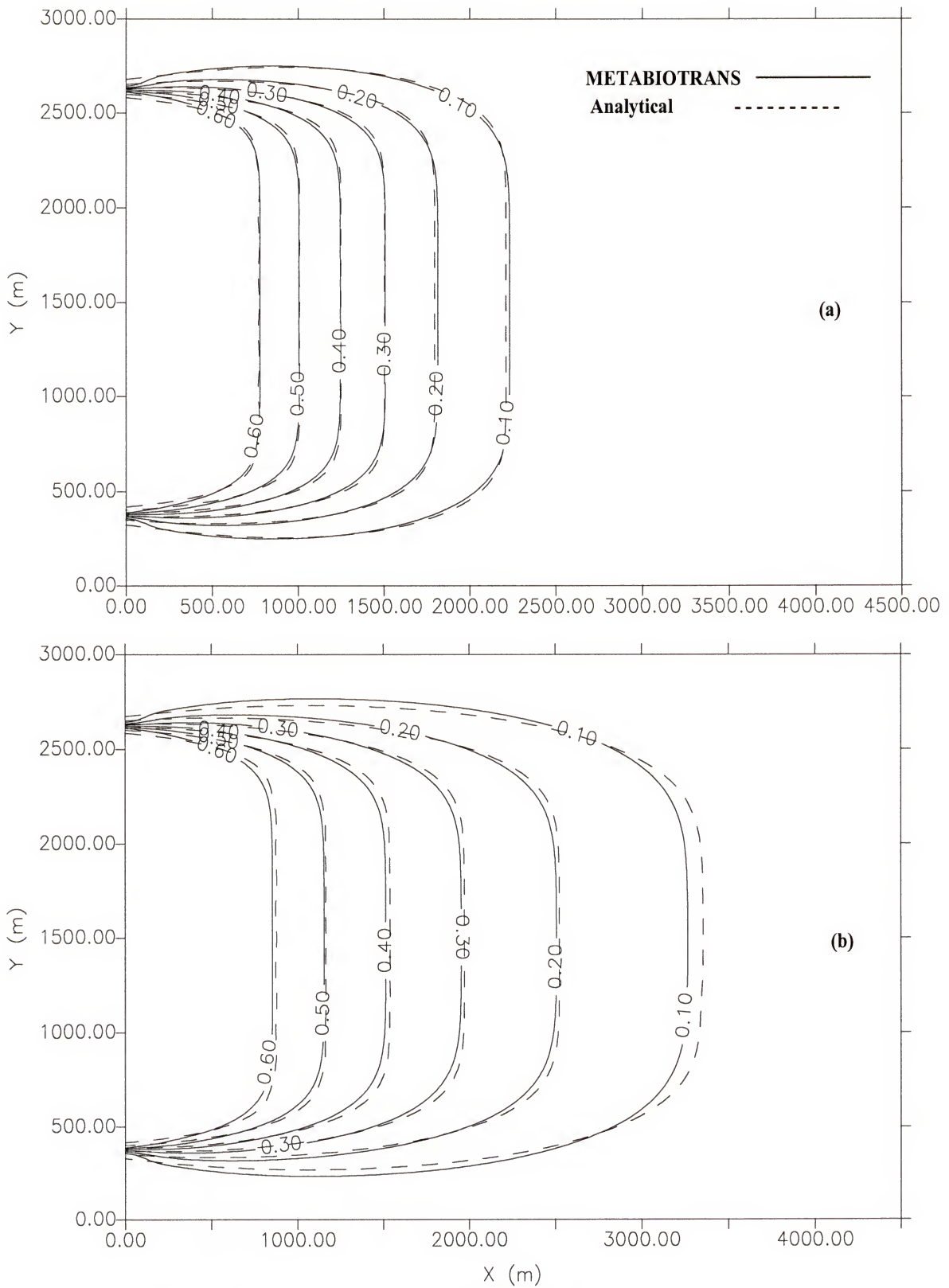


Figure 5-6 Comparison between METABIOTRANS and analytical solution for test problem 6. (a) $t = 1000$ days and (b) $t = 2000$ days.

zero, equations (5-21 to 27) yield the analytical solution for this problem, where only equation 5-27 changes as follows:

$$\beta = \frac{1}{R} \sqrt{V^2 + 4D_x \eta^2 D_y} \quad (5-32)$$

Model parameters values for test problem 7 are as follows:

Velocity (V)	= 2.0 m/d
Longitudinal dispersion coefficient (D_x)	= 400 m ² /d
Transverse dispersion coefficient (D_y)	= 40 m ² /d
Solute concentration at inflow boundary (S_o)	= 1.0 mg/l
Retardation factor (R)	= 2.0
Maximum distance along x-axis	= 4500 m
Maximum distance along y-axis (aquifer width) (W)	= 3000 m
Element size in x-direction (Δx)	= 25.0 m
Element size in y-direction (Δy)	= 25.0 m
Time interval (Δt)	= 20 d
Total time (t_t)	= 2000 d
Solute source width (W_s)	= 2200 m
Y-coordination of solute source (Y_c)	= 1500 m

METABIOTRANS effectively simulates the 2-D solute transport with retardation.

Figure 5-7 suggests that the model solution and analytical solution for test problem 7 are consistent with one another.

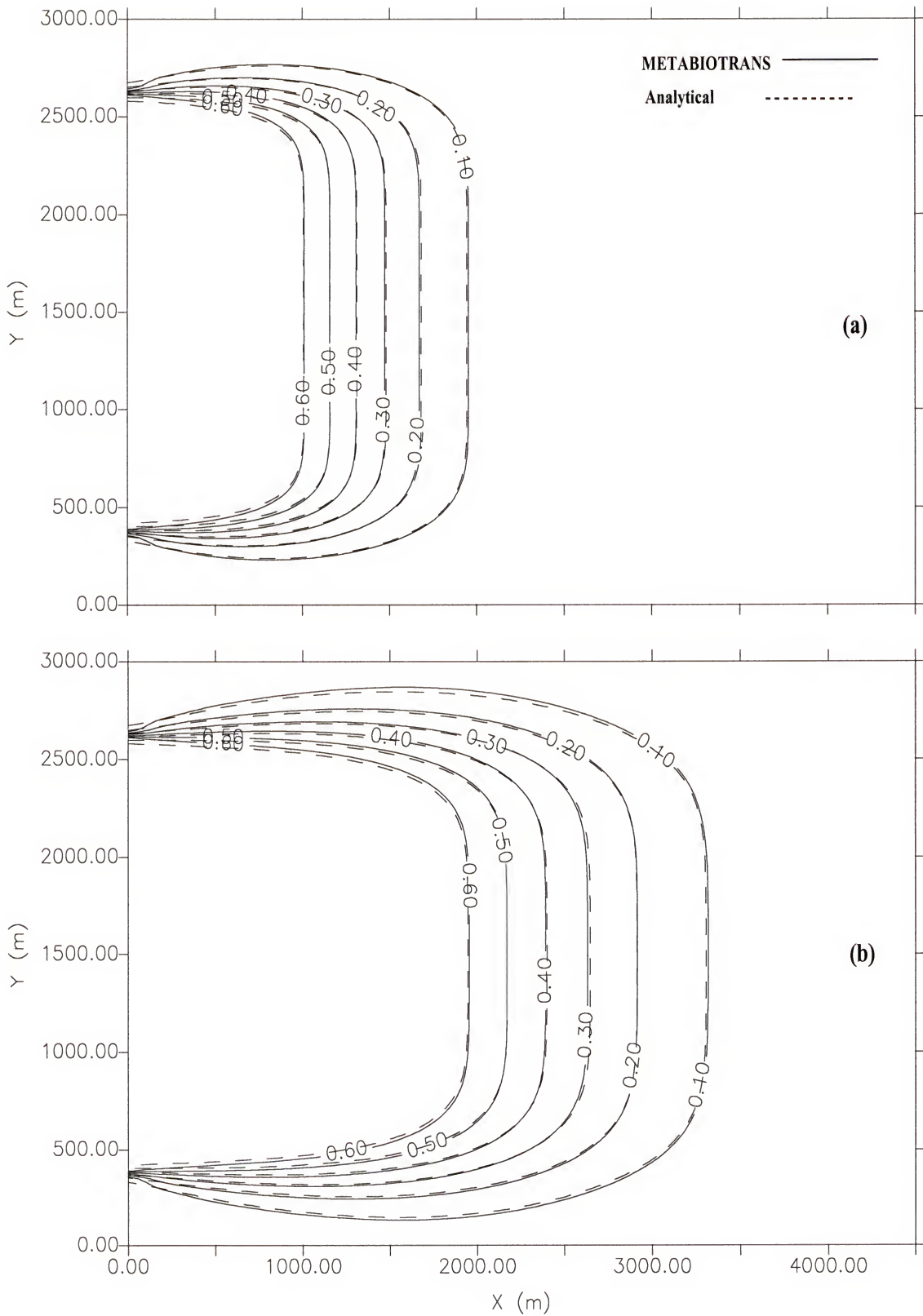


**Figure 5-7 Comparison between METABIOTRANS and analytical solution
for test problem 7. (a) $t = 1000$ days and (b) $t = 2000$ days**

5.4. Three-dimensional solute transport validation

An extension to equation 5-14 to represent 3-D solute transport yields:

$$R \frac{\partial S}{\partial t} = D_x \frac{\partial^2 S}{\partial x^2} + D_y \frac{\partial^2 S}{\partial y^2} + D_z \frac{\partial^2 S}{\partial z^2} - V \frac{\partial S}{\partial x} - \lambda S \quad (5-33)$$

For an aquifer of a finite width and height and a contaminant source of a finite width and height, the following boundary and initial conditions can be used to develop the analytical solution to equation 5-33:

$$S = S_0 \quad \text{at } x = 0, \quad (5-34)$$

$$S = S_0 \quad \text{at } Y_c - W_s/2 < y < Y_c + W_s/2, \quad (5-35)$$

$$S = S_0 \quad \text{at } Z_c - H_s/2 < z < Z_c + H_s/2, \quad (5-36)$$

$$S, \frac{\partial S}{\partial y} = 0 \quad \text{at } y = 0, \quad (5-37)$$

$$S, \frac{\partial S}{\partial y} = 0 \quad \text{at } y = W, \quad (5-38)$$

$$S, \frac{\partial S}{\partial z} = 0 \quad \text{at } z = 0, \quad (5-39)$$

$$S, \frac{\partial S}{\partial z} = 0 \quad \text{at } z = H, \quad (5-40)$$

$$S, \frac{\partial S}{\partial x} = 0 \quad \text{at } x = \infty \quad (5-41)$$

$$\text{and } S = 0 \quad \text{for } 0 < x < \infty, 0 < y < W, \text{ and } 0 < z < H \quad \text{at } t = 0 \quad (5-42)$$

in which D_z is the dispersion coefficients in z direction [L^2T^{-1}], H is the aquifer height [L], H_s is the solute source height [L], and Z_c is the z -coordinate of the center of the source plane. The analytical solution for equation 5-33, with the boundary and initial conditions mentioned above (equations 5-34 to 42), was first derived by Cleary and Ungs (1978) as follows:

$$S(x,y,z,t)=S_0 \sum_{m=0}^{\infty} \sum_{n=0}^{\infty} L_{mn} O_m P_n \cos(\zeta z) \cos(\eta y) \left\{ \exp\left[\frac{x(V-\beta R)}{2D_x}\right] \operatorname{erfc}\left[\frac{x-\beta t}{2\sqrt{D_x t/R}}\right] + \exp\left[\frac{x(V+\beta R)}{2D_x}\right] \operatorname{erfc}\left[\frac{x+\beta t}{2\sqrt{D_x t/R}}\right] \right\} \quad (5-43)$$

$$\text{where } L_{mn} = \begin{cases} 0.5 & m=0 \text{ and } n=0 \\ 1 & m=0 \text{ and } n>0 \\ 1 & m>0 \text{ and } n=0 \\ 2 & m>0 \text{ and } n>0 \end{cases} \quad (5-44)$$

$$O_m = \begin{cases} \frac{Z_2 - Z_1}{H} & m=0 \\ \frac{[\sin(\zeta Z_2) - \sin(\zeta Z_1)]}{m\pi} & m>0 \end{cases} \quad (5-45)$$

$$P_n = \begin{cases} \frac{Y_2 - Y_1}{W} & n=0 \\ \frac{[\sin(\eta Y_2) - \sin(\eta Y_1)]}{n\pi} & n>0 \end{cases} \quad (5-46)$$

$$\text{where } Y_1 = Y_c - W_s/2, \quad (5-47)$$

$$Y_2 = Y_c + W_s/2, \quad (5-48)$$

$$Z_1 = Z_c - H_s/2, \quad (5-49)$$

$$Z_2 = Z_c + H_s/2, \quad (5-50)$$

$$\eta = n\pi/W, \quad \text{for } n=0, 1, 2, 3, \dots \quad (5-51)$$

$$\zeta = m\pi/H, \quad \text{for } m=0, 1, 2, 3, \dots \quad (5-52)$$

$$\text{and } \beta = \frac{1}{R} \sqrt{V^2 + 4D_x (\eta^2 D_y + \zeta^2 D_z + R \lambda)} \quad (5-53)$$

The main goal of this section is to examine the behavior of METABIOTRANS in modeling 3-D solute transport problem. In the same manner as the previous section, three

additional validation problems are employed to illustrate the performance of METABIOTRANS with 3-D solute transport problems.

5.4.1. Test problem 8: Solute transport with zero decay and no retardation

In this test problem a 3-D advection-dispersion solute transport problem is modeled via METABIOTRANS. The main purpose of this problem is to compare METABIOTRANS results with analytical solution results. The analytical solution of this problem is the equivalent to equation 5-43 for $R = 1.0$ and $\lambda = 0$. In this case, equations 5-43 and 5-53 reduce to:

$$S(x, y, z, t) = S_0 \sum_{m=0}^{\infty} \sum_{n=0}^{\infty} L_{mn} O_m P_n \cos(\zeta z) \cos(\eta y) \left\{ \exp\left[\frac{x(V - \beta)}{2D_x}\right] \operatorname{erfc}\left[\frac{x - \beta t}{2\sqrt{D_x t}}\right] + \exp\left[\frac{x(V + \beta)}{2D_x}\right] \operatorname{erfc}\left[\frac{x + \beta t}{2\sqrt{D_x t}}\right] \right\} \quad (5-54)$$

$$\beta = \sqrt{V^2 + 4D_x(\eta^2 D_y + \zeta^2 D_z)} \quad (5-55)$$

Model parameter values for this example are chosen as follows:

Velocity (V)	= 1.0 m/d
Longitudinal dispersion coefficient (D_x)	= 100 m ² /d
Transverse dispersion coefficient (D_y)	= 10 m ² /d
Vertical dispersion coefficient (D_z)	= 10 m ² /d
Solute concentration at inflow boundary (S_0)	= 1.0 mg/l
Maximum distance along x-axis	= 1000 m
Maximum distance along y-axis (aquifer width) (W)	= 500 m
Maximum distance along z-axis (aquifer height) (H)	= 500 m
Element size in x-direction (Δx)	= 25.0 m
Element size in y-direction (Δy)	= 25.0 m

Element size in z-direction (Δy)	= 25.0 m
Time interval (Δt)	= 6 d
Total time (t_t)	= 300 d
Solute source width (W_s)	= 400 m
Y-coordination of solute source (Y_c)	= 250 m
Solute source height (H_s)	= 400 m
Z-coordination of solute source (Z_c)	= 250 m

This problem was simulated with METABIOTRANS using 16000 cubic elements and 50 time steps. Figure 5-8 provides results of both METABIOTRANS and the analytical solution at $z = 250$ ft and $t = 300$ days. As the figure shows, the two solutions are in good agreement with each other. The analytical solution shows that the relative concentration line 0.1 travels a distance of 670 m into the aquifer (in x-direction), while the same concentration line moved a distance of 660 m using METABIOTRANS, producing a 1.5% error. On the other hand, concentration line 0.4 travels 450 and 410 feet for the analytical and METABIOTRANS solutions, respectively, with an error of 8.8%. The METABIOTRANS solution to test problem 5-8 indicates that it successfully simulates 3-D advection-dispersion saturated groundwater problems.

5.4.2. Test problem 9: Solute transport with decay and no retardation

Test problem 9 is a 3-D advection-dispersion transport of a solute subjected to first order decay. Modeling solute transport with decay using METABIOTRANS was studied for 1- and 2-D problems via test problems 2 and 6, respectively. This test problem is an extension of the validation study, performed in problems 1 and 5, to 3-D problems. The analytical solution of this case can be represented by equation 5-43 using a retardation

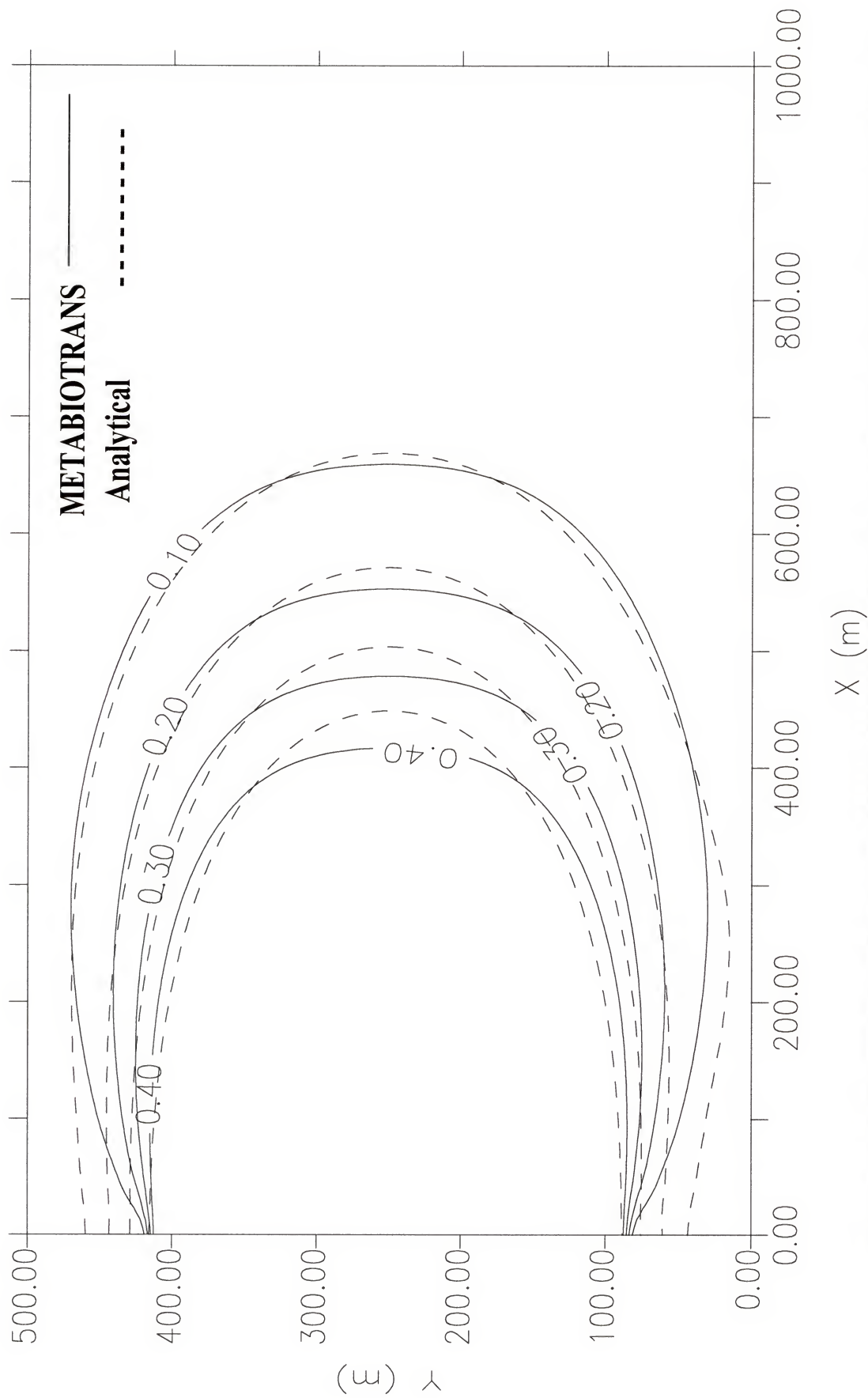


Figure 5-8 Comparison between METABIOTRANS and analytical solution for test problem 8.

factor of 1.0. This will reduce equations 5-43 and 5-53 to:

$$S(x, y, z, t) = S_0 \sum_{m=0}^{\infty} \sum_{n=0}^{\infty} L_{mn} O_m P_n \cos(\zeta z) \cos(\eta y) \left\{ \exp \left[\frac{x(V - \beta)}{2D_x} \right] \operatorname{erfc} \left[\frac{x - \beta t}{2\sqrt{D_x t}} \right] + \exp \left[\frac{x(V + \beta)}{2D_x} \right] \operatorname{erfc} \left[\frac{x + \beta t}{2\sqrt{D_x t}} \right] \right\} \quad (5-56)$$

$$\beta = \sqrt{V^2 + 4D_x (\eta^2 D_y + \zeta^2 D_z + \lambda)} \quad (5-57)$$

Model parameter values for this problem are:

Velocity (V)	= 1.5 m/d
Longitudinal dispersion coefficient (D_x)	= 100 m ² /d
Transverse dispersion coefficient (D_y)	= 10 m ² /d
Vertical dispersion coefficient (D_z)	= 10 m ² /d
Solute concentration at inflow boundary (S_0)	= 1.0 mg/l
First order decay rate (λ)	= 0.001
Maximum distance along x-axis	= 1000 m
Maximum distance along y-axis (aquifer width) (W)	= 500 m
Maximum distance along z-axis (aquifer height) (H)	= 500 m
Element size in x-direction (Δx)	= 25.0 m
Element size in y-direction (Δy)	= 25.0 m
Element size in z-direction (Δz)	= 25.0 m
Time interval (Δt)	= 6 d
Total time (t_i)	= 300 d
Solute source width (W_s)	= 400 m
Y-coordination of solute source (Y_c)	= 250 m
Solute source height (H_s)	= 400 m

Z-coordination of solute source (Z_c) = 250 m

Figure 5-9 presents a comparison between METABIOTRANS solution and the analytical solution for test problem 9 at $z = 250$ m and after 300 days. According to the analytical solution, relative concentration line 0.1 moves into the aquifer for a distance of 780 m. The METABIOTRANS solution, on the other hand, predicts the movement of the same concentration line to be 820 m into the aquifer. Comparing these two values would yield a relative error of 4.5%. For the 0.3 concentration line the traveling distances are 590 and 585 m for the analytical and METABIOTRANS solutions, respectively, with an error of 0.9%. The maximum error for all the relative concentration lines was 4.5%, which suggests that METABIOTRANS effectively solves this type of problem.

5.4.3. Test problem 10: Solute transport with retardation and zero decay

In this test problem 3-D advection dispersion solute transport with linear sorption will be considered. The analytical solution of this problem can be obtained using equations 5-43 to 53. However, the first order decay rate parameter (λ) should be set to zero. In this case, equation 5-53 will be reduced to:

$$\beta = \frac{1}{R} \sqrt{V^2 + 4D_x(\eta^2 D_y + \zeta^2 D_z)} \quad (5-58)$$

Model parameters values of this example are chosen as follows:

Velocity (V)	= 2.0 m/d
Longitudinal dispersion coefficient (D_x)	= 200 m ² /d
Transverse dispersion coefficient (D_y)	= 20 m ² /d
Vertical dispersion coefficient (D_z)	= 20 m ² /d
Solute concentration at inflow boundary (S_o)	= 1.0 mg/l
Retardation factor (R)	= 2.0

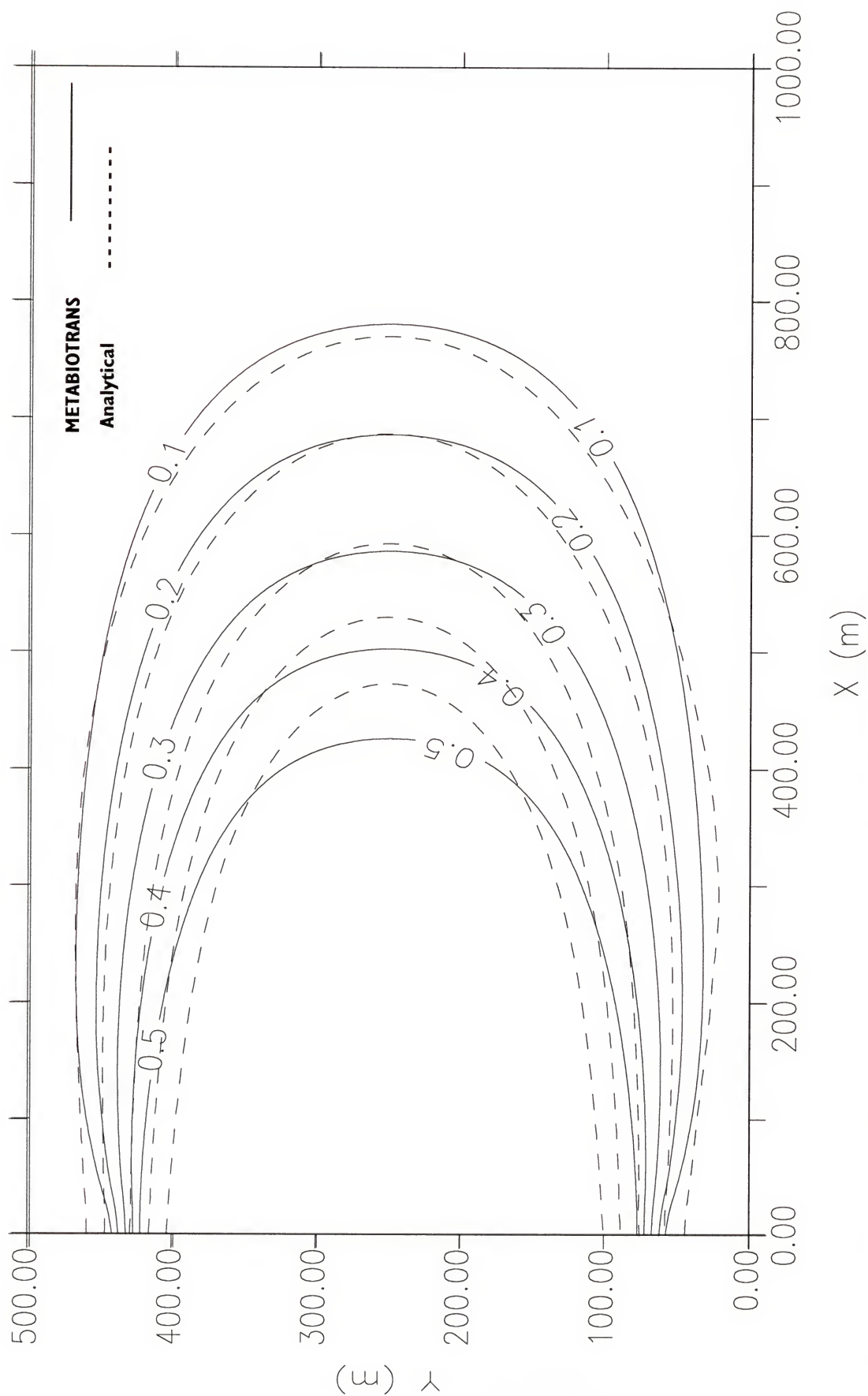


Figure 5-9 Comparison between METABIOTRANS and analytical solution for test problem 9.

Maximum distance along x-axis	= 1000 m
Maximum distance along y-axis (aquifer width) (W)	= 500 m
Maximum distance along z-axis (aquifer height) (H)	= 500 m
Element size in x-direction (Δx)	= 25.0 m
Element size in y-direction (Δy)	= 25.0 m
Element size in z-direction (Δz)	= 25.0 m
Time interval (Δt)	= 6 d
Total time (t_i)	= 300 d
Solute source width (W_s)	= 400 m
Y-coordination of solute source (Y_c)	= 250 m
Solute source height (H_s)	= 400 m
Z-coordination of solute source (Z_c)	= 250 m

Relative concentration lines at $z = 250$ m and $t = 300$ days for both the METABIOTRANS and the analytical solutions are shown in Figure 5-10. This figure clearly illustrates that the two solutions are in good agreement with one another.

5-5. Multi-solutes transport

Test problem 11: 1-D Multi-solutes transport with biodegradation

Chen et al. (1992) presented experimental and simulation results of the transport and biodegradation of toluene and benzene in the presence of dissolved oxygen in a soil column. A constant composition solution of toluene (20 mg/l) and benzene (20 mg/l) was fed to the column. They collected and analyzed effluent samples for both toluene and benzene concentrations. Chen et al. (1992) also used a mathematical model to predict the effluent concentration at the end of the column. They used independent laboratory

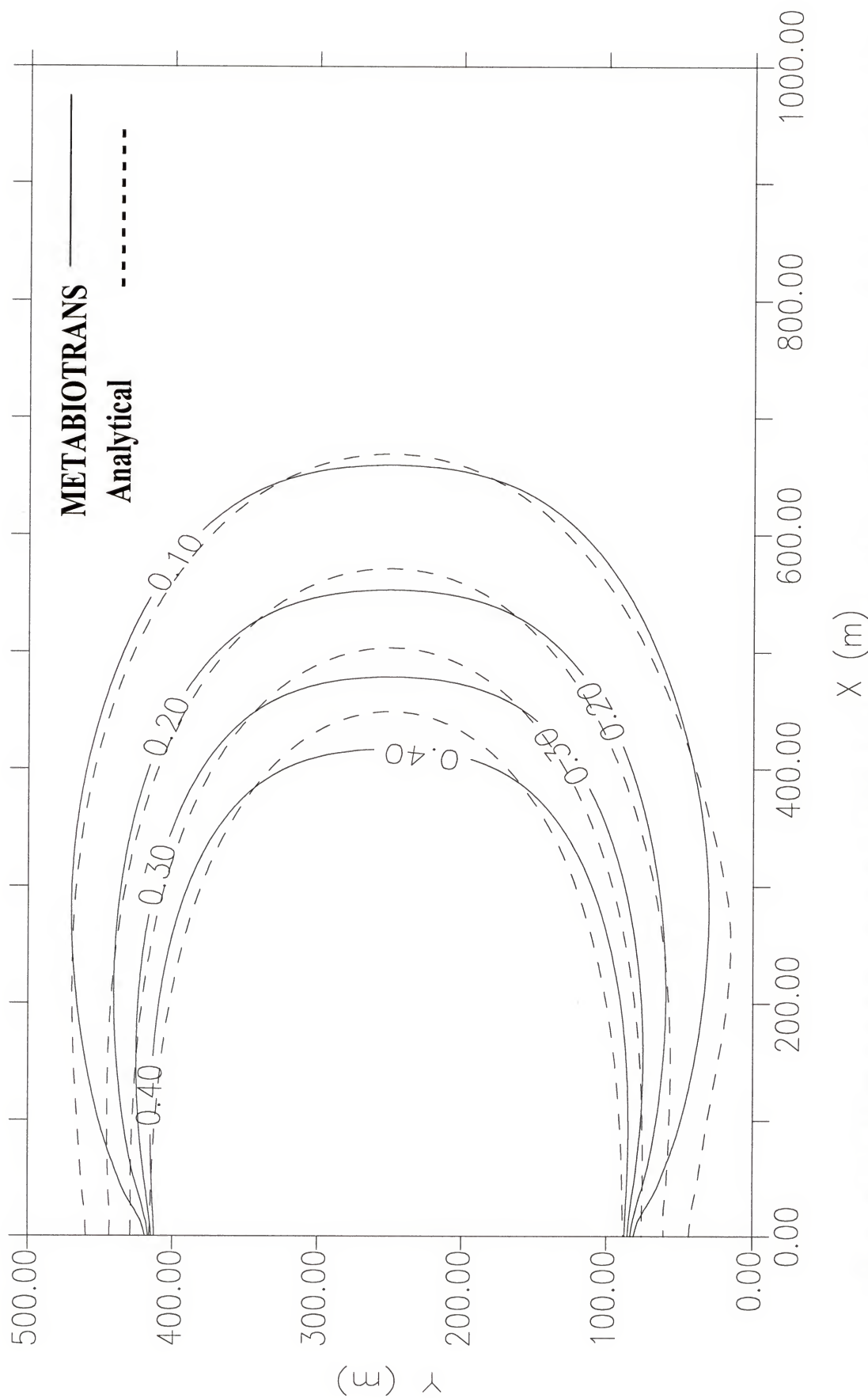


Figure 5-10 Comparison between METABIOTRANS and analytical solution for test problem 10.

measurements and experiments to determine model input parameters. The same experiment is simulated as a final validation problem of METABIOTRANS. The main purpose of this test problem is to test the model as a tool for simulating the transport and biotransformation of multi-solutes in the presence of multi-bacterial species, and to study the interaction between the different solutes and bacterial species in the system. Two microbial species are assumed to exist in the column; one of which is responsible for biodegrading toluene in the presence of dissolved oxygen, while the other is assumed to be accountable for the benzene biodegradation. The change of dissolved oxygen concentration in the system is due to both microbial activities. The following model parameter values are obtained from Chen et al. (1992):

Flow and transport parameters:

Column length	= 0.56 m
Element size in x-direction (Δx)	= 0.01 m
Porosity (n)	= 0.38
Average velocity (V_x)	= 0.33 m/d
Longitudinal dispersivity (α_l)	= 0.0224 m
Simulation time	= 10 days

Biological parameters:

Microbial species 1:

Maximum specific growth rate (μ_{\max})	= 9.9 d ⁻¹
Death rate (B)	= 0.1 d ⁻¹
Initial biomass concentration (M_0)	= 0.82 mg/l

Electron donor and acceptor used are toluene and Dissolved oxygen, respectively.

Microbial species 2:

Maximum specific growth rate (μ_{\max}) = 8.3 d⁻¹

Death rate (B) = 0.1 d⁻¹

Initial biomass concentration (M_o) = 0.21 mg/l

Electron donor and acceptor used are benzene and Dissolved oxygen, respectively.

Toluene:

Concentration at inflow boundary (C_{T-in}) = 20 mg/l

Half saturation constant (K_T) = 17.4 mg/l

Yield Coefficient (Y_T) = 0.9132

Initial concentration (C_{To}) = 0.0 mg/l

Benzene:

Concentration at inflow boundary (C_{B-in}) = 20 mg/l

Half saturation constant (K_B) = 12.2 mg/l

Yield Coefficient (Y_B) = 0.9302

Initial concentration (C_{Bo}) = 0.0 mg/l

METABIOTRANS results are compared to simulations performed by Chen et al. (1992), laboratory data, and results generated using BIOMOC (a USGS contaminant transport and biodegradation model). Figure 5-11 illustrates the change in the relative benzene and toluene concentrations at the column end with time. In the case of toluene, (Figure 5-11a) Chen et al. simulation under-predicts the experimental data, while the BIOMOC over-predicted the experimental data. Though seems to slightly over-predict the experimental data at its peak, METABIOTRANS predictions appear to be closer to

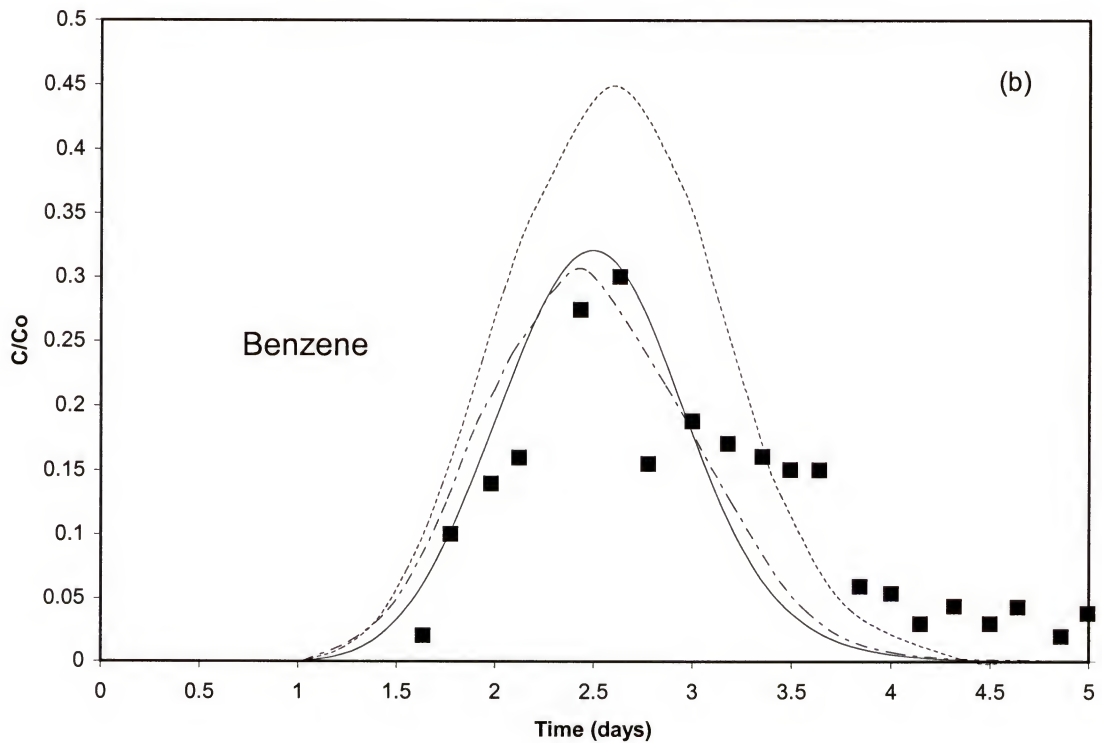
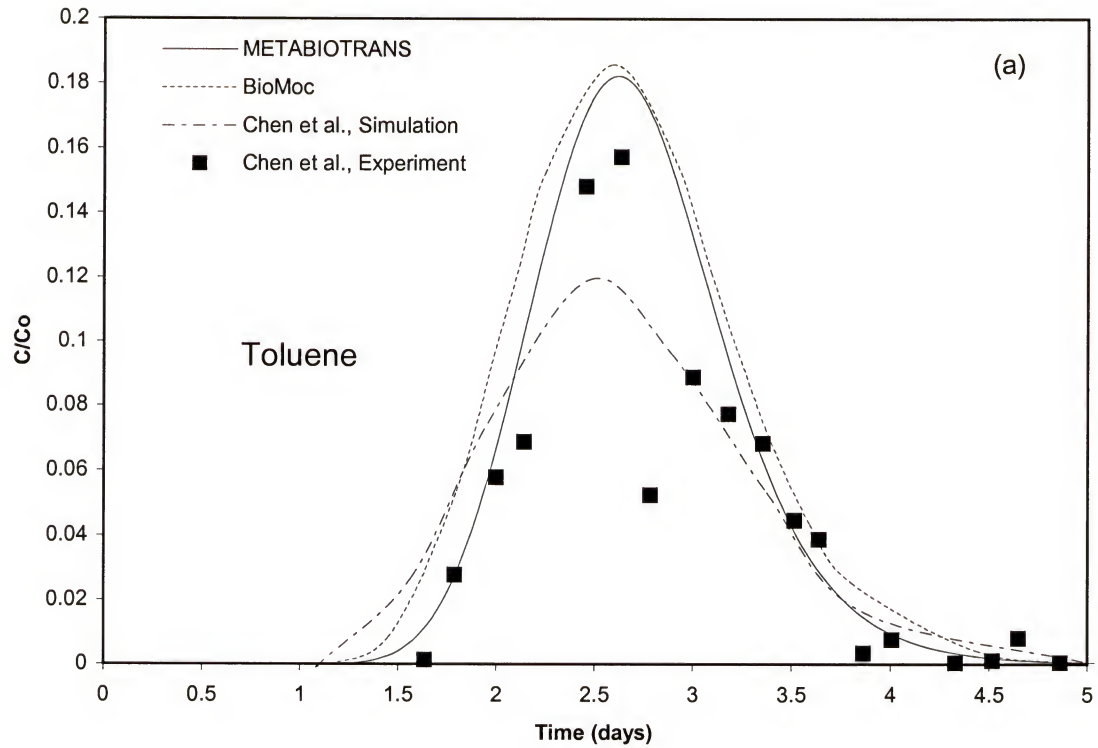


Figure 5-11 comparison between METABIOTRANS, BioMOC, and Chen et al., simulation and lab data for test problem 11. (a) Toluene and (b) benzene.

experimental data than the other two simulations. In addition, METABIOTRANS gave a very good match with the toluene experimental data over the rising limb of the breakthrough curve (BTC) (much better than the other two models). For the falling limb portion of the BTC, on the other hand, Chen et al. results are better than those of BIOMOC which continues to over-predict toluene concentrations. METABIOTRANS predictions along the falling limb of the BTC are closer to the experimental data than both solutions. It may be concluded that METABIOTRANS results are, overall, closer than the other two models in representing the experimental data for toluene (Figure 5-11a).

Figure 5-11b shows the change of benzene concentration predicted by all models in the same test problem. Though all three models seem to over-predict the experimental data at the rising limb and the peak concentration, the BIOMOC prediction showed the greatest error.

METABIOTRANS predictions at this portion of the BTC are still the closest to the experimental data. However, none of the three models were able to simulate experimental data along the falling limb of the BTC. Though Chen et al. (1992) used two different microbial species in their lab experiments, their model allowed the use of only one microbial species (with initial concentration of 0.82 mg/l). Because they used the high initial biomass concentrations, underestimation of the concentration values is predicted. Similarly, in BIOMOC simulations, only the other microbial species is used (with initial biomass of 0.21 mg/l). Using the smaller initial biomass might explain its general trend of over-predicting the experimental data.

METABIOTRANS allows the user to assume as many microbial species as they specified in the system, which is probably the main reason that METABIOTRANS results were generally closer to experimental data than the other two models. Another interesting result is that METABIOTRANS solution is closer to BIOMOC than results of Chen et al. for the case of toluene (where the correct initial biomass was used in BIOMOC for toluene) and closer to Chen et al. solution than BIOMOC in the case of benzene (where the correct initial biomass was used by Chen et al. for benzene) (Figures 5-11a and b). Differences between METABIOTRANS results and the other two models are probably due to the use of two microbial species in METABIOTRANS. These two species reduce concentration of Dissolved oxygen (D.O.) more rapidly than one species. In addition, the mathematical representation of the biodegradation process itself is slightly varied among the three models. These reasons contributed, with different weights, to the dissimilarity of the three models results; however, the closeness of the METABIOTRANS predictions to the experimental data suggests that the model accurately simulates the transport and biodegradation of multi-solutes in the presence of multi-bacterial species.

CHAPTER 6

METABIOTRANS APPLICATION AND SENSITIVITY ANALYSIS

6.1 Introduction

In this chapter METABIOTRANS is used to study the effects of the different single-valued biological parameters (such as μ_{\max} , K_a , B , and K_i) on the spatial mass distribution of both microorganisms and metal in the aquifer. Two examples are presented in this chapter; the first of which is a two-dimensional problem, while the second is three-dimensional. Availability of both electron donors and nutrients in the aquifer is crucial for the biotransformation process to occur. Therefore, in most cases, the addition of both solutes may be required to enhance the biotic reduction of the metal. However, in order to focus the efforts presented in this chapter on the impact of the biological parameters on the reduction process, an abundance of electron donor and nutrient is assumed in both examples. The effects of the availability of electron donors on metals reduction will not be discussed here, but later in a stochastic study in chapter 8.

The two examples presented in this chapter relate the reduction of a single metal (Cr(VI)), by a single microbial species, to the different biological parameters that control the reduction process. Ten different runs are used in each example to evaluate sensitivities of the metal and microbial distribution in an aquifer to changes in the four parameters mentioned before. Comparisons between concentrations and spatial moments of both Cr(VI) and biomass distributions will be conducted.

6.2. Example 1

Biologically mediated metals reduction depends on many single-valued parameters that appear in the reaction terms of the governing equations (Equations 4-35 to 38). These parameters are the bacterial maximum growth rate (μ_{\max}), the metal specific half saturation coefficient (K_a), the inhibition factor (K_i), and the microbial death rate (B) [Equation 4-35 to 38]. The actual reduction rate is the outcome of combining all of these parameters. However, each parameter by itself could affect reduction rates and, therefore, could influence the distribution of both contaminant and biomass in the subsurface. In the parameter sensitivity studies that follow, a two-dimensional x - y homogeneous aquifer is assumed with dimensions 50 m \times 25 m (Figure 6-1a) and a constant velocity in x -direction (V_x) of 0.5 m/d. The longitudinal and transverse dispersivities are chosen to be the same with a value of 0.1 m. An instantaneous discharge of 1 mg/l of chromium (Cr(VI)) at time $t = 0$ is released as an areal source of contamination with dimensions 5 m \times 3 m. The left and right boundaries are assigned constant head values, whereas the top and bottom boundaries are considered impervious. The input parameters for the first example can be summarized as follows:

Discretization parameters:

Aquifer dimensions in X- and Y-directions (m)	= 50 m x 25 m
Element size in X-direction (Δx)	= 0.2 m
Element size in Y-direction (Δy)	= 0.2 m
Number of elements	= 31,250
Time step for transport equation (Δt_r)	= 0.5 day
Time step for biological equations (Δt_b)	= 0.005 day

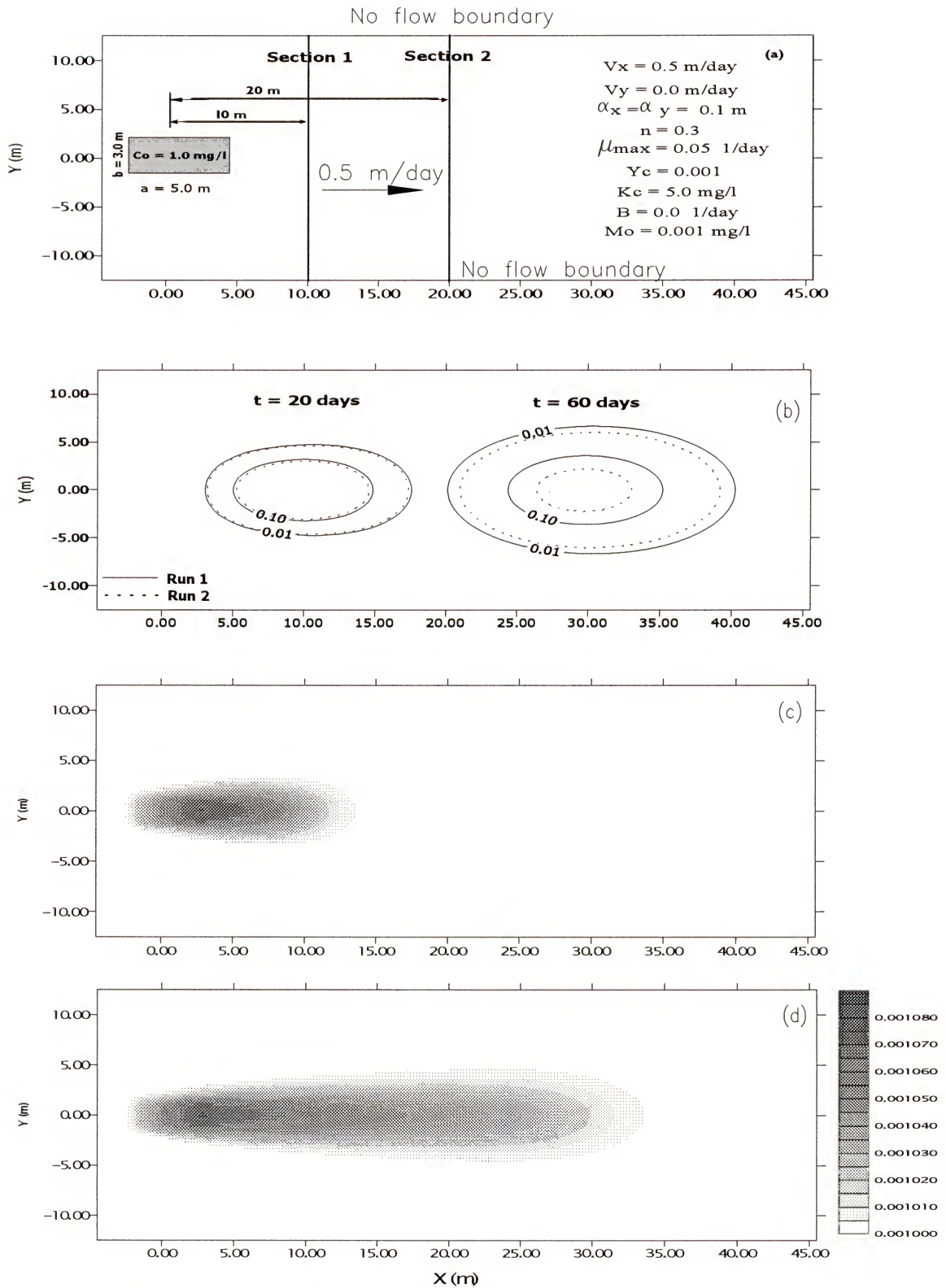


Figure 6-1 (a) Layout of example 1.

(b) Cr(VI) concentrations for runs 1 and 2 after 20 and 60 days.

(c) Biomass concentrations for run 2 after 20 days.

(d) Biomass concentrations for run 2 after 60 days.

Flow and transport parameters:

Velocity in X-direction (V_x)	= 0.5 m/d
Velocity in Y-direction (V_y)	= 0.0 m/d
Dispersivity in X-direction (α_x)	= 0.1 m
Dispersivity in Y-direction (α_y)	= 0.1 m
Porosity (n)	= 0.3
Size of the initial source of contamination (a x b)	= 5.0 m x 3.0 m
Initial concentration of Cr(VI) (C_0)	= 1.0 mg/l

Biological parameters

Initial biomass concentration (M_0)	= 0.01 mg/l
Microorganisms' maximum growth rate (μ_{\max})	= 0.05 day ⁻¹
Microorganisms' death rate (B)	= 0.00 day ⁻¹
Cr(VI) yield coefficient (Y_c)	= 0.001
Cr(VI) half saturation coefficient (K_c)	= 5.0 mg/l
Inhibition factor (K_i)	= 1.0 mg/l
Concentrations of other electron acceptors (E_e)	= 0.0 mg/l

In order to eliminate the impact of other factors that could affect the reduction process (other than the four single-valued biological parameters mentioned above) an abundance of electron donors and nutrients is assumed to exist everywhere in the aquifer. Therefore, it is assumed that $S \gg K_s$ and that changes in the concentrations of both electron donors and nutrients are small compared to their concentrations (equation 4-11). These assumptions operate to reduce the number of biological variables in the governing equation to the four parameters mentioned above (Equations 4-3 to 4-5). In addition, it is

assumed that Cr(VI) is the only available electron acceptor in the aquifer; therefore, the inhibition factor I_b (Equation 4-11) is assigned a value of 1. For the ten model runs of the two example problems, the two-dimensional concentration distribution is obtained at two times, $t = 20$ days and 60 days after Cr(VI) release.

Biological parameters used in runs 2-10 are presented in Table 6-1. The first run (Run 1) is considered a reference case in which no reduction occurs, creating thereby a simple 2-D convection-dispersion solute transport problem. The other nine runs are then simulated with different sets of biological parameters that describe reduction of Cr(VI) to Cr(III) (Table 6-1). By comparing results of the other runs to Run 1, an estimate of the Cr(VI) reduction for each run is obtained.

Table 6-1 The biological input parameters for the ten runs of Example 1.

Parameter	μ_{\max} (day ⁻¹)	K_c (mg/l)	K_i (mg/l)	B (day ⁻¹)
Run 1	--	--	--	--
Run 2	0.05	5	10	0
Run 3	0.1	5	10	0
Run 4	0.2	5	10	0
Run 5	0.05	3	10	0
Run 6	0.05	1	10	0
Run 7	0.05	5	0.01	0
Run 8	0.05	5	0.001	0
Run 9	0.05	5	10	0.005
Run 10	0.05	5	10	0.025

Figure 6-1b shows the concentration lines of Cr(VI) after 20 and 60 days for Runs 1 and 2. Due to a constant velocity of 0.5 m/d in the X-direction, the plume travels 10 and 30 m in the X-direction after 20 and 60 days, respectively. The same figure clearly shows the reduction in Cr(VI) concentrations in Run 2 compared to Run 1 at both times; however, the reduction is more noticeable after 60 days because the Cr(VI) plume was exposed to more microorganisms at that time. The concentration distribution of the biomass is shown in Figures 6-1c and 6-1d after 20 and 60 days, respectively. These two figures show nascent microbial growth at the initial position of the Cr(VI) release and a continued growth in areas where Cr(VI) plume travels in the aquifer. Microorganisms responsible for Cr(VI) reduction are assumed to be attached to the aquifer materials. Therefore, the increase in the biomass concentrations at any location depends on two factors: (1) local transient Cr(VI) concentrations and (2) the contact time between the microorganisms and Cr(VI) plume at that location. Consider, for example, bacteria located at the up gradient edge of the initial zone of Cr(VI) [$x=0$]. Although they are exposed to high metal concentrations, the contact time is too short to support significant growth. As a result, the position of maximum biomass concentration is shifted slightly down gradient from the location of the initial Cr(VI) release, where Cr(VI) concentrations are still high but the contact time is longer. As the Cr(VI) plume moves, Cr(VI) concentrations decrease due to dispersion and microbial-mediated reduction. Therefore, further down gradient of the point of release, bacteria experience longer contact time but with reduced Cr(VI) concentrations and, therefore, microbial growth is slower. It should be noted that there is no reduction in biomass concentrations anywhere in the aquifer for two reasons [Figures 6-1c and 6-1d]. The first reason is that microbes

are assumed to be attached to the aquifer materials; therefore, they do not undergo transport. The second reason is that the microbial death rate was assumed to be zero in Run 2. Thus, the plume-like characteristics of the microbial biomass distribution is only due to the convection and dispersion of the Cr(VI) plume alone.

6.2.1. Effect of Microbial Growth Rate (μ_{\max})

The first parameter to be investigated here is the maximum specific growth rate μ_{\max} (equation 4-28). Along with the two basic runs (Run 1 and 2), two additional runs (Run 3 and 4) are used to examine the impact of this parameter on Cr(VI) reduction. Figure 6-2a(i) illustrates the effect of μ_{\max} on the concentration lines 0.01 and 0.1 after 20 and 60 days. This figure shows, as expected, that with the increase of μ_{\max} , microbial activity increases in the aquifer and, therefore, more Cr(VI) reduction occurs. This effect is clear at both times (20 and 60 days); however, because both microbial growth rate (dM/dt) and Cr(VI) reduction rate ($-dC/dt$) [equations 4-34 and 4-36] increases as a function of microbial mass in the aquifer, more Cr(VI) reduction occurs at $t = 60$ days. The total biotransformed mass of Cr(VI) in each of the ten runs is presented in Table 6-2. This table illustrates that doubling μ_{\max} from 0.05 to 0.1 increases the mass of Cr(VI) reduced by 26% (from 44% to 70%). However, when it was doubled further to 0.2 days⁻¹, only a 21% increase in the reduced metal mass is obtained. The reason for this is that the reduction rate [$-dC/dt$, in equations 4-34 and 4-36] is a time variant and dependant on changes in both Cr(VI) and biomass concentrations. Therefore, when μ_{\max} is increased, Cr(VI) concentrations decrease faster and as a result, the reduction rate decreases at later time compared to the case when μ_{\max} is smaller. Figure 6-2a shows the effects of increasing μ_{\max} on the microbial population in the aquifer.

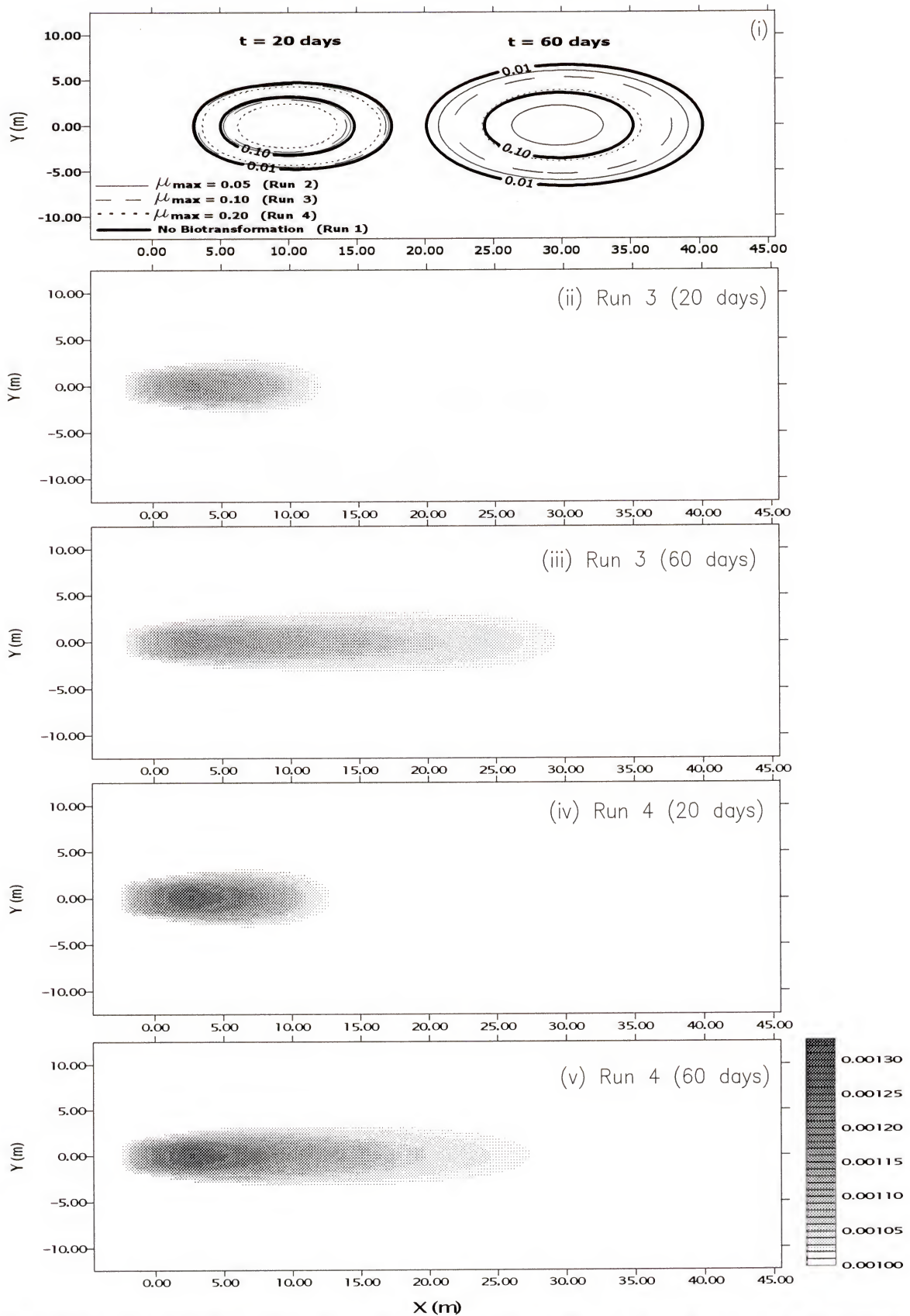


Figure 6-2a Effect of microbes growth rate (μ_{\max}) on Cr(VI) and biomass concentrations.

It is clear that biomass concentrations increased more in run 4 ($\mu_{\max} = 0.2 \text{ day}^{-1}$) than in run 3 ($\mu_{\max} = 0.1 \text{ day}^{-1}$) at both time steps. It is also clear that the biomass increased in the aquifer from $t=20$ days to $t=60$ days for both runs. Table 6-2 lists biomass increases after 60 days as 0.58%, 0.92%, and 1.20% for Runs 2, 3, and 4, respectively.

Table 6-2 Percentage of reduced Cr(VI) mass and developed biomass from the initial mass after 60 days for example 1.

Run	Biotransformed mass of Cr(VI)	Biomass developed
1	0.00	0.00
2	44.25	0.58
3	69.60	0.92
4	91.24	1.20
5	61.77	0.82
6	93.84	1.24
7	27.76	0.43
8	12.16	0.22
9	39.56	-25.47
10	25.83	-77.54

Another way to quantify the effect of the biotic processes on the concentration distribution of both Cr(VI) and bacteria in the aquifer is to use moment analysis. Zero, first, second, third, and fourth spatial moments of the concentration distributions of both Cr(VI) and biomass are calculated to evaluate the Cr(VI) reduction and microbial growth,

and to characterize the morphology of the Cr(VI) plume and the microbial biomass distribution. Spatial moments are defined as:

$$M_i = \frac{1}{M} \int_{\mathcal{R}^2} n \bar{C} x_i \, d\mathbf{x} \quad (6-1)$$

$$M_{ii} = \frac{1}{M} \int_{\mathcal{R}^2} n \bar{C} x_i^2 \, d\mathbf{x} - M_i^2, \quad M_{ii}^* = \frac{M}{IM} M_{ii} \quad (6-2)$$

$$s = \left(\frac{1}{M} \int_{\mathcal{R}^2} n \bar{C} (x_i - M_i)^3 \, d\mathbf{x} \right) / M_{ii}^{3/2}, \quad s^* = \frac{M}{IM} s \quad (6-3)$$

$$\kappa = \left(\frac{1}{M} \int_{\mathcal{R}^2} n \bar{C} (x_i - M_i)^4 \, d\mathbf{x} \right) / M_{ii}^2, \quad \kappa^* = \frac{M}{IM} \kappa \quad (6-4)$$

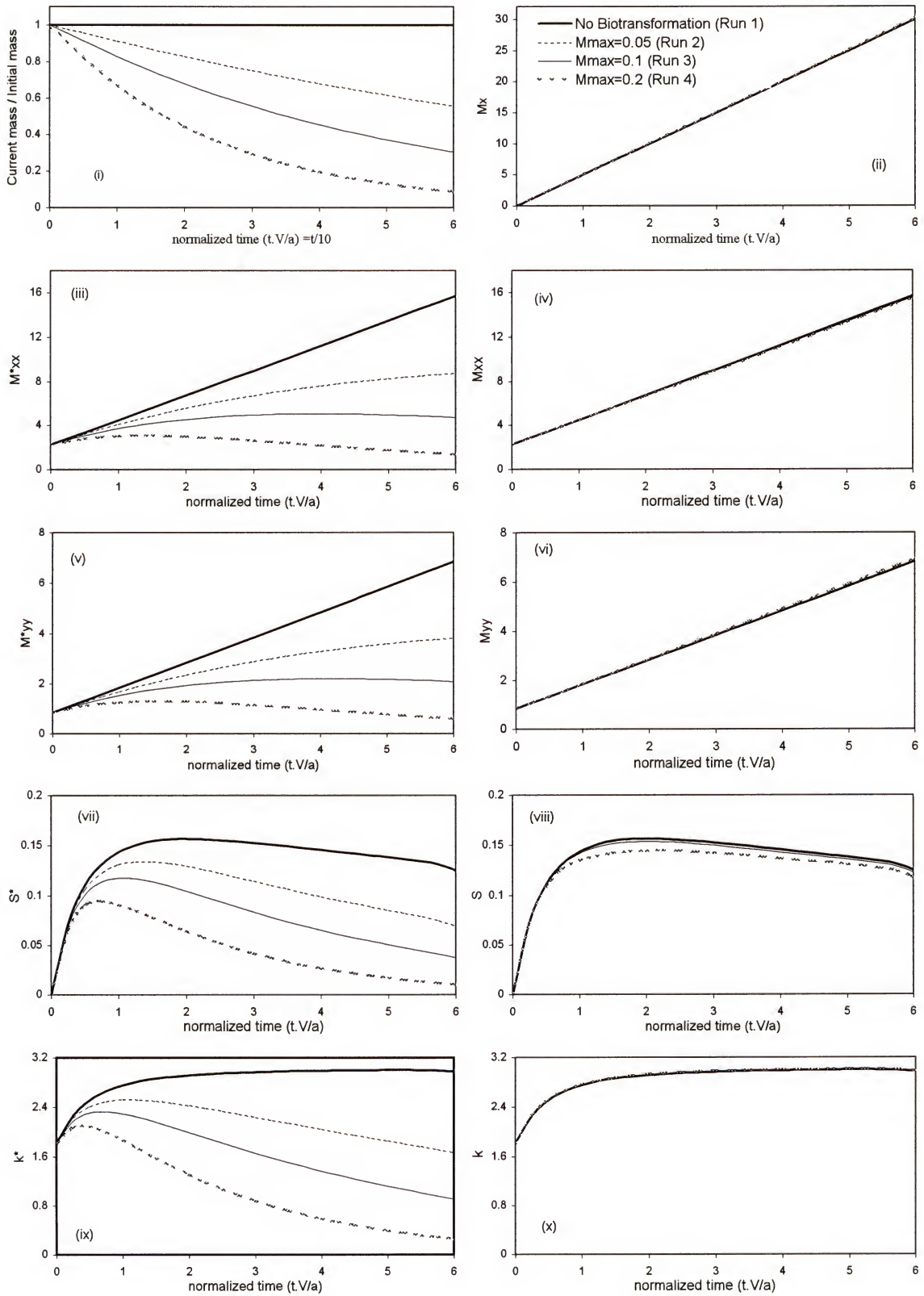
where $M = \int_{\mathcal{R}^2} n \bar{C} \, d\mathbf{x}$ is the current solute/bacterial mass in the aquifer, IM is the initial solute/bacterial mass in the aquifer, M_i is the first normalized moment in x_i direction, M_{ii} is the second central normalized moment in x_i direction, s is the skewness, and κ is the kurtosis.

Two approaches can be employed to normalize these moments. In the first approach, the initial solute\microbial mass is used to normalize the 2nd, 3rd, and 4th spatial moments identified as M_{ii}^* , s^* , and κ^* , respectively. In the second approach, the current solute\microbial mass (changes with time) is used to produce analogous spatial moments identified as M_{ii} , s , and κ , respectively (Equations 6-2 to 6-4). Only the current solute/bacterial mass will be used to normalize the first moment.

Each one of the two approaches reveals different insights and has different implications. Using the initial mass gives the absolute moments of the contaminant and the biomass concentrations and provides information about plume morphology that can be referenced to a non-reacting tracer. On the other hand, using the current mass reveals

information consistent with the more classic application of moment analysis (for example the second moment would give an idea about dispersion). Differences between the two approaches do not appear in typical mass conservative modeling simply because the initial mass in these cases equals the current mass. For example, the second normalized moment reveals information on the effects of the hydrodynamic dispersion and obscures information on biotransformation effects. Using the initial mass to normalize spatial moments reveals the coupled effects of advection, dispersion, and Cr(VI) reduction processes on the absolute concentration moments. This approach might be of interest to scientists and engineers seeking to analyze concentration or biomass data obtained from sites of active bioremediation. It is thought that both sets of moments can be useful when analyzing subsurface natural attenuation; therefore, moments obtained using both approaches will be presented for both Cr(VI) and biomass.

The normalized zero moment, which represents the ratio of the current Cr(VI) mass in the aquifer to its initial mass, is shown in Figure 6-2b(i). This figure clearly shows the continuous loss of Cr(VI) mass with time due to reduction. Run 1 (the case of “no biotransformation”) represents a conservative mass transport problem; thus, the quality of the mass balance obtained with the model is illustrated in Figure 6-2b(i). This figure also suggests, as discussed before, that the Cr(VI) reduction rate decreases at later times compared to rates depicted at early times. This was particularly true for run 4; however, this was not the case in runs 2 and 3 as Cr(VI) concentrations did not decrease, within the same time period, or to the extent that it exerts clear effects on the reduction rate. It is also clear from Figure 6-2b(i) that with higher values of μ_{\max} , more reduction occurs and, therefore, less Cr(VI) mass remains in the aquifer.

Figure 6-2b Effect of M_{max} on the spatial moments of Cr(VI) plume.

Despite the apparent reduction in Cr(VI) concentrations, due to biotransformation, second moments (in both directions) normalized by the current solute mass (M_{ii}) [Figures 6-2b(iv and vi)] imply that dispersion did not change compared to the case of conservative constituent [Figure 6-2b(iv and vi)]; this is because Cr(VI) reduction depends on Cr(VI) concentrations. Therefore, reduction in areas that have the same concentrations (leading, trailing, and lateral edges of the plume) occurs approximately with the same rate and, as a result, the Cr(VI) plume maintains its elliptical shape (with the same spatial moments) at all times. Consequently, Cr(VI) reduction appears to equally affect the numerator and the denominator in Equation 6-2, thereby maintaining the same ratio.

Using the current solute mass to normalize the spatial moments presents a misleading indication with regard to transient changes in the plume size; this is especially true at late times, when Cr(VI) mass decreases dramatically. On the other hand, when the initial solute mass is used to normalize the spatial moments, a clear reduction in the second moment (M_{ii}^*) is evident [Figure 6-2b(iii and v)]. These moments provide information on the transient rate of change in plume size as affected by reduction.

Figure 6-2b(ii) shows that the longitudinal first moment of Cr(VI) (M_x), which represents the position of the plume center of mass, did not change in any of the different cases compared to the case of “no biotransformation”. Based on the classical formulations of the moments, one could conclude that changing the value of μ_{\max} in homogenous aquifers with uniform initial biomass distribution does not affect the convection (M_x) or the dispersion (M_{xx} and M_{yy}) processes; however, it significantly affects the concentration values and, therefore, the plume size in both directions (M_{xx}^*

and M_{yy}^*). This is also clear from Figure 6-2a(i), where the center of the contaminant plume is moving with nearly the same velocity in the four runs.

Figure 6-2b(vii and viii) shows that skewness (s and s^*) decreases with an increase in μ_{\max} . Skewness values for all cases are small; however, they tend to increase at early times, most likely due to effects of the left boundary (which causes the plume to be slightly asymmetric). Yet, as the plume moves downgradient, the effects of the left boundary decrease as does the skewness. In the transverse direction of the plume, skewness (not shown) is almost zero (order of 10^{-14}) for all cases. Placing the initial plume away from both upper and lower boundaries minimized any effects both boundaries could have on the skewness in the transverse direction. It is clear from Figure 6-2b(vii) that increasing the value of μ_{\max} causes the plume to rapidly dissipate (compared to the runs of smaller μ_{\max}) the asymmetry caused by the left boundary. Finally, Figure 6-2b(ix) shows that the fourth moments changed dramatically with an increase in μ_{\max} , whereas Figure 6-2b(x) shows that a change of μ_{\max} has no effect on the kurtosis values (when using the current mass), which implies that the plume follows Gaussian distribution.

Figure 6-2c(ii) shows the change in the location of the biomass centroid (M_x) with time. The center of bacterial biomass was initially located in the center of the aquifer (used as reference in this figure). Then, with the microbial growth near the location of the initial contaminant release, the centroid of the biomass shifts upgradient (in the negative X-direction). Nonetheless, as the Cr(VI) plume migrates down gradient, the spatial distribution of microbial growth shifts as well and, as a result, the biomass centroid moves downgradient. However, the velocity of this shift is slower than the initial

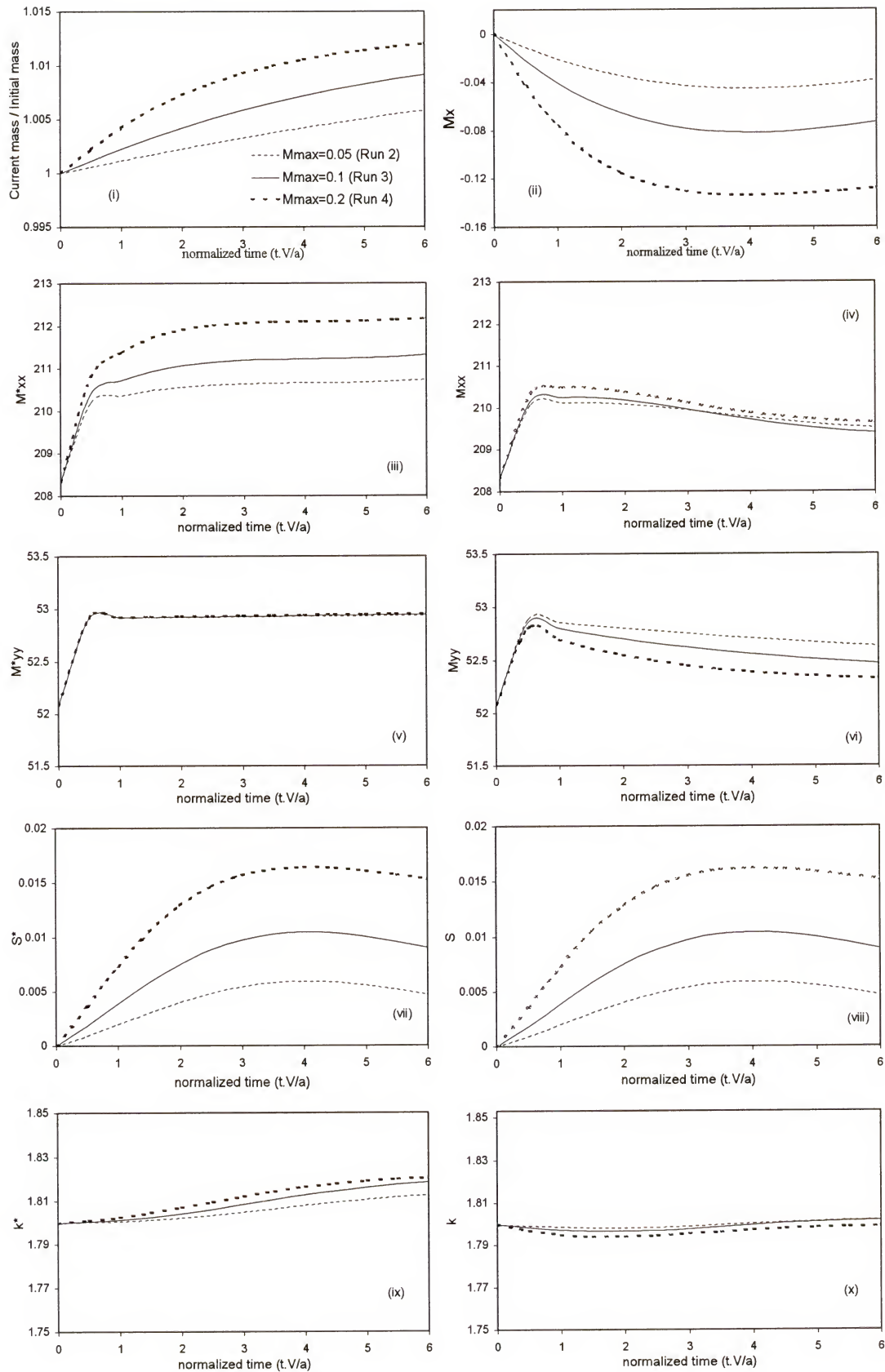
upgradient velocity because less Cr(VI) exists to support microbial growth. As μ_{\max} is increased (Run 4), bacteria grow faster and, therefore, the up gradient shift in the biomass centroid is greater than that of the other runs (2 and 3) [Figure 6-2c(iii)].

The second moment of the biomass concentration distribution (M_{ii}^* and M_{ii}) has a high initial value due to the fact that biomass was uniformly distributed everywhere in the aquifer at $t = 0$. However, as the Cr(VI) plume moves through the aquifer, slight changes in the second moment in both directions are observed compared to the relatively high initial values [Figure 6-2c(iii - vi)]. The skewness of the biomass distribution [Figure 6-2c(vii and viii)] is a reflection of the greater microbial growth occurring near the initial position of the Cr(VI) plume. Finally, in the simulations conducted, the peakness of the biomass concentration distribution is found to be relatively insensitive to μ_{\max} [Figure 6-2c(ix, and x)].

6.2.2. Effect of Cr(VI) Half Saturation Coefficient (K_c)

In this section results from two more runs (5 and 6, Table 6-1) are examined along with runs 1 and 2 to elaborate the effects of K_c on the reduction process. As expected, increasing K_c has an inverse effect on the biotransformation rate. That is illustrated in Figure 6-3a(i), where decreasing K_c from 5 to 1 dramatically decreases Cr(VI) concentrations in the aquifer at both times (20 and 60 days).

Reducing K_c to a fifth of its original value has almost the same effect as increasing μ_{\max} by a factor of four [Table 6-2]; however, the relation between the two parameters is not that direct as the influence of the K_c depends significantly on Cr(VI) concentrations and the magnitude of the inhibition factor (equation 4-11).

Figure 6-2c Effect of M_{\max} on spatial moments of biomass distribution.

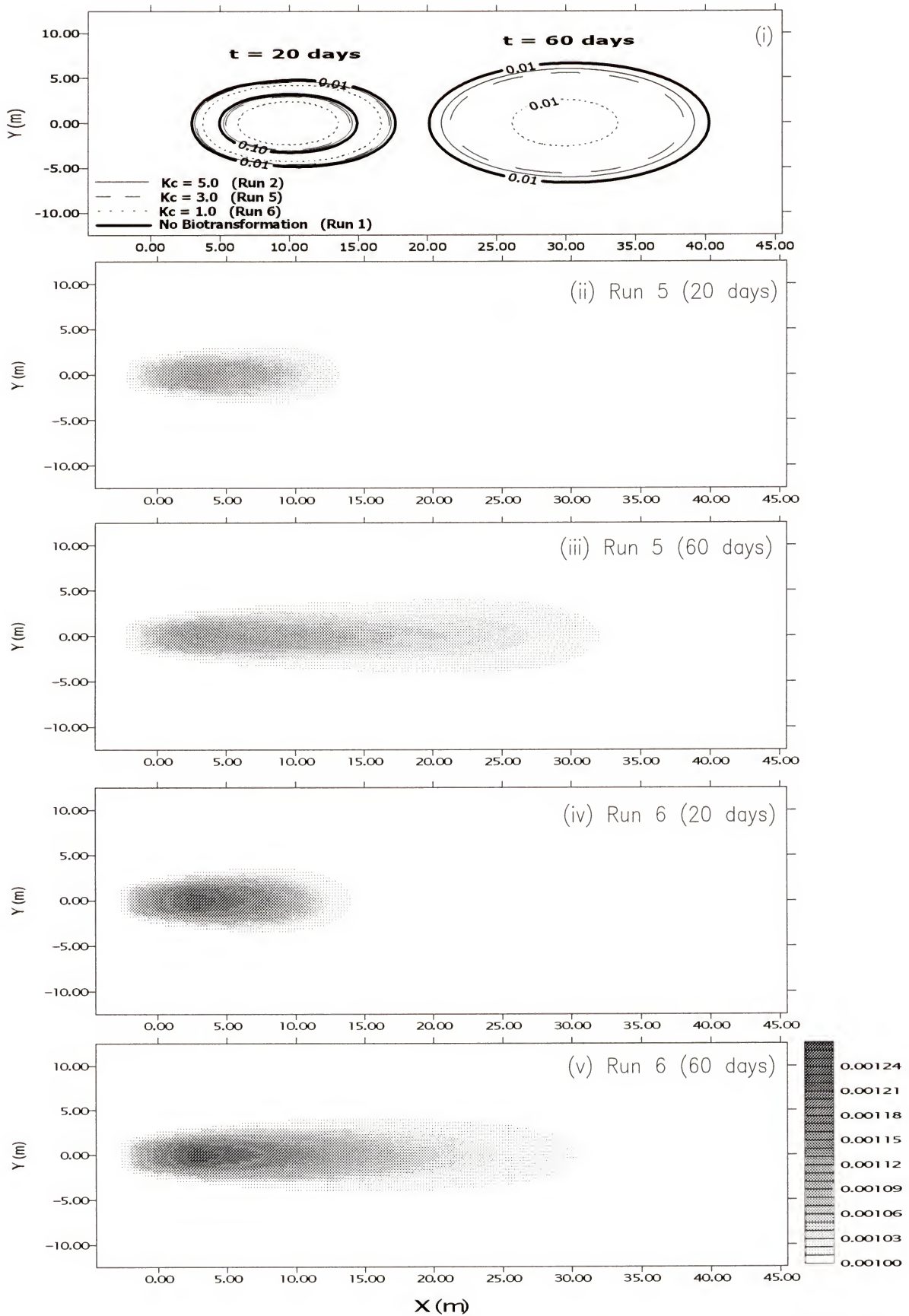


Figure 6-3a Effect of half saturation coefficient (K_c) on Cr(VI) and biomass concentrations.

When Cr(VI) concentrations are much less than the half saturation coefficient ($[\text{Cr(VI)}] \ll K_c$), biotransformation reactions approach first order behavior. Under these condition μ_{\max} and K_c have opposite effects on Cr(VI) reduction rates. However, when $[\text{Cr(VI)}] \gg K_c$, the reduction reaction appears almost zero order. Figure 6-3a shows that reducing the the Cr(VI) half saturation coefficient increases the biomass concentration in the aquifer especially near the origin of the Cr(VI) plume.

Figure 6-3b shows the effects of the Cr(VI) half saturation coefficient on spatial moments of Cr(VI) concentration distributions in the aquifer. By Increasing K_c , the Cr(VI) reduction decrease [Figure 6-3b(i)] and the Cr(VI) plume expands over both longitudinal and transverse directions [Figures 6-3b(iii and v)]. Similar to μ_{\max} , changing K_c did not have a significant effect on the dispersion. However, a minor decrease in longitudinal dispersion is noted when K_c was given a value of 1 [Figure 6-3b(iv)].

Similarly, skewness and kurtosis were essentially insensitive to K_c [Figure 6-3b(viii and x)]. For K_c equals 1, a slight increase in the kurtosis occurs. Associated with the large decreases in Cr(VI) concentrations both the third and the fourth moments decreased relative to the case of “no biotransformation” as K_c decreased [Figures 6-3b(vii and ix)].

Figure 6-3c shows the effect of changing K_c on the spatial moments of the biomass concentration distribution. As mentioned above, the effects of decreasing K_c are similar to those when increasing μ_{\max} .

6.2.3. Effects of inhibition factor (K_i)

The inhibition factor reflects the Cr(VI) concentration that exerts toxic effects on the resident bacteria. Decreasing K_i limits biotransformation activities in areas of the aquifer

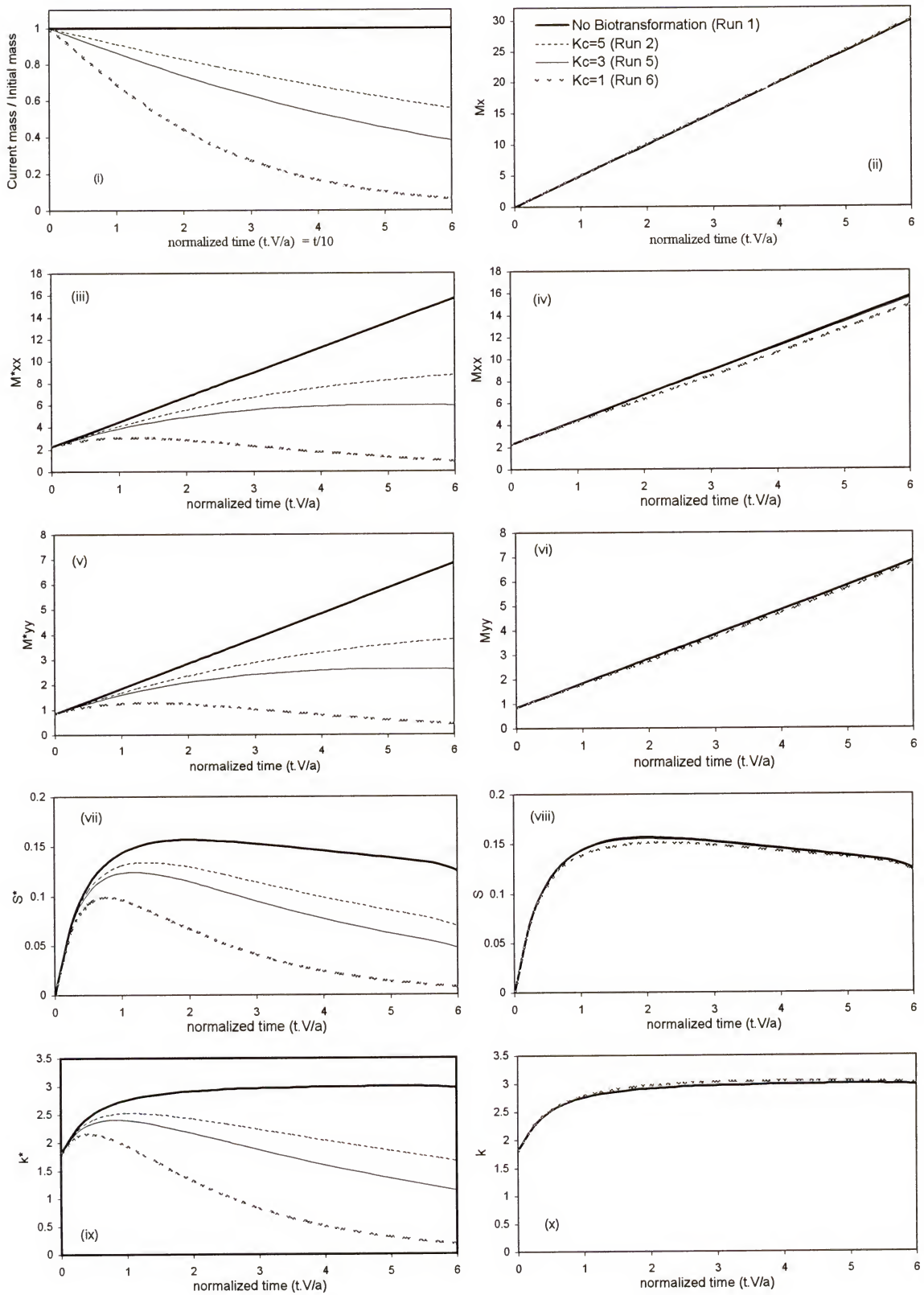
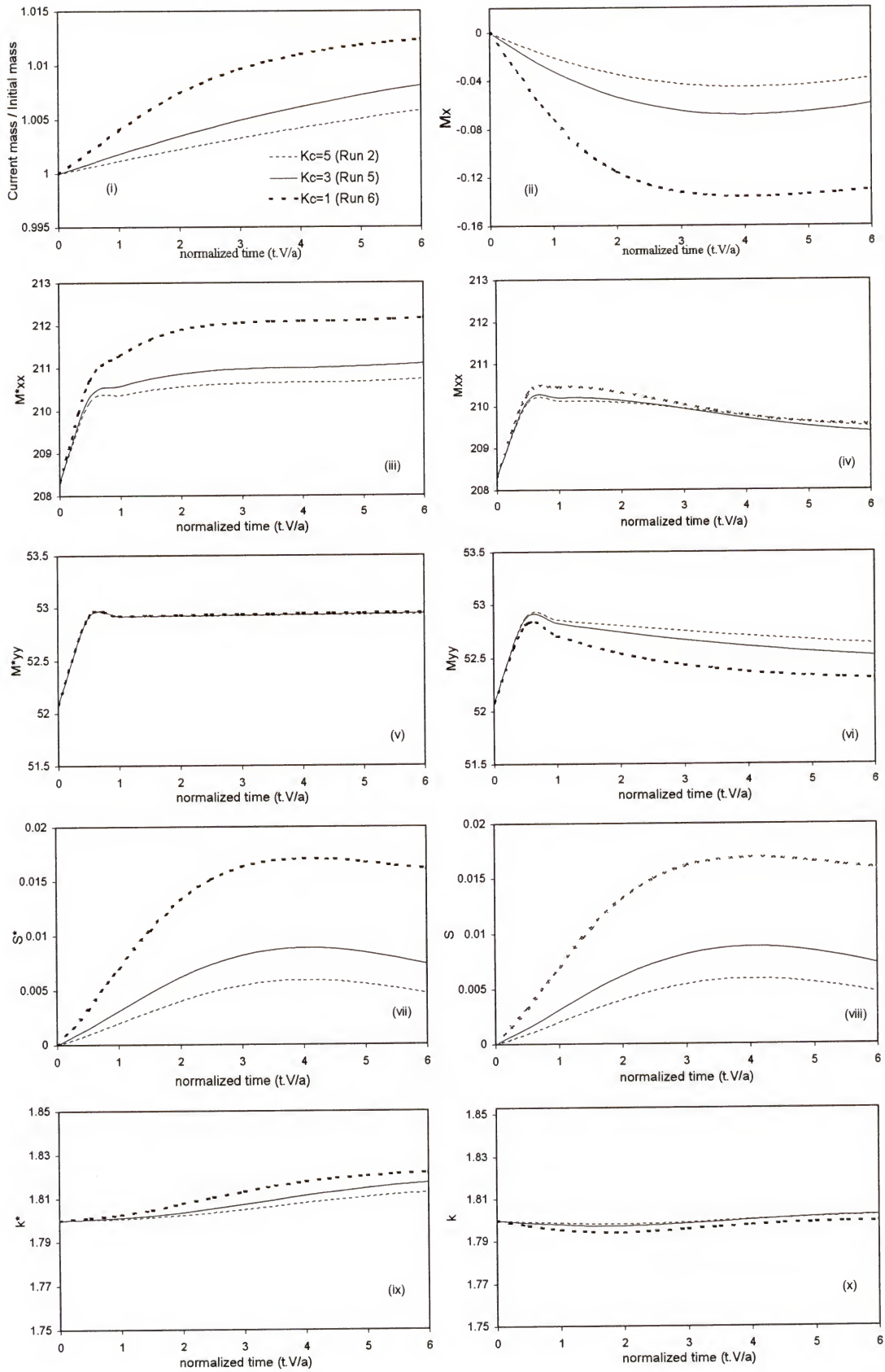


Figure 6-3b Effect of K_c on the spatial moments of Cr(VI) plume.

Figure 6-3c Effect of K_c on spatial moments of biomass distribution.

where Cr(VI) concentrations exceed K_i [Figure 6-4a]. However, the effects of varying both Cr(VI) concentration and half saturation coefficient are coupled to the effect of changing K_i (Equation 4-11). For example, increasing K_i 10 times ($0.001 \rightarrow 0.01$) induced enhanced Cr(VI) reduction; however, with further increases ($0.01 \rightarrow 10$) almost the same reduction occurs. Therefore, one can conclude that there is a value of K_i above which it no longer influences Cr(VI) reduction. Microbial sensitivity to K_i is closely related to the maximum Cr(VI) concentration in the aquifer at any location and time.

Perturbations in K_i exert significant control over the biomass distribution in the aquifer [Figure 6-4a(ii-v)]. When K_i is decreased, regions of maximum biomass concentration are more spread along the pathway of the Cr(VI) plume. A reasonable explanation for this behavior is that bacteria at high Cr(VI) concentrations were inhibited and could not reduce Cr(VI), leaving most of the Cr(VI) mass to be reduced by bacteria that exist where lower Cr(VI) concentrations prevail (below inhibition level K_i) [Runs 7 and 8, Figure 6-4a(ii-v)].

In general, Cr(VI) reduction is not sensitive to a change in K_i . Four orders of magnitude range of K_i values had to be examined in order to show effects of this parameter [Figure 6-4a(i)]. Conversely, Cr(VI) concentration variances (2^{nd} moments normalized by the initial Cr(VI) mass) are sensitive to a change in the K_i [Figures 6-4b(iv and vi)]. However, the effects are invisible in the second central moments normalized by the current mass of Cr(VI). Decreasing K_i from 10 to 0.001 increases both third and fourth moments normalized by the initial Cr(VI) mass at later times [Figures 6-4b (vii and ix)]. For the lower moment normalized with the current Cr(VI) mass, the effects of varying K_i are not seen.

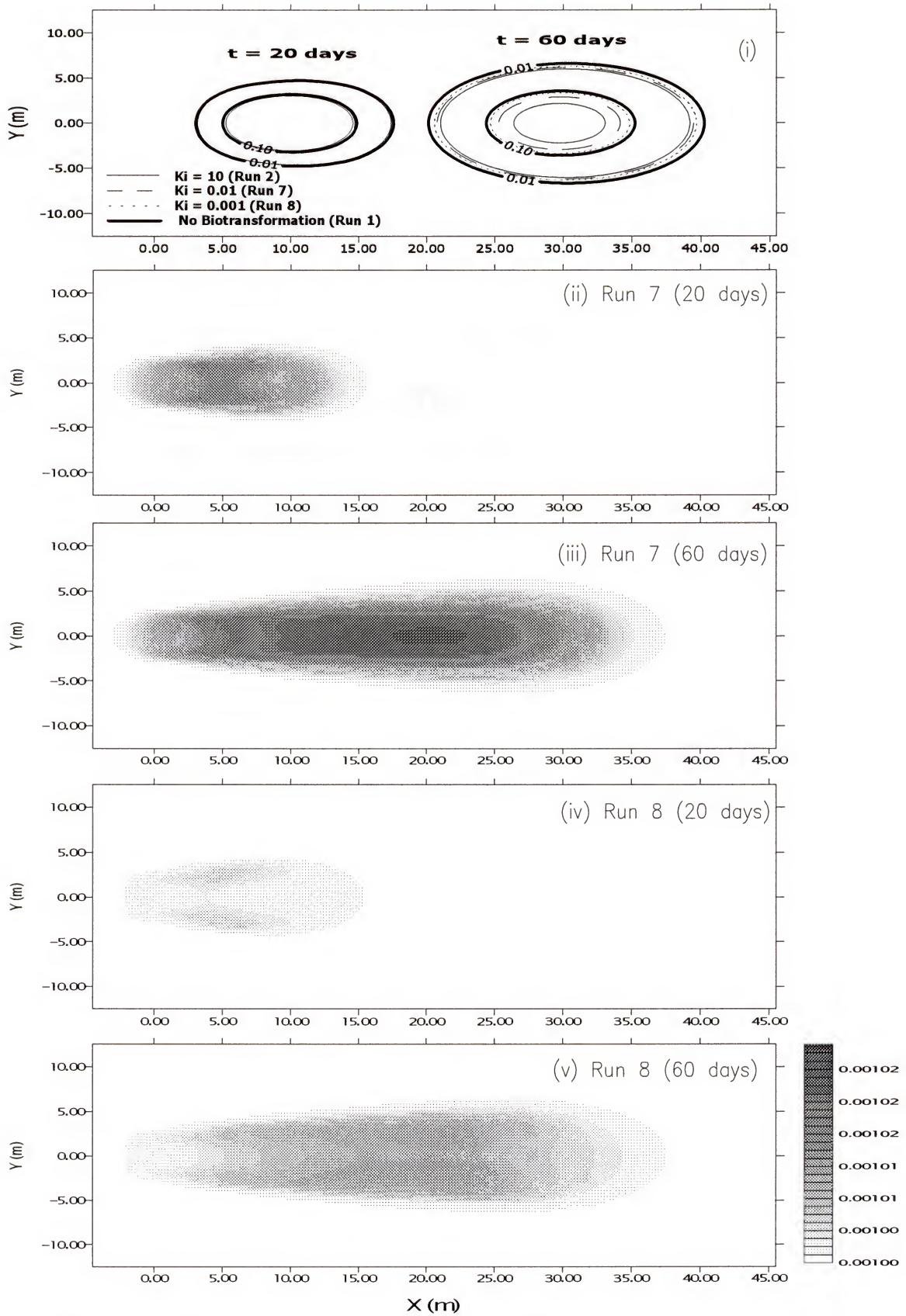


Figure 6-4a Effect of inhibition factor (K_i) on Cr(VI) and biomass concentrations.

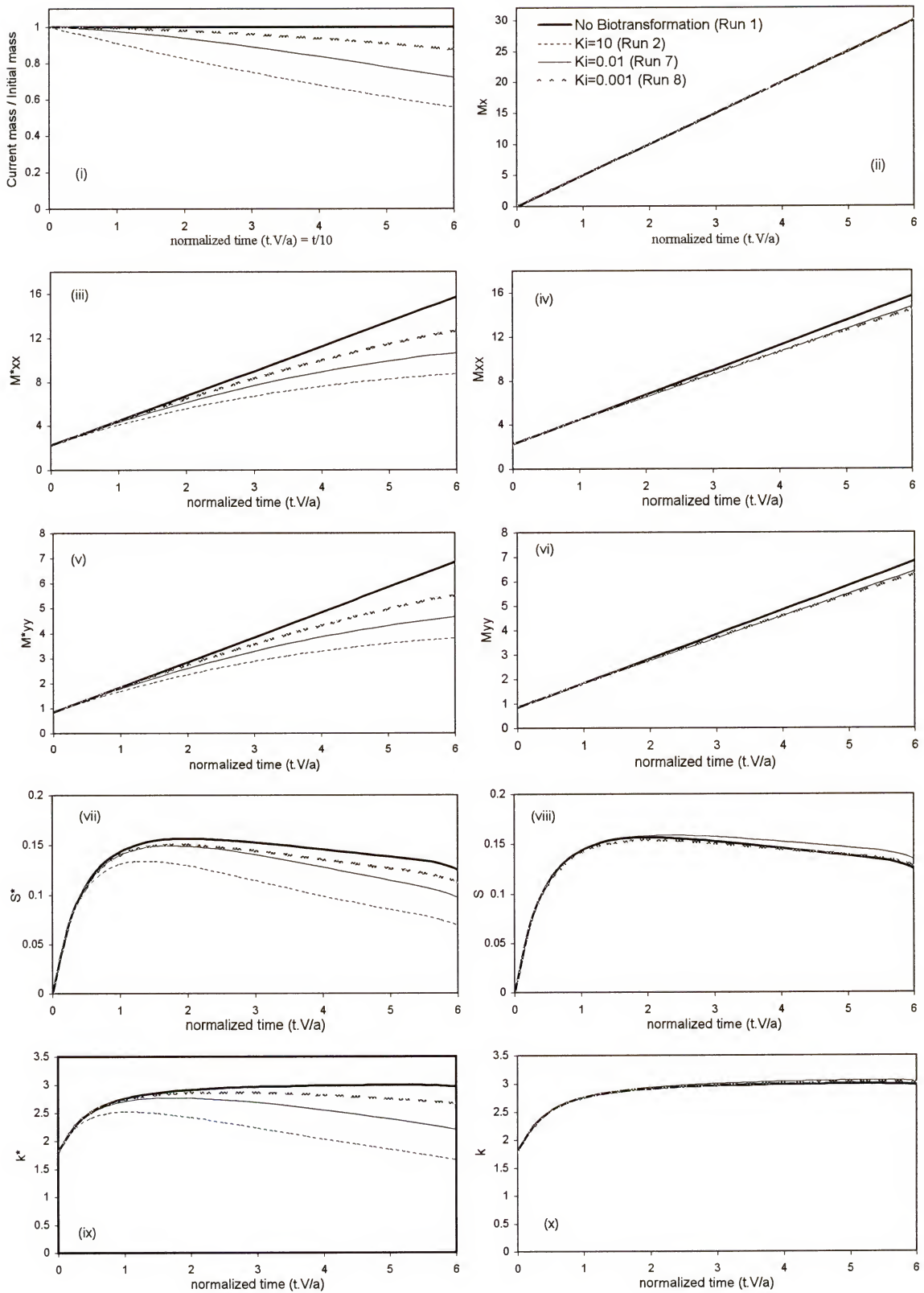


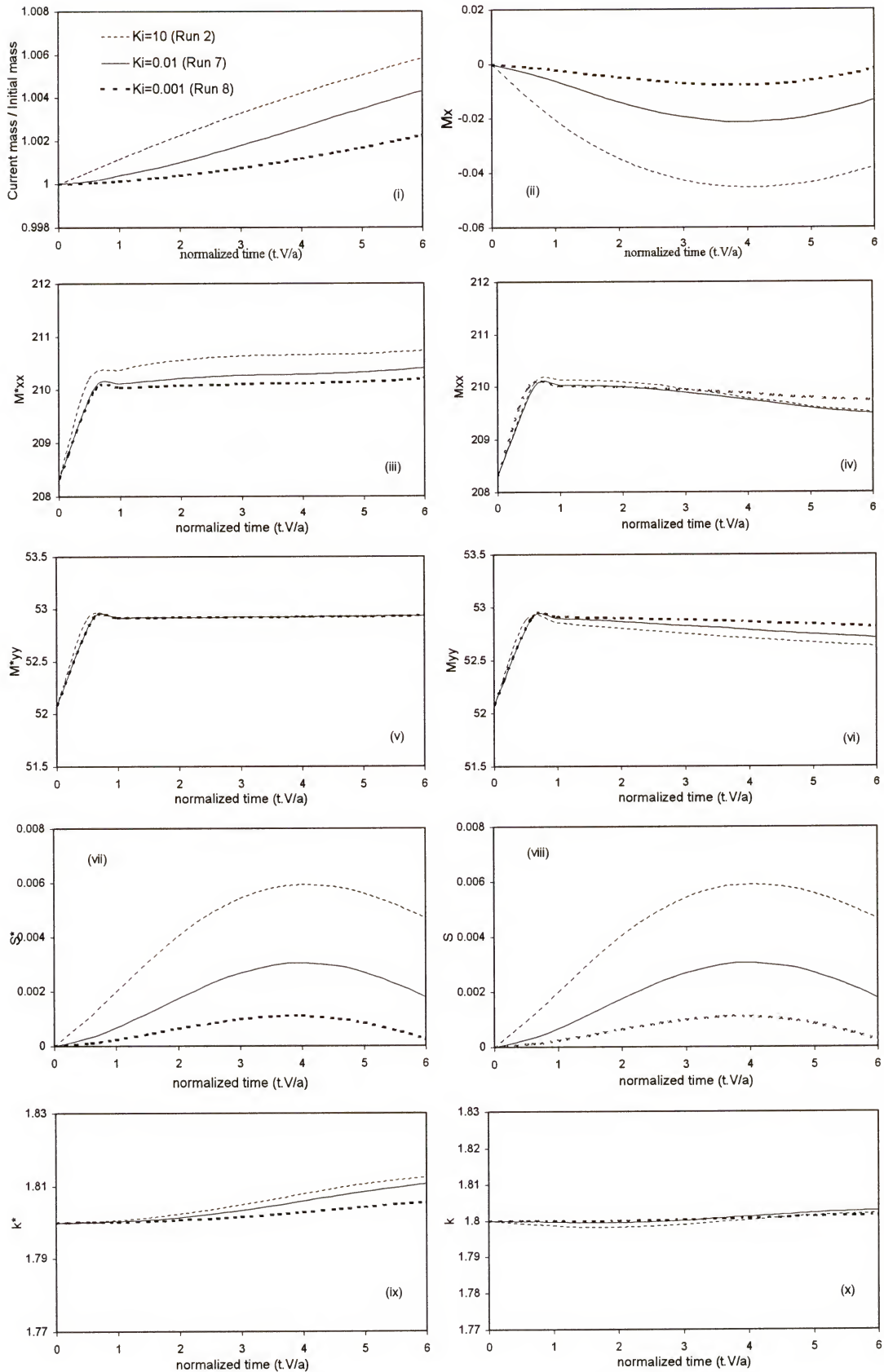
Figure 6-4b Effect of K_i on the spatial moments of Cr(VI) plume.

Only slight changes in the skewness and kurtosis values are observed (when normalized by the current mass of Cr(VI)) against the case of non-reactive contaminant (Gaussian distribution) [Figures (viii and x)].

Figure 6-4c shows the effects of changing K_i on the spatial moments of the biomass distribution. As expected, increasing K_i decreases growth inhibition; as a result, the biomass increases in Run 2 compared to both 7 and 8 [Figure 6-4c(i)]. Changes in K_i affect the biomass distribution and, consequently, the first longitudinal moment [Figure 6-4c(ii)]. Decreasing K_i inhibits bacterial growth until Cr(VI) concentrations decrease by dilution to levels permitting growth; consequently, bacteria grow over a larger area of the aquifer. This in part explains why there is no significant shift in the centroid of biomass compared to Runs 3, 4, 5, and 6. Another result of the near-uniform biomass distribution (with the decrease in the value of K_i) is the significant reduction in the skewness values of the distribution [Figures 6-4c(vii and viii)] as compared to previous runs.

6.2.4. Effects of Bacterial Death Rate (B)

The fourth and final parameter examined is the microorganisms' death rate (B). Unlike the microbial maximum growth rate, increasing the death rate affects all bacteria in the aquifer, not only those exposed to Cr(VI). Therefore, a reduction in biomass concentrations is observed in Figures 6-5a(ii-v)] as compared to all previous runs. As a result, less biotransformation occurs [Figure 6-5a] and, therefore, less Cr(VI) is reduced at the end of the Run 10 as compared to Run 9 [Table 6-2]. Because the death rate uniformly affects all the microorganisms in the aquifer, no effect is observed on the dispersion, skewness, or kurtosis [Figures 6-5b(iv, vi, viii, and x)]. The death rate does affect the apparent size of the Cr(VI) plume; thus, the second, third, and fourth moments

Figure 6-4c Effect of K_i on spatial moments of biomass distribution.

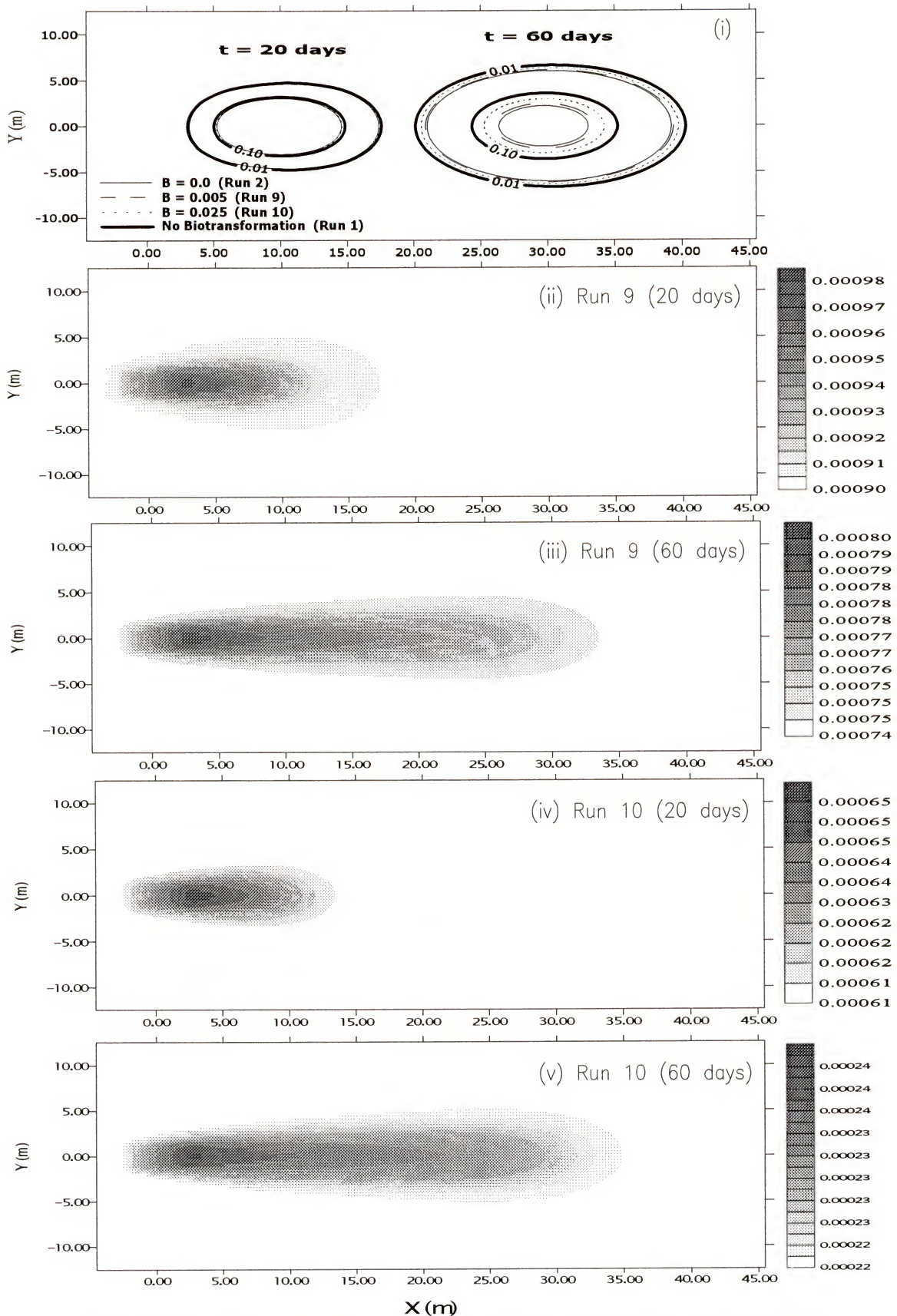
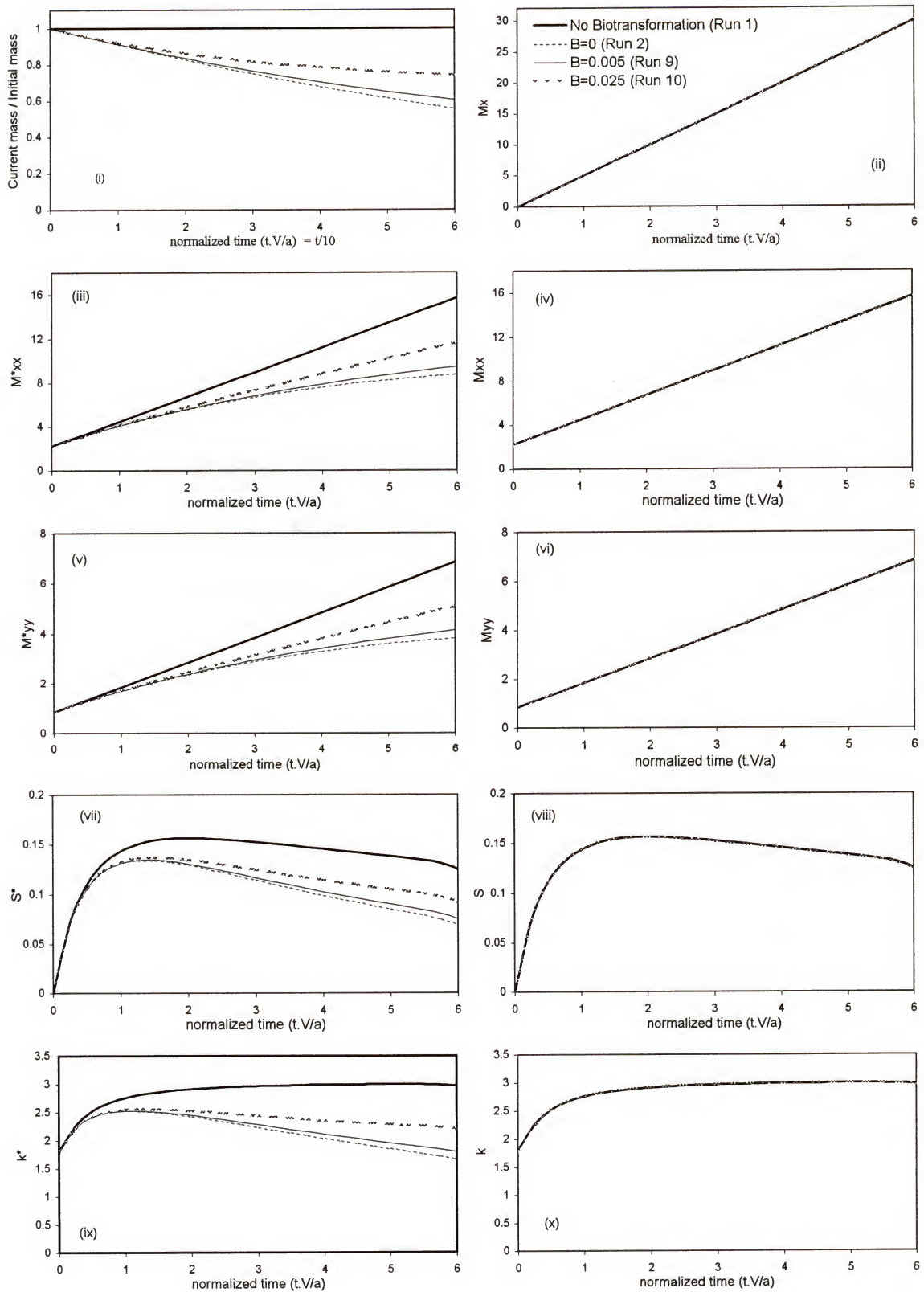


Figure 6-5a Effect of death rate (B) on Cr(VI) and biomass concentrations.

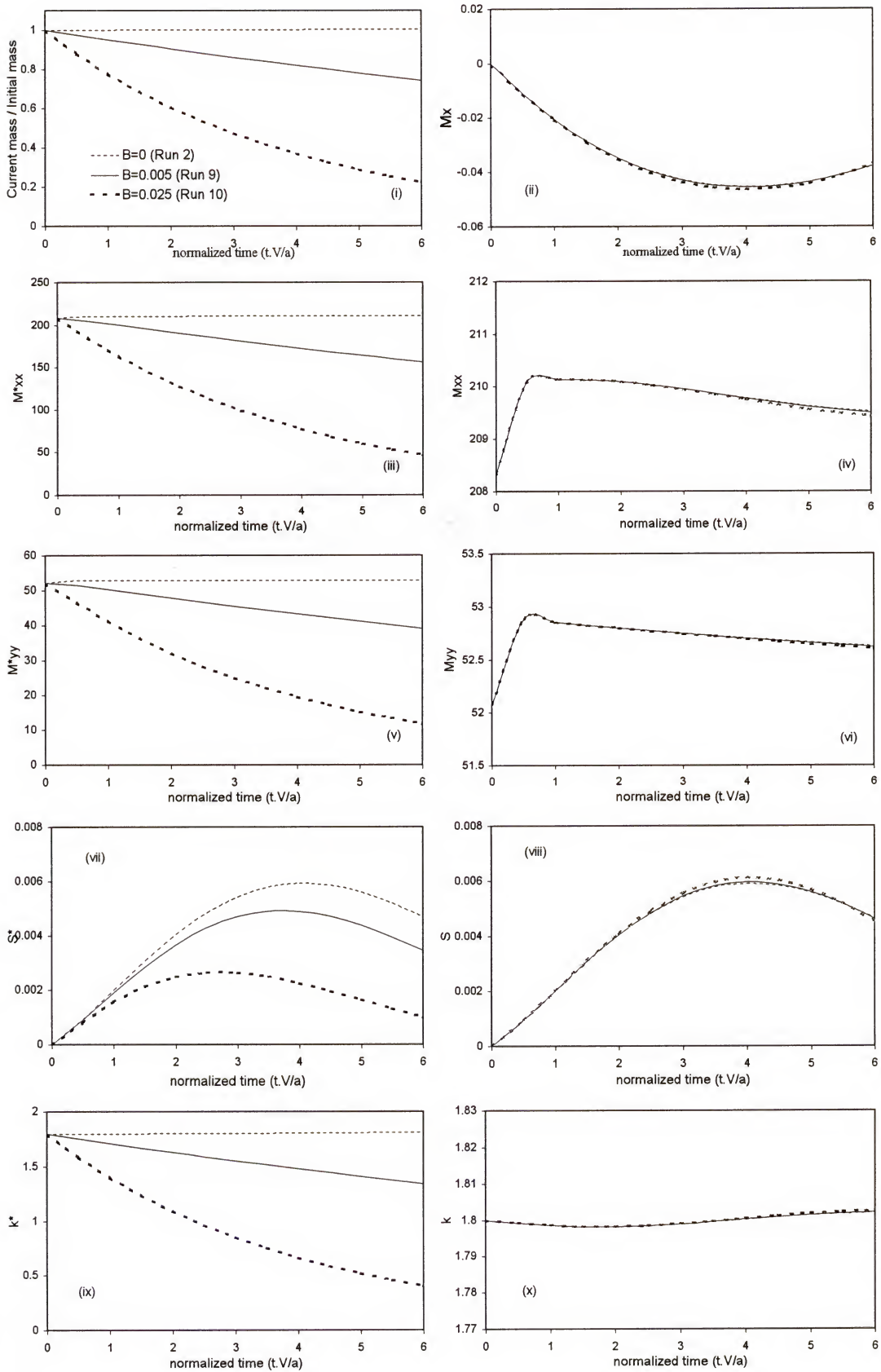
Figure 6-5b Effect of B on the spatial moments of Cr(VI) plume.

of the Cr(VI) plume normalized by the initial Cr(VI) mass tend to approach towards the case of non-reactive contaminant [Figures 6-5b(iii, v, vii, and ix)]. Similar effects on the biomass distribution can be seen in Figure 6-5c.

6.2.5. Effects of all Biological Parameters on Mass Flux

To evaluate natural attenuation or bioremediation having concentration data alone is not enough to determine whether concentrations reductions are due to dispersion, sorption, or biotransformation. A possible assessment approach can be used by quantifying the mass flux across many sections of the aquifer, then compared to each other, or compared against the initial contaminant mass in the system (if available). In numerical or mathematical modeling, however, this is not the case, because modelers have full control on all parameters and, therefore, can relate any change in the concentration to a specific parameter. In this section, Cr(VI) mass flux is quantified at two sections [Figure 6-1a] for the purpose of evaluating the reduction process. Mass fluxes at sections 1 and 2 (10 and 20 m away from the center of the initial Cr(VI) plume, respectively) [Figure 6-1a] are calculated at each time step.

Figure 6-6a illustrates the mass flux curves (MFC) of the different cases of μ_{\max} at the two sections. The Y-axis in this figure represents a dimensionless mass flux (mass flux normalized by the initial mass of Cr(VI) in the system, the velocity in X-direction, and the width of the initial contamination source). The X-axis represents a dimensionless normalized time (time divided by the width of the initial Cr(VI) source and the groundwater velocity in X-direction ($t V_x/a$)). From Figure 6-6a, it is clear that increasing μ_{\max} increases biotransformation activities in the aquifer and; therefore, produces a

Figure 6-5c Effect of B on spatial moments of biomass distribution.

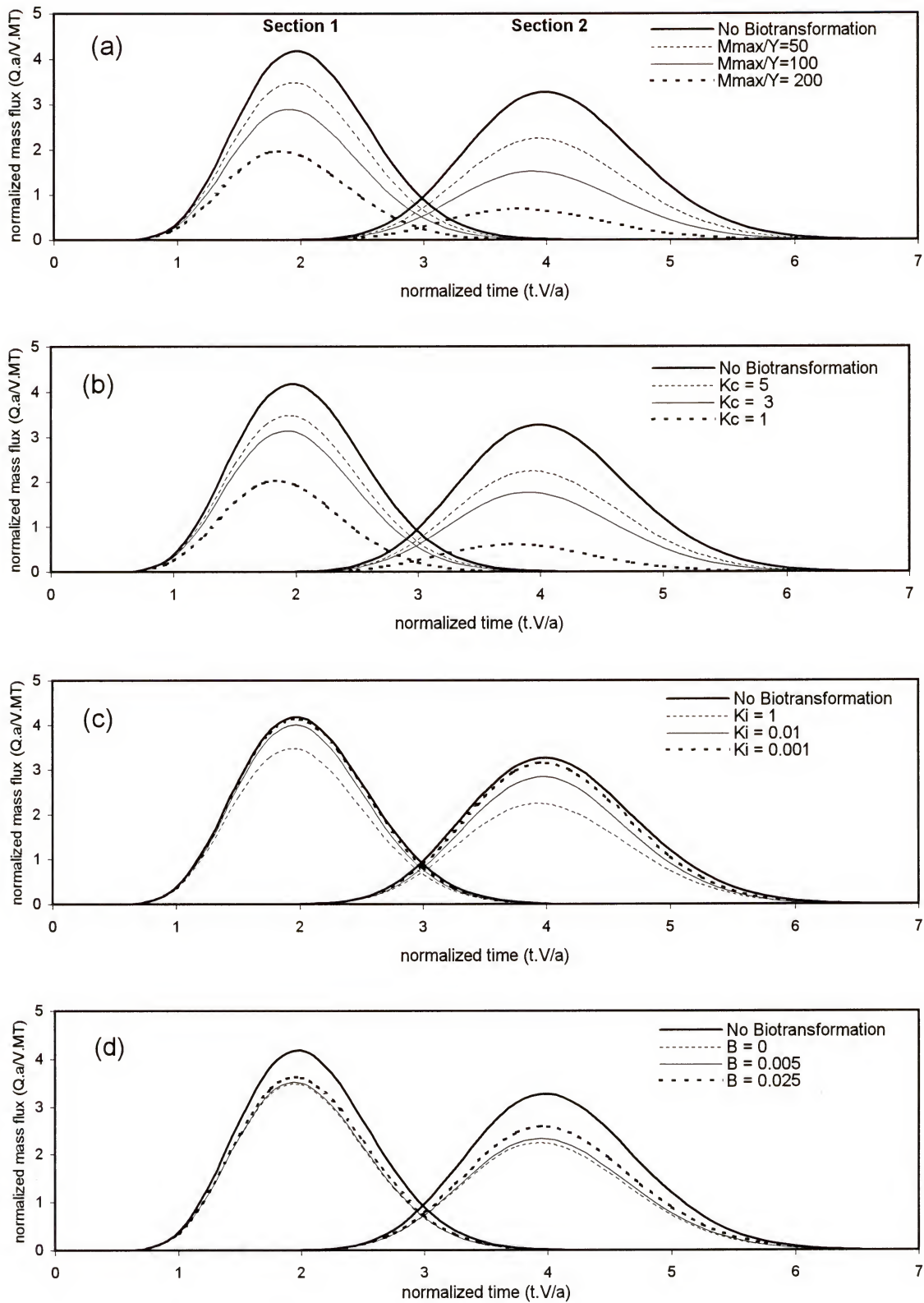


Figure 6-6 Effect of the different biological parameters on the mass fluxes at sections 1 and 2.

reduction in the area under the flux curve. This conclusion can be drawn easily by comparing the MFC at each section. Another important conclusion, derived from the same graph, is that in the absence of biotransformation (bold solid lines), no loss in the Cr(VI) mass occurs from section 1 to section 2. Obviously, when biotransformation activity exists (the other three cases) the mass that crosses section 2 is less than that which crosses section 1. This conclusion is very clear for the case of $\mu_{\max} = 0.2$ [Figure 6-6a]. A similar effect on the mass fluxes at each of two sections is noticed but with a decrease of the Cr(VI) half saturation coefficient [Figure 6-6b].

Increasing the inhibition factor increases the biotransformation activities in the aquifer and, therefore, the Cr(VI) mass that crossed section 2 is less than that which crossed section 1 (which is less than the initial Cr(VI) mass) [Figure 6-6c]. Increasing the bacterial death rate reduces the bacterial population in the aquifer and, as a result, the Cr(VI) mass flowing across both sections of Run 10 is greater than that which crosses the same respective sections of Run 9 [Figure 6-6d].

6.3. Example 2

In this example, a three-dimensional homogeneous aquifer is assumed with dimensions $40 \text{ m} \times 20 \text{ m} \times 20 \text{ m}$ (Figure 6-7) and a constant velocity in x -direction (V_x) of 0.5 m/d . The longitudinal and transverse dispersivities are chosen to be the same with a value of 0.1 m . An instantaneous release of 1 mg/l of chromium (Cr(VI)) at time $t=0$ is released as an volumetric source of contamination with dimensions $2 \text{ m} \times 2 \text{ m} \times 2 \text{ m}$. The y - z boundaries are assigned constant head values, whereas the other boundaries are considered impervious. The input parameters for this example are as follows:

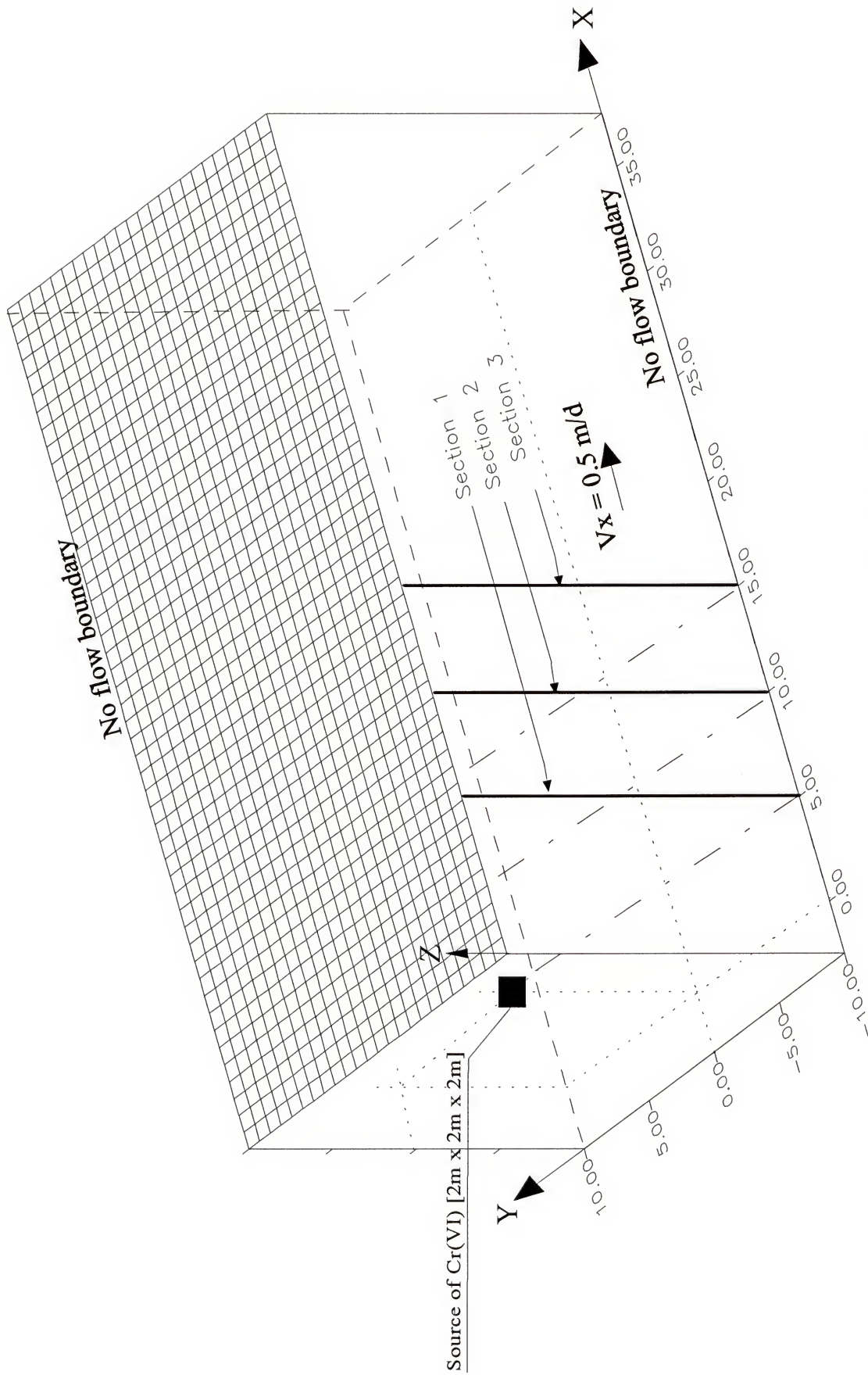


Figure 6-7 Layout of the example 2.

Discretization parameters:

Aquifer dimensions in X- and Y-directions (m)	= 40 m x 20 m x 20 m
Element size in X-direction (Δx)	= 1 m
Element size in Y-direction (Δy)	= 1 m
Element size in Z-direction (Δz)	= 1 m
Number of elements	= 16,000
Time step for transport equation (Δt_r)	= 0.5 day
Time step for biological equations (Δt_b)	= 0.005 day

Flow and transport parameters:

Velocity in X-direction (V_x)	= 0.5 m/d
Velocity in Y-direction (V_y)	= 0.0 m/d
Velocity in Z-direction (V_z)	= 0.0 m/d
Dispersivity in X-direction (α_x)	= 0.1 m
Dispersivity in Y-direction (α_y)	= 0.1 m
Dispersivity in Z-direction (α_z)	= 0.1 m
Porosity (n)	= 0.3
Size of the initial source of contamination (a x b)	= 2.0m x 2.0m x 2.0m
Initial concentration of Cr(VI) (C_0)	= 1.0 mg/l

Biological parameters (base case)

Initial biomass concentration (M_0)	= 0.01 mg/l
Microorganisms' maximum growth rate (μ_{max})	= 0.1 day ⁻¹
Microorganisms' death rate (B)	= 0.00 day ⁻¹
Cr(VI) yield coefficient (Y_c)	= 0.01

Cr(VI) half saturation coefficient (K_c)	= 10.0 mg/l
Inhibition factor (K_i)	= 10.0 mg/l
Concentrations of other electron acceptors (E_e)	= 0.0 mg/l

Similar to the first example, an abundance of electron donors and nutrients is assumed to exist everywhere in the aquifer. Therefore, the only single-valued biological parameters that affect biotransformations are the specific microbial maximum growth rate of the bacterial species μ_{\max} , the Cr(VI) half saturation coefficient (K_c), the inhibition factor (K_i), and the microbial death rate (B) [Equations 4-3 to 4-5]. Cr(VI) is assumed to be the only electron acceptor in the aquifer; therefore, the inhibition factor I_b (Equation 4-11) is assumed to be 1.

Ten runs, similar to those of example 1, are conducted to study the effects of the above parameters on the Cr(VI) reduction (Table 6-3). In Run 11 the dissolve constituent is assumed non-reactive, which yields a simple 3-D convection-dispersion solute transport problem. Figure 6-8a shows three views of the distribution of Cr(VI) concentrations in the aquifer after 15 and 50 days. As expected, due to constant velocity of 0.5 m/d in the X-direction, the plume has traveled 7.5 and 25 m into the aquifer in the X-direction after 15 and 50 days, respectively. Because X-Z and X-Y views are taken at the center of the aquifer and due to the symmetry of the problem, Figures 6-8a(i and iii) look exactly the same. Dispersivities in the three directions are the same, Figure 6-8a shows that the plume is elliptical in shape in X-Z and X-Y views and circular in Y-Z view. This is because, unlike the velocity in X-direction, both transverse components of the groundwater velocity are assumed to be zero.

Table 6-3 lists nine model runs where different sets of biological parameters were

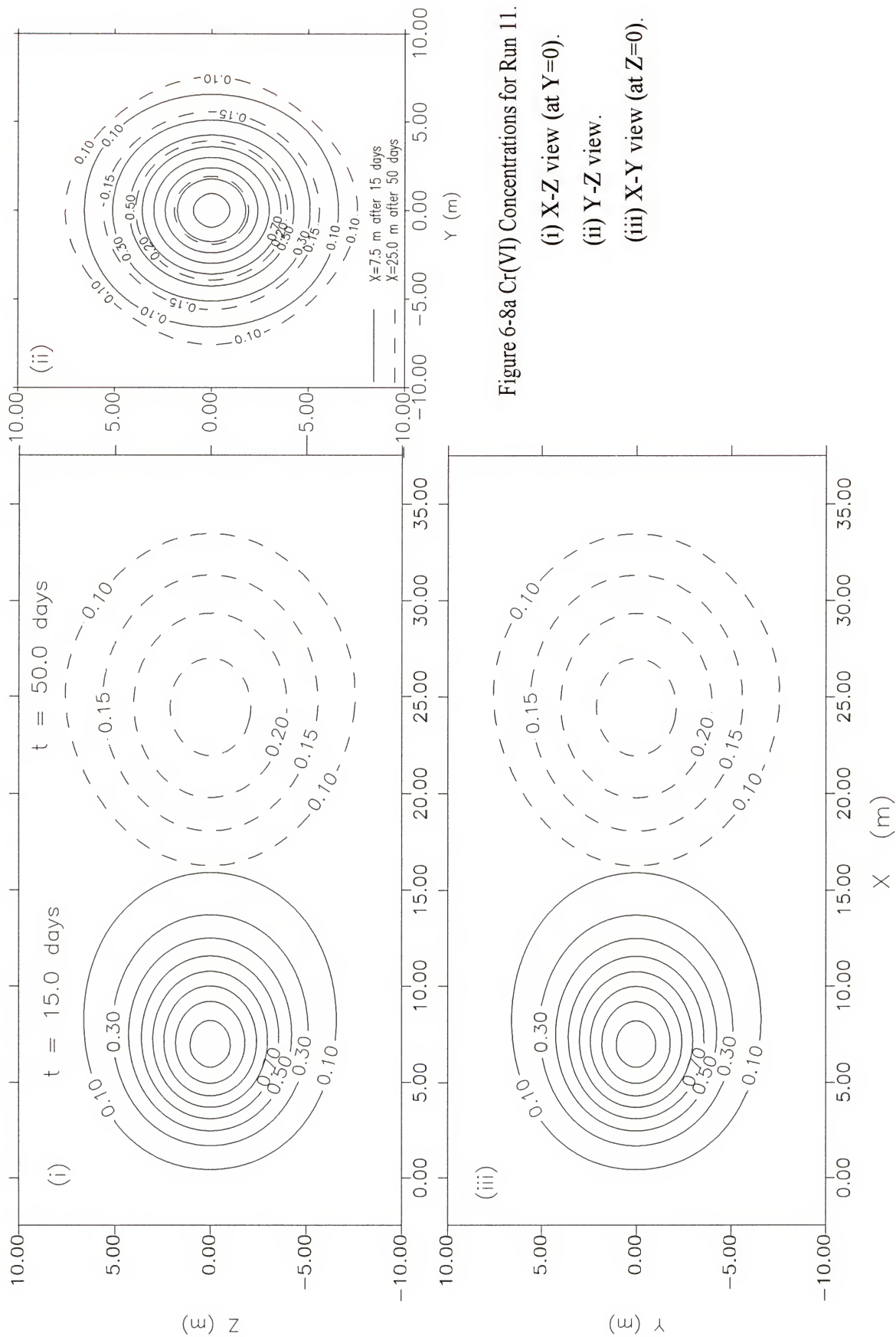


Figure 6-8a Cr(VI) Concentrations for Run 11.

(i) X-Z view (at $Y=0$).

(ii) Y-Z view.

(iii) X-Y view (at $Z=0$).

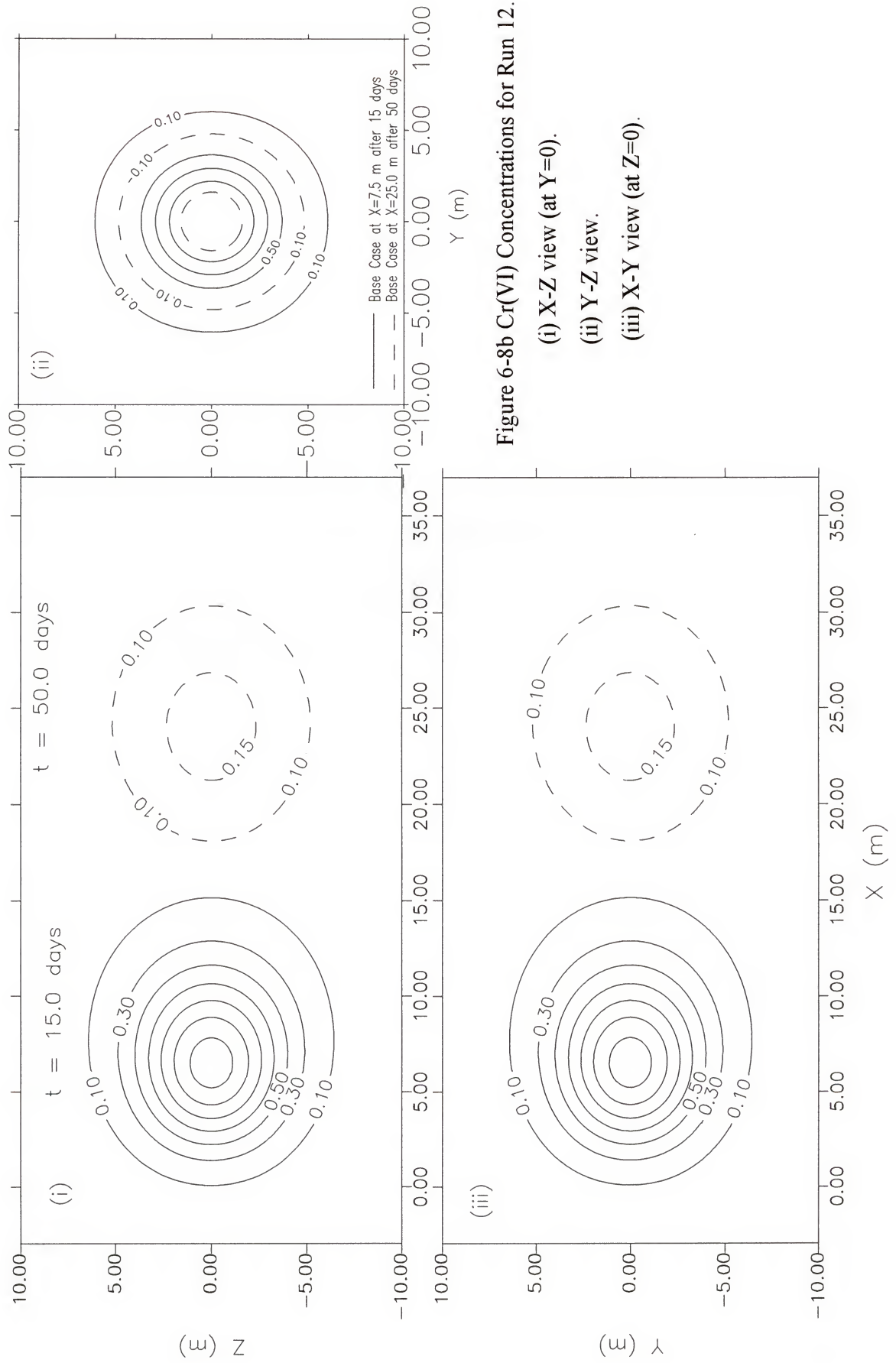


Figure 6-8b Cr(VI) Concentrations for Run 12.

(i) X-Z view (at $Y=0$).

(ii) Y-Z view.

(iii) X-Y view (at $Z=0$).

Table 6-3 Biological input parameters for different runs of Example 2.

Parameter	μ_{\max} (day ⁻¹)	K_c (mg/l)	K_i (mg/l)	B (day ⁻¹)
Run 12	0.1	10	10	0
Run 13	0.05	10	10	0
Run 14	0.2	10	10	0
Run 15	0.1	5	10	0
Run 16	0.1	1	10	0
Run 17	0.2	10	0.01	0
Run 18	0.2	10	0.1	0
Run 19	0.2	10	10	0.005
Run 20	0.2	10	10	0.025

varied to study the effects of each parameter on the Cr(VI) reduction (Table 6-3).

Run 12 is considered the base run from which results of other simulations will be compared.

Figure 6-8b shows three views of Cr(VI) concentrations predicted via Run 12 after 15 and 50 days. This figure illustrates reduction in Cr(VI) concentrations at $t = 50$ days compared to those at 15 days. A decrease of Cr(VI) concentrations is evident at both times when comparing Run 12 [Figure 6-8b] to Run 11 [Figure 6-8a]. Biomass concentrations for Run 12 after 15 and 50 days are shown in Figures 6-8c and 6-8d, respectively. As mentioned previously, microbes grow only where Cr(VI) exists. Therefore, increases in biomass concentrations are only noted in those areas where the Cr(VI) plume migrates.

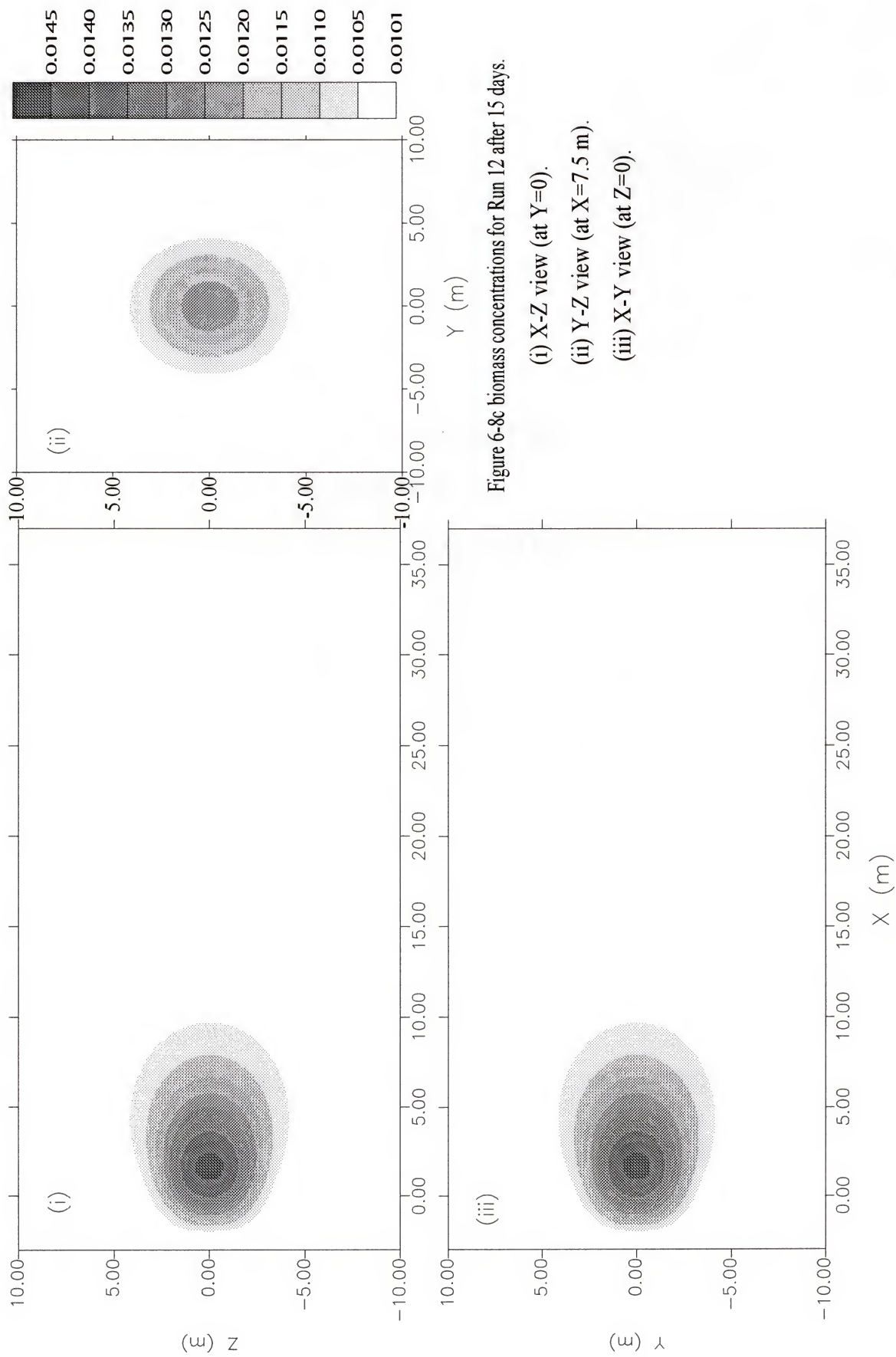


Figure 6-8c biomass concentrations for Run 12 after 15 days.

- (i) X-Z view (at $Y=0$).
- (ii) Y-Z view (at $X=7.5$ m).
- (iii) X-Y view (at $Z=0$).

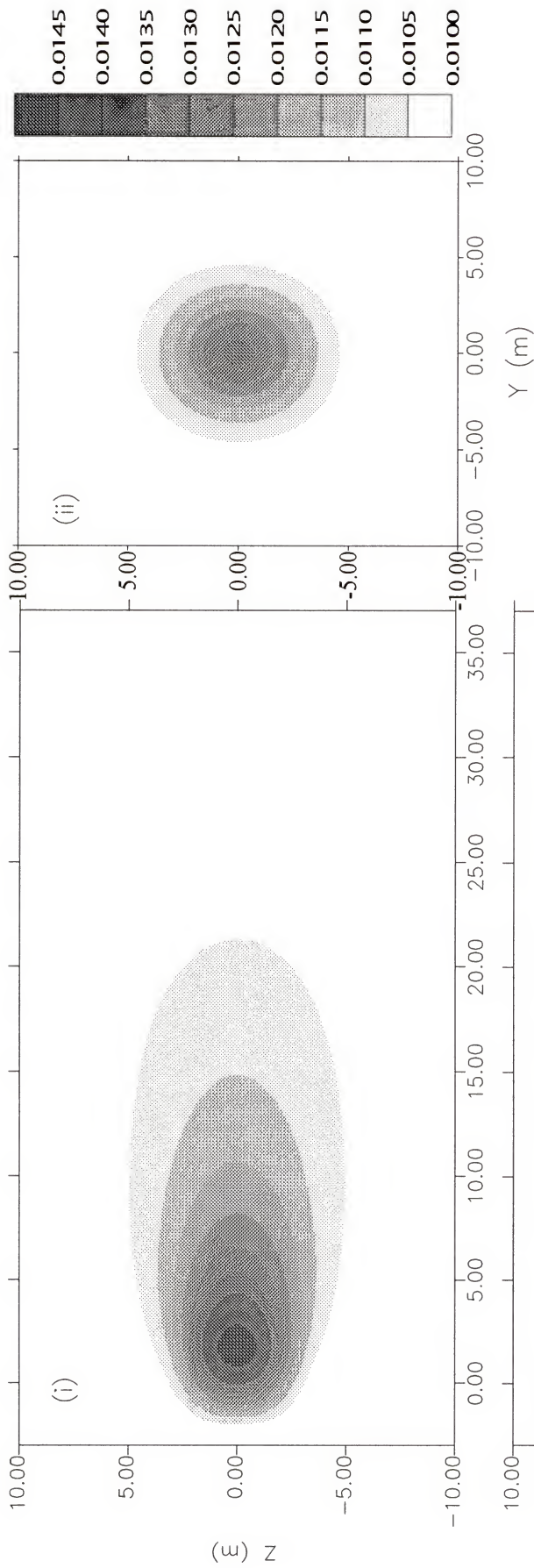


Figure 6-8d biomass concentrations for Run 12 after 50 days.

- (i) X-Z view (at $Y=0$).
- (ii) Y-Z view (at $X=7.5$ m).
- (iii) X-Y view (at $Z=0$).

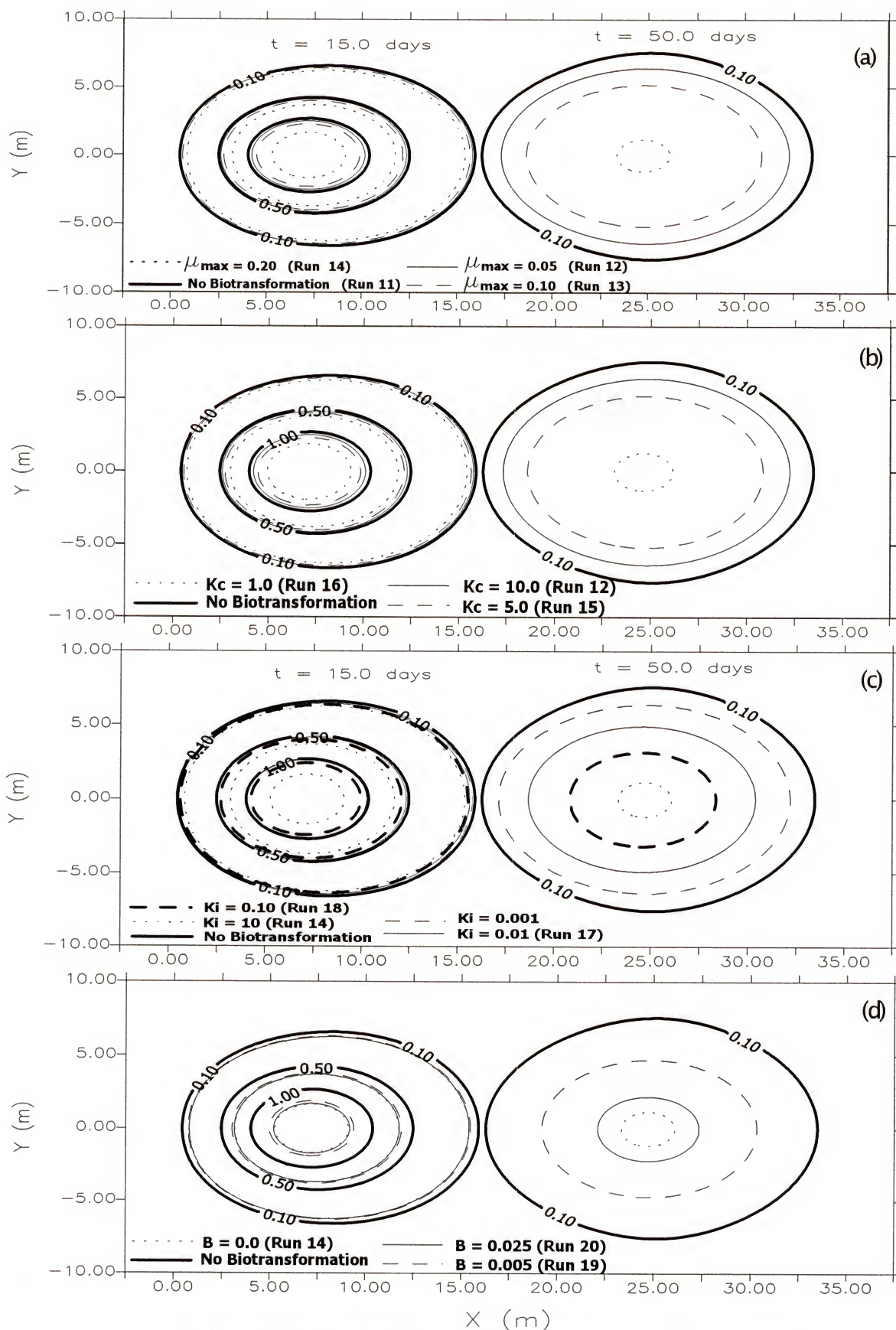


Figure 6-9 Effect of the different biological parameters on Cr(VI) concentrations.

6.3.1 Effects of Microbial Growth Rate (μ_{\max})

In addition to the two base runs (11 and 12), Runs 13 and 14 are used to demonstrate the effects of μ_{\max} . Figure 6-9a illustrates Cr(VI) concentration lines of Runs 11-14 after 15 and 50 days. This figure shows, as expected, that with an increase in μ_{\max} there is more Cr(VI) biotransformation. Such effects are clear at both times (15 and 50 days); however, more biotransformation occurs at $t = 50$ days due to the existence of more microbes at that time which, as a result, increases both the microbial growth rate (dM/dt) and the Cr(VI) reduction rate ($-dC/dt$).

Figure 6-10a shows the effects of increasing the microbial maximum growth rate on the microbial population in the aquifer. It is clear that the biomass concentration increased in run 14 ($\mu_{\max} = 0.2 \text{ day}^{-1}$) as compared to run 13 ($\mu_{\max} = 0.05 \text{ day}^{-1}$) at both times (15 and 50 days). Biomass concentrations increased in the aquifer from $t=15$ days to $t=50$ days for both runs because more bacteria was exposed to the Cr(VI) plume at the later time.

The zero moment, which represents the ratio of the current mass in the system to the initial mass of Cr(VI) is shown in Figure 6-10b(i). This figure clearly demonstrates the loss of Cr(VI) mass with time due to biotransformation. The case of “no biotransformation” gives a conservative mass transport, as expected. This figure can serve, in addition to implementing the conservative transport nature of the plume in the case of “no biotransformation”, as a successful validation example of the model mass balance calculations. It is also clear in Figure 6-10b(i) that with higher values of μ_{\max} , more biotransformation occurs and, therefore, less contaminant mass remains in the aquifer at the end of each simulation.

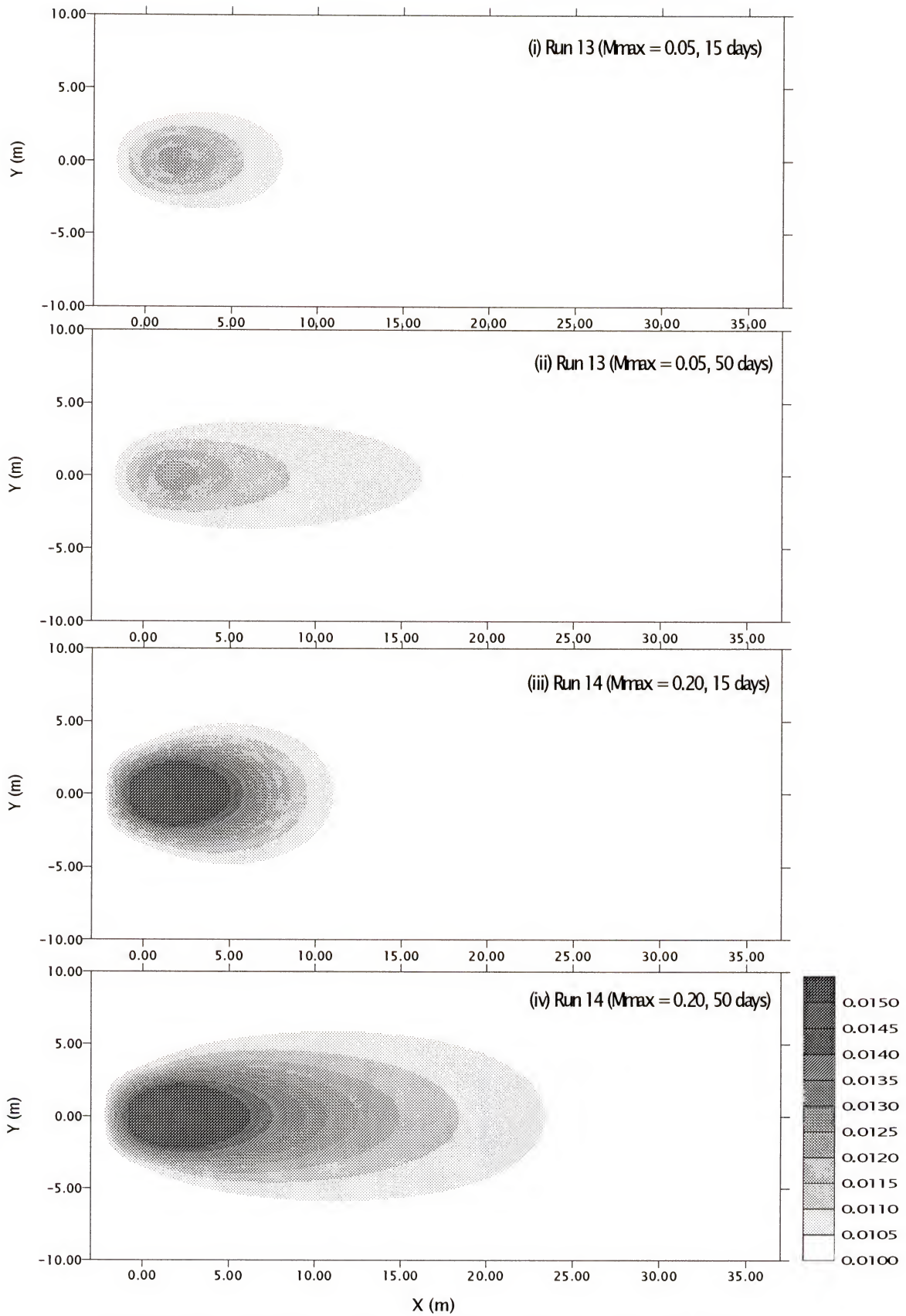


Figure 6-10a Effect of μ_{\max} on biomass concentrations.

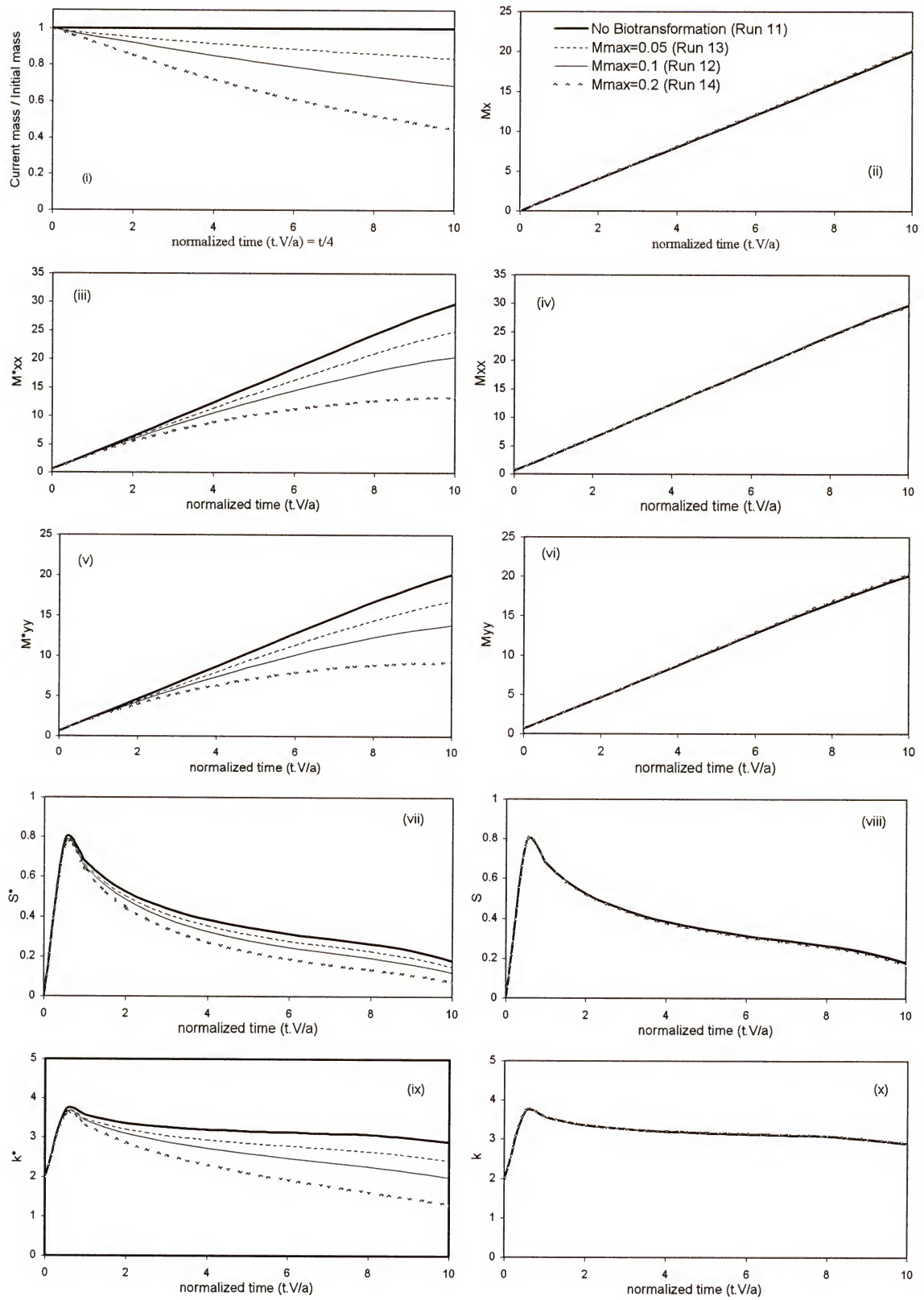


Figure 6-10b Effect of maximum specific growth rate on spatial moments of Cr(VI) plume.

Table 6-4 Percentage of biotransformed mass of Cr(VI) after 50 days for example 2.

Run	Biotransformed Cr(VI) mass
11	0.00
12	40.61
13	22.97
14	65.68
15	63.99
16	99.24
17	29.64
18	58.67
19	60.99
20	44.91

It is clear that the contaminant mass decreases with time for all the three cases (Runs 12-14). Similarly, Table 6-4 shows that with the increase of the value of μ_{\max} , the total mass of Cr(VI) reduced at the end of simulations increases. For example, the percentage of the biotransformed Cr(VI) mass is almost doubled in Run 12 (41%) compared to Run 13 (23%) when μ_{\max} is doubled ($0.05 \rightarrow 0.1 \text{ day}^{-1}$). However, when μ_{\max} is increased four times in Run 14 (0.2 day^{-1}) an increase of less than three times was observed for Cr(VI) biotransformed mass (66%) as compared to run 13 (23%) [Table 6-4].

Despite the apparent reduction in concentrations and plume size, due to Cr(VI) reduction, the second moment normalized by the current solute mass (M_{ii}) implies that dispersion did not change compared to the case of “no biotransformation” [Figure 6-10b(iv and vi)]. The reason for this, as mentioned in example 1, is that the reduction in

solute mass is occurring at approximately the same rate as the reduction in the second absolute moment (Equation 6-2). Therefore, using the current solute mass to normalize the second moment would give a misleading indication about the plume size reduction due to biotransformation especially at large time values (when biotransformation reduces Cr(VI) mass dramatically). On the other hand, when using the initial solute mass to normalize absolute moments, a clear reduction in the second moment (M_{ii}^*) due to biotransformation is observed [Figure 6-10b(iii and v)]. This type of moment provides information to those interested in studying the change in the Cr(VI) plume size caused by biotransformation processes.

Figure 6-10b(ii) shows that the longitudinal first moment of Cr(VI) (M_x), which represents the position of the plume center of mass, did not change among all different cases. One can conclude that biotransformation processes, in homogenous aquifers with uniform initial biomass distribution, do not affect convection (M_x) or the dispersion (M_{xx} and M_{yy}) of the contaminant plume; however, they do significantly affect concentrations and variances in both directions (M_{xx}^* and M_{yy}^*). This is clear from Figure 6-9a, where the center of the contaminant plume is located at almost the same position for all cases. The same figure shows a decrease in concentration values and contaminant plume size, which is more significant with the increase of μ_{max} .

Figure 6-10b(vii and viii) shows that the skewness (s and s^*) decreases with the increase of μ_{max} . Skewness values for all cases are small; however, they tend to increase at early times, most likely, due to the effect of the left boundary, which causes the plume to be slightly asymmetric. As the plume moves further downgradient in the aquifer, the boundary effect decreases and as does the skewness. Skewness in the Y-direction (not

shown) is almost zero (order of 10^{-16}) for all cases. Having the initial plume far from both upper and lower boundaries limits the effect of these boundaries on the skewness in Y-direction. Furthermore, it is clear from figure 6-10b(vii) that increasing the value of μ_{\max} also increases the rate at which the plume recovers faster from the induced asymmetry.

Finally, Figure 6-10b(ix) shows that the fourth spatial moment varying dramatically with the increase in μ_{\max} due to the decrease in the concentration values. On the other hand, Figure 6-10b(x) shows that changing μ_{\max} has no effect on the kurtosis when using the current mass, which implies that the plume follows a Gaussian distribution.

6.3.2. Effects of Cr(VI) half Saturation Coefficient (K_c)

Runs 15 and 16 (Table 6-3) are compared with run 12 to study the impacts of the half saturation coefficient of Cr(VI) on the Cr(VI) concentration distributions in the aquifer. Increasing the value of K_c produces an inverse effect on the reduction rate. This is apparent from figure 6-9b, where decreasing K_c from 10 to 5 and then to 1 dramatically decreases metal concentrations in the aquifer at both 15 and 50 days. Reducing K_c to one half of its original value ($10 \rightarrow 5$ mg/l) increases the biotransformed mass of Cr(VI) from 41% to 64% (Runs 12 and 15) [Table 6-4]. Almost the same effect is obtained by doubling the value of μ_{\max} (Runs 12 and 14) [Table 6-4]. The relation between the two parameters is not linear as the effect of the K_c depends significantly on the metal concentrations and the inhibition factor (equation 4-11). If metal concentrations are much less than the half saturation coefficient ($A \ll K_a$), Cr(VI) reduction approaches a first order linear process. At which case, both parameters have opposite effects on the natural attenuation of the Cr(VI) plume.

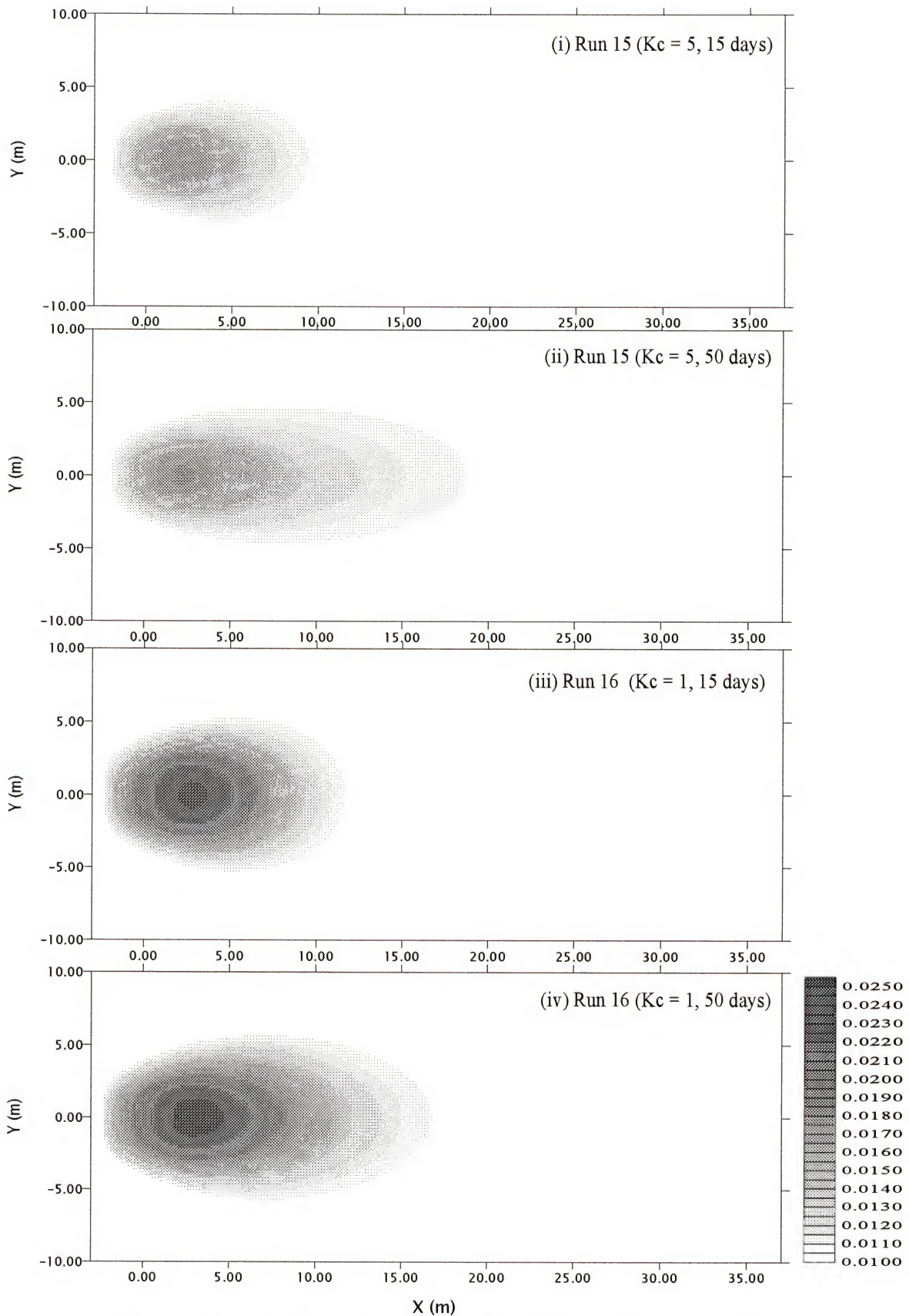


Figure 6-11a Effect of K_c on biomass concentrations.

Figure 6-11a shows that reducing the value of the Cr(VI) half saturation coefficient increases the biomass concentration in the aquifer especially at the location of Cr(VI) initial release.

Figure 6-11b, illustrates the impacts of K_c on the spatial moments of the Cr(VI) plume. Increasing K_c reduces the reduction rates and, therefore, leaves more Cr(VI) mass in the aquifer [Figure 6-11b(i)]. Additionally, increasing the same parameter increases the second moment normalized by initial Cr(VI) mass in both directions [Figures 6-11b(iii and v)]. Similar to effects of changing μ_{\max} , changing K_c did not significantly affect the dispersion in both directions [Figure 6-11b(iv and vi)].

Changing the same parameter had less effect on both skewness and kurtosis [Figure 6-11b(viii and x)] than that it had on other moments. When K_c has a value of 5, a slight increase on the kurtosis values occurs compared to all other cases. However, due to the decrease in the concentration values, both the third and fourth moments dramatically decreased from the case of “no biotransformation” with the decrease of K_c [Figures 6-11b(vii and ix)].

6.3.3. Effects of inhibition factor (K_i)

Increasing K_i increases the Cr(VI) reduction and, therefore, decreases the resident metals concentrations in the aquifer [Figure 6-9c]. Increasing K_i 10 times ($0.01 \rightarrow 0.1$) increased the percentage of the biotransformed mass 29% (from 30% to 59% in Runs 17 and 18) [Table 6-4]. However, when it was further increased 100 times ($0.1 \rightarrow 10$), only a 7% increase in the biotransformed Cr(VI) mass was observed (from 59% to 66%, Runs 18

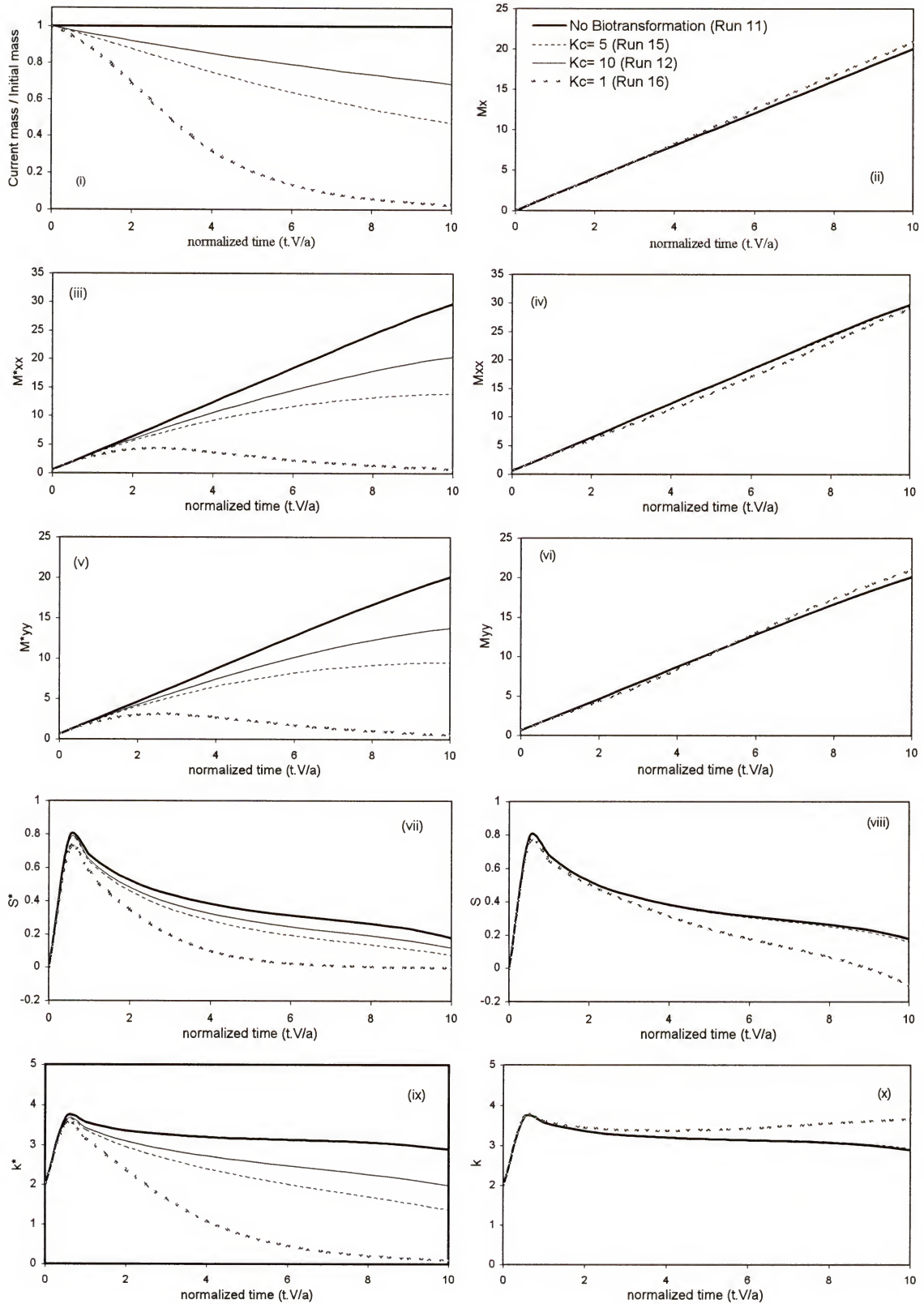


Figure 6-11b Effect of K_c on spatial moments of Cr(VI) plume.

and 14) [Table 6-4]. Therefore, one can conclude that K_i has an upper limit value after which its effect on the reduction process becomes negligible.

As seen with the two-dimensional simulations, changing K_i significantly influences the biomass distribution in the aquifer [Figure 6-12a]. When K_i was decreased, areas of maximum biomass concentration were spread over larger areas along the path of the contaminant movement. Bacteria are inhibited until metals concentrations decrease (due to dispersion) below the toxic level (represented by K_i). Thus, maximum biomass concentrations tend to increase at the outer lateral edges of the Cr(VI) plume at early times and increase in the middle of the plume at later times (when Cr(VI) concentrations have decreased due to dispersion) [Runs 17 and 18, Figure 6-12a].

Cr(VI) mass reduction is not as sensitive to the change in K_i [Figure 6-12b(i)] as it was with K_c and μ_{max} . Dispersion, on the other hand, is more sensitive to the change in the K_i [Figures 6-12b(iv and vi)]. When $K_i = 0.01$, dispersion in both directions is reduced from the case of “no biotransformation”. As mentioned above, that is due to the effect of the inhibition factor on the biomass distribution in the aquifer. When the value of K_i was increased, both dispersion values are increased back to the case of “no biotransformation”.

Increasing K_i from 0.01 to 0.1 slightly increases kurtosis at later times [Figures 6-12b(x)]. However, continuing to increase its value from 0.1 to 10 reduces both skewness and kurtosis values again to that of the case of “no biotransformation” (Gaussian distribution).

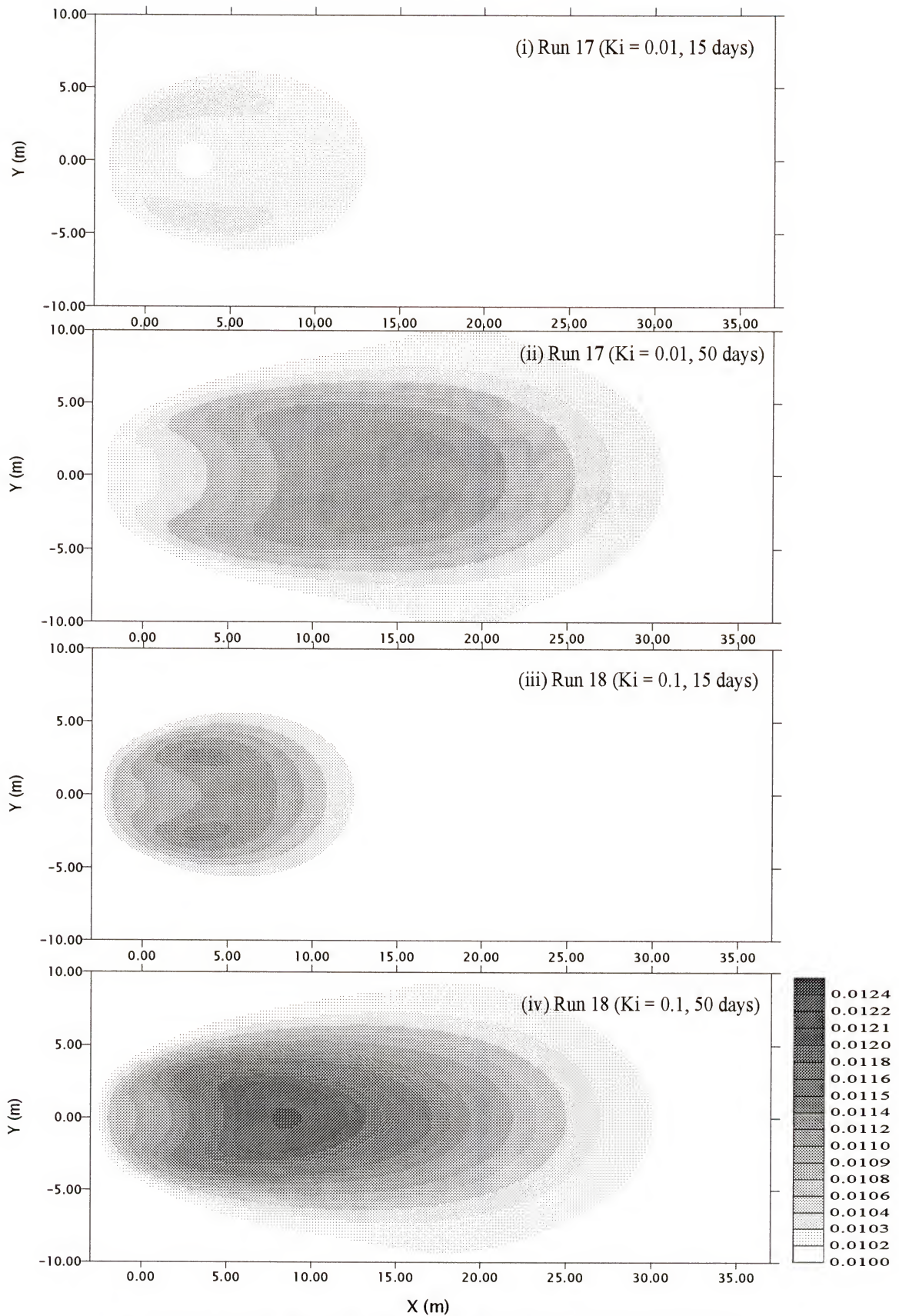
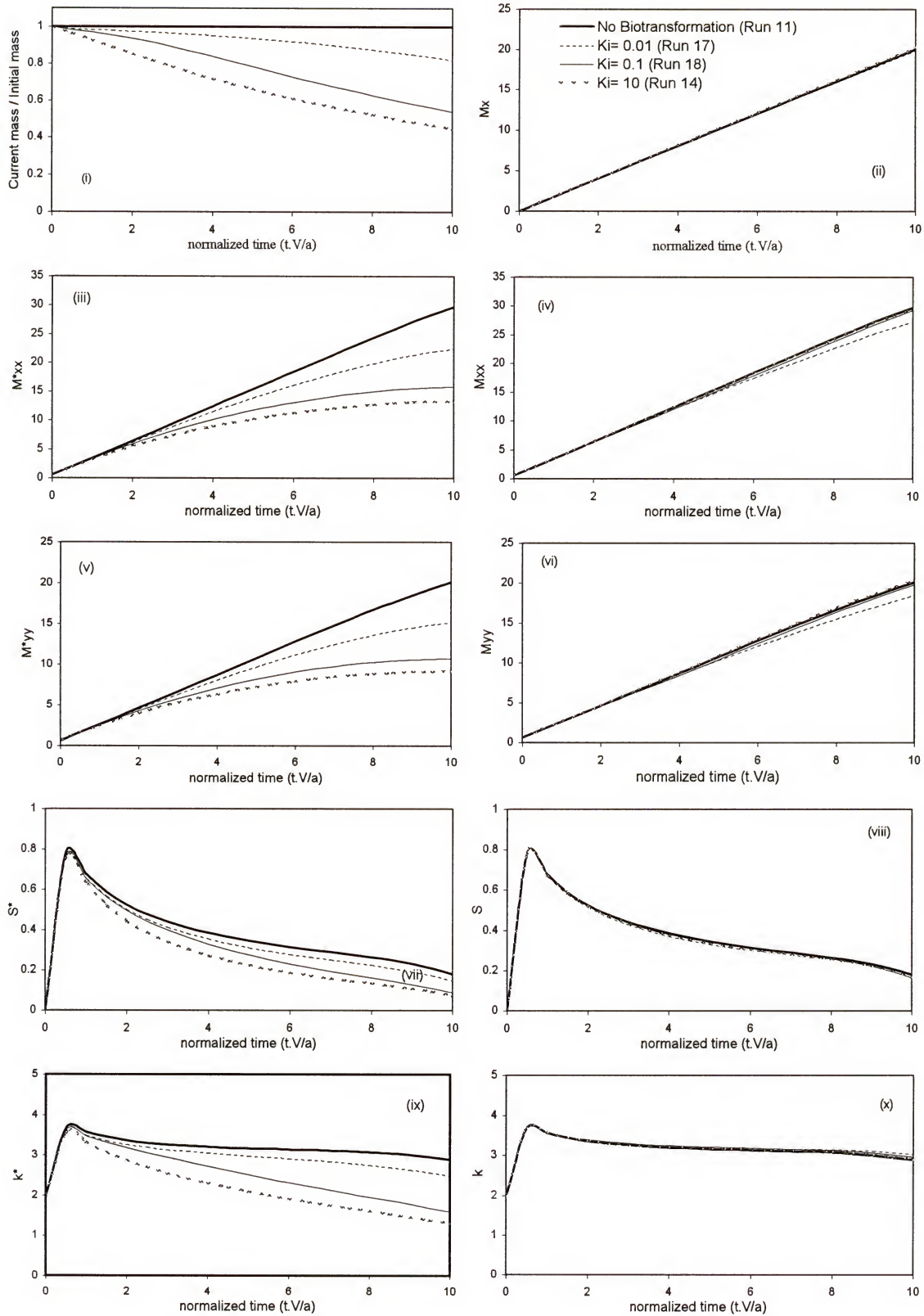


Figure 6-12a Effect of K_i on biomass concentration.

Figure 6-12b Effect of K_i on spatial moments of Cr(VI) plume.

6.3.4. Effects of Bacterial Death Rate (B)

The last parameter of interest is the microorganisms' death rate (B). It should be expected that an increase in the death rate reduces the biomass in the aquifer; as a result, there will be a decrease in the biotransformation activities in the aquifer [Figure 6-9d]. Unlike the growth rate parameter, which only manifest changes when nutrients are available, the death rate parameter affects all microorganisms in the aquifer starting at $t = 0$ to produce a decrease in the biomass throughout the aquifer. With less biomass [Figure 6-9d], there is a consequent drop in Cr(VI) reduction rate [Figure 6-13b(i)]. Table 6-4 illustrates that increasing the death rate from 0.0 to 0.025 reduces the percentage Cr(VI) biotransformed mass from 66% to 45% (Runs 14, 19 and 20).

Because the death rate uniformly affects all the microorganisms in the aquifer, there is no effect on longitudinal and transverse dispersion, skewness, or kurtosis [Figures 6-13b(iv, vi, viii, and x)]. However, due to its effect on Cr(VI) concentrations, changing the death rate affects the Cr(VI) plume morphology in both directions and therefore affects the second, third, and fourth moments (normalized by the initial Cr(VI) mass) [Figures 6-13b(iii, v, vii, and ix)].

6.3.5. Effects of all Biological Parameters on Mass Flux

Mass fluxes at sections 1, 2, and 3 at 10, 20, and 30 m away from the center of the initial Cr(VI) plume, respectively, were measured at each time step. Figure 6-14a illustrates the MFC of the different cases of μ_{\max} at the three sections. The normalized flux (Y-axis) in this figure is a dimensionless quantity that equals the actual mass flux divided by the initial mass of Cr(VI) in the system, the velocity in X-direction, and the width of the initial contamination source ($Q_a / M_t V_x$). On the other hand, the X-axis

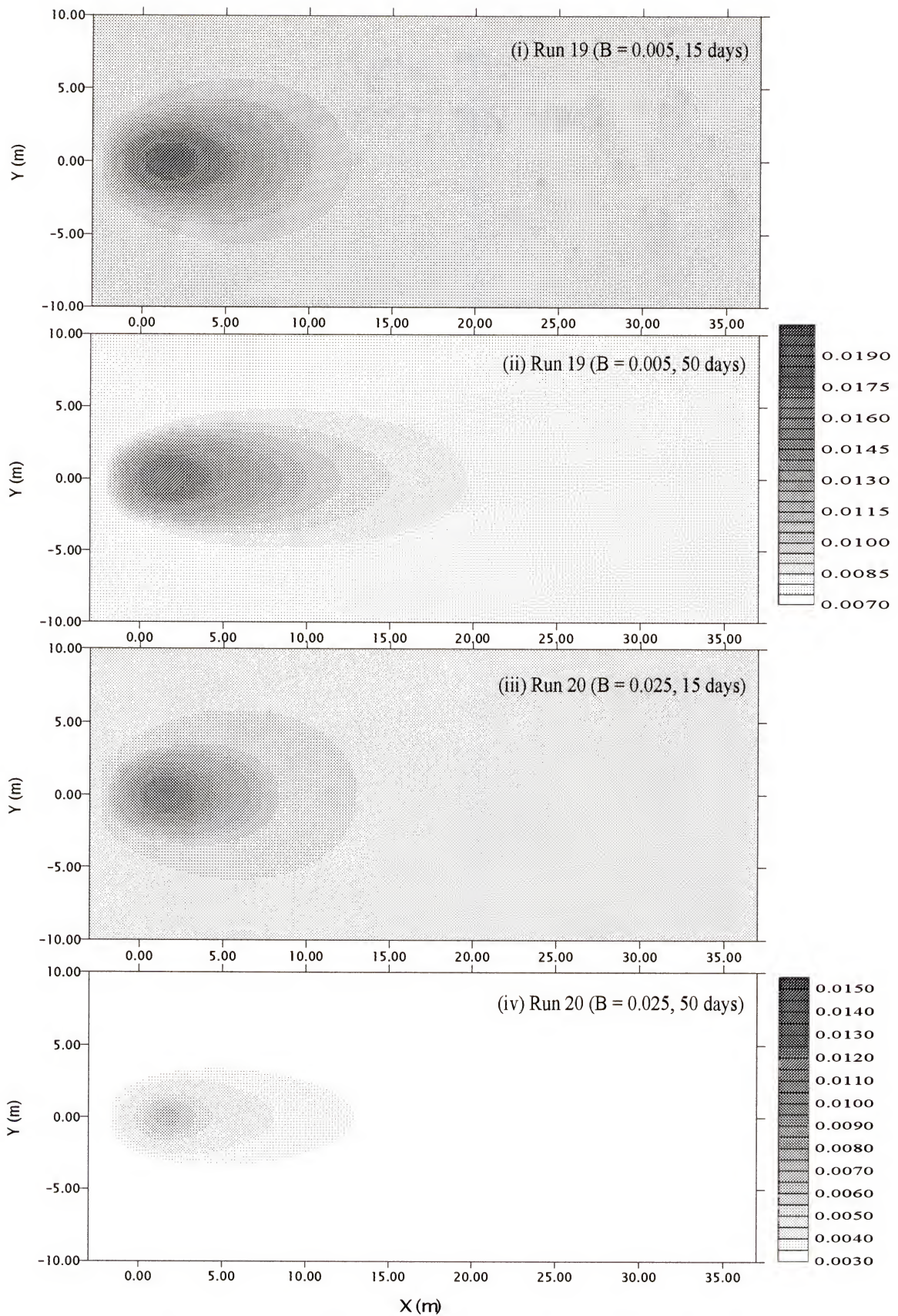
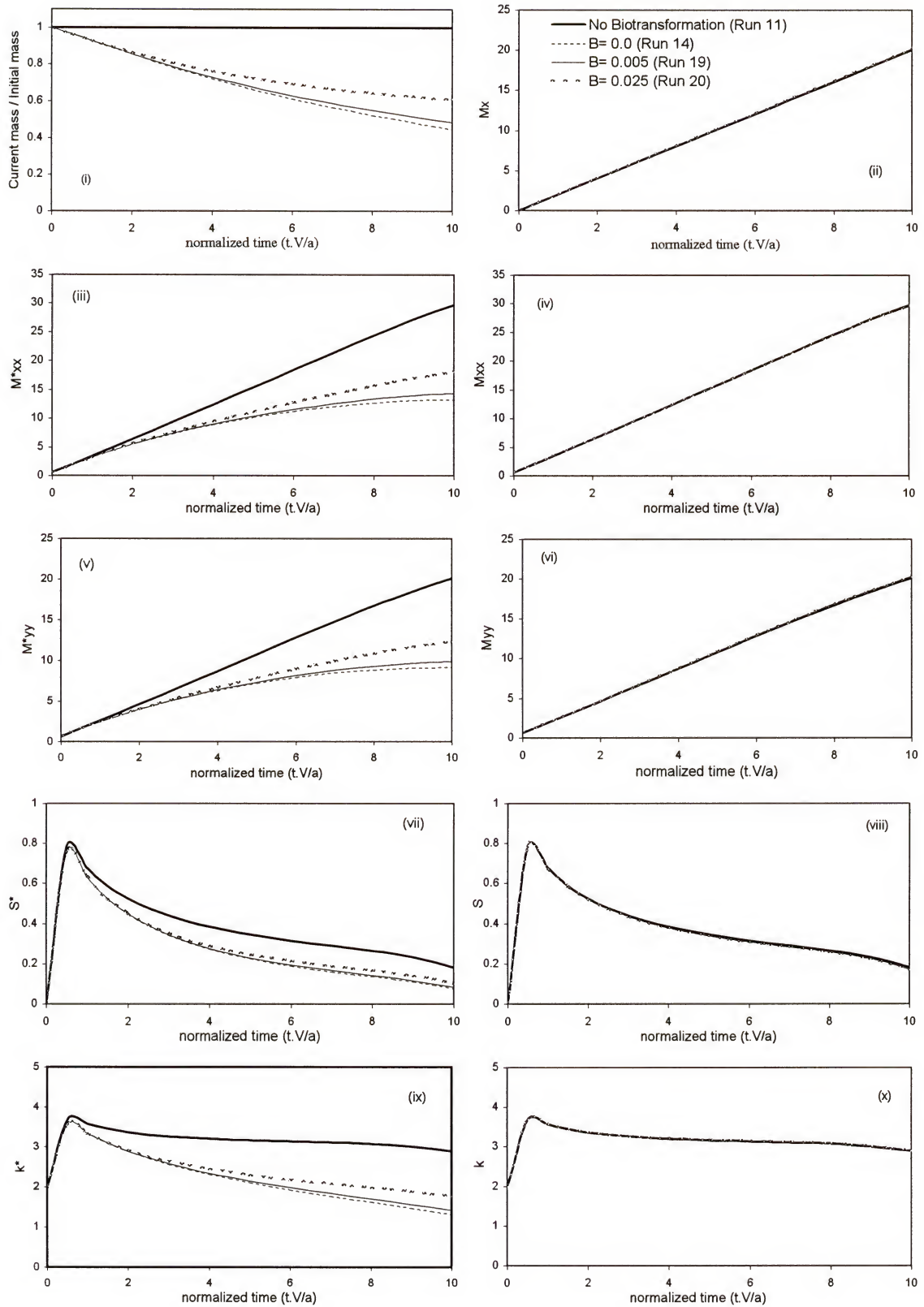


Figure 6-13a Effect of B on biomass concentrations.

Figure 6-13b Effect of B on spatial moments of Cr(VI) plume.

represents the normalized time, a dimensionless value that represents the time divided by the width of the initial Cr(VI) source and the groundwater velocity in X-direction (tV_x/a).

It is obvious from Figure 6-14a that an increase in μ_{\max} yields an increase in the Cr(VI) biotransformation and therefore a reduction in the area under the BTC. This conclusion can be drawn by comparing the MFC at the three sections. Another important observation is that when no biotransformation occurs (bold solid lines), the cumulative flux is the same between observation planes. On the other hand, when there are biotransformation activities in the aquifer (the other three cases), mass loss occurs from section 1 to section 2 and to section 3. This conclusion is apparent for the case of $\mu_{\max} = 0.20$ [Figure 6-14a]. Similar effects on Cr(VI) mass fluxes at each section are noticed with a decrease in the Cr(VI) half saturation coefficient [Figure 6-14b]. Increasing the inhibition factor increases the biotransformation activities in the aquifer and, therefore, a decrease in Cr(VI) fluxes between successive sections is noted.

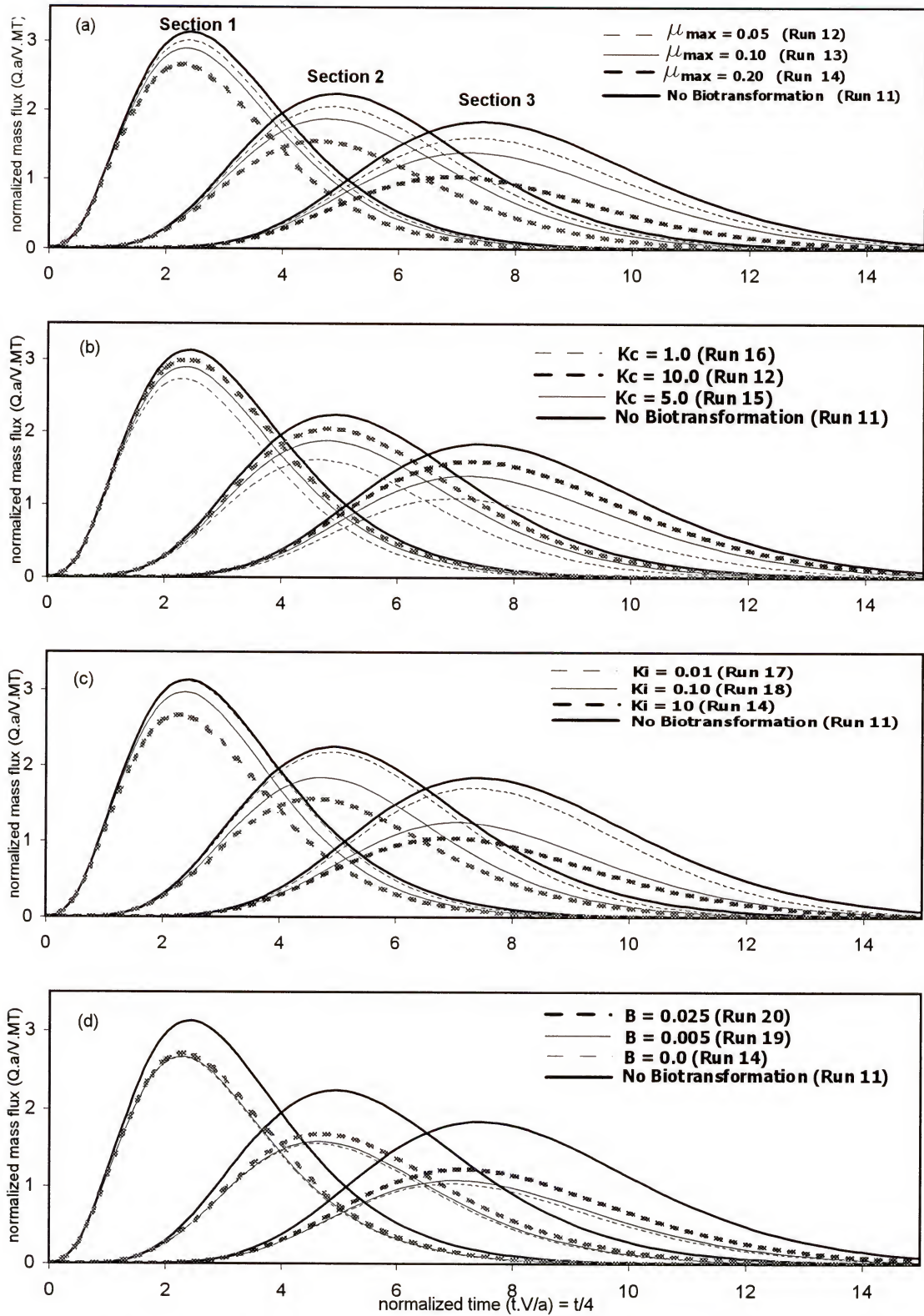


Figure 6-14 Mass fluxes at the three sections for Runs of Example 2.

CHAPTER 7

EFFECT OF ELECTRON DONORS AND NUTRIENTS AVAILABILITY ON THE BIOLOGICAL TREATMENT OF A METAL IN THE SUBSURFACE

7.1. Introduction

Biodegradation is mediated by microorganisms that couple oxidation of an electron donor and reduction of an electron acceptor. When oxygen is available, it acts as the electron acceptor in a process called aerobic biodegradation. However, in the absence of oxygen, microorganisms use other organic or inorganic chemicals as alternative electron acceptors to anaerobically degrade an electron donor. Thus, hydrocarbons, which often act as electron donors, can be biodegraded under aerobic or anaerobic conditions. Metals, on the other hand, cannot be biodegraded; however, they can be biotransformed from a toxic to less-toxic form. Metals can serve as electron acceptors in the reduction-oxidation reactions. As a result, the availability of electron donors and nutrients in an aquifer can play a significant role in the biotransformation of metals.

In this chapter, effects of electron donor and nutrient availability in the aquifer on metals and biomass concentration distributions and spatial moments are studied through three different cases. In the first case, twelve different scenarios are used to investigate the effects of numbers and positions of electron donors and nutrients injection wells on the reduction of Cr(VI). Next, the effects of doubling injection rates of the electron donor and the nutrient are investigated in case 2 via 12 additional scenarios similar to those in case 1. Finally, the effects of bacterial growth inhibition are studied in case 3.

Many factors affect the biotransformation of metals in the subsurface; some of which are biological, while others are physical. The impacts of the different single-valued biological parameters on Cr(VI) reduction are addressed in chapter 6. Another important factor that potentially affects the remediation efficiency of aquifers contaminated with metals is the availability of electron donors and nutrients in the aquifer. Furthermore, treatment of the contaminant immediately after its release is likely to be more efficient and less costly than treating a larger contaminant plume several years after its initial release. In this chapter we will emphasize both issues by studying several different scenarios of introducing an electron donor and a nutrient into the aquifer by varying the number and positions of injection wells with different injection rates.

The effects of pertinent inhibition constants are also considered in this chapter. The inhibition factor represents the toxic level of substrate concentration above which microbes do not grow (Equation 4-16). Increasing injection rates could increase the concentration of the electron donors and nutrients in the aquifer to toxic levels that may have a deleterious effect upon remediation and, therefore, on the reduction or removal efficiency of the Cr(VI). In this case injection of electron donors and nutrients through one well or three wells may be more effective than a line source. Otherwise, reducing the pumping rate from each well with an associated increase in the number of wells may be a better approach wherever inhibition is a concern.

7.2. Problem Description

A hypothetical problem is formulated to evaluate the impacts of the electron donors and nutrients availability on the biological treatment of a metal plume (Figure 7-1a).

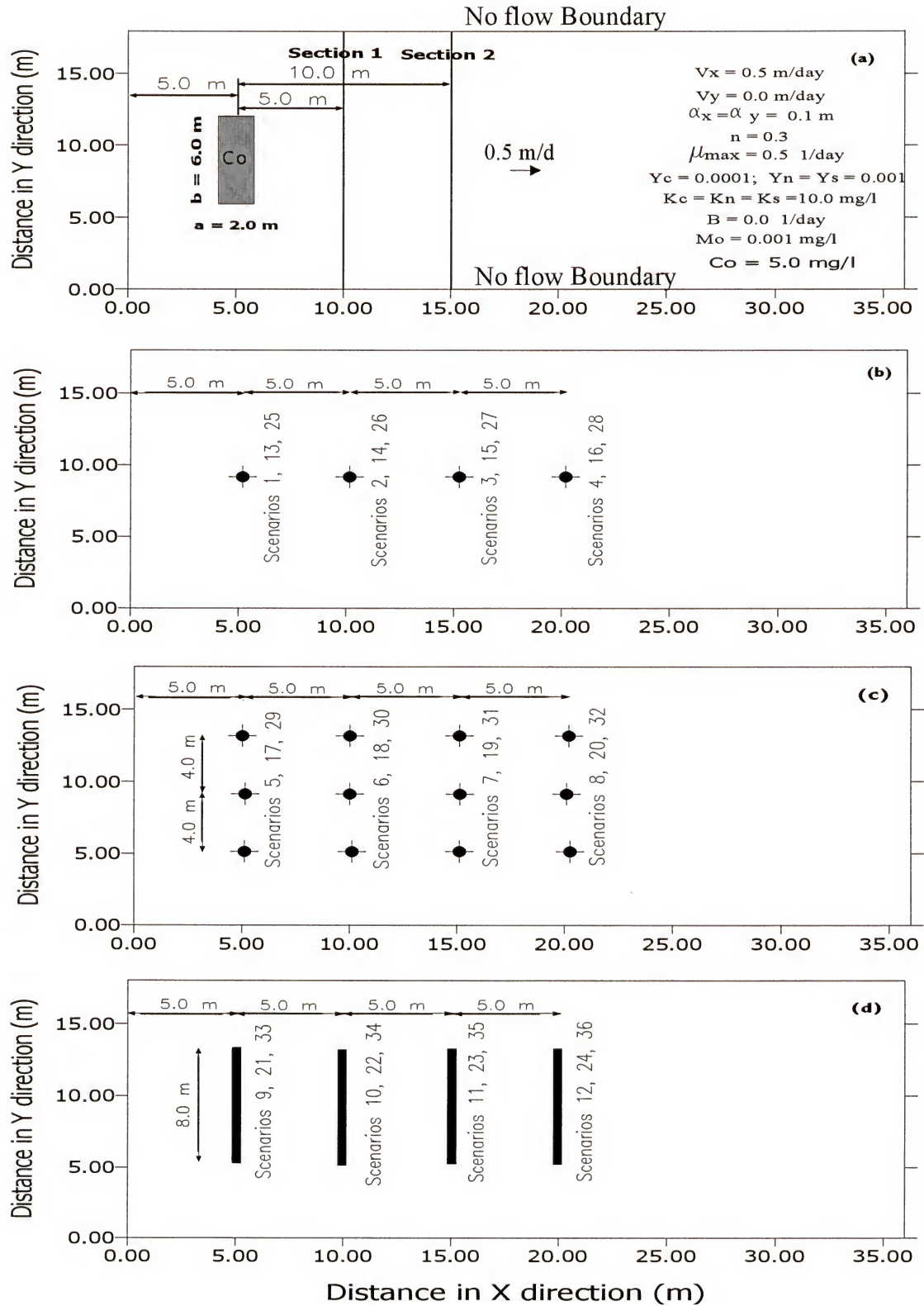


Figure 7-1 (a) Layout of the problem.

(b) Nutrient and electron donor pump positions for one well.

(c) Nutrient and electron donor pump positions for three wells.

(d) Position of Nutrient and electron donor line source.

In this problem, a two-dimensional x - y homogeneous aquifer is assumed with dimensions $36 \text{ m} \times 18 \text{ m}$ (Figure 7-1a) and a constant velocity in the x -direction (V_x) of 0.5 m/d . The longitudinal and transverse dispersivities are chosen to be the same with a value of 0.1 m . An instantaneous release of 1 mg/l of chromium (Cr(VI)) at time $t = 0$ is released as an areal source of contamination with dimensions $2 \text{ m} \times 6 \text{ m}$ and 5 m away from the left boundary. The left and right boundaries are assigned constant head values, whereas the top and bottom boundaries are considered impervious. Bacterial population is assumed to exist everywhere in the aquifer with initial uniform distribution. The input parameters for this example are shown in Figure 7-1a and can be summarized as following:

Discretization parameters:

Aquifer dimensions in X- and Y-directions (m)	= $36 \text{ m} \times 18 \text{ m}$
Element size in X-direction (Δx)	= 0.2 m
Element size in Y-direction (Δy)	= 0.2 m
Number of elements	= $16,200$
Time step for transport equation (Δt_r)	= 0.5 day
Time step for biological equations (Δt_b)	= 0.005 day

Flow and transport parameters:

Velocity in X-direction (V_x)	= 0.5 m/d
Velocity in Y-direction (V_y)	= 0.0 m/d
Dispersivity in X-direction (α_x)	= 0.1 m
Dispersivity in Y-direction (α_y)	= 0.1 m
Porosity (n)	= 0.3
Size of the initial source of contamination (a x b)	= $2.0 \text{ m} \times 6.0 \text{ m}$

Initial concentration of Cr(VI) (C_0) = 5.0 mg/l

Initial concentration of the electron donor and the nutrient = 0.0 mg/l

Biological parameters

Initial biomass concentration (M_0) = 0.01 mg/l

Microorganisms' maximum growth rate (μ_{\max}) = 0.5 day⁻¹

Microorganisms' death rate (B) = 0.0 day⁻¹

Cr(VI) yield coefficient (Y_c) = 0.0001

Cr(VI) half saturation coefficient (K_c) = 10.0 mg/l

Electron donor yield coefficient (Y_s) = 0.001

Electron donor half saturation coefficient (K_s) = 10.0 mg/l

Nutrient yield coefficient (Y_n) = 0.001

Nutrient half saturation coefficient (K_n) = 10.0 mg/l

Concentrations of other electron acceptors (E_e) = 0.0 mg/l

Three different cases are considered in this chapter. In each case, 12 different pumping scenarios are explored. One injection well is placed 0 m, 5 m, 10 m, and 15 m downstream from the center point of the chromium initial release in the first four scenarios, respectively, (Figure 7-1b). Similarly, three wells (4 m apart in the y direction) are used in scenarios 5-8 (Figure 7-1c). Finally, a line source of nutrient and electron donor (8 m length in y direction) is used in scenarios 9-12 with the same longitudinal distances, downgradient of the metal initial release, as those of scenarios 1-4, respectively, (Figure 7-1d).

In case 1, electron donor and nutrient injection rates are assumed to be 2.5 mg/day from each well in scenarios 1-8 (i.e. the total injection rate is 2.5 mg/d in scenarios 1-4 and 7.5 mg/d in scenarios 5-8). Because each well is represented by 5 nodes, injection from each node is assumed to be 0.5 mg/day/node. However, for the line source the injection rate per length is assumed to be 2.5 mg/day/m (Scenarios 9-12).

For the second case, the injection rates are doubled to 5.0 mg/day/well for scenarios 13-20 and 5.0 mg/day/m for scenarios 21-24. In both cases the inhibition factor is assumed to be very high, suggesting that all solutes have no toxic effect on the microorganisms. However, in the third case, the inhibition factors for all three solutes (Cr(VI), electron donor, and nutrient) are decreased to a value of 1 mg/l. Therefore, in this case, when the concentration of any of the three solutes exceeds 1 mg/l at any location in the aquifer, microbial growth is inhibited at that location.

Figures 7-2a(i and ii) show the concentration lines for both the electron donor and the nutrient for scenario 1 after 10 and 35 days, respectively. These concentration lines are predicted assuming no biological reactions in order to estimate the coverage area of the two solutes in the aquifer. Because the two solutes are injected with the same injection rate and from the same locations, concentration distributions of both solutes are the same.

Similarly, Figures 7-2a(iii, iv, v, and vi) show electron donor and nutrient concentrations for scenarios 5 and 9. Nutrient and electron donor concentrations for scenarios (2,6,10), (3,7,11), and (4,8,12) are similar to those in Figures 7-2a(i, ii), (iii, iv), and (v, vi), but shifted to the right 5, 10, and 15 m, respectively. Figure 7-2b is similar to Figure 7-2a but for cases 2 and 3 where injection rates are double those of case 1.

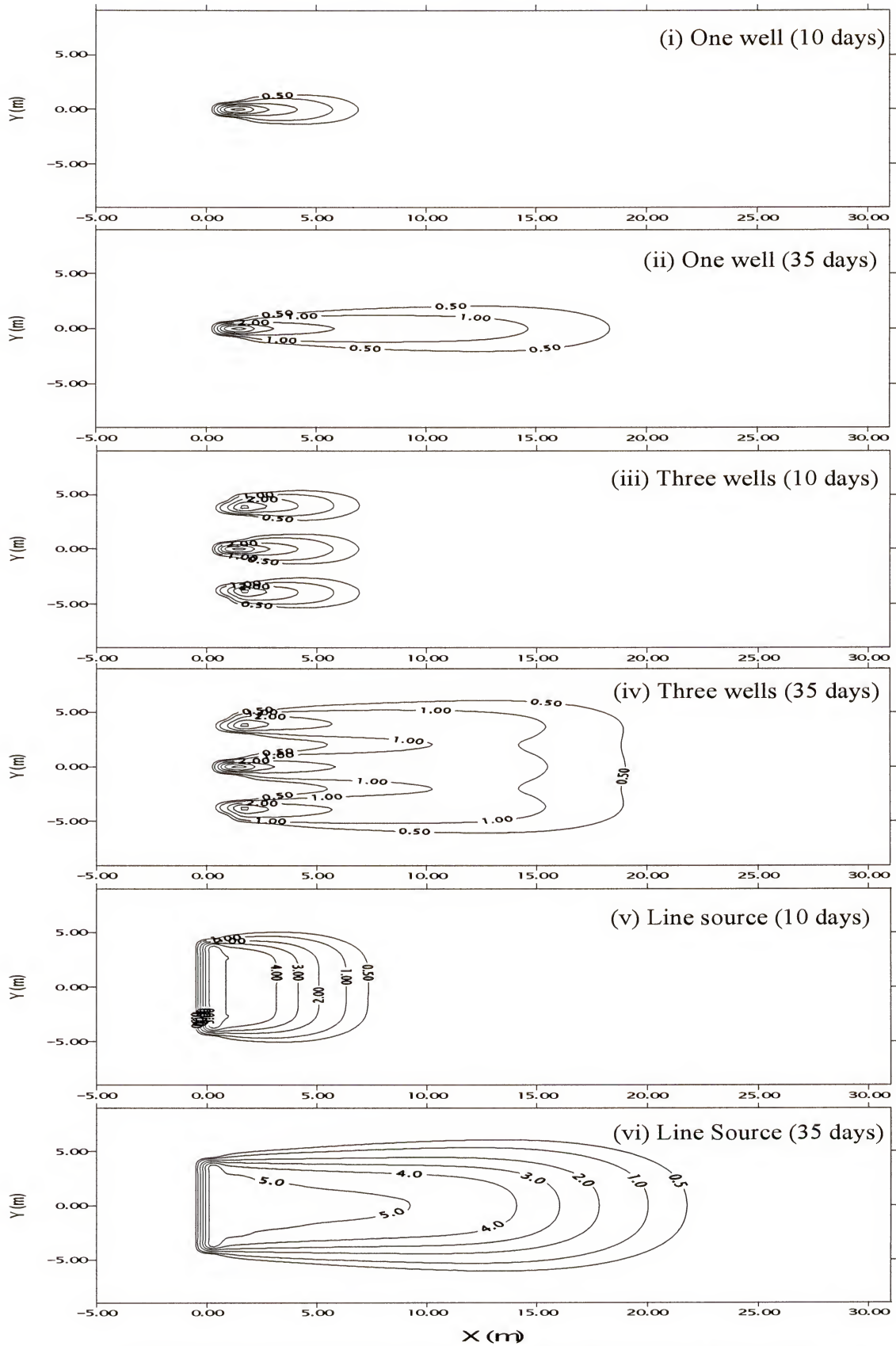


Figure 7-2a concentration lines of nutrient and electron donor for case 1.

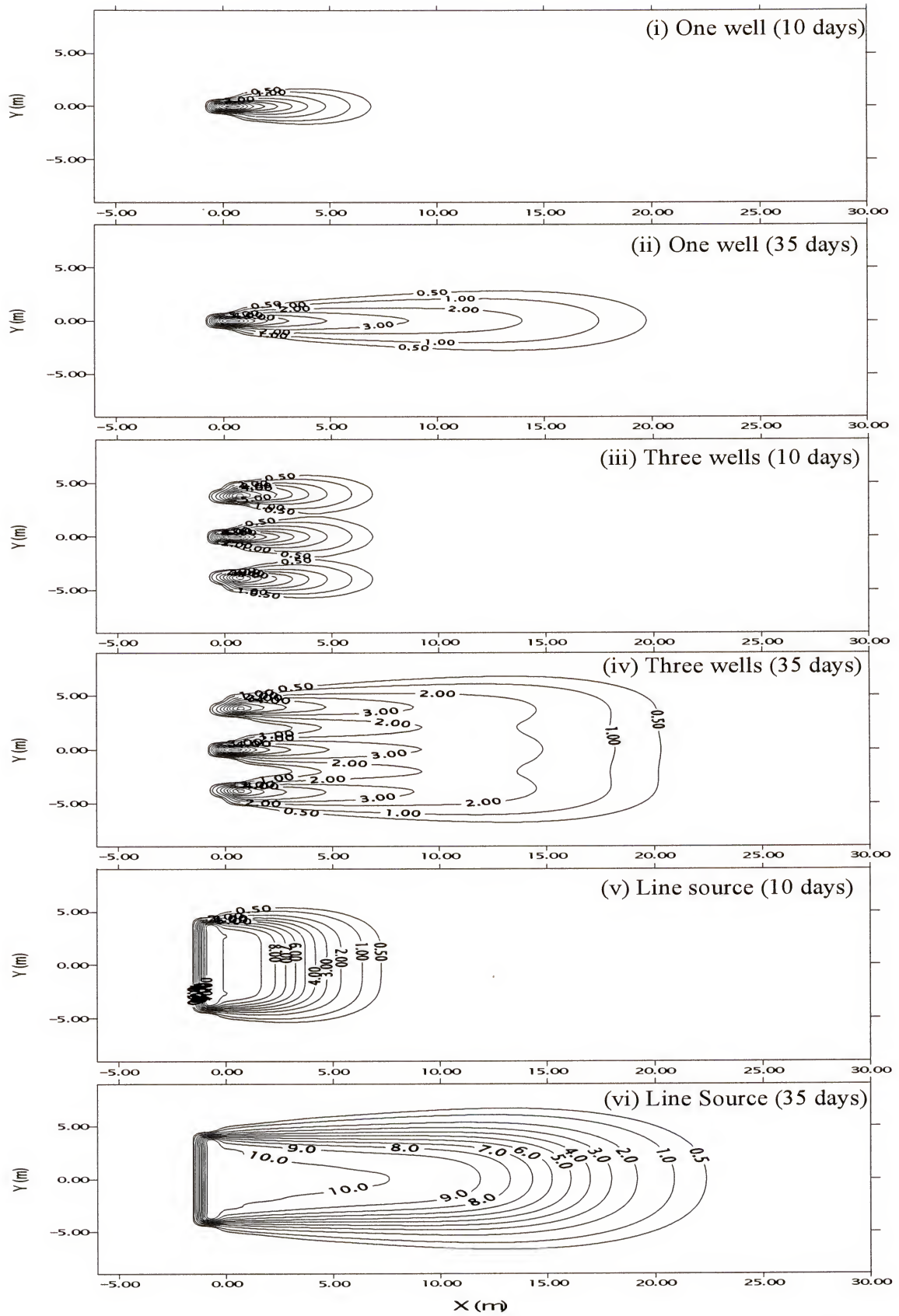


Figure 7-2b concentration lines of nutrient and electron donor for cases 2 and 3.

7.3. Case 1

7.3.1. One Well Treatment

As mentioned above, 12 different scenarios are studied in case 1 (Figure 7-1). In scenarios 1-4, one treatment well is used (Figure 7-1b) with electron donor and nutrient loading rates of 2.5 mg/day. Figure 7-3a shows the Cr(VI) concentrations in each of these 4 scenarios after 10 and 35 days compared to the case of “no biotransformation”. In all four scenarios, it is clear that one well reduces the concentrations only in the front and trailing edges of the Cr(VI) plume, with no effect on the lateral edges of the plume. When the well is placed exactly at the center of the Cr(VI) initial release, clear reduction on the trailing edge of Cr(VI) plume is evident at both times [Figure 7-3a(i)].

When the remediation well is placed 5 m downstream of the initial release [Figure 7-3a(ii)], reduction at the leading edge of the Cr(VI) plume is enhanced. This is probably due to the fact that both the nutrient and the electron donor were introduced downgradient from the initial location of Cr(VI) plume, creating an area of remediation into which the Cr(VI) plume would eventually migrate. Consequently, reductions in Cr(VI) concentration are greater in scenario 2 than in scenario 1 (compare Figures 7-3a(i and ii)).

Placing the injection well 10 and 15 m downstream from the location of Cr(VI) initial release (scenarios 3 and 4) delays Cr(VI) reduction beyond 10 days because more than 10 days are required for the Cr(VI) plume to migrate into the remediation area. Once the Cr(VI) plume moves into the remediation area, biotransformation is observed [Figures 7-3a(iii and iv)]. Placing the treatment well 10 m downgradient of the contaminant initial release induced Cr(VI) reduction at both trailing and leading edges of the plume after 35 days [Figure 7-3a(iii)]. In scenario 4, however, Cr(VI) reduction occurs only at the leading edges [Figure 7-3a(iv)].

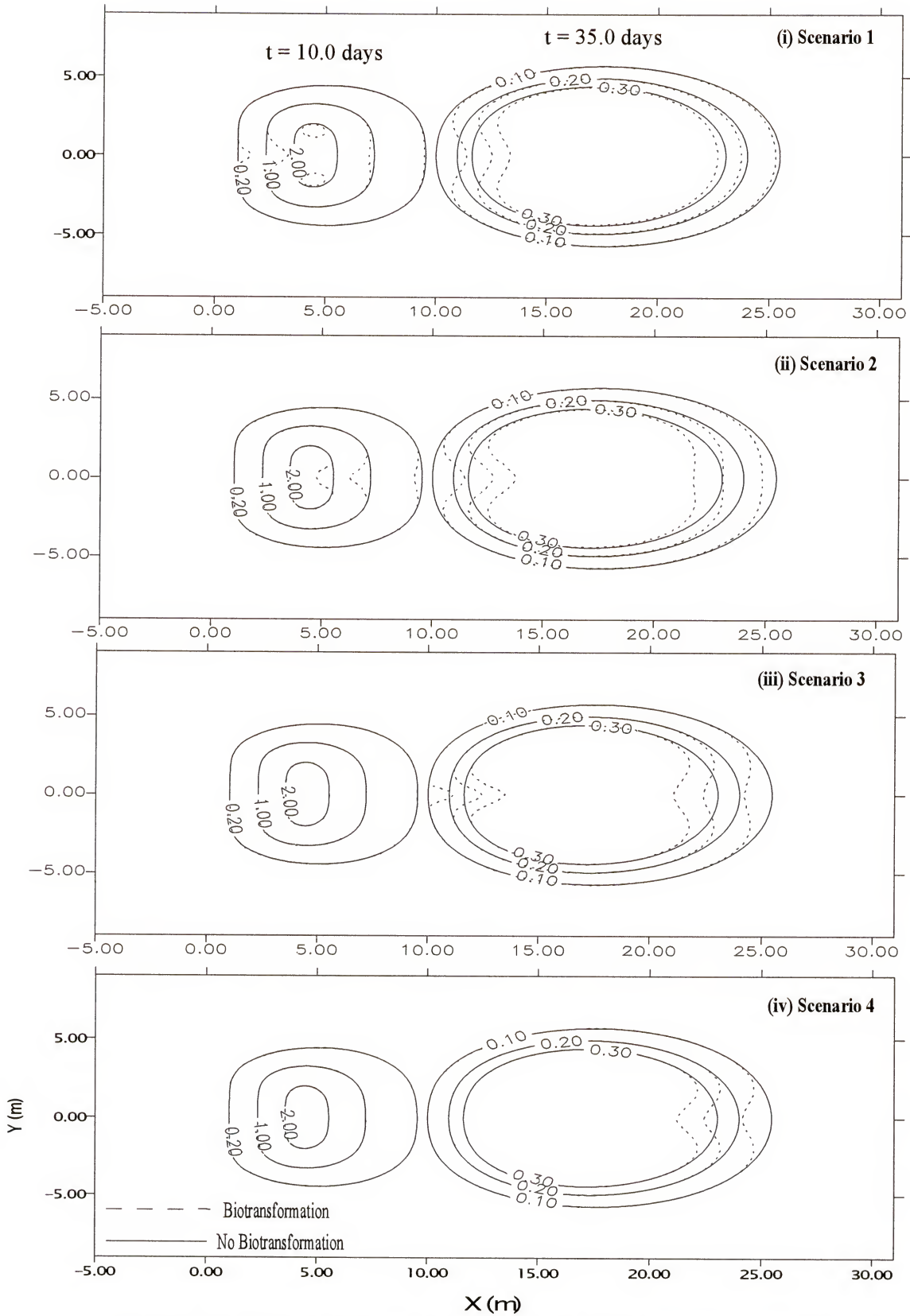


Figure 7-3a Effect of one well location on the Cr(VI) concentrations for case 1. (i) at the center of the initial plume, (ii) at 5 m, (iii) at 10 m and (iv) at 15 m.

Figure 7-3b shows the biomass concentration distribution for the first four scenarios (1-4). Microorganisms require an electron donor, a nutrient, and an electron acceptor to grow. For that reason, an increase in biomass is only observed near and downgradient from the injection zones (Figure 7-2a) where all three solutes exist. For the same reason, no increase in the biomass is observed after 10 days in scenarios 3 and 4 (not shown).

Figure 7-3b(i) shows the biomass concentration of scenario 1 after 10 days. Because all solute (Cr(VI), electron donor, and nutrient) plumes move in the positive X-direction, biomass concentrations increase in that direction after 35 days [Figure 7-3b(ii)] compared to those after 10 days [Figure 7-3b(i)]. However, when the injection well is placed 5, 10 and 15 m away from the contaminant initial release, biomass distribution changes accordingly [Figures 7-3b(iii-vi)]. It is clear that after 35 days, lower biomass concentrations exist in the aquifer for scenario 4 [Figure 7-3b(vi)] compared to scenario 1 [Figure 7-3b(ii)]. This is because the remediation area in scenario 4 is situated far from the location of the Cr(VI) initial plume and, consequently, more time is needed for the Cr(VI) plume to move into the remediation area.

Figure 7-3c shows spatial moments of Cr(VI) concentration distribution. It is clear from Figure 7-3c(i) that Cr(VI) reduction occurs as the plume approaches the injection well [Figure 7-3c(i)]. Therefore, the decrease in the Cr(VI) total mass occurs later in scenario 4 compared to the other scenarios. Although the biotransformation effect in scenario 2 started later than in scenario 1, the total mass of Cr(VI) biotransformed is greater in case 2 after 36 days (36 days = 9 on the normalized time scale). The reason for this is that the injection of the nutrient and the electron donor starts at $t = 0$ in both

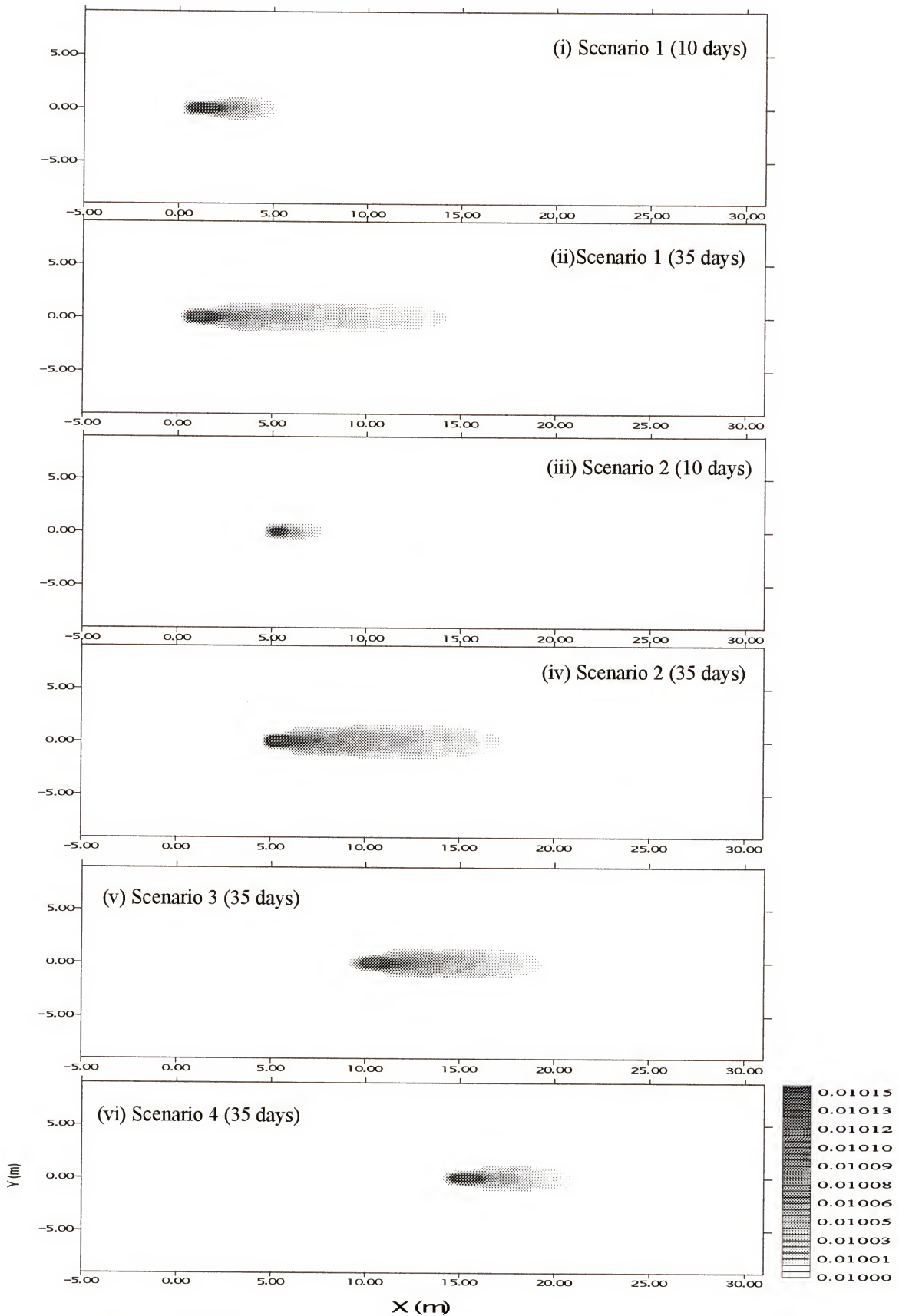


Figure 7-3b Effect of one well location on biomass concentrations for case 1.

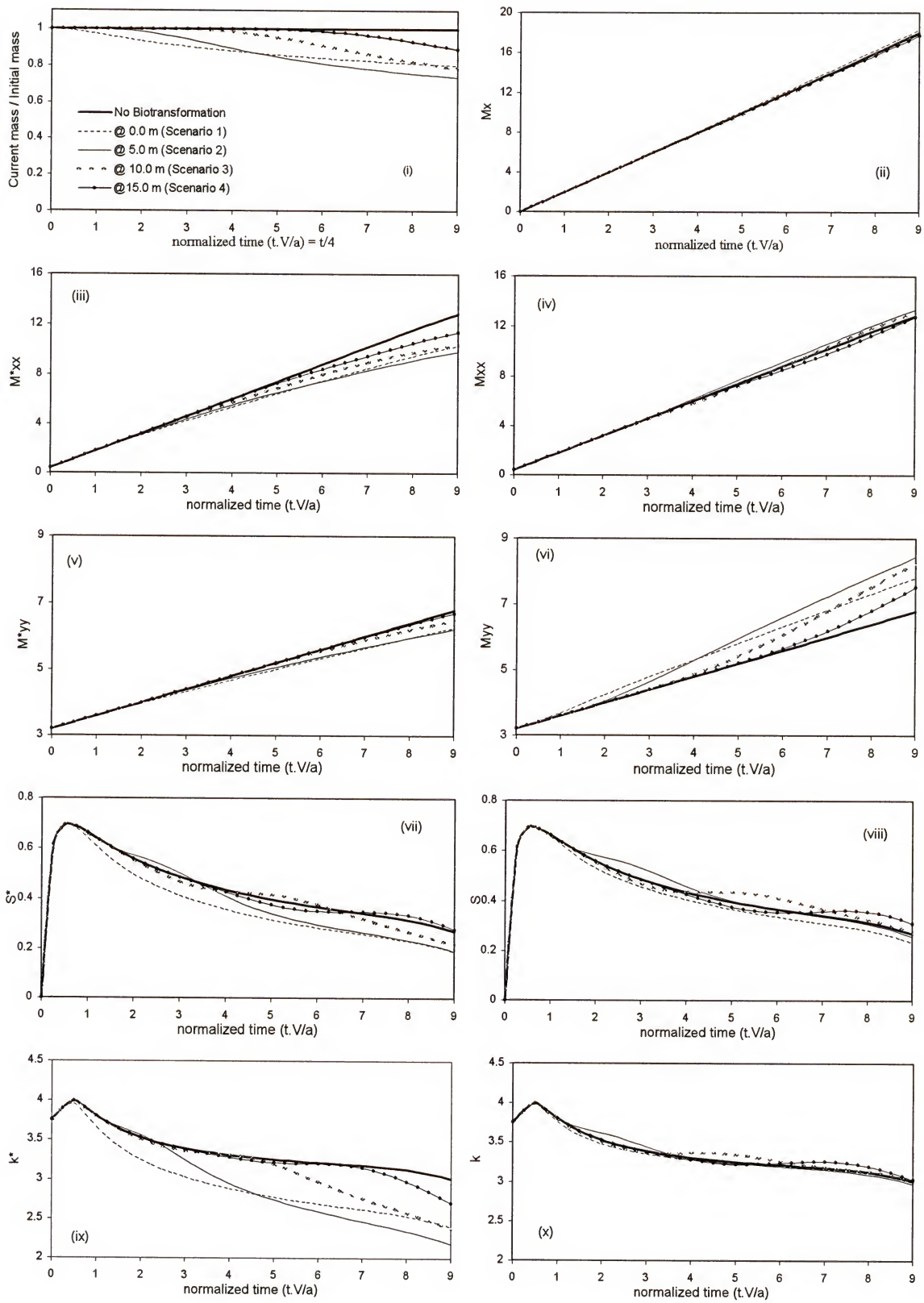


Figure 7-3c Effect of 1 well position on Cr(VI) plume's spatial moments for case 1.

scenarios; therefore, when the Cr(VI) plume migrates into the remediation area in scenario 2, it encounters a developed plume of the nutrient and the electron donor. However, when the remediation well was placed further away from the location of the contaminant initial release (scenarios 3 and 4), less Cr(VI) reduction was observed. This is because the Cr(VI) plume needed more time to reach the remediation area in these two scenarios [Figure 7-3c(i)].

Figure 7-3c(ii) illustrates the first spatial moment of the Cr(VI) plume (centroid of the plume) for the first four scenarios. The reduction in Cr(VI) concentrations using one injection well was not enough to affect the position of the plume centroid as characterized through classic moment analysis. Similarly, minor effects on the longitudinal dispersion, due to the change in the injection well position, were noted among the scenarios [Figure 7-3c(iv)]. However, when the initial Cr(VI) mass is used to normalize the second moment (refer to equations 6-2 to 6-4), the effects of the well position become more evident [Figure 7-3c(iii)]. Furthermore, when the injection well is placed 5 m downgradient from the position of the initial release of the contaminant zone (scenario 2), more Cr(VI) mass is biotransformed and, therefore, longitudinal dispersion decreases [Figure 7-3c(iii)].

An increase in the transverse dispersion is noticed when the current Cr(VI) mass is used to normalize the second moment [Figure 7-3c(vi)]. This occurs because one remediation well increases biotransformation at the trailing and leading edges of the Cr(VI) plume more than at lateral edges. However, the opposite is observed for transverse moments normalized with the initial Cr(VI) mass [Figure 7-3c(v)]. The closer the injection well to contaminant initial position, the greater the effect on the dispersion

[Figure 7-3c(v)]. The apparent transverse dispersion is less sensitive to the changes in the Cr(VI) mass than the apparent longitudinal dispersion [Figures 7-3c(iii, iv, v, and vi)].

The effects of using one remediation well on the skewness and peakness of the Cr(VI) plume are shown in Figures 7-3c(vii-x)]. It can be seen from these figures that in scenario 1 the effect on the skewness and peakness occurred early. However, for the other three scenarios, the effect is observed when the Cr(VI) plume meets the nutrient and the electron donor plumes. For scenarios 2-4, the skewness follows that of the case of “no biotransformation” until the Cr(VI) plume enters the active remediation area, where Cr(VI) reduction occurs on the leading edge of the plume. This induces a reduction in skewness values. For that reason, the skewness in scenario 1 is less than the case of “no biotransformation” at all times [Figure 7-3c(vii)]. As the Cr(VI) plume passes well positions in scenarios 2-4, Cr(VI) reduction is induced at the trailing edge, which induces skewness to increase again (compare scenarios 2-4 with the “no biotransformation” case in Figures 7-3c(vii and viii)). Once the Cr(VI) plume moves beyond the remediation area, microbial activities decrease and skewness decreases, as a result of dispersion to a zero value that characterizes the Gaussian distribution of the contaminant plume (scenarios 2 and 3). Similar effects on the peakness are noticed [Figures 7-3c(ix and x)]; however, peakness approaches a value of three that also characterizes Gaussian distribution.

Figure 7-3d illustrates the spatial moments of the concentration distribution of the microbial biomass. As mentioned before, bacteria only grow where all three solutes (electron donor, electron acceptor and nutrient) exist. Therefore, microbial growth occurs early in scenario 1 and much later in other scenarios depending on the time at which Cr(VI) plume reaches the active remediation area [Figure 7-3d(i)].

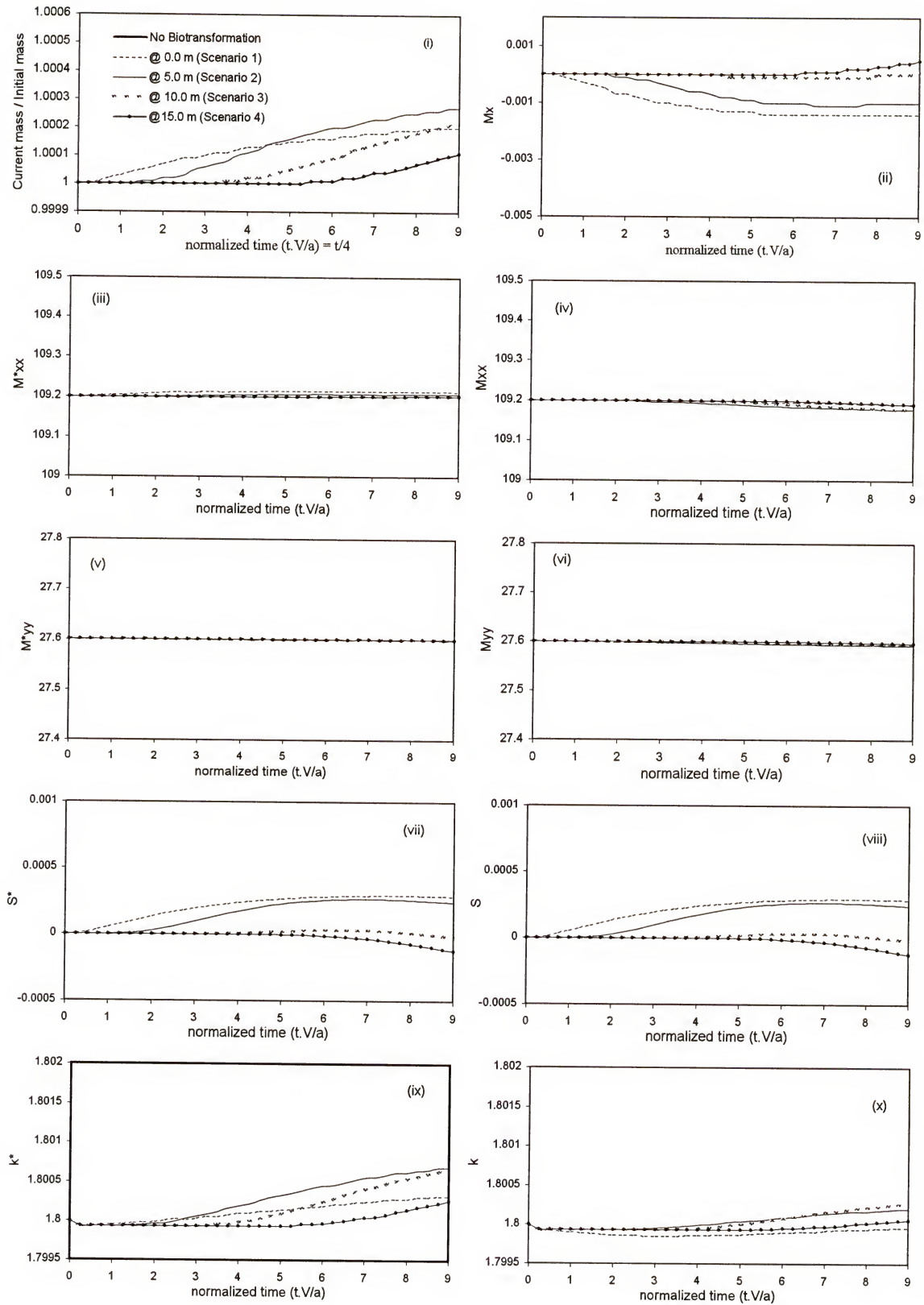


Figure 7-3d Effect of 1 well position on biomass spatial moments for case 1.

More biomass exists after 36 days in scenario 2 than in scenario 1 [Figure 7-3d(i)]. Furthermore, because the contact time between the three solutes was the smallest in scenario 4, biomass increase was the least of all four scenarios.

Figure 7-3d(ii) reveals how the centroid of bacterial mass changed with time between the four scenarios. The position of the centroid at any time is referenced to its initial position, which is the centroid of the aquifer (recall that the initial biomass distribution was assumed to be uniform). As bacteria grow near and immediately downgradient from the injection wells, the biomass centroid shifts towards the injection area. Therefore, a negative shift is noticed in scenarios 1 and 2 because injection wells are located upgradient of the aquifer centroid; furthermore, because the injection well in scenario 1 is placed at further distance from the center of the aquifer, the shift is more negative than with scenario 2. Similarly, a shift in the centroid of biomass can be explained for scenarios 3 and 4 [Figure 7-3d(ii)], however, this shift is positive.

As can be seen from Figures 7-3d(iii-vi), minor effects on the biomass dispersion are observed. Two reasons explain the apparent insensitivity: 1) the total change in the biomass in the system is very small (max 0.025%) [Figure 7-3c(i)]; therefore, the net change in the biomass in the system was not enough to affect the dispersion values of the biomass distribution; and 2) the initial biomass distribution was initially characterized by a large dispersion value (as it was assumed to be uniformly distributed everywhere in the aquifer); thus, any small change in biomass is not likely to manifest itself in a significant change in biomass dispersion.

Obvious effects on the skewness values are noticed in Figures 7-3d(vii and viii). These figures clearly show that when the injection well in scenarios 1 and 2 is placed

upgradient from the center of the aquifer (initial centroid of biomass distribution), biomass concentrations increase at well position (Figure 7-3b) and, therefore, skewness increases. Opposite effects on the skewness are noticed in scenarios 3 and 4 [Figures 7-3d(vii and viii)].

Peakness values of the biomass distribution are given in Figures 7-3d(ix and x). Because more bacterial growth is observed in scenario 2 [see Figures 7-3b and 7-3d(i)], peakness values of this scenario are larger than the other three scenarios. Although the total increase in the biomass in the aquifer at the end of the simulation (after 36 days) is almost the same in scenarios 1 and 3 [Figure 7-3d(i)], the peakness value of the biomass distribution at the same time is greater in scenario 3 than it is in scenario 1. This is because the active remediation area (contact area between all three solutes) in scenario 3 is smaller than that in scenario 1 [Figure 7-2a]. As a result, biomass spreads over a smaller area in the aquifer after 36 days [Figure 7-3b]. Combining this with the fact that the total increase in biomass of scenario 3 equals that of scenario 1 at late time [Figure 7-3d(i)] explains the larger biomass peakness that is observed at late time in scenario 3 [Figures 7-3d(ix and x)].

In order to introduce a more practical evaluation of the remediation scenarios, the term bioremediation efficiency (η) is introduced. This term denotes the ratio of the total mass of Cr(VI) reduced at the end of the simulation (36 days) to the initial mass released [Table 7-1]. Confirming previous discussion, using one injection well 5 m downgradient from the contaminant zone (scenario 2) produced the highest bioremediation efficiency (26%). On the other hand, when the injection well is placed 15 m downgradient of the contaminant zone (scenario 4) more than 50% reduction in the efficiency (11%) is noted.

Strategic selection of the electron donor and nutrient well position is important as it affects the bioremediation efficiency of the system.

Table 7-1 Percentage of Cr(VI) biotransformed mass (bioremediation efficiency η) and increase in biomass (η_b) for all 36 scenarios after 36 days.

		Case 1			Case 2			Case 3		
		#	η	η_b	#	η	η_b	#	η	η_b
One well	at 0.0 m	1	19.84	0.02	13	39.65	0.04	25	40.22	0.04
	at 5.0 m	2	26.38	0.03	14	47.65	0.05	26	45.55	0.05
	at 10.0 m	3	21.37	0.02	15	38.49	0.04	27	32.00	0.03
	at 15.0 m	4	10.97	0.01	16	20.30	0.02	28	13.20	0.01
Three wells	at 0.0 m	5	33.24	0.03	17	65.04	0.07	29	80.42	0.08
	at 5.0 m	6	45.73	0.05	18	80.12	0.08	30	51.48	0.05
	at 10.0 m	7	37.52	0.04	19	67.01	0.07	31	35.13	0.04
	at 15.0 m	8	19.31	0.02	20	35.85	0.04	32	13.96	0.01
Line source	at 0.0 m	9	78.78	0.08	21	92.46	0.10	33	56.77	0.08
	at 5.0 m	10	96.52	0.10	22	99.15	0.10	34	65.50	0.07
	at 10.0 m	11	90.31	0.09	23	96.03	0.10	35	43.40	0.05
	at 15.0 m	12	58.01	0.06	24	69.82	0.07	36	19.65	0.02

The previous discussion of scenarios 1-4 clearly confirms that Cr(VI) reduction occurs when the plume moves into the remediation area (electron donor and nutrient plumes). Biotransformation rates largely depend on the concentration of all three solutes. For that reason, placing the injection well downstream from the contaminant source zone delays merging of all plumes. This enables electron donor and nutrient concentration to increase in the aquifer and, thus, biotransformation rates increase. However, placing the injection wells further downgradient from the contaminant plume can result in the spreading of the contaminant in the transverse direction before it intersects with the remediation area, which can result in a reduction of the bioremediation efficiency. In addition, placing the injection far from the location of the contaminant source would

increase the time before all plumes intersect with each other. As a result, not only does remediation efficiency decrease in this case, but also remediation time increases.

In conclusion, injection wells should not be situated too close to the contaminant zone as some of the contaminant mass could escape from the remediation area before nutrient and electron donor concentrations are able to reach effective levels; nor the wells should be situated too far from the contaminant source as the bioremediation area will not be large enough to capture the dispersed contaminant plume.

7.3.2. Three Wells Treatment

As observed in scenarios 1-4, using one electron donor and nutrient injection well enhances the biotransformation at the leading and trailing edges of the Cr(VI) plume with minimal effects on its lateral edges. For that reason, two more wells were added in scenarios 5-8. The positions of these two wells (4 m apart in the transverse direction from the well used in scenarios 1-4, Figure 7-1c) were chosen to enhance Cr(VI) reduction at the lateral edges of the plume. Although the injection rate from each well in scenarios 5-8 is the same as that of scenarios 1-4, the total injected mass of the nutrient and electron donor is increased due to the increase in the number of wells [Figures 7-2a(iii and iv)]. However, the total reduced mass of the Cr(VI) in scenarios 5-8 is not expected to be three times that of scenarios 1-4. The reason for this is that the two new wells are placed in relatively low Cr(VI) concentrations regions (lateral edges of the Cr(VI) plume). As a result, biotransformation rates at these regions are less than those at the position of the central well.

Figure 7-4a shows the Cr(VI) concentrations after 10 and 35 days for scenarios 5-8. Similar to scenarios 1-4, reduction in Cr(VI) concentrations at the leading and trailing edges of the plume is noticed due to the injection of the electron donor and the nutrient

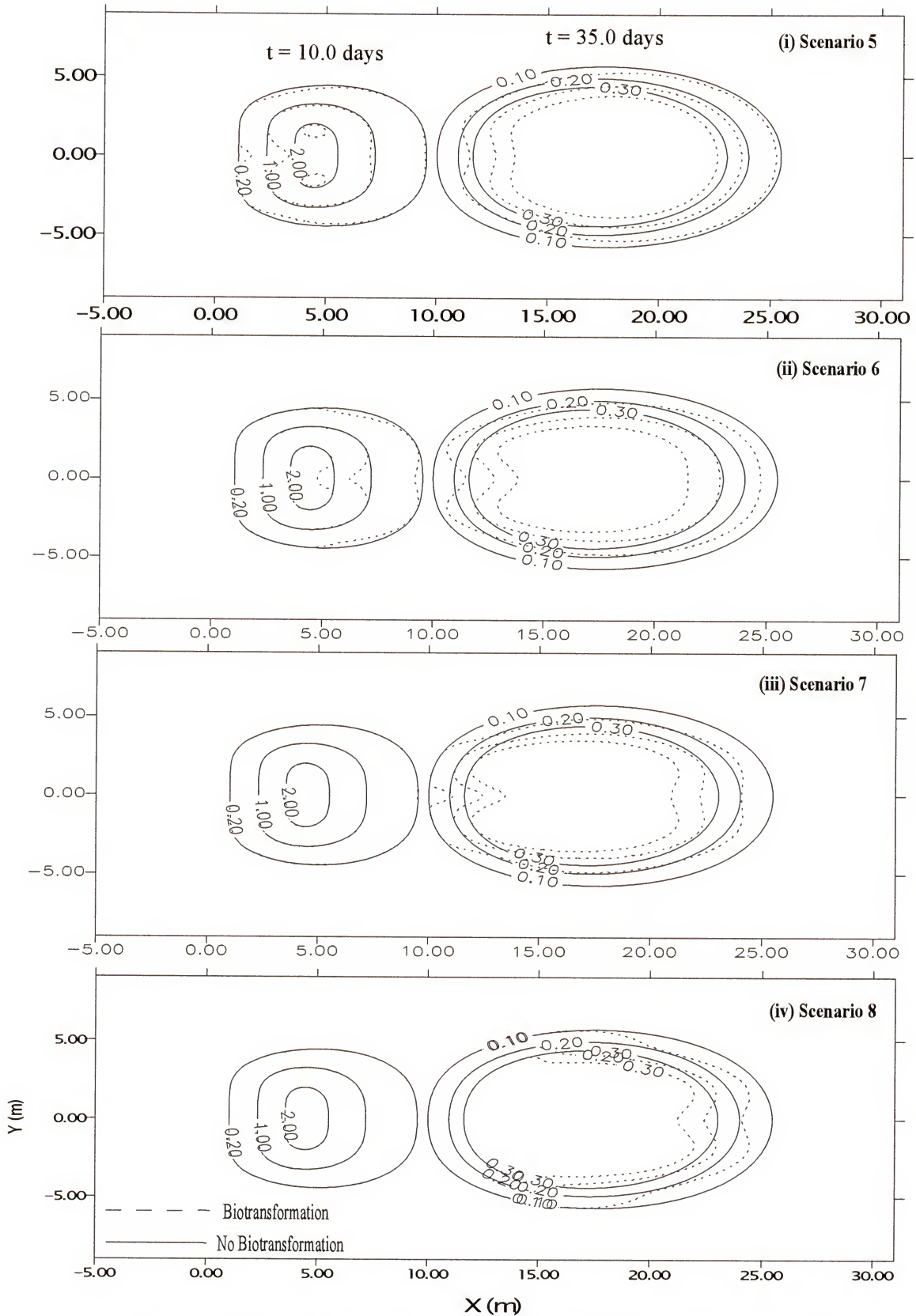


Figure 4a Effect of three wells location on the Cr(VI) concentrations for case 1. (i) at the center of the initial plume, (ii) at 5 m, (iii) at 10 m and (iv) at 15 m.

from the center well. The same figure shows clear evidence of Cr(VI) reduction at the lateral edges of the plume in all four scenarios due to the two additional injection wells (compare Figures 7-4a and 7-3a). Nevertheless, the position of the three wells significantly influences the total mass of metal biotransformed and remediation efficiency (see Table 7-1). Similar to the conclusion obtained from scenarios 1-4, placing the three wells at the center of the contaminant source (scenario 5) was not the best remediation scenario among scenarios 5-8 [Figure 7-4a(i)].

Although scenarios 6 and 7 produce similar remediation effects on the front edge of the Cr(VI) plume after 35 days, placing the three injection wells closer to the contaminant zone in scenario 6 results in more reduction at the trailing edge of the Cr(VI) plume [Figures 7-4a(ii and iii)]. On the other hand, when the three injection wells were placed 15 m downgradient of the contaminant zone (scenario 8), no Cr(VI) reduction is observed at the trailing edge of the Cr(VI) plume and there is limited improvement at the leading edge compared to scenario 7 [Figure 7-4a(iv)]. Therefore, scenario 6 presents the best scenario for Cr(VI) reduction among these four scenarios (5-8). It should be noted that for scenario 8, 35 days is not enough time for the trailing edge of the Cr(VI) plume to enter the treatment zone. Had the numerical simulation been conducted for a longer duration and beyond the compliance boundaries defined here, greater treatment efficiency would have been seen.

Similar conclusions to those drawn from scenarios 1-4 can be obtained from Table 7-1. That is, scenario 6 with 46% bioremediation efficiency is the best when using three injection wells, while scenario 8 (19%) is the worst. Although scenario 5, with 33% bioremediation efficiency, is not the best scenario among scenarios (5-8), it produced

higher remediation efficiency than all first four scenarios (1-4), where one well injection well is used (Table 7-1). Using three injection wells is undoubtedly more expensive than using one injection well; however, above ground conditions may preclude placement of injection wells downgradient from the contaminant source. Thus, using three wells near the initial contaminant zone, although it does not produce the higher bioremediation efficiency, can present a potential solution for such case.

Similar to Figure 7-3b, Figure 7-4b illustrates the biomass concentration for scenarios 5-8 after 10 and 35 days. This figure clearly emphasizes the fact that biotransformation activities occur only at regions where all three solutes, as well as bacteria, exist. In addition to the points discussed before with Figure 7-3b, this Figure (7-4b) shows that, although injection rates are equal between wells, microbial growth rate around the central injection well is larger than that around the other two wells. The primary explanation for this behavior is that concentrations of Cr(VI), a limiting growth substrate, are less around the two lateral wells (due to transverse dispersion) than those around the central well. Longitudinal dispersion, on the other hand, causes reduction in Cr(VI) concentration in the X-direction and, therefore, the maximum value of biomass concentration in scenario 8 is less than that of scenario 5 [Figure 7-4b(vi and ii)].

Figure 7-4c displays the spatial moments of the Cr(VI) plume. As expected, using three wells increases the total mass of metal reduced [Figure 7-4c(i)] as compared to the first four scenarios (1-4) where one injection well was used [Figure 7-3c(i)]. In general, the effect of changing the wells positions in scenarios 5-8 on the spatial moments [Figure 7-4c] is similar to that noted in scenarios 1-4 [Figure 7-3c]; however, the effects are amplified. However, two additional observations are worth noting here.

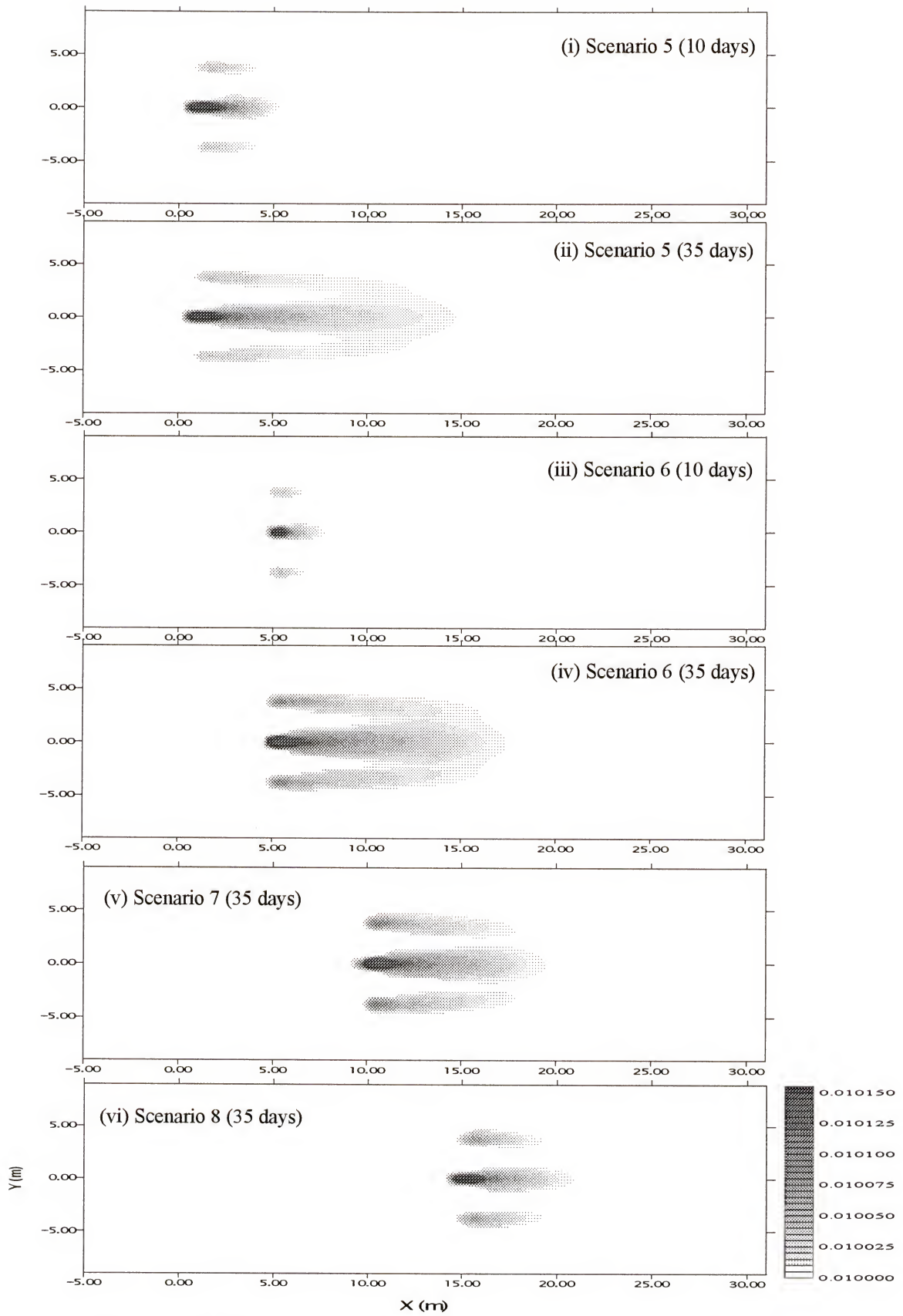


Figure 7-4b Effect of three wells location on biomass concentrations for case 1.

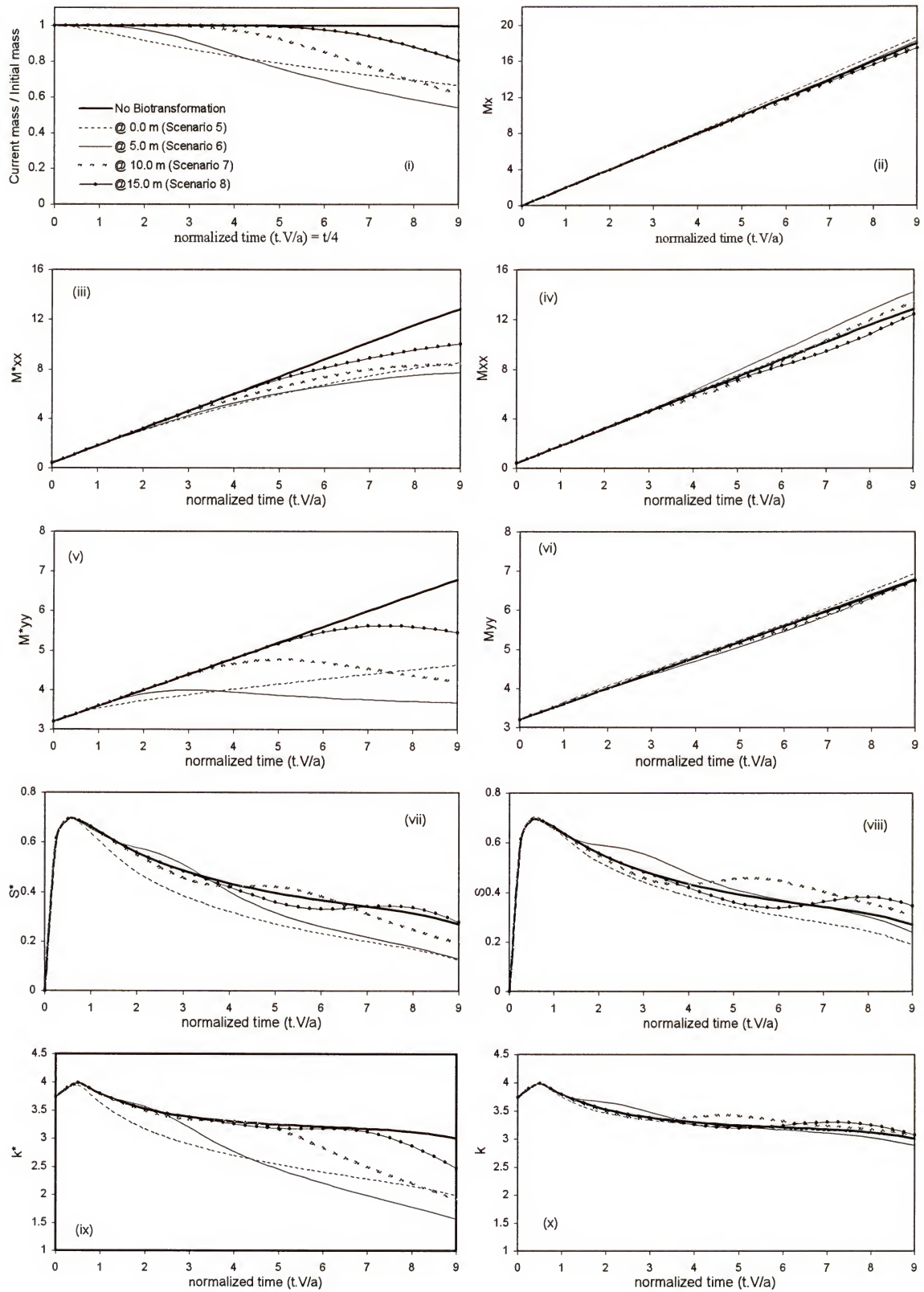


Figure 7-4c Effect of 3 well positions on Cr(VI) plume's spatial moments for case 1.

The first is that using three wells enhances the biotransformation at the lateral edges of the Cr(VI) plume and, consequently, slight changes in the longitudinal dispersion are noted [Figure 7-4c(iv)]. Results from scenario 6 show that because more reduction occurs at the trailing edge of the plume [Figure 7-4a(ii)], longitudinal dispersion is increased compared to the case of “no biotransformation” [Figure 7-4c(iv)].

Conversely, the same figure shows that when more reduction occurs at the leading edge of the Cr(VI) plume in scenario 8 [Figure 7-4a(iv)], dispersion decreases. Finally, in scenario 7, where reduction occurs at both the trailing and leading edges of the Cr(VI) plume [Figure 7-4a(iii)], minor effects on the rate of dispersion are observed [Figure 7-4c(iv)]. The second observation is that differences between the values of the transverse dispersion among these four scenarios (5-8) are reduced [Figure 7-4c(vi)] compared to the first four scenarios. Reduction in Cr(VI) concentrations at the lateral edges (caused by the additional two lateral injection wells), together with the reduction in the central region (caused by the central injection well), generate an approximately uniform reduction effect on the Cr(VI) plume in the transverse direction.

Figure 7-4d illustrates the spatial moments of the biomass concentration distribution. This figure supports the same conclusions obtained from Figure 7-3d. However, using three wells amplifies differences between spatial moments generated under the four scenarios.

7.3.3. Line Source Treatment

Although using three injection wells provides more bioremediation than using one injection well, the maximum remediation efficiency obtained is only 46% (scenario 6, Table 7-1). In order to attain additional bioremediation, a line source injection of the electron donor and the nutrient is used in scenarios 9-12 [Figure 7-1d].

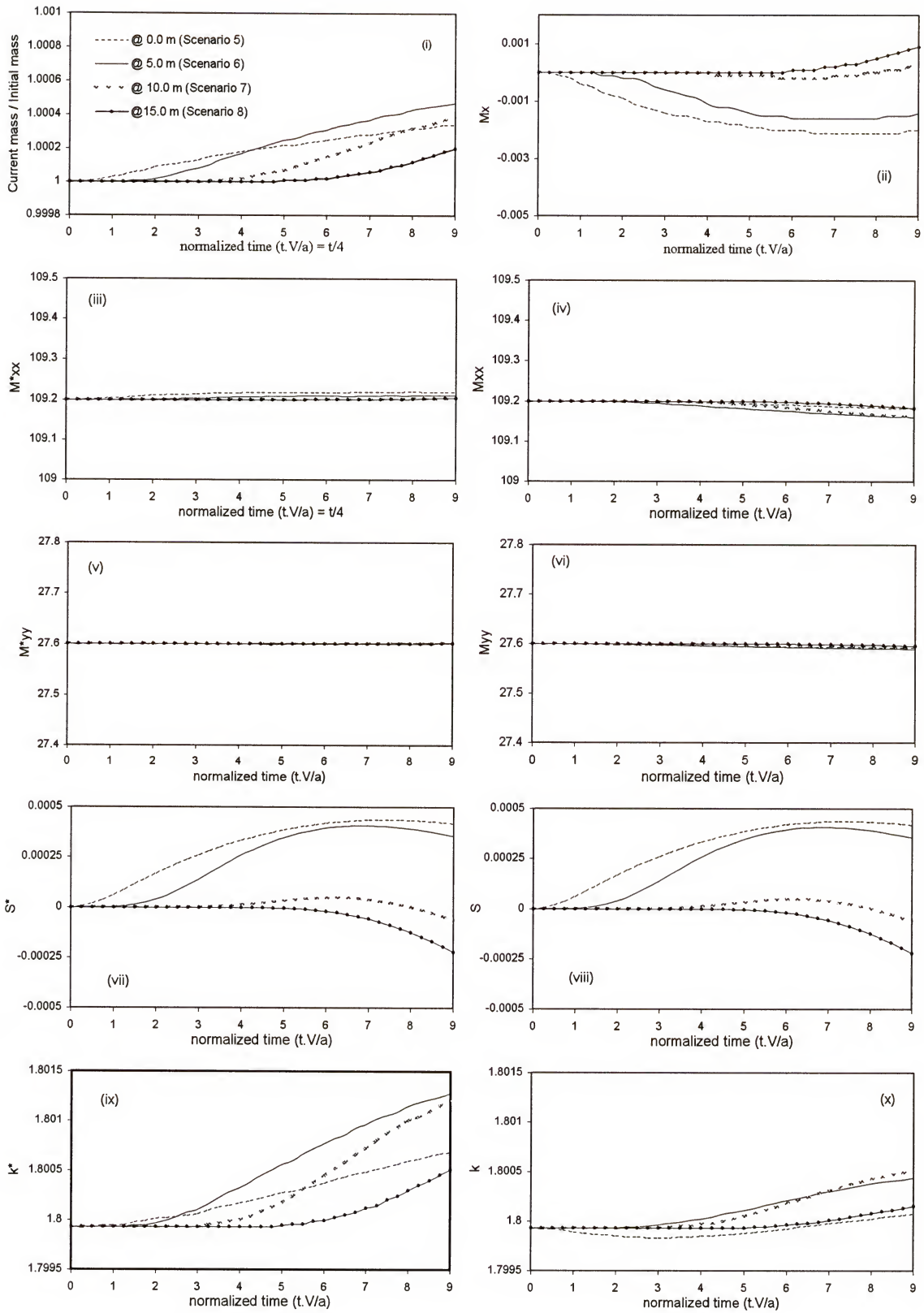


Figure 7-4d Effect of 3 well positions on biomass spatial moments for case 1.

Similar to the previous 8 scenarios, the injection rate from each node is maintained at 0.5 mg/node/day. In this case, the number of injection nodes is increased to 40 nodes, creating a line source of 8 m length in the Y-direction [Figure 7-1d]. Therefore, the injection rate is assumed to be 2.5 mg/m/day. Usage of the line source for a nutrient and an electron donor produces a more uniform introduction of these two solutes in the aquifer [Figure 7-2(v and vi)].

Figure 7-5a presents Cr(VI) concentration contours for scenarios 9-12 after 10 and 35 days. The figure shows enhanced reduction in Cr(VI) concentrations in all four scenarios (9-12) compared to the corresponding previous ones (1-4 and 5-8). When the injection line of the electron donor and nutrient is placed at the center of the contaminant initial position (scenario 9), the greatest Cr(VI) reduction is obtained at the trailing edge of its plume [Figure 7-5a(i)]. When the line source is situated exactly above the contaminant source, some of the Cr(VI) mass (dotted concentration lines in Figure 7-5a(i)) escaped from the remediation area which was not formed yet [Figure 7-2a(v and vi)]. Thus, this Cr(VI) mass, associated with the leading edge of the plume, will remain in the aquifer and will not undergo any biotransformation. The bioremediation efficiency obtained from this scenario (9) is 79%, which is more than that of the previous 8 scenarios.

When the line source is placed 5 m downgradient of the location of the contaminant initial release (scenario 10), the bioremediation efficiency increased to 96.5%; i.e. almost all of the Cr(VI) mass, released at $t = 0$, is reduced. It is also clear from Figure 7-5a(ii), that by day 35, nearly complete remediation has occurred. Placing the line source 10 m downstream

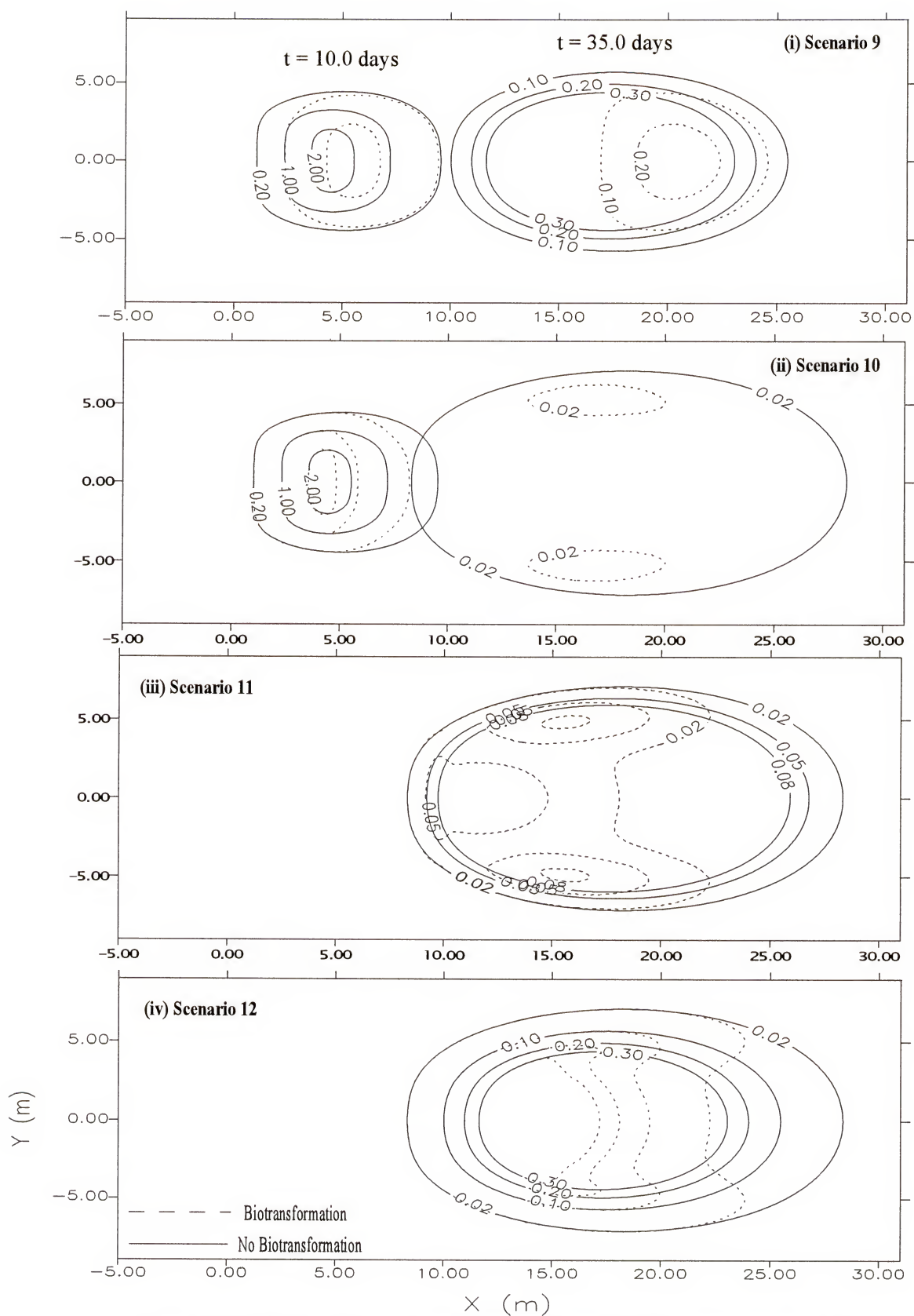


Figure 7-5a Effect of line source location on the Cr(VI) concentrations for case 1. (i) at the center of the initial plume, (ii) at 5 m, (iii) at 10 m and (iv) at 15 m.

from the contaminant source (scenario 11), caused most of Cr(VI) mass to disappear after 35 days (90.3%, Table 7-1). However, as explained before, no effect on the Cr(VI) concentration at $t = 10$ days is noted. Finally, scenario 12 (with 58% bioremediation efficiency) presents less remediation efficiency compared to the other three scenarios (9-11). More time is required for this scenario to present comparable results to the other three scenarios (9-11). However, it should be mentioned that scenarios 9 and 12, despite their incompatible effectiveness to scenarios 10 and 11, generated more bioremediation than the first 8 scenarios. These two scenarios could be used when there are aboveground restrictions that preclude the application of scenario 10 or 11. Scenario 12 may be a good solution when the compliance boundary, at which Cr(VI) concentrations should not exceed certain levels, lies further downgradient in the aquifer (beyond the boundaries of the assumed domain); however, care must be taken to introduce enough nutrient and electron donor to reduce the chromium plume.

Figure 7-5b shows the biomass concentration after 10 and 35 days for scenarios 9-12. This figure also reflects the zone of biological active areas in aquifer, i.e. the remediation area at which all three solutes intersects. Large increases in the areas of maximum bacterial concentration were observed compared to previous scenarios [compare Figure 7-5b with 7-3b and 7-4b]. A more uniform, plume-shaped, distribution of the bacterial population can be seen in Figure [7-5b]. This is due the uniform injection of the electron donor and nutrient [Figure 7-2a(v and vi)].

Figure 7-5c presents spatial moments of the Cr(VI) plume for scenarios 9-12. As mentioned before, Figure 7-5c(i) reveals that more than 95% of the Cr(VI) initial mass is biotransformed when the line source is placed 5 m downstream from the contaminant

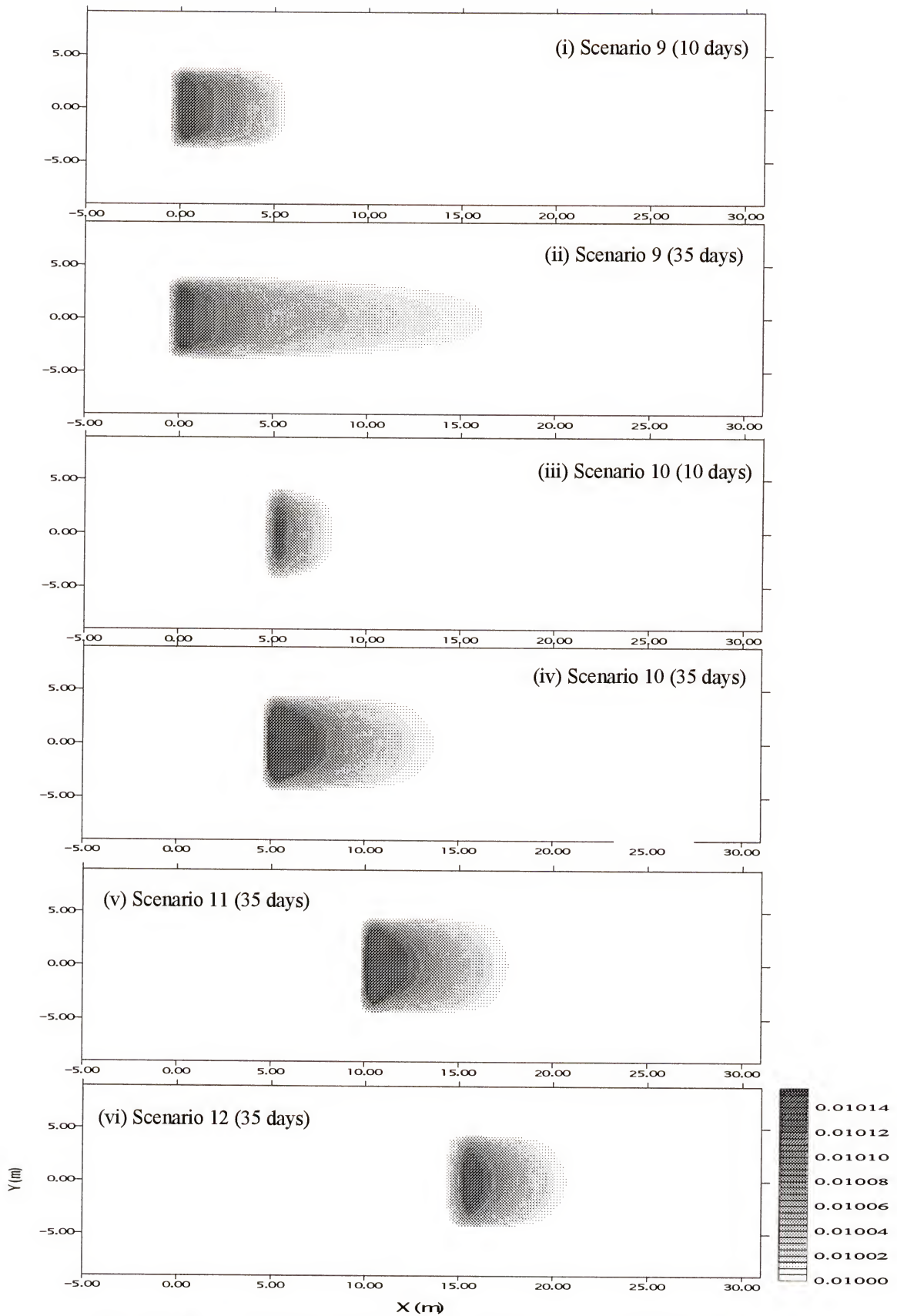


Figure 7-5b Effect of line source location on biomass concentrations for case 1.

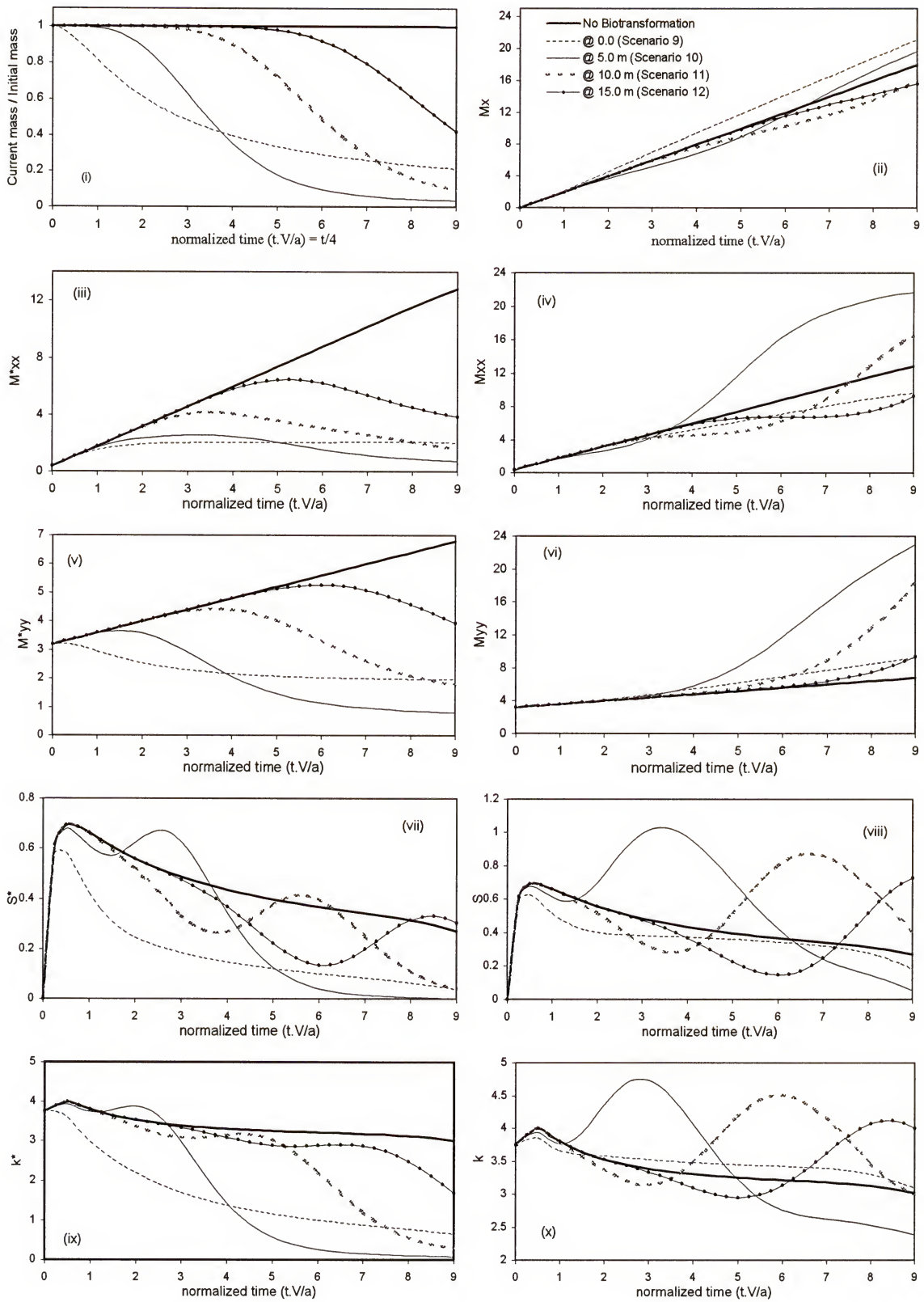


Figure 7-5c Effect of line source position on Cr(VI) plume's spatial moments for case 1.

initial release (scenario 10). The same figure also illustrates that scenario 11 produces reduction results comparable to those of scenario 10; however, Cr(VI) reduction occurred sooner in scenario 10. An additional observation from Figure 7-5c(i) is that the biotransformation rate decreases dramatically as the Cr(VI) concentration decrease. Therefore, the removal of the last 10% of the Cr(VI) mass could require more time than that required to remove the first 90%. Another important observation is that the biotransformation rate in scenarios 10-12 accelerates faster than that of scenario 9. The reason behind that, as mentioned before, is that in scenario 9 when Cr(VI) concentration is high early in the simulation, nutrient and electron donor concentrations are still low. On the other hand, by the time nutrient and electron donor concentrations have increased around the contaminant source (later in the simulation) (refer to layout of scenario 9 Figure 7-1d), the Cr(VI) plume has already migrated from the treatment zone. Therefore, one of the three solutes always has low concentrations and thus acts as a limiting substrate in the areas where all three solutes intersect. On the other hand, in the other three scenarios, the Cr(VI) plume moves into a developed nutrient and electron donor plumes. Therefore, all three solutes intersect with each other with relatively high concentrations, causing biotransformation rates to be high. This discussion explains the main advantages of placing the injection well(s) sufficiently downgradient of the contaminant source.

When the line source is placed exactly at the position of the initial release of the contaminant, larger reductions in Cr(VI) concentrations occur at the trailing edge of the plume compared to that of the leading edge [Figure 7-5a(i)]. Therefore, a shift in the Cr(VI) plume centroid to the right is noticed and, as a result, an increase in the first

moment of the Cr(VI) plume is observed as compared to the case of “no biotransformation” [Figure 7-5c(ii)]. On the other hand, the same figure implies that because more reduction in the Cr(VI) concentrations occurred at the leading edge in scenarios 11 and 12 [Figure 7-5a(iii and iv)], a decrease in the first moment is observed. The Cr(VI) plume in scenario 10, however, experienced biotransformations at the leading edge at early simulation times and then at the trailing edge at later times. As a result, the first moment decreases at early times (as compared to the case of “no biotransformation”) and then increased at later times.

Figures 7-5c(iii) and (iv) present changes in the second longitudinal spatial moment of the Cr(VI) plume when normalized by the initial and current Cr(VI) mass, respectively (equation 6-2). As discussed in chapter 6, using the current mass reveals the mathematical characteristics of the plume (in this case the hydrodynamic dispersion) [Figure 7-5c(iv)]. On the other hand, using the initial mass explains the effect of biotransformation [Figure 7-5c(iii)]. Obviously, the two figures are dissimilar. In Figure 7-5c(iii) the biotransformation effect reduced the second longitudinal moment in scenario 10 dramatically because the Cr(VI) mass was reduced dramatically [Figure 7-5c(i)]. The decrease in the second longitudinal moment in the other three scenarios, compared to the “no biotransformation” case, is less than that of scenario 10 (depending on the reduction rate in Cr(VI) mass). Figure 7-5c(iv) implies that dispersion in scenario 10 increases compared to the case of “no biotransformation”. This is because Cr(VI) mass is almost totally removed from the aquifer except few separate parts [Figure (7-5a(ii))].

In scenario 9, dispersion initially decreases relative to the case of “no biotransformation” because reduction occurs to the trailing edge at that time. It then

increases with a similar rate to that of the “no biotransformation” case at later times when the plume escapes from the remediation area. In scenarios 11 and 12, longitudinal dispersion initially decreases as the leading edge of the Cr(VI) plume intersects the remediation area, and then increases as reduction proceeds towards the trailing edge of the plume [Figure 7-5c(iv)]. Changes in the transverse dispersion [Figure 7-5c(vi)] occur due to the fact that reduction is greater at the center of the plume than that at the lateral edges of the plume (because concentrations of all solutes are higher in the middle of the plume). Therefore, transverse dispersion values increase for all four scenarios compared to the case of “no biotransformation”. However, the differences between the transverse dispersion of four scenarios depend on the Cr(VI) reduction rates in different sections of the aquifer.

Figures 7-5c(vii and viii) clearly show the effect of the position of the line source on the skewness values of the Cr(VI) plume. That is, skewness increase (compared to the “no biotransformation” case) when the Cr(VI) plume passes through the zone of active remediation, and decreases elsewhere, approaching a zero value. This denotes a Gaussian distribution. It is clear from that figure then that the Cr(VI) plume migrates into the remediation area early in scenario 10 and very late in scenario 12. Additionally, the same figure indicates that in scenario 9, the Cr(VI) plume did not pass through the remediation zone because both the electron donor and nutrient were injected at the same location as the Cr(VI) source. As a result, reduction in the Cr(VI) concentrations continuously occurred at the trailing edge and, therefore, a continuous reduction in the skewness values, compared to the case of “no biotransformation”, is noted [Figure 7-5c(vii and viii)]. When the line source is placed on the initial contaminant source, reduction in the

Cr(VI) concentration in the trailing edge is more than the leading edge. Therefore, skewness in this case is less than in the case of “no biotransformation”. In the remaining three scenarios (10-12), skewness matches the case of “no biotransformation” prior to the arrival of the Cr(VI) plume into the remediation area. However, once the Cr(VI) plume reaches the remediation zone, biotransformation occurs from the leading edge of the plume, which produces a decrease in skewness. Conversely, as the Cr(VI) plume passes the injection well, biotransformation begins to occur at the trailing end, which increases skewness. Yet, once the plume has migrated beyond the well, Cr(VI) reduction diminishes; consequently, skewness decreases again [Figures 7-5c(vii and viii)]. Similarly, changes in peakness values with time can be explained [Figure 7-5c(ix and x)].

Due to an increase in the injection mass of the electron donor and the nutrient, microorganisms developed more biomass in scenarios 9-12 [Figure 7-5d(i)]. In these four scenarios, dispersion in the X-direction decreased compared to previous scenarios (1-8) [Figure 7-5d(iii and iv)]. In addition, increases in the values of the skewness and peakness are also noticed [Figure 7-5d(vii-x)]. Figure 7-5d stresses the same conclusions obtained from Figures 7-3d and 7-4d; however, due to the increase in the injection rate of the electron donor and the nutrient, differences between the scenarios 9-12 are clearer than those obtained before.

7.4. Case 2

Another 12 scenarios (13-24) are used in this case in order to investigate the effect of increasing the injection rate of the nutrient and electron donor on the bioremediation efficiency. Numbers and positions of the wells in these new 12 scenarios are exactly the same as the first 12 scenarios used in case 1 [Figure 7-1b, c, and d]. However, the injection rate per each node is doubled to 1mg/node/day.

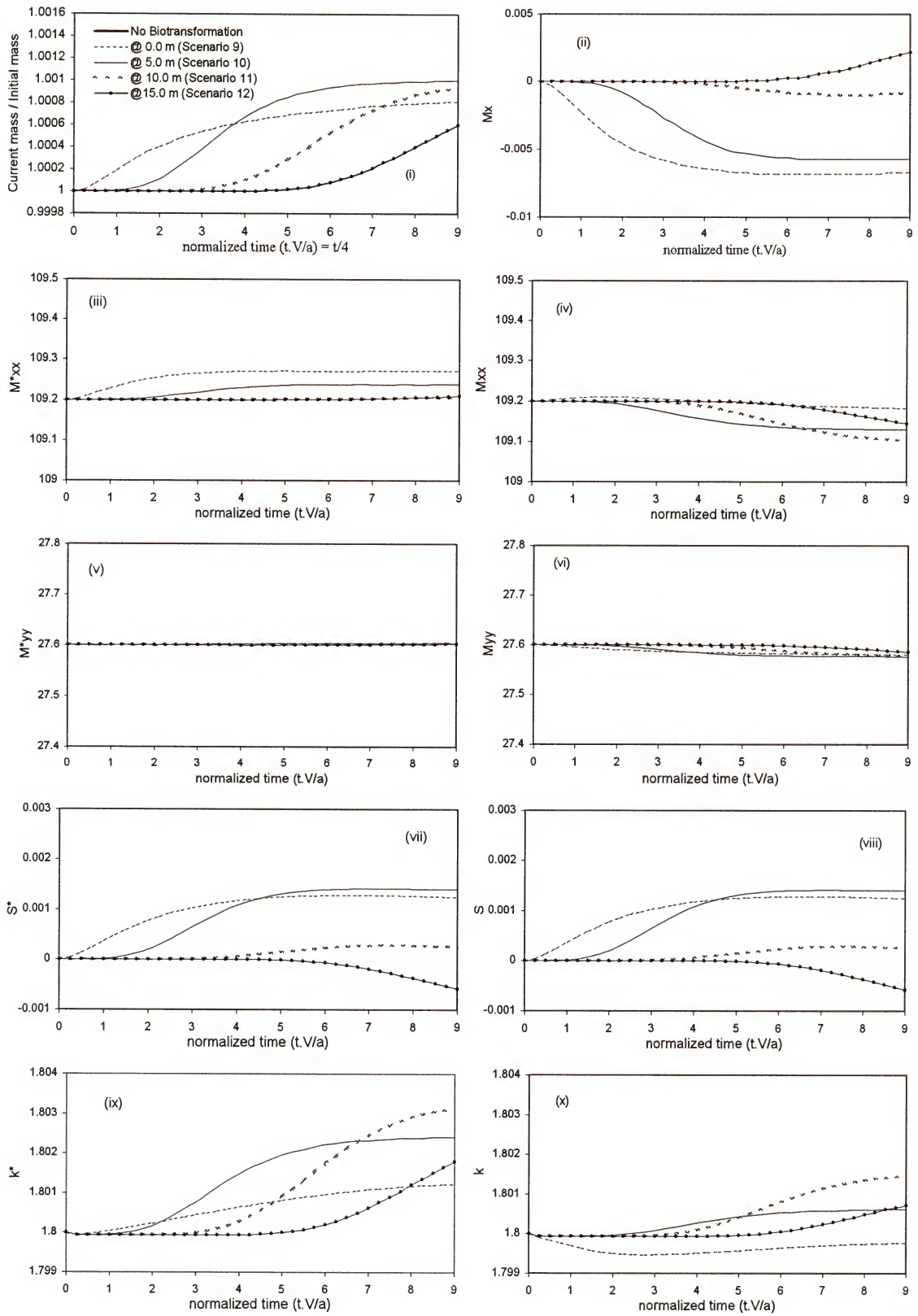


Figure 7-5d Effect of line source position on biomass spatial moments for case 1.

Therefore, the injection rate from each well in scenarios 13-20 is 5 mg/day and from each line source (simulated in scenarios 21-24) is 5 mg/m/day. Figure 7-2b shows the concentrations of the nutrient and the electron donor of scenarios 13, 17, and 21 at $t = 10$ and 35 days. Because injection rates were doubled, compared to case 1, nutrient and electron donor concentration values in Figure 7-2b are almost twice as much as the corresponding values in Figure 7-2a. Consequently, the remediation area in all 12 scenarios of case 2 is more rich with solutes that are essential to enhance remediation. Therefore, one should expect that remediation efficiencies (η) of scenarios 13-24 to be greater than those of scenarios 1-12 (Table 7-1). Thus, the purpose of the following discussion is to characterize the enhanced bioremediation.

7.4.1. One Well Treatment

Figure 7-6a represents Cr(VI) concentrations of the first four scenarios in case 2 (13-16). In this figure, unlike Figure 7-3a where Cr(VI) concentrations were compared to those of the case of “no biotransformation”, Cr(VI) concentrations of the different scenarios in case 2 are compared to the corresponding scenarios of case 1. This figure clearly shows the effect of increasing the injection rate in reducing the Cr(VI) concentrations at both time steps - regardless of the well position. For example, in Figure 7-6a(i), a comparison between Cr(VI) concentration lines of scenarios 1 and 13 is shown. This Figure demonstrates that scenario 13 provides better remediation than scenario 1.

Similarly, scenarios 14, 15, and 16 presents more reduction in Cr(VI) concentrations than scenarios 2, 3, and 4, respectively [Figure 7-6a]. Because only one injection well is used in each of the four scenarios, reductions in the Cr(VI) concentrations, although larger than those in case 1, still occur at both trailing and leading

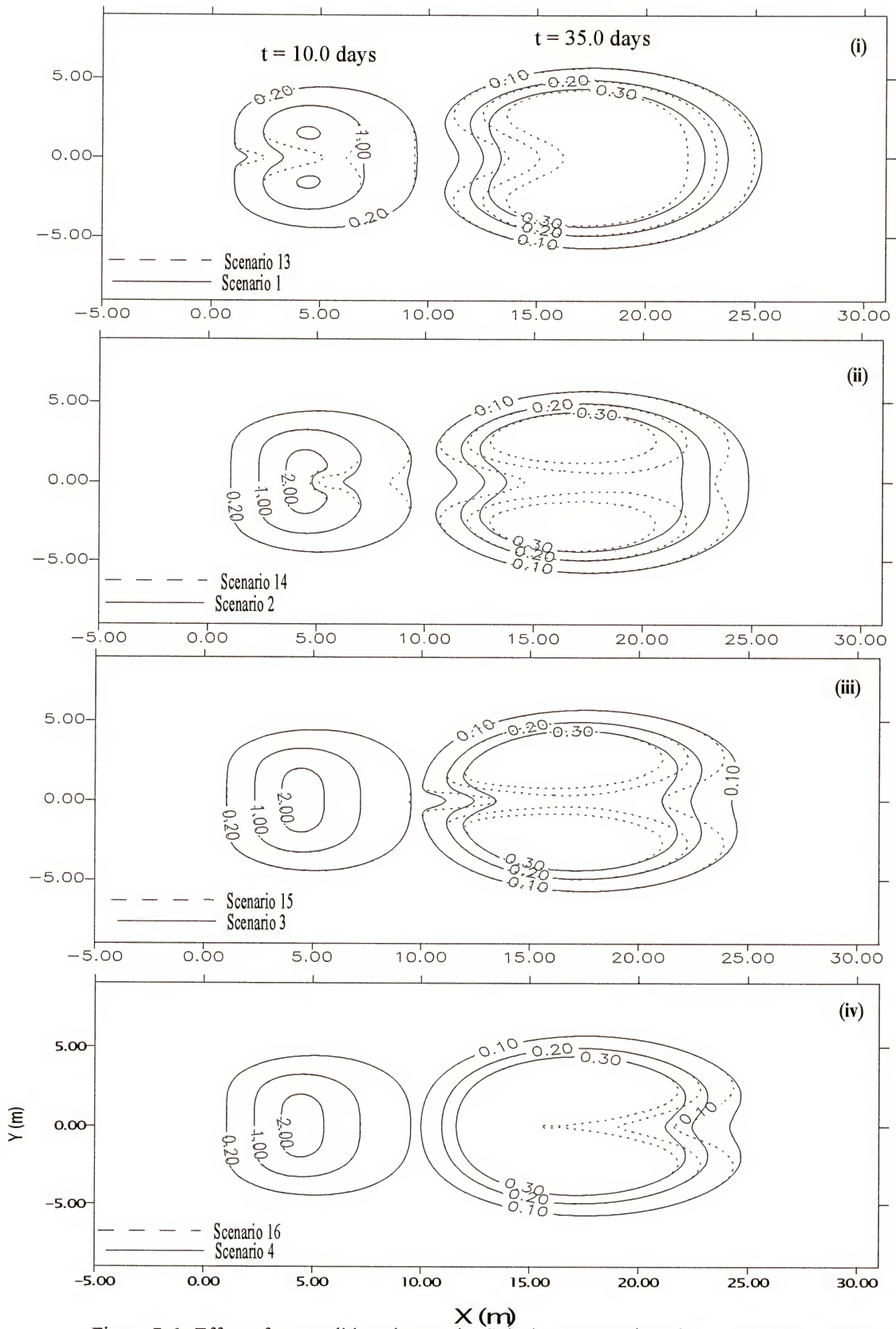


Figure 7-6a Effect of one well location on the Cr(VI) concentrations for case 2 compared to case 1.
 (i) at the center of the initial plume, (ii) at 5 m, (iii) at 10 m and (iv) at 15 m.

edges of the Cr(VI) plume (location of active remediation area). However, in scenarios 14 and 15, the increased injection rate produces Cr(VI) reductions that extended to the center of the Cr(VI) plume [Figures 7-6a(ii and iii)].

Figure 7-6a does not explicitly reveal the gain in the Cr(VI) reduced mass as a result of doubling the injection rate. Therefore, bioremediation efficiency is used to evaluate that gain. The gain in bioremediation efficiency (G) using scenarios from case 2 referenced to those from case 1 (equation 7-1) are given in Table 7-2.

$$G = \frac{\eta_{i+12} - \eta_i}{\eta_i} \times 100 \quad (7-1)$$

where i is the scenario number of case 1 (1 → 12).

Table 7-2 Percentage gained (G) in the bioremediation efficiency between cases 2 and 1 and the percentage loss (L) between cases 3 and 2.

		Case 2 Vs 1		Case 3 Vs 2	
		Scenarios	G	Scenarios	L
One Well	at 0.0 m	13 Vs 1	99.87	25 Vs 13	1.45
	at 5.0 m	14 Vs 2	80.61	26 Vs 14	-4.40
	at 10.0 m	15 Vs 3	80.12	27 Vs 15	-16.85
	at 15.0 m	16 Vs 4	85.09	28 Vs 16	-34.95
Three wells	at 0.0 m	17 Vs 5	95.65	29 Vs 17	23.65
	at 5.0 m	18 Vs 6	75.20	30 Vs 18	-35.75
	at 10.0 m	19 Vs 7	78.59	31 Vs 19	-47.57
	at 15.0 m	20 Vs 8	85.65	32 Vs 20	-61.05
Line source	at 0.0 m	21 Vs 9	17.36	33 Vs 21	-38.60
	at 5.0 m	22 Vs 10	2.72	34 Vs 22	-33.94
	at 10.0 m	23 Vs 11	6.32	35 Vs 23	-54.80
	at 15.0 m	24 Vs 12	20.35	36 Vs 24	-71.85

Doubling the injection rate in scenario 1 almost doubled the biotransformed Cr(VI) mass in scenario 13 and, therefore, doubled the bioremediation efficiency (Table

7-1). This is also clear in Table 7-2, as G equals almost 100%. On the other hand, scenarios 14, 15, and 16 showed less gain in the bioremediation efficiency. Scenarios 14 and 15 produced the smallest gain (G) among all four scenarios (Table 7-2). This suggests that wells located at 5 and 10 m (scenarios 2 and 3 in case 1) are more efficient in reducing Cr(VI) than those at 0 and 15 m (scenarios 1 and 4) and, therefore, less responsive to doubling the injection rates. Hence, any further increase in the injection rates is not expected to improve the remediation efficiency in these two scenarios. The maximum remediation efficiency among the 8 scenarios with one injection well is 48% (scenario 14). Therefore, in order to improve the bioremediation efficiency, increasing the number the wells would be one possible approach.

The bioremediation efficiency of scenario 16 (20%) remains the lowest among scenarios 13 to 16 (Table 7-1). However, the gain in remediation efficiency achieved in scenario 16 (85%, Table 7-2) is second to that of scenario 13. This occurred because the remediation area in scenario 13 was created in a relatively high Cr(VI) concentration region and, therefore, reduction rates were high. In scenario 16, on the other hand, Cr(VI) plume migrated into the remediation area after it experienced a decrease in the concentration values due to dispersion. In addition, the contact time between the Cr(VI) plume and the remediation area is greater in scenario 13 than that of scenario 16 [Figure 7-6b].

Figure 7-6b shows biomass concentrations for all four scenarios (13-16) at both times (10 and 35 days). Comparing this figure with Figure 7-3b shows that increasing the

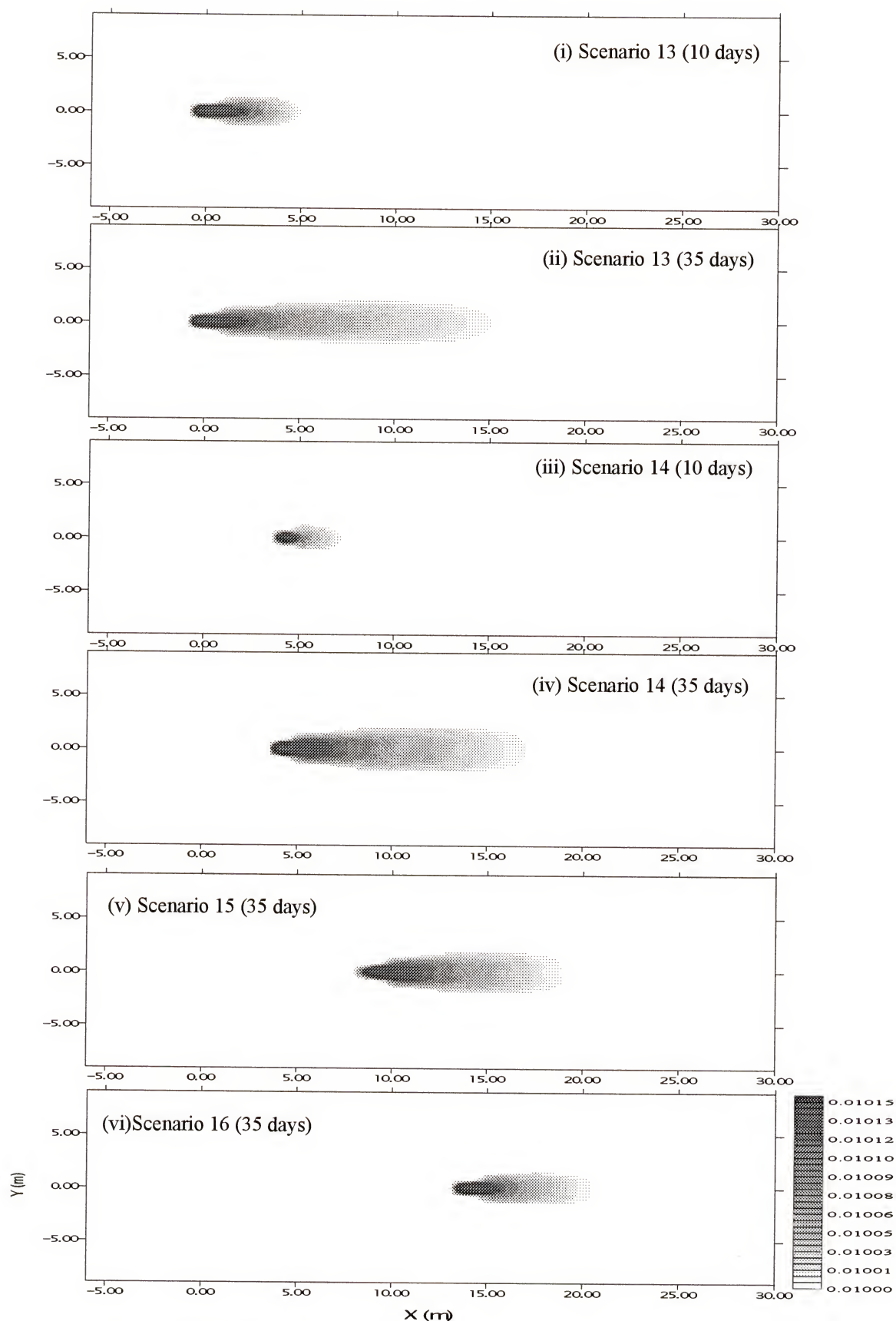


Figure 7-6b Effect of one well location on biomass concentrations for case 2.

loading rate of the electron donor and the nutrient enhanced biomass growth. As a result, the remediation area in scenarios 13-16 (contact area between all three solutes) is also increased [Figure 7-6b]. This increase in biomass concentrations is the direct cause of the gain in the bioremediation efficiency discussed earlier.

Figure 7-6c presents the spatial moments of the Cr(VI) plume for scenarios 13-16. This figure is similar to Figure 7-3c. Figure 7-6c supports conclusions drawn from Figure 7-3c; in addition, this figure displays amplified differences between the four scenarios due to the increase in microbial mediated Cr(VI) reduction. For example, placing the injection well 5.0 m downstream from the Cr(VI) initial release produces the most remediation (scenario 14) [Figure 7-6c(i)]. However, increasing the injection rate did not improve reduction at the edges of the plume [Figure 7-6a]. Therefore, more wells are still needed to enhance Cr(VI) biotransformations at the lateral edges of the plume.

Similarly, Figure 7-6d shows the spatial moments of the biomass distribution generated under scenarios 13-16. An increase in the values of most of the spatial moments is noticed compared to those of scenarios 1-4 of case 1 [Figure 7-3d]. However, doubling the injection rate appears to have minimal effect on the biomass dispersion distribution in both directions.

7.4.2. Three Wells Treatment

Figure 7-7a compares the Cr(VI) concentrations of scenarios 17-21 (in which three injection wells are used) to the corresponding scenarios (5-9) from case 1. Similar to scenarios 13-16, this figure shows that doubling the injection rate presents further reductions in Cr(VI) concentrations in all four scenarios compared to those of case 1. These reductions, however, were not limited to the front and trailing edges of the Cr(VI) plume, but instead extended to its lateral edges [Figure 7-7a] due to increasing the

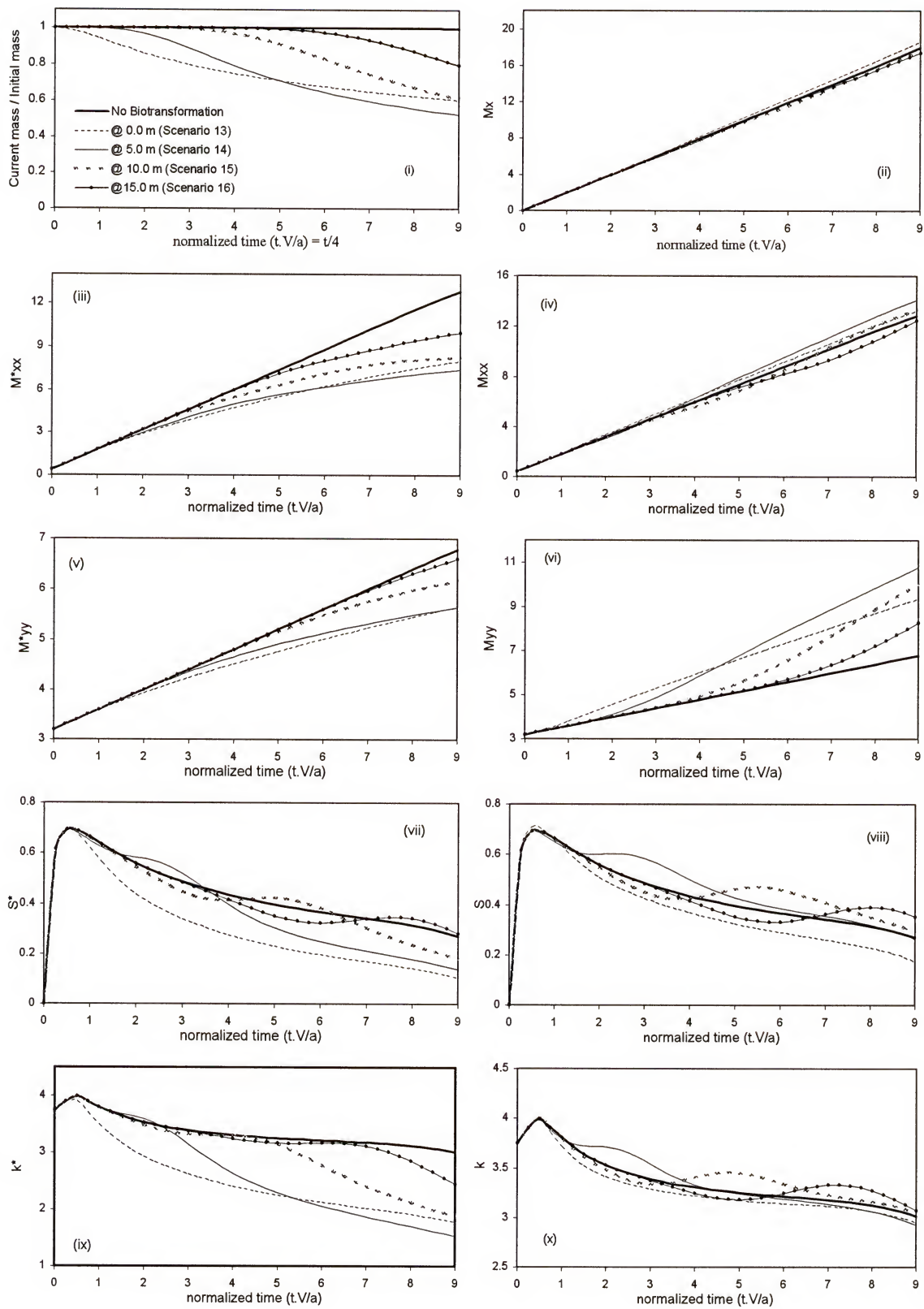


Figure 7-6c Effect of 1 well position on Cr(VI) plume's spatial moments for case 2.

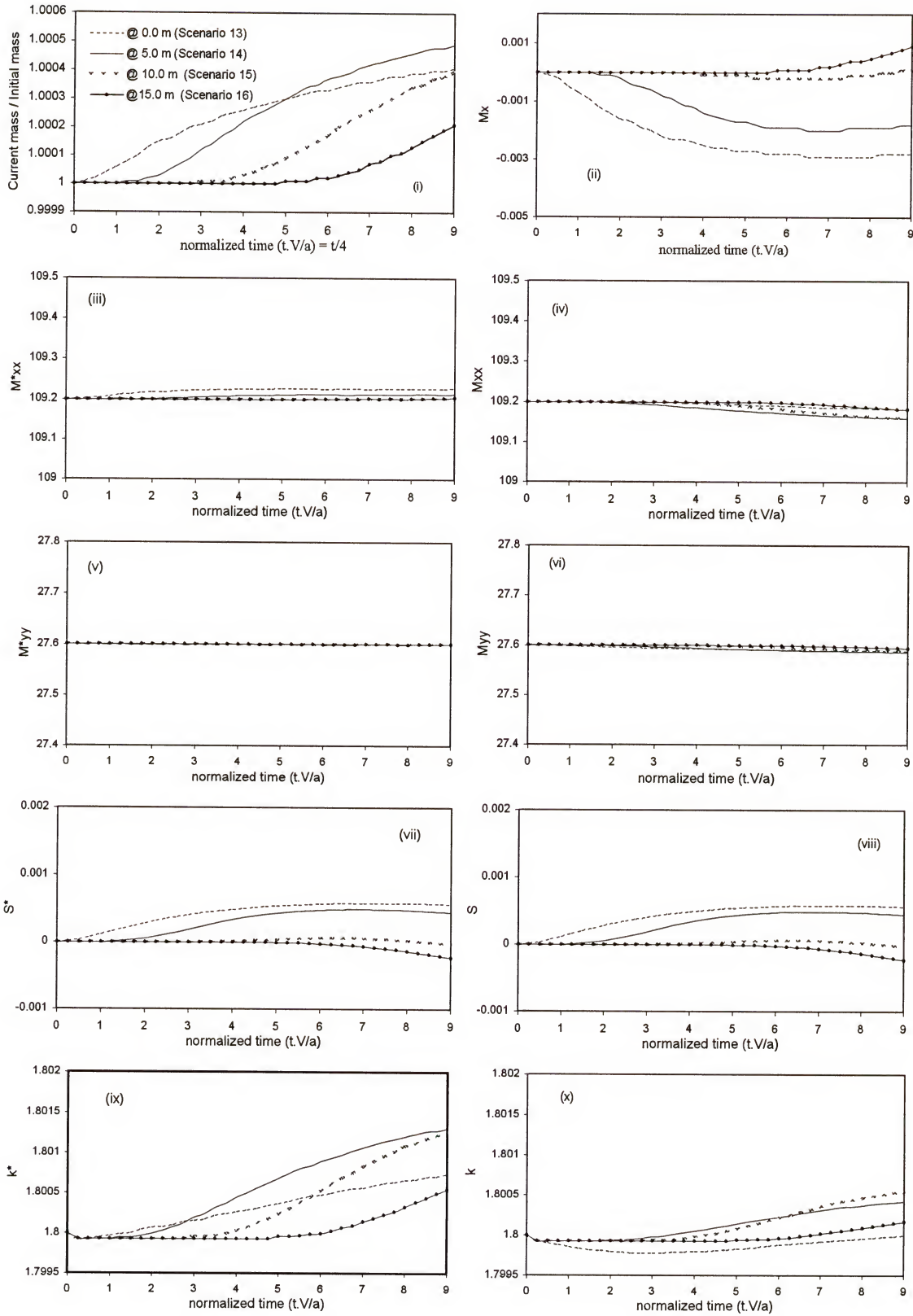


Figure 7-6d Effect of 1 well position on biomass spatial moments for case 2.

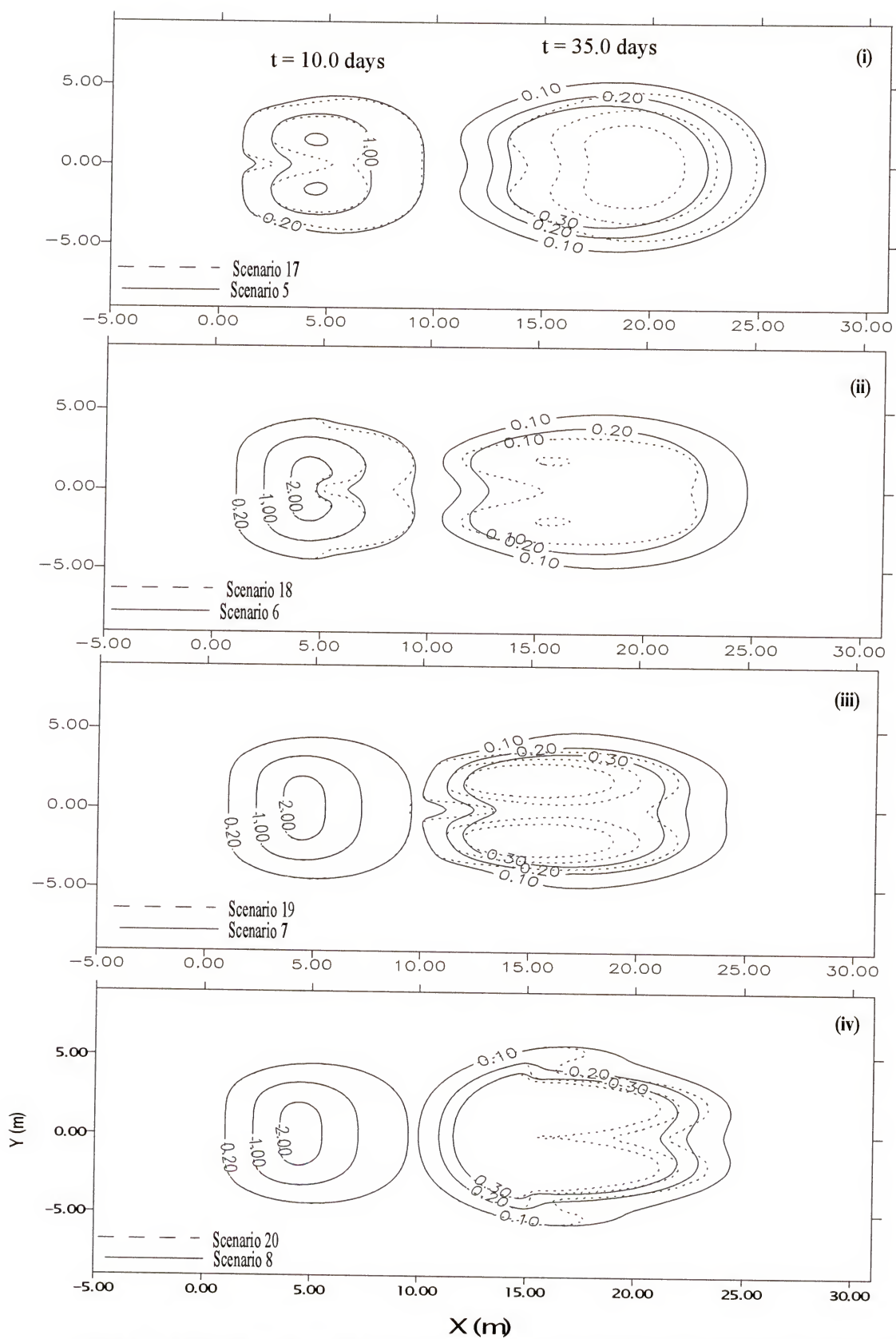


Figure 7-7a Effect of three wells location on the Cr(VI) concentrations for case 2 compared to case 1.
 (i) at the center of the initial plume, (ii) at 5 m, (iii) at 10 m and (iv) at 15 m.

injection rates from the two lateral wells. However, reductions in Cr(VI) concentrations at the lateral edges are less than those achieved at the center of the Cr(VI) plume [Figure 7-7a]. This is because lower Cr(VI) concentrations at the lateral edges of the plume (due to dispersion) produce lower reduction rates. The role of the two lateral wells in reducing Cr(VI) concentrations is more evident at later times (35 days) than earlier times (10 days) [Figures 7-7a(i and ii)]. This is because after 10 days the Cr(VI) plume has not merged into the effective remediation area of the two lateral wells. The remediation areas created by the two lateral injection wells preclude the Cr(VI) plume from dispersing in the lateral direction. The influence of these wells does not appear until lateral edges of the Cr(VI) plume merges into their area of impact. For that reason, with a closer look at Figures 7-6a(i and ii), it can be noticed that the efficiency of the two lateral wells is more evident in scenario 18, when they were placed 5 m downgradient of the contaminant zone. In conclusion, it is always preferable to place the two lateral wells downstream of the position of the central well.

By comparing the bioremediation efficiencies of the four scenarios (17-20) (Table 7-1), it is clear that scenario 18 provides the best remediation (80%). Despite yielding a gain in remediation efficiency of 85% (Table 7-2) from doubling injection rates, scenario 20 (similar to scenario 8) characterizes an unsatisfactory Cr(VI) reduction (36%, Table 7-1) compared to the other four scenarios (17-20). Doubling injection rates in scenarios 1, 4, 5, and 8 (results of scenarios 13, 16, 17, and 19) produced a significant increase in the gain of bioremediation efficiency (over 85% increase in G, Table 7-2). Therefore, doubling injection rates in these scenarios is an economically sound alternative when other scenarios are not available.

Figure 7-7b illustrates biomass distribution generated under scenarios 17-20 after 10 and 35 days. This figure also depicts the extension of the remediation areas under each scenario, where all solutes exist and biologically mediated Cr(VI) reduction occurs accordingly. The increase in biomass is evident in these four scenarios as compared to the corresponding ones from case 1. Furthermore, the increase in biomass is greatest downgradient from the central well compared to that occurs at the lateral ones. This is because all three solutes exist with higher concentrations at the central areas of the aquifer than the lateral areas (refer to Figure 7-2).

Figure 7-7c depicts various spatial moments of the Cr(VI) plume for scenarios (17-20). By comparing this figure to Figure 7-4c, doubling the injection rate amplifies the differences between plume moments generated for the different scenarios. Figure 7-7c(ii) shows that doubling the injection rate in scenario 17 increased the apparent travel velocity of the first moment. This occurred because wells at the contaminant initial location favored reduction at the trailing edge of the Cr(VI) plume over the leading edge [Figure 7-7a(i)]. That caused the center of the Cr(VI) plume to shift downgradient. On the other hand, injection in scenario 20 favored reduction at the leading edge of the Cr(VI) plume [Figure 7-7a(iv)] which caused a decrease in the apparent plume velocity. For scenarios 18 and 19, reductions occurred throughout the Cr(VI) plume [Figures 7-7a(ii, and iii)] which in turn resulted in minor differences in the displacement of the first moments when compared to the case of “no biotransformation” [Figure 7-7c(ii)]. Effects on dispersion are more obvious in these four scenarios (17-20) than those of the corresponding ones in case 1 (5-9) [Figures 7-7c(iii-vi)]. However, in both cases, transient changes in the second moment appear similar.

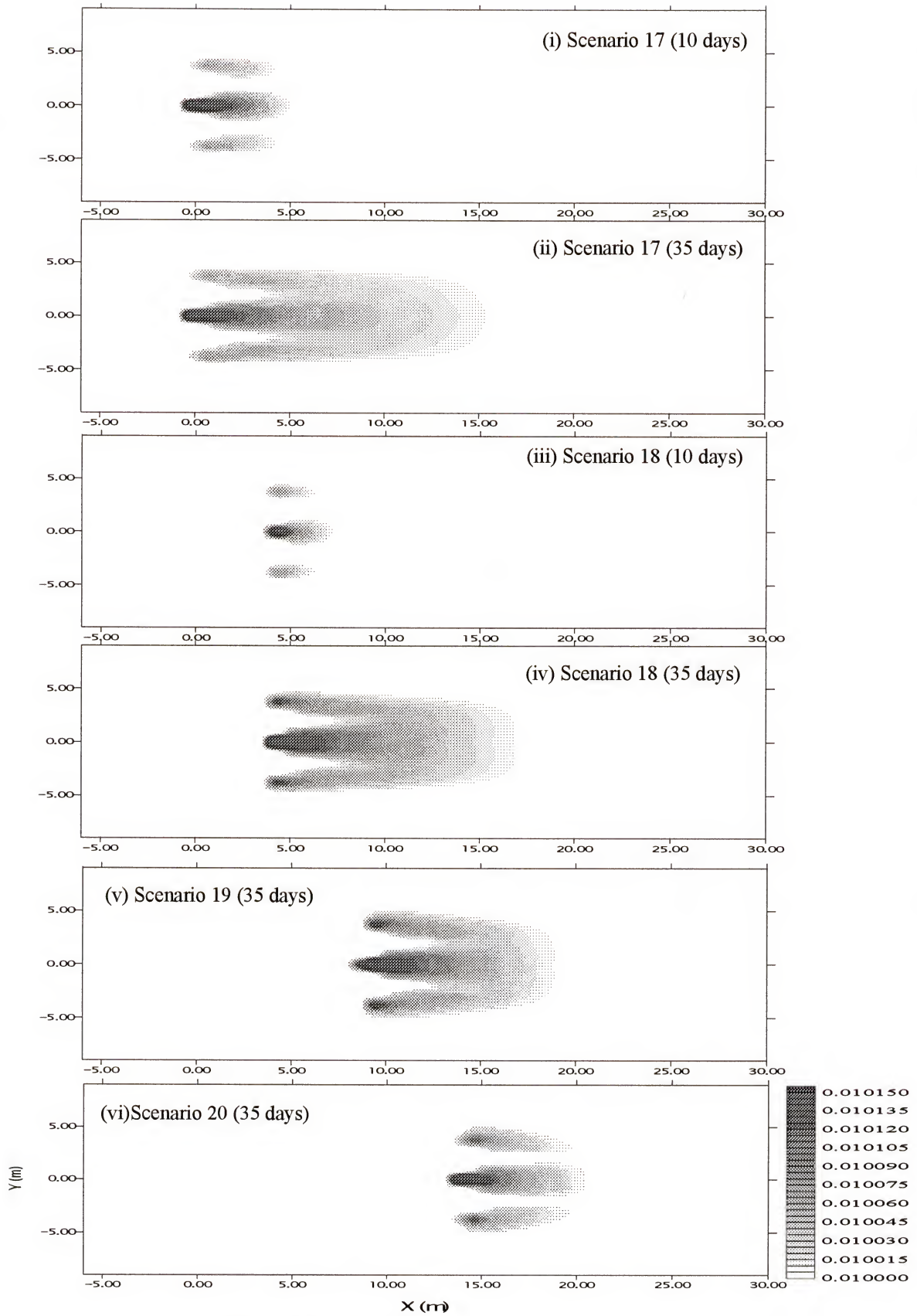


Figure 7-7b Effect of three wells location on biomass concentrations for case 2.

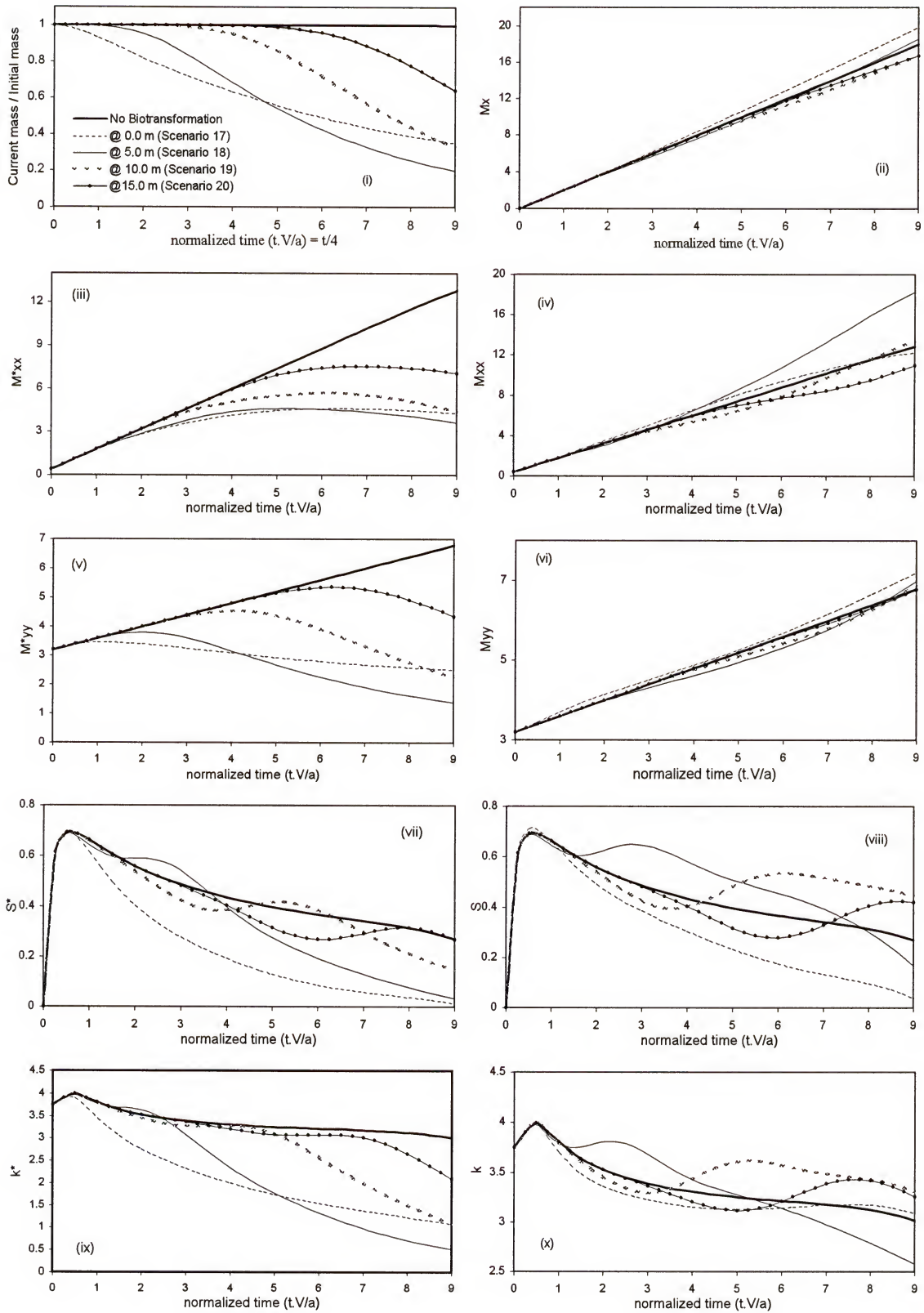


Figure 7-7c Effect of 3 well position on Cr(VI) plume's spatial moments for case 2.

Figure 7-7c(vii-x) indicates that the time interval at which skewness and peakness values are increased is longer in the scenarios of case 2 than that of the scenarios of case 1 [Figure 7-4c(vii-x)]. That time interval, as mentioned before, denotes the contact period between the Cr(VI) plume and the active remediation zone. The longer that time period the more reductions in Cr(VI) concentrations are achieved and, therefore, the higher the bioremediation efficiency attained. As a result, these four scenarios (17-20) produce greater Cr(VI) reduction than scenarios (5-9).

The effect on biomass moments is most evident in the lower moments where there appears an enhancement of differences seen between scenarios (see Figures 7-4d and 7-7d).

7.4.3. Line Source Treatment

Figure 7-8a compares Cr(VI) concentrations distributions from scenarios 21-24 to those of scenarios 9-12, respectively. This figure shows that doubling the injection rate from the line source of nutrient and electron donor increases Cr(VI) reduction. However, because using a line source injection rate of 2.5 mg/m/day was enough to stimulate the bacteria to transform most of the Cr(VI) mass in the aquifer, doubling the injection rate in scenarios 22-23 only slightly improved the remediation efficiency (Table 7-1). For example, despite the fact that more than 99% of Cr(VI) mass was reduced in scenario 22 [Table 7-1], less than 3% improvement over the efficiency of scenario 10 where the injection rate was half (Table 7-2). Figure 7-8a(ii) suggests that most of the small improvement occurred early in the remediation ($t = 10$ days). Thus, adding more nutrients and electron donor is not the only means of enhancing bioremediation, nor does it always lead to proportionally greater remediation. Proper design of the injection well positions appears to be a crucial issue. This conclusion is even more evident when comparing the

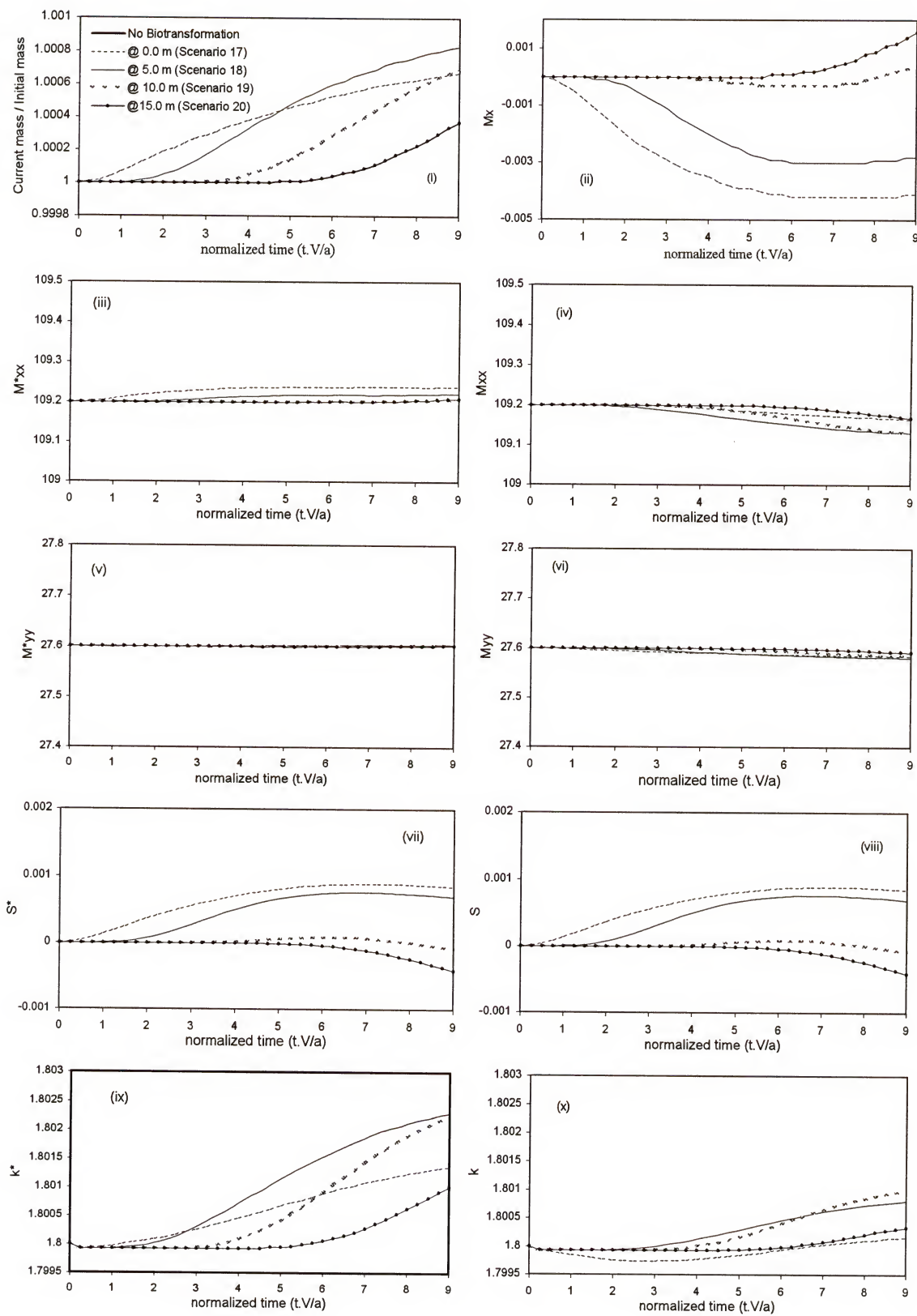


Figure 7-7d Effect of 3 well position on biomass spatial moments for case 2.

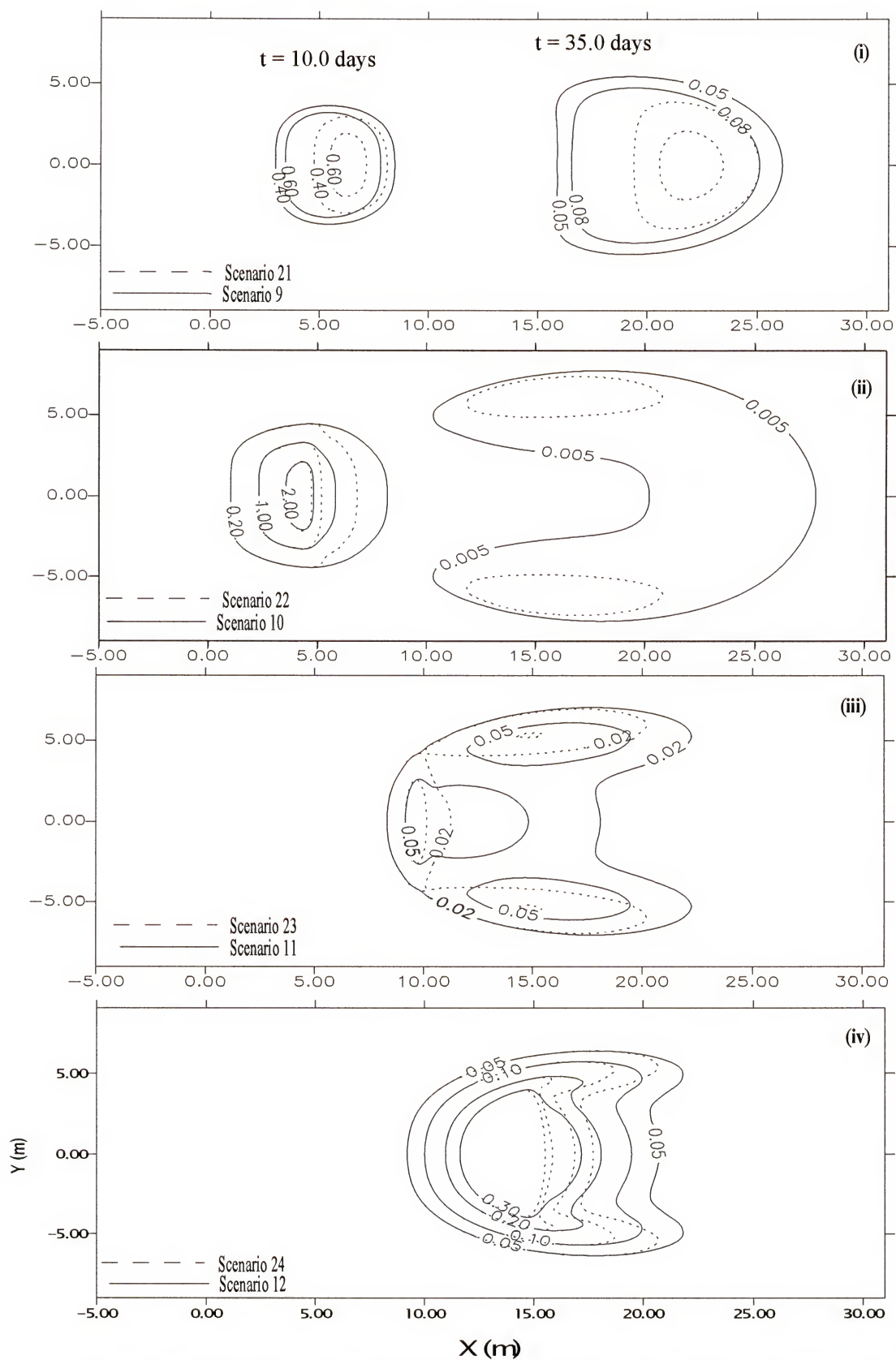


Figure 7-8a Effect of line source location on the Cr(VI) concentrations for case 2 compared to case 1.
 (i) at the center of the initial plume, (ii) at 5 m, (iii) at 10 m and (iv) at 15 m.

bioremediation efficiency of scenario 18 (80% remediation using total injection rate of 15 mg/day) with that of scenario 24 (70% remediation using total injection rate 40 mg/day) (Table 7-1).

Figure 7-8b presents the areal extent of the active remediation as reflected in increased microbial biomass for scenarios 21-24 after 10 and 35 days. Comparing this figure with Figure 7-5b reveals two important observations: 1) higher biomass concentrations are developed in scenarios 21-24 as compared to scenarios 9-12 due to doubling the injection rates; and 2) the remediation areas in scenarios 21-24 are smaller than the corresponding areas in scenarios 9-12. To explain this, it should be noted that most of the biological reduction occurred earlier in scenarios 21-24 than in scenarios 9-12 (due to the increase in the injection rate); thus, most of the available Cr(VI) mass was removed over the upgradient edge of the remediation zone. As a result, less Cr(VI) concentrations were available to support bacterial growth downgradient [compare Figures 7-8c(i) and 7-5c(i)]. As mentioned before, removing low concentrations of a contaminant using biological treatment can be difficult, as biotransformation rates depend on the contaminant concentration in the aquifer. That is clear in Figure 7-8c(i), where Cr(VI) reduction rate decreases at later times (scenarios 21 and 22).

Compared to the case of “no biotransformation”, the time change in the second central moments is shown to decrease in scenarios 21-24; however, they increased compared to scenarios in case 1 (9-12) [Figure 7-8c(iii-vi)]. Dispersion increased in scenarios 22, 23, and 24 for moments based on current plume mass (Figure 7-8c(i)). This increases the peak value after about 24 days (6 on the normalized time scale) for scenario 22 (Figure 7-8c(i)), after which the change in the second moment with respect to time

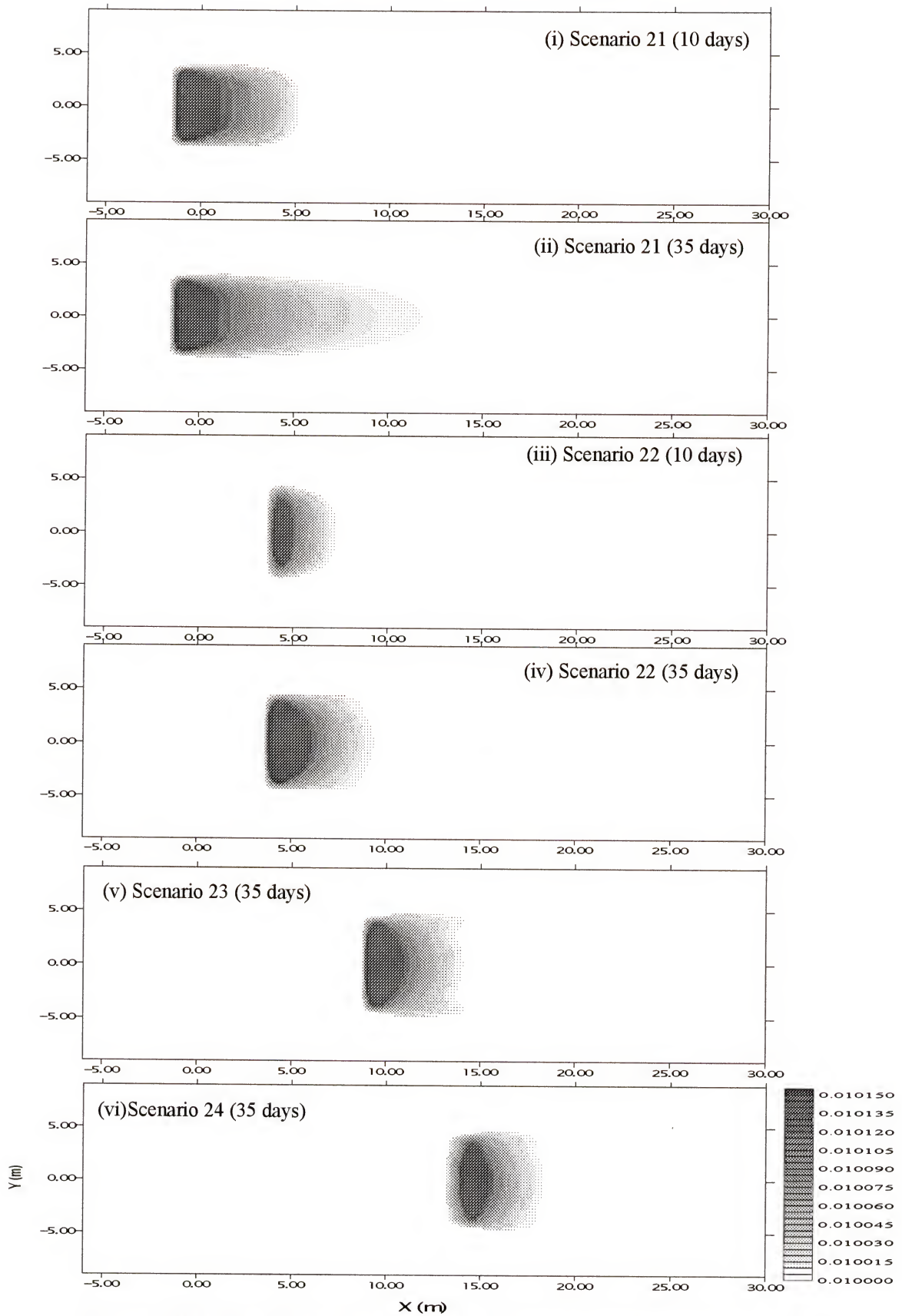


Figure 7-8b Effect of line source location on biomass concentrations for case 2.

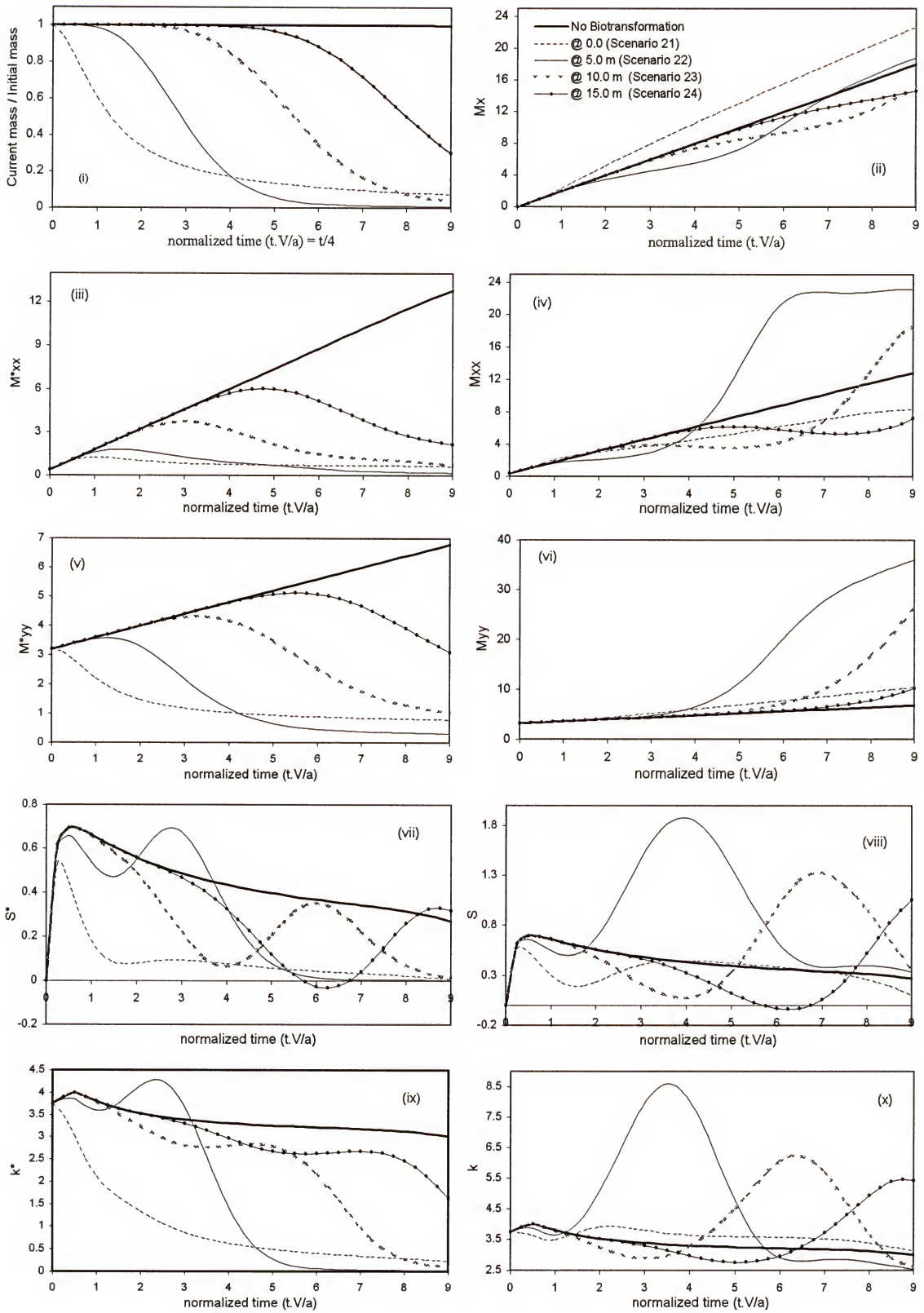


Figure 7-8c Effect of line source position on Cr(VI) plume's spatial moments for case 2.

approaches a value of zero [Figure 7-8c(iv)]. That increase in the longitudinal dispersion is due to regions of small concentrations of Cr(VI) that still exist at that time [Figure 7-8a(ii)]. For the same reason, values of the lateral dispersion are also high for the same scenario [Figure 7-8c(vi)]. On the other hand, Figures 7-8c(iii and v) (where initial Cr(VI) mass is used to normalize the second moment) imply that both dispersions reach very small values (almost zero) for scenario 22. The reason for this, as mentioned earlier, is the removal of most of Cr(VI) mass in scenario 22. Skewness and peakness of scenario 22 [Figures 7-8c(vii and ix)] emphasize that most of the biotransformation occurs at early times. As a result, skewness reached peak values shortly after the plume entered the remediation zone and decreased as Cr(VI) mass decreased.

Figure 7-8d presents the different spatial moments of the biomass concentrations of scenarios 21-24. This figure stresses on the same points covered by Figure 7-5d. However, if both figures are carefully compared, one can notice that most of the differences between spatial moments occur earlier in scenarios 21-24 than those in scenarios 9-12. This is due to the increase in injection rates that forces biological activities to occur early, leaving less Cr(VI) to support later microbial growth. Therefore, increasing the injection rate of nutrients and electron donors into the aquifer not only enhances the bioremediation, but also reduce the remediation time in most cases.

7.5. Case 3

Increasing injection rates of nutrients and electron donors in the aquifer does not always enhance the biotransformation process. The inhibition factor (Equation 4-28) should be taken into consideration before increasing the injection rates. This factor represents a concentration of a specific solute (Cr(VI), nutrient, or electron donor) above which that solute could have a toxic effects on metal-reducing microorganisms.

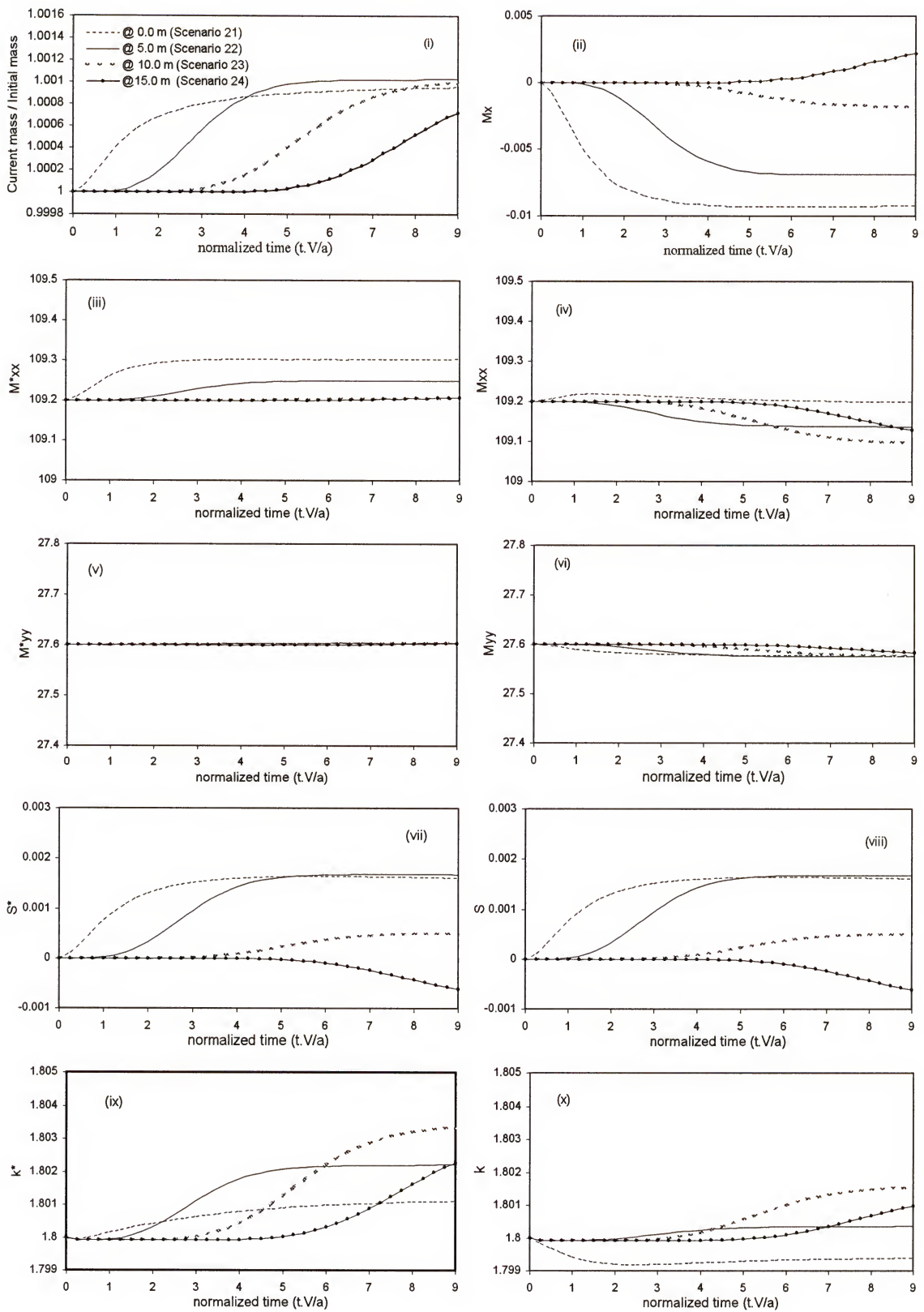


Figure 7-8d Effect of line source position on biomass spatial moments for case 2.

Therefore, increasing injection rates with the disregard of this factor could result in lower than expected remediation results. In case 3, another 12 scenarios (25-36), similar to those used in case 2 (scenarios 13-24), are used. However, an inhibition factor of 1.0 mg/l for all three solutes (Cr(VI), nutrient, electron donor) is assumed here.

7.5.1. One Well Treatment

When only one injection well is used (scenarios 25-28), the increase in the concentration of the injected nutrient and electron donor is still less than the toxic level almost everywhere in the aquifer. Therefore, minor effects on the total Cr(VI) biotransformed mass are noticed [Table 7-1]. At $t = 10$ days (because concentrations of nutrient and electron donor are slightly over the toxic level) less Cr(VI) reduction is observed in scenarios 25 and 26 as compared to 13 and 14 [Figure 7-9a(i and ii)]. The same figures also reveal that until concentrations of both solutes decrease below toxic levels at $t = 35$ days (as a result of dispersion), little change in Cr(VI) concentrations are simulated. When the injection well was placed further down stream in scenarios 27 and 28, the Cr(VI) plume merges into regions of higher nutrient and electron donor concentrations at $t = 35$ days (above the inhibition level). As a result, less efficient Cr(VI) remediation is simulated [Figure 7-9a(iii and iv)]. The loss of bioremediation efficiency as given by equation 7-2 is greater in scenarios 27 and 28 than that of scenarios 25 and 26 (Table 7-2).

$$L = \frac{\eta_{i+12} - \eta_i}{\eta_i} \times 100 \quad (7-2)$$

where i is the scenario number of case 2 (13→ 24).

A major change in the biomass distribution in the aquifer is evident by comparing Figure 7-9b of scenarios 25-28 (case 3) with Figure 7-6b of scenarios 13-16 (case 2).

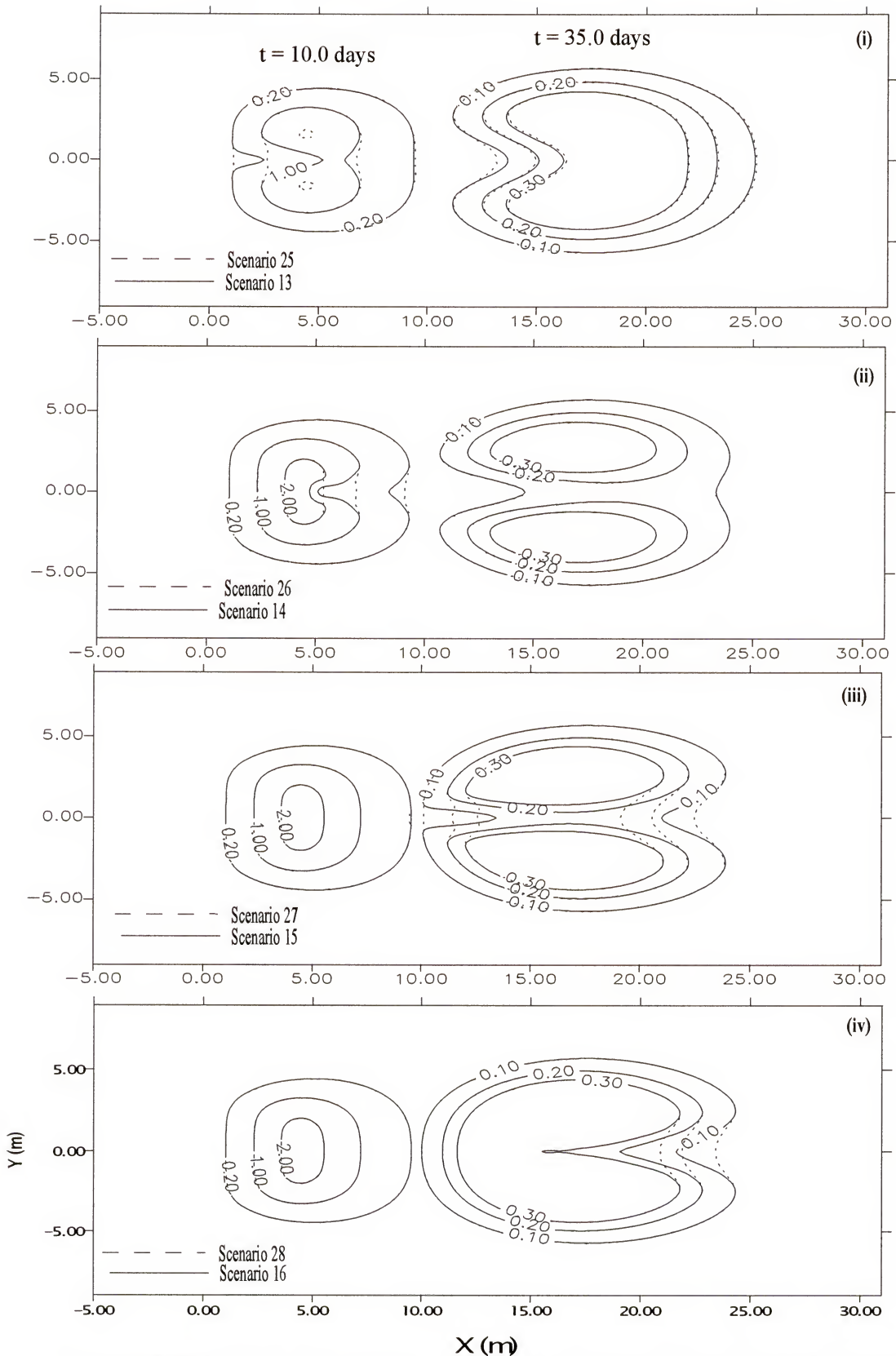


Figure 7-9a Effect of one well location on the Cr(VI) concentrations for case 3 compared to case 2. (i) at the center of the initial plume, (ii) at 5 m, (iii) at 10 m and (iv) at 15 m.

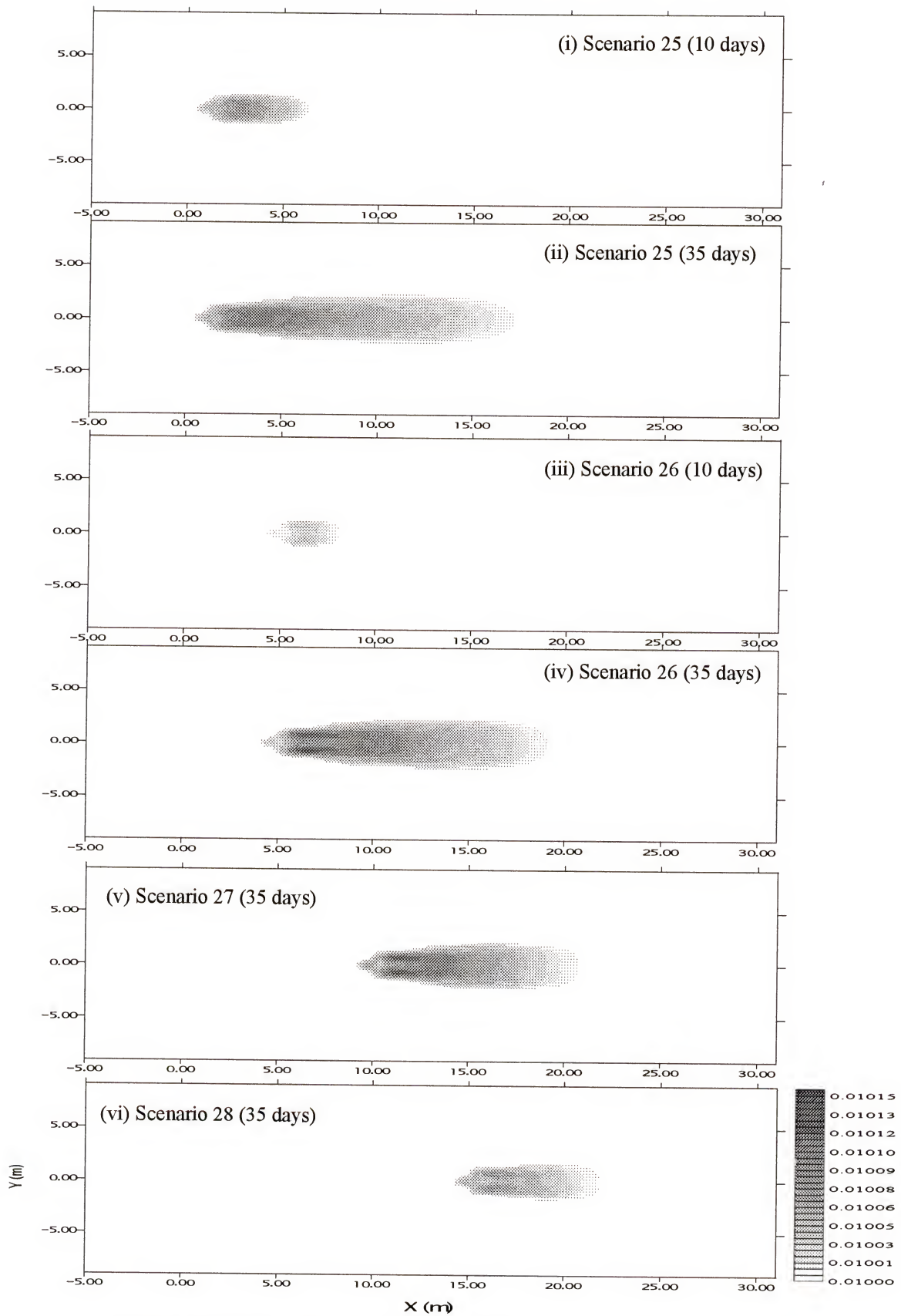


Figure 7-9b Effect of one well location on biomass concentrations for case 3.

That is, biomass concentrations at the well position are less in case 3 scenarios than those of case 2 as a result of reducing the inhibition factor. However, as dispersion operates to reduce nutrient and electron donor concentrations below the inhibition level (downgradient of the well position), a consequent increase in biomass is observed in all four scenarios [Figure 7-9b]. Biomass is distributed over larger areas in case 3 because microorganisms begin to grow later in each scenario of case 3 than in those of case 2. Concentrations of all solutes then drop (due to both dispersion and biotransformation) to low levels that cannot support bacterial growth; consequently, biomass concentrations decrease again at the leading edges of the Cr(VI) plume [Figure 7-9b].

As mentioned before, considering the inhibition factor in scenarios 25-28 (where only one injection well is used) slightly affects characteristics of both the Cr(VI) plume and bacterial populations. As a result, minor changes in the spatial moments of both the Cr(VI) plume and the biomass distribution are observed when comparing Figures 7-9(c and d) to Figures 7-6(c and d), respectively. However, changes in both skewness and peakness values are more recognizable [Figures 7-6c and 7-9c]. Having increased the areal extent of simulated microbial growth in the aquifer also increases the available contact time between the three solutes. Thus, skewness and peakness associated with the Cr(VI) plume in scenarios of case 3 evolve slower than those of case 2 [Figure 7-9c(vii-x)].

7.5.2. Three Wells Treatment

The effect of considering the inhibition factor is more evident in scenarios 29-32 (where three injection wells are used). This is because the injected mass of the nutrient and the electron donor is greater, which produces concentrations exceeding the inhibition factor over larger areas in the aquifer. In general, reducing the inhibition factor limits the

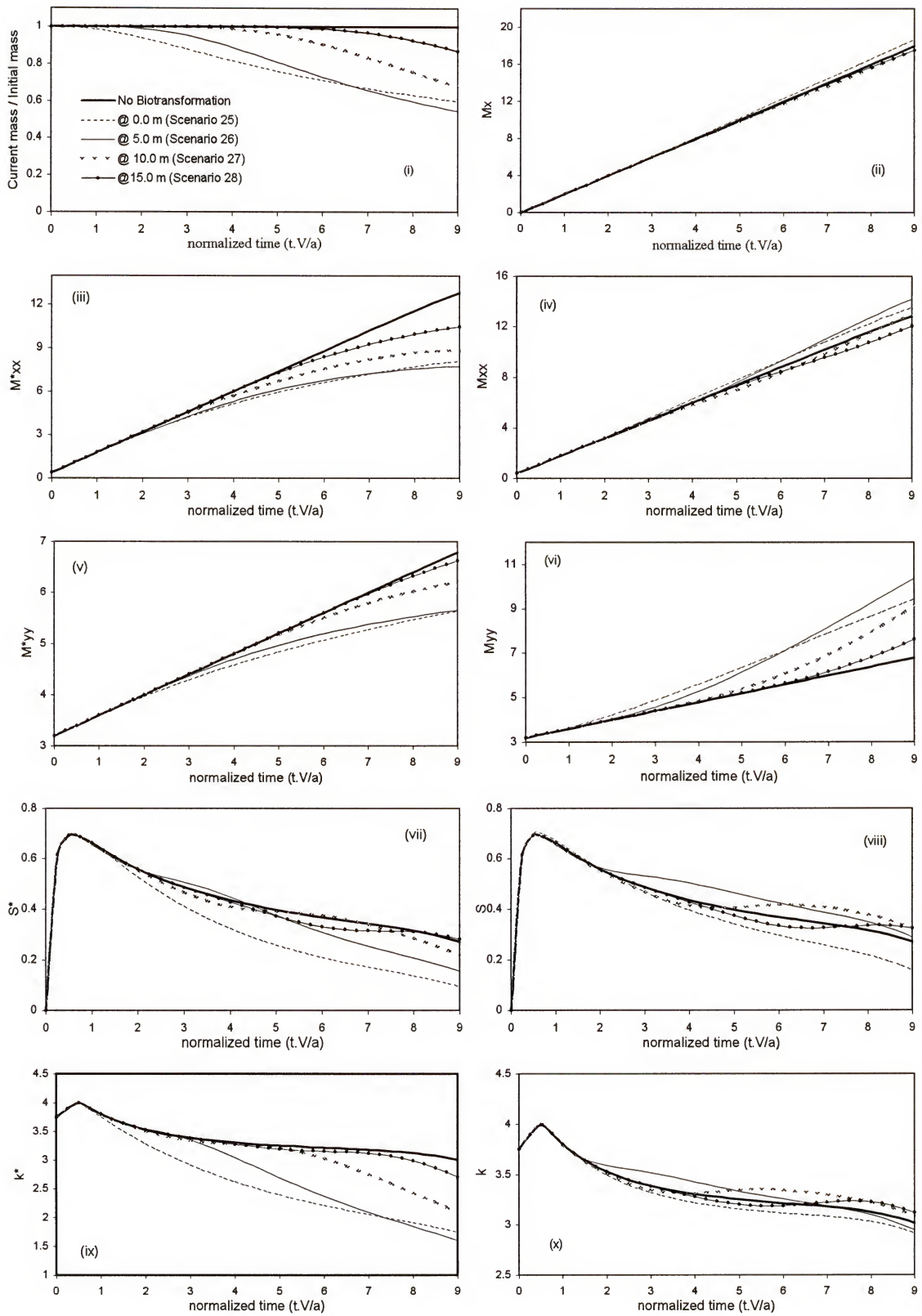


Figure 7-9c Effect of 1 well position on Cr(VI) plume's spatial moments for case 3.

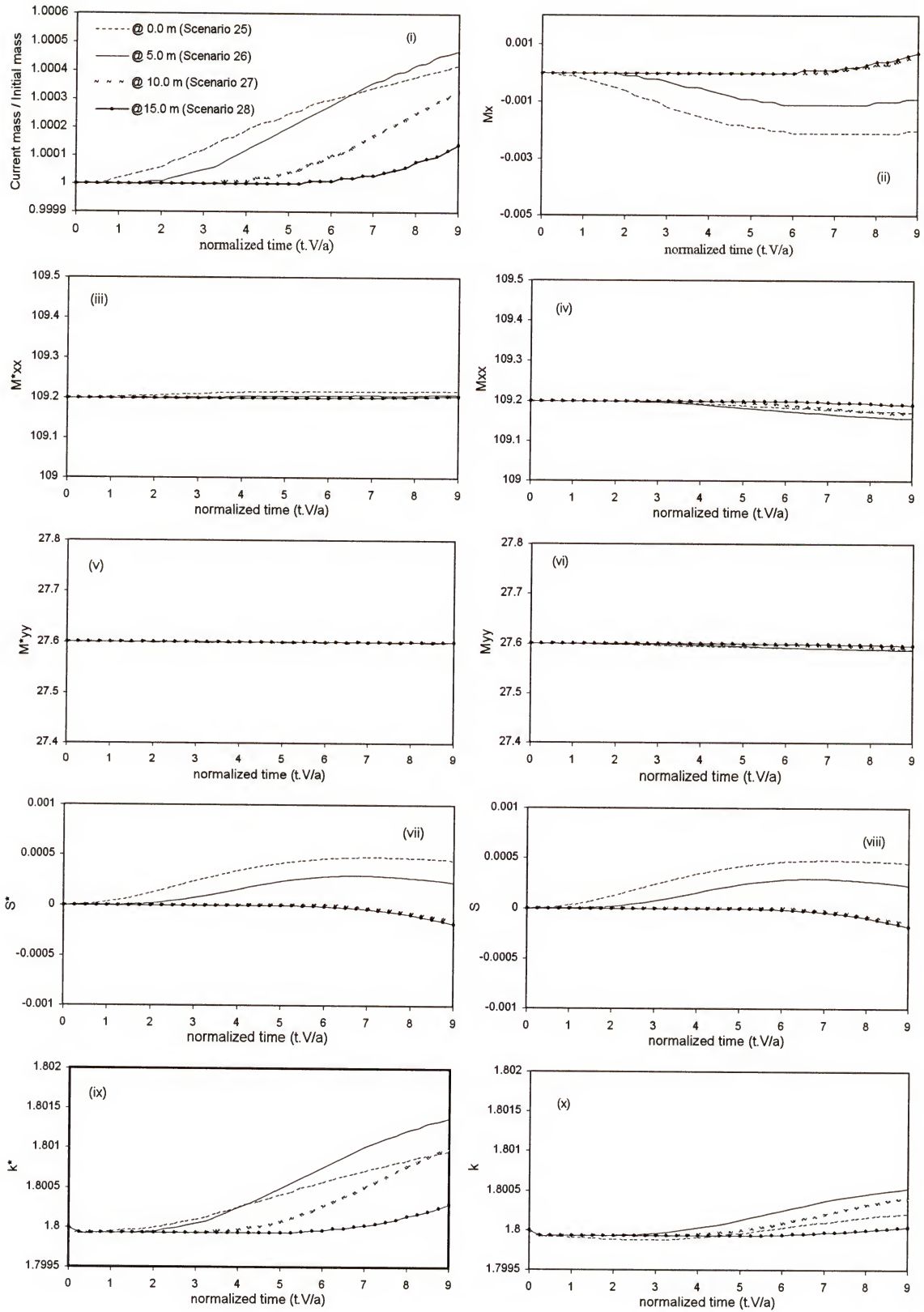


Figure 7-9d Effect of 1 well position on biomass spatial moments for case 3.

biological activities and decreases bioremediation efficiency (Table 7-1). However, unexpectedly, bioremediation efficiency is greater in scenario 29 than in scenario 17 of case 2 (Table 7-1), with a gain of 24% (Table 7-2). That is also clear from Figure 7-10a, where more reduction in Cr(VI) concentrations in scenario 29 is observed as compared to scenario 17 after $t = 35$ day. One possible explanation of this observation is that in scenario 17 microorganisms used the nutrient and the electron donor (at the location of the injection well) immediately after injection; thus, Cr(VI) reduction occurs over a small area where the nutrient and the electron donor are available with very high concentrations. Therefore, microbial and Cr(VI) concentrations become very small in all other areas of the aquifer and, as a result, growth rates dramatically decrease. In scenario 29, on the other hand, reducing the inhibition level provides the nutrient, the electron donor, and Cr(VI) the opportunity to disperse over a larger area in the aquifer before biological reactions occur. Then, with solutes better mixed over a larger portion of the aquifer (under the inhibition level), Cr(VI) reduction occurs at a higher rate. Consequently, the total reduced mass of Cr(VI) in scenario 29 is more than that in scenario 17. Decreasing the inhibition factor presents similar effects on remediation to those obtained when injection wells were placed further downgradient of the contaminant initial position. For that reason bioremediation efficiencies of scenarios 29 and 18 are similar [Table 7-1].

For the other three scenarios (30-32), the contact time between all solutes was not sufficient to reduce solute concentrations below inhibition levels. Therefore, bacteria growth is inhibited during most of the available contact time.

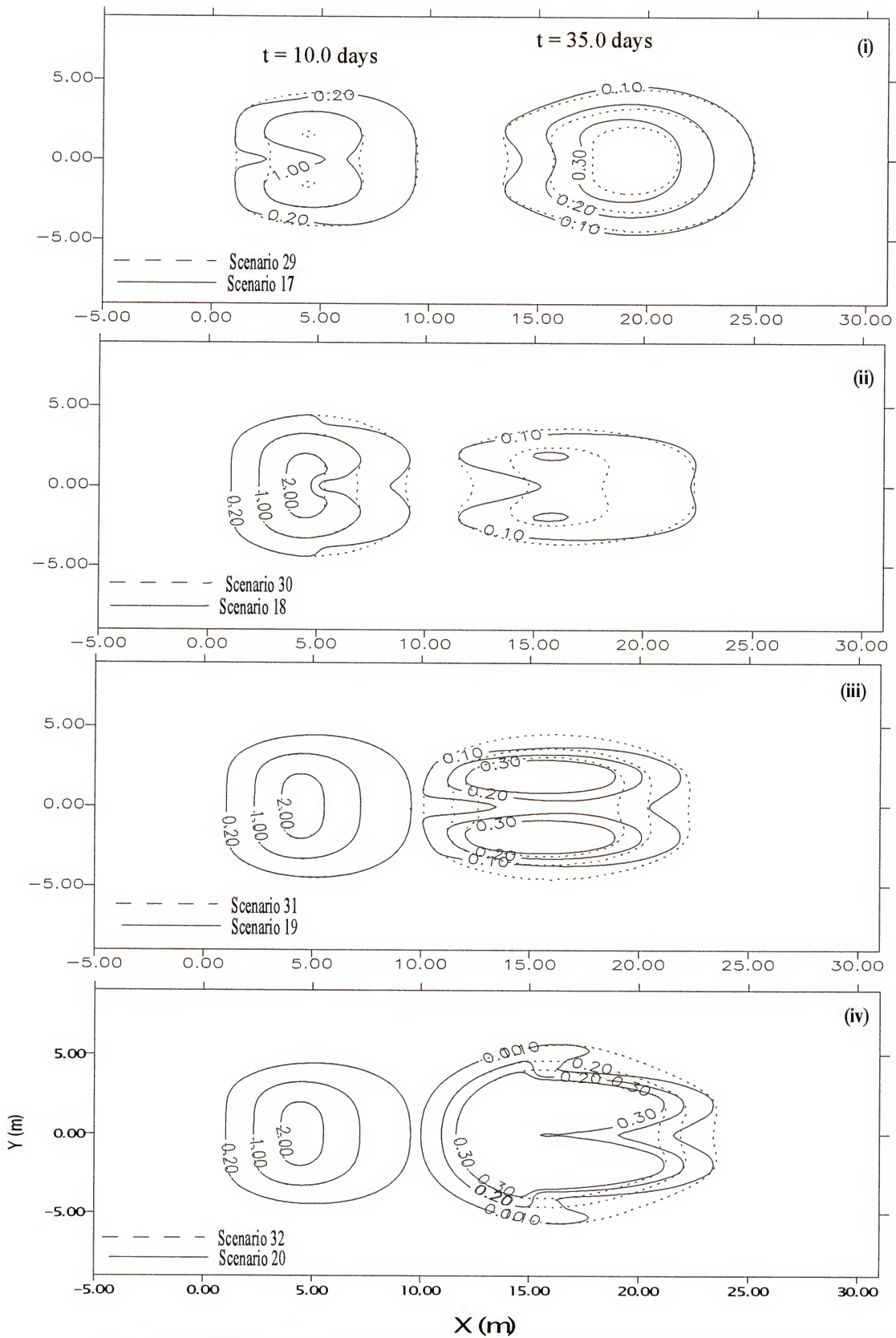


Figure 7-10a Effect of three wells location on the Cr(VI) concentrations for case 3 compared to case 2.
 (i) at the center of the initial plume, (ii) at 5 m, (iii) at 10 m and (iv) at 15 m.

Figure 7-10b also emphasizes this point, as there is less biomass at well positions in scenarios 29-32 than those of scenarios 17-21 [Figure 7-7b].

Figures 7-10(c and d) provide the spatial moments of both Cr(VI) and bacterial plumes of scenarios 29-32. Comparing these figures to Figures 7-7(c and d), respectively, reveals that reducing the inhibition factor exerts damping effects on all spatial moments of scenarios 30-32.

Figure 7-10c(i) clearly shows that there was a delay in the reduction in Cr(VI) mass in scenarios 30-32 as compared to scenarios 18-20 [Figure 7-7c(i)]. This is again due to the existence of the nutrient and the electron donor with concentrations greater than the inhibition level thereby preventing any biological activities to occur at early times [Figure 7-10d(i)].

7.5.3. Line Source Treatment

Finally, when a line source of nutrient and electron donor is used in case 3, less biotransformation occurs in all four scenarios (33-36) [Figure 7-11a] than in corresponding scenarios from case 2 [Figure 7-8a]. Increasing concentrations of both the nutrient and electron donor over large areas of the aquifer inhibits biotransformation over the same areas. This is evident from Table 7-1, where large reductions in bioremediation efficiency are shown in scenarios 33-36 as compared to scenarios 21-24. More than 30% loss in the efficiency occurs in all scenarios, with a maximum of 72% in scenario 36 [Table 7-2]. Bioremediation efficiencies of scenarios 33-36 are even less than those of the corresponding scenarios of case 1 (9-12). This clearly illustrates the importance of the evaluation of the inhibition factor prior to executing any remediation action.

A completely different biomass distribution is simulated in scenarios (33-36) [Figure 7-11b], compared to scenarios 21-24 of case 2 [Figure 7-8b].

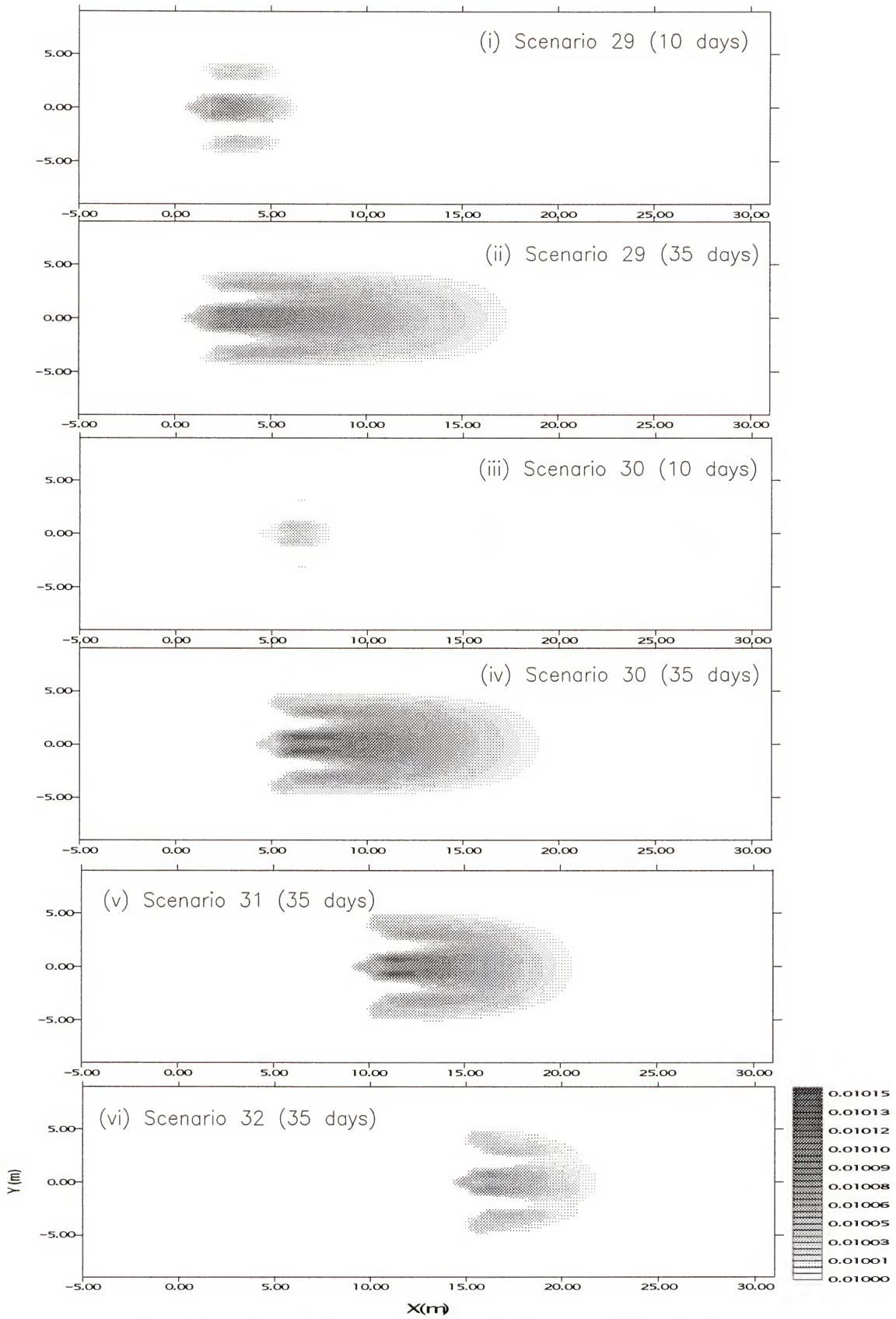


Figure 7-10b Effect of three wells location on biomass concentrations for case 3.

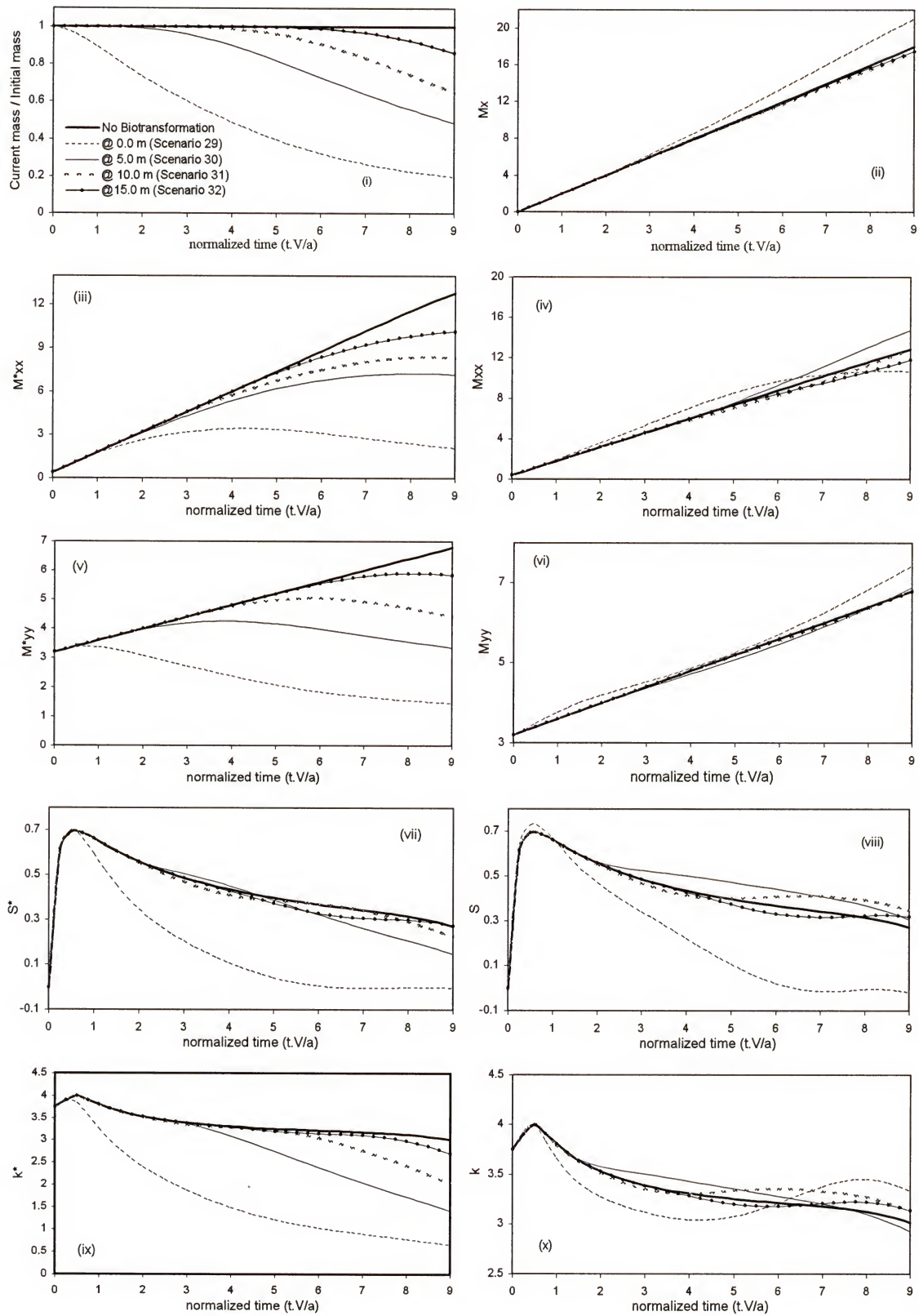


Figure 7-10c Effect of 3 well position on Cr(VI) plume's spatial moments for case 3.

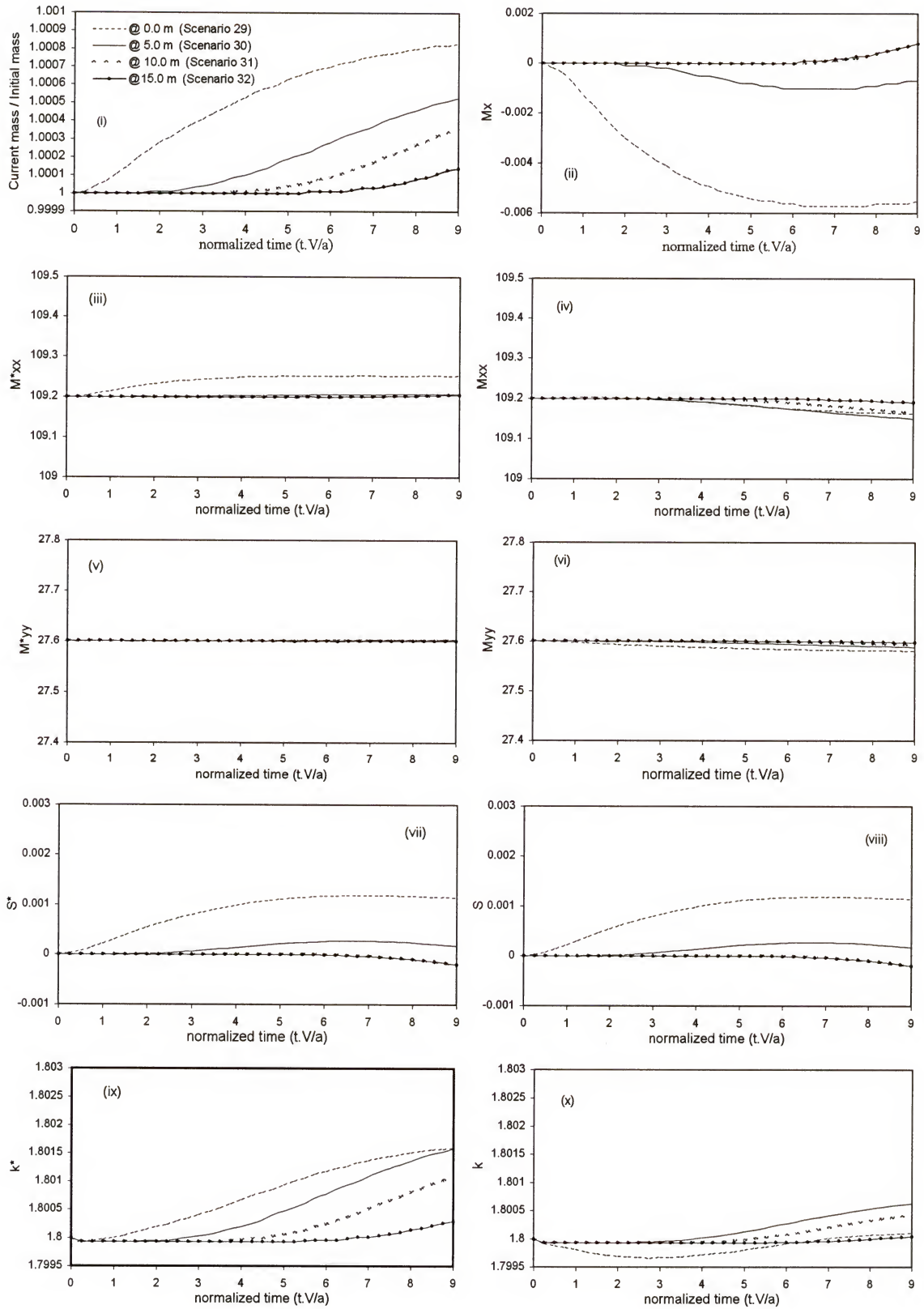


Figure 7-10d Effect of 3 well position on biomass spatial moments for case 3.

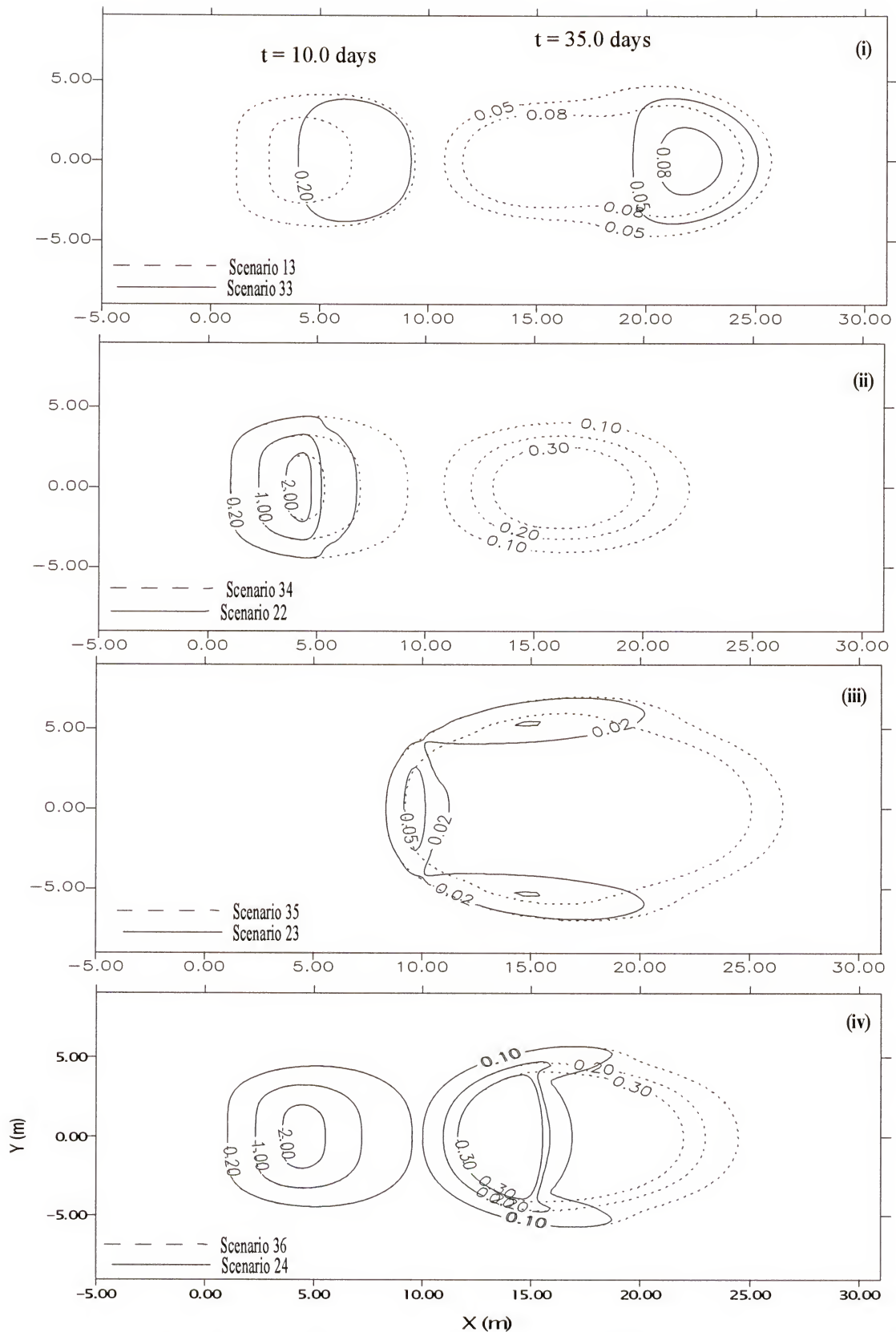


Figure 7-11a Effect of line source location on the Cr(VI) concentrations for case 3 compared to case 2.
 (i) at the center of the initial plume, (ii) at 5 m, (iii) at 10 m and (iv) at 15 m.

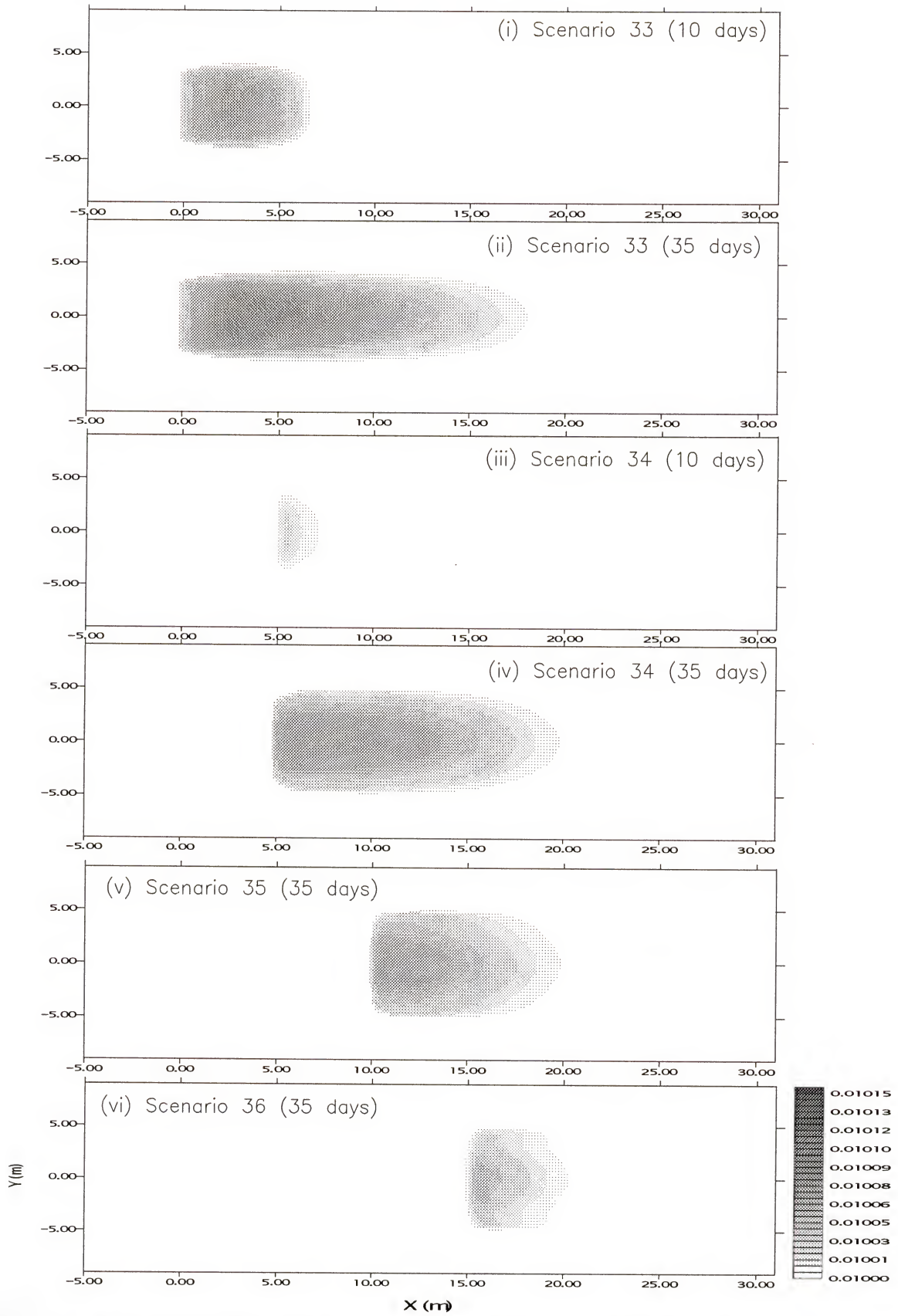


Figure 7-11b Effect of line source location on biomass concentrations for case 3.

Instead of the increase in biomass at the line source position in case 2 [Figure 7-8b], a uniform biomass distribution is produced downgradient in case 3 [Figure 7-11b]. For this reason, a dramatic decrease in all spatial moments of Cr(VI) plume are seen in scenarios 33-36 [Figure 7-11c] compared to those in case 2 [Figure 7-8c]. Limiting biological reactions to those regions where concentrations of all solutes are less than the inhibition factor resulted in having a nearly spatially constant biotransformation rates everywhere in the aquifer. Therefore, the effect on dispersion, skewness, and peakness is dampened compared to the case of “no biotransformation” [Figures 7-11c(iv, vi, viii, and x)]. Similarly, reducing the inhibition factor lessens the effects on the spatial moments of biomass in all four scenarios (33-36, Figure 7-11d), compared to scenarios 21-24 [Figure 7-8d].

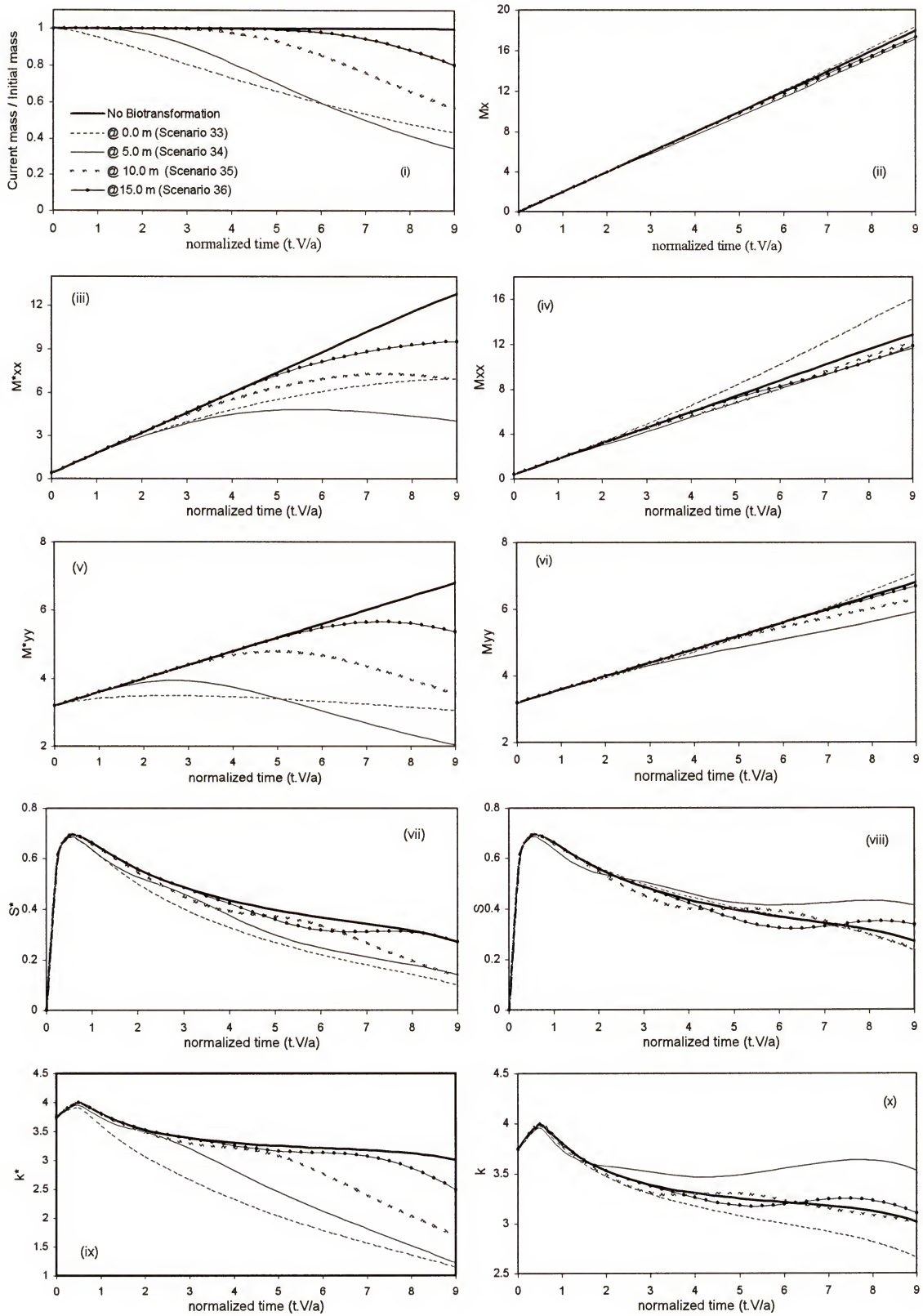


Figure 7-11c Effect of line source position on Cr(VI) plume's spatial moments for case 3

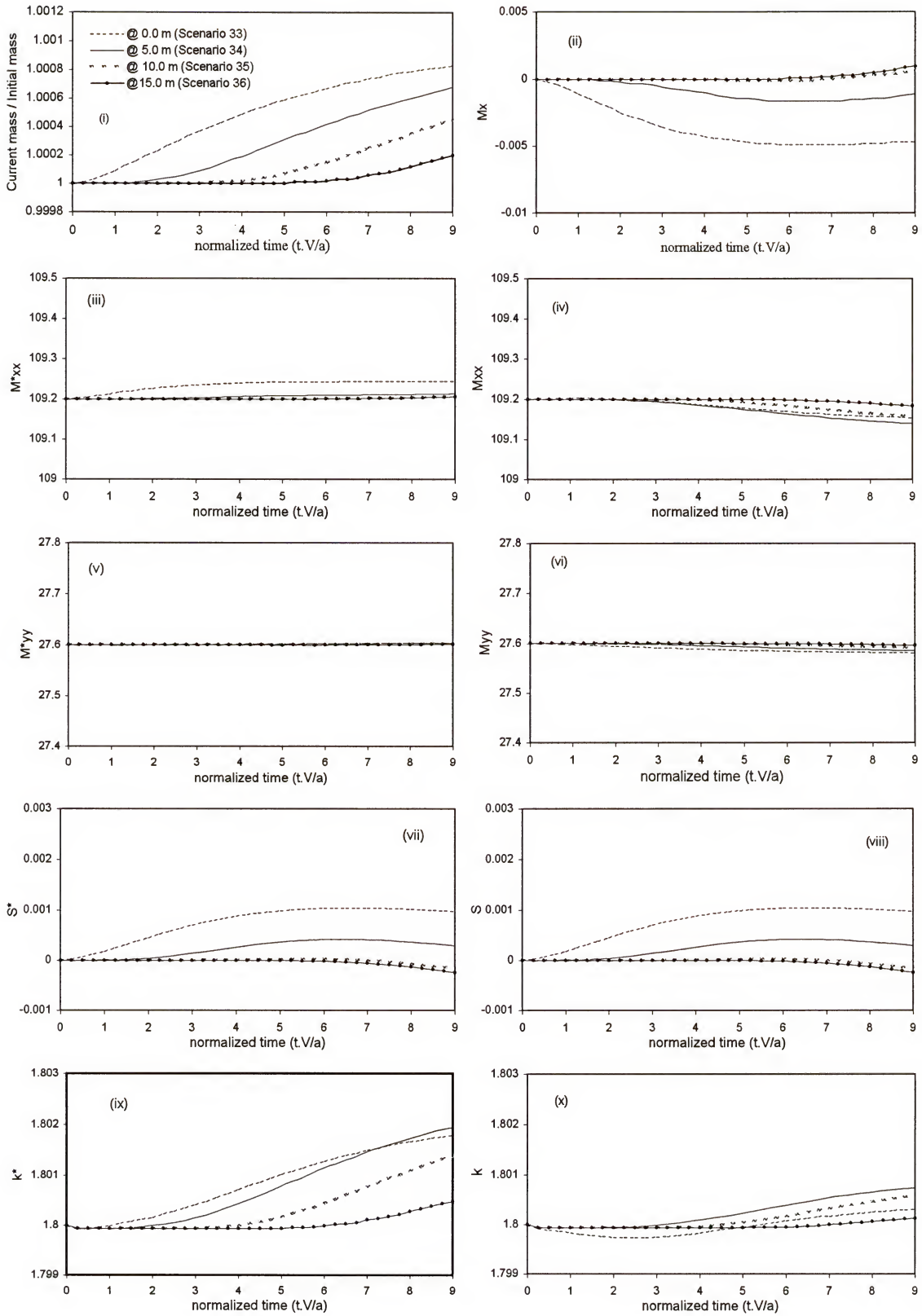


Figure 7-11d Effect of line source position on biomass spatial moments for case 3.

CHAPTER 8

MONTE CARLO EVALUATION OF CHROMIUM REDUCTION IN TWO-DIMENSIONAL HETEROGENEOUS AQUIFERS

8.1. Introduction

Conditions affecting metal biotransformations in the subsurface can be separated into three groups including physical, chemical, and biological factors. Physical heterogeneity, represented by the spatial variability in hydraulic conductivity, has been studied extensively to characterize field-scale dispersion (Gelhar et al. 1979; Gelhar and Axness 1983; and Dagan 1984 and 1988). The term “chemical heterogeneity” is used to describe spatial variability of abiotic contaminant reaction parameters. This may include spatial variations in abiotic degradation rates and contaminant sorption coefficients derived from spatially heterogeneous aquifer materials (Bellin et al. 1993; Burr et al. 1994, Hu et al. 1995 and 1997; Valocchi 1989; Cvetkovic and Shapiro 1990; Dagan and Cvetkovic 1993; and Cvetkovic et al. 1998). In an earlier investigation Garabedian et al. (1988) assumed simple linear reversible equilibrium sorption and concluded that the distribution and mixing of a reactive solute is influenced by spatial dependent sorption characteristics. Finally, there is biological heterogeneity represented by a heterogeneous spatial distribution of microbial species, biomass, and activities. Though this is the least understood of the three factors of variability, spatial distributions of biological processes are believed to have a significant effect on contaminant transport in the subsurface.

Factors affecting the biotransformation of metals include the biomass concentration, the rates of microbial growth and death, the availability of electron donors and nutrients, the existence of other electron acceptors, and the interaction between the different microbial species in the system [see previous chapters]. Though it has been recognized in the literature [Baker (1986) and Schafer and Kinzelbach (1991)], the effects of biomass heterogeneity on contaminant transport have not gained much attention. Furthermore, the correlation between the spatial heterogeneity of aquifer materials and biomass concentrations has received limited consideration.

Taking a stochastic approach, both Miralles-Wilhelm et al. (1997) and Scholl (2000) examined biodegradation at the field scale. Miralles-Wilhelm et al. (1997) presented an analytical model to quantify subsurface oxygen-limiting biodegradation at the field scale. Their model incorporates effects of chemical and microbiological heterogeneities. The purpose of the modeling exercise was to obtain field-scale effective coefficients of retardation, dispersion, and decay of a soluble contaminant undergoing advection, sorption, and biodegradation in the subsurface. To simplify the analytical model, they assumed a steady state microbial population. Therefore, ignored the transient effects of the microbial growth. Miralles-Wilhelm et al. (1997) concluded that the effective contaminant decay rate is less than the spatial mean.

Scholl (2000) performed numerical simulations using the USGS model (BIOMOC) to study the effects of spatially distributed rates of biodegradation and hydraulic conductivity on plume-scale rates of biodegradation derived from field data. Three sets, 10 realizations each, with different degrees of heterogeneity were used. Similar to Miralles-Wilhelm et al. (1997) study, Scholl (2000) ignored biomass growth,

death, and growth inhibition. Scholl (2000) concluded that using an effective hydraulic conductivity/flow velocity and biomass distribution underestimates the time required to remediate a contaminated aquifer.

In this chapter, Monte Carlo simulations are used to study the effects of correlated and uncorrelated physical (hydraulic conductivity) and biological (biomass concentration) heterogeneity on the reduction of Cr(VI) in the subsurface. Unlike previous investigations found in the literature, microbial growth is simulated, as is the transient and spatial availability of electron donors in the aquifer. Thus, the effects of physical and biological variability on both metal and biomass concentrations are examined.

8.2. Monte Carlo Simulations

The objective of Monte Carlo simulations is to assess the effects of spatial variability in aquifer physical and biological properties on the biotransformation process. This effect is studied through changes in solute and biomass distributions and the effectiveness of biotransformation. The latter is represented by the total untransformed Cr(VI) mass that remains in the aquifer. By comparing Monte Carlo simulations to homogeneous scenarios of assumed uniform physical and biological properties, one can evaluate the importance of physical and biological heterogeneity and the significance of possible correlation between them. Furthermore, Monte Carlo simulations provide predictions for the ensemble mean concentrations of different species as well as the uncertainty of these predictions, which are represented by concentration variances. Quantifying the uncertainty of the prediction has been recognized as crucial information for remediation design and risk assessment studies.

The general approach taken in this chapter can be described in four steps. First, spatial correlation functions of each parameter are specified and then used in conjunction with a random field generator (RFG) to create multiple realizations of spatially varying parameters (conductivity, K , and biomass, M , in this case). The RFG is based on the Fast Fourier Transform approach described and used by *Hassan et al.* [1997, 1998]. Second, the flow problem is solved over all realizations of the two-dimensional conductivity field under the appropriate boundary conditions.

A schematic representation of the two-dimensional hypothetical problem is shown in Figure 8-1a. The left and right boundaries are assigned constant head values, whereas the top and bottom boundaries are considered impervious. Using the specified heads boundaries, a hydraulic gradient is imposed to produce a macroscopic mean velocity of 0.5 m/d along the longitudinal direction. The heterogeneous conductivity field in turn produces local velocities with both longitudinal as well as transverse components. Once the flow equations are solved and the velocity field is obtained, the third step is to simulate the fate and transport of Cr(VI) and an electron donor in the presence of a growing mass of bacteria; hence, coupled equations are solved that describe microbial growth and the fate and transport of metal and electron donor. The solution of these equations progresses over discrete time steps for the total simulation period. Finally, quantities of concern are obtained from each realization including Cr(VI) fluxes and concentrations of both Cr(VI) and biomass. The ensemble of these solutions is then analyzed for the statistics of concern, e.g., mean concentrations, concentration variance, and spatial moments of the mean Cr(VI) and biomass distributions. The bioremediation efficiency calculated in this chapter is also obtained from the mean Cr(VI) plume.

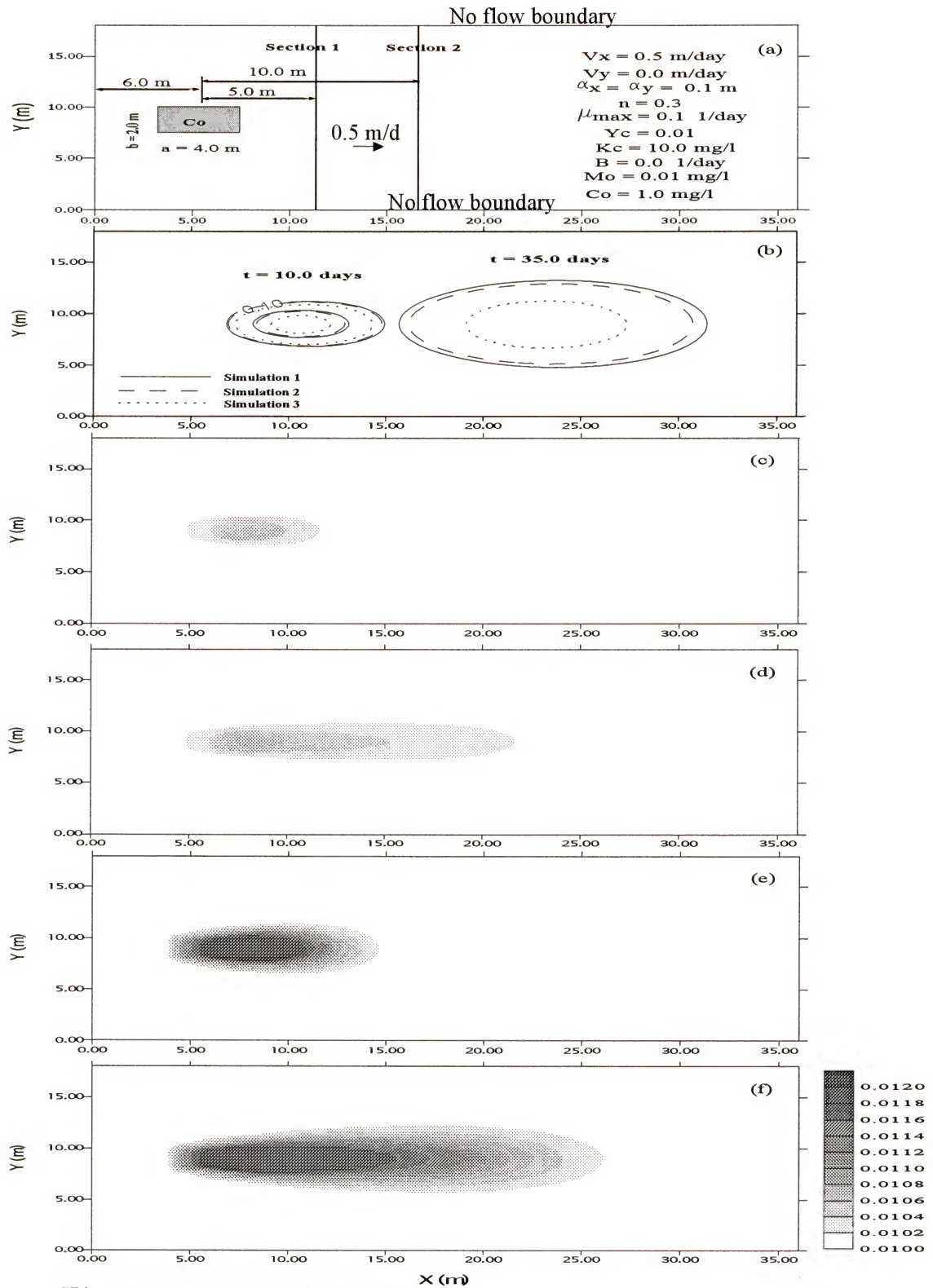


Figure 8-1 (a) Problem layout.

(b) Cr(VI) concentration lines of deterministic cases.

(c) Biomass concentration lines of Simulation 2 at $t=10$ days.

(d) Biomass concentration lines of Simulation 2 at $t=35$ days.

(e) Biomass concentration lines of Simulation 3 at $t=10$ days.

(f) Biomass concentration lines of Simulation 3 at $t=35$ days.

To generate the heterogeneous K and M distributions, a statistically homogeneous, isotropic, and second-order stationary random field with spatial correlation structure is assumed. The conductivity and biomass are assumed to have a lognormal distribution with an exponential covariance structure ($Cov(r) = \sigma^2 e^{-r/\lambda}$), in which σ^2 is the process variance, r is the spatial lag, and λ is the correlation length that describes the distance over which conductivity or biomass values are spatially correlated. To use the RFG, the variance, the correlation length, and the geometric (or arithmetic) mean of the conductivity and biomass are specified. In this chapter, a log K variance of 1.0, a log M variance of 1.0 and 3.0, a unit correlation length, and an arithmetic mean for M of 0.01 mg/l are used. The discretization of the finite element mesh is kept at 5 elements per correlation length for all the simulations presented here. An initial release of Cr(VI) with concentration of 1 mg/l is assumed. Modeling input parameters are summarized as following:

Discretization parameters:

Aquifer dimensions in X- and Y-directions (m)	= 36 m x 18 m
Element size in X-direction (Δx)	= 0.2 m
Element size in Y-direction (Δy)	= 0.2 m
Number of elements	= 16,200
Time step for transport equation (Δt_r)	= 0.5 day
Time step for biological equations (Δt_b)	= 0.005 day

Flow and transport parameters:

Velocity in X-direction (V_x)	= 0.5 m/d
Velocity in Y-direction (V_y)	= 0.0 m/d

Dispersivity in X-direction (α_x)	= 0.1 m
Dispersivity in Y-direction (α_y)	= 0.1 m
Porosity (n)	= 0.3
Size of the initial source of contamination (a x b)	= 4.0 m x 2.0 m
Initial concentration of Cr(VI) (C_0)	= 1.0 mg/l

Biological parameters

Microorganisms' death rate (B)	= 0.00 day ⁻¹
Cr(VI) yield coefficient (Y_c)	= 0.01
Cr(VI) half saturation coefficient (K_c)	= 10.0 mg/l
Inhibition factor (K_i)	= 10.0 mg/l
Concentrations of other electron acceptors (E_e)	= 0.0 mg/l

Because an abundance of electron donors and nutrients is assumed to exist everywhere in the aquifer (unless mentioned otherwise), it can be assumed that $S \gg K_s$ (equation 4-16). In addition, it is assumed that changes in the concentrations of electron donors and the nutrients are small compared to their initial concentrations.

Four general cases are investigated in this chapter. In the first case, only physical heterogeneity (hydraulic conductivity) is considered; whereas, in the second case biological heterogeneity (biomass concentration) alone is studied. In the third case, both heterogeneities are treated as correlated processes and investigated simultaneously. Finally, in the fourth case, spatial variability in electron donor concentrations is examined. Within each case, a sensitivity analysis is performed that involves other parameters such as the microbial growth rate and the variance (σ^2) of the initial biomass concentration in the aquifer. Table 8-1 summarizes all simulations considered.

Table 8-1. Summary of differences between all Simulations

<i>Simulation</i>	<i>Number of Realizations</i>	<i>Random Variable</i>	μ_{\max}	<i>Variance of K and/or M</i>
1	Homogenous	--	0	--
2	Homogenous	--	0.1	--
3	Homogenous	--	0.5	--
4	500	K	0	1.0
5	500	K	0.1	1.0
6	500	K	0.5	1.0
7	250	M	0.1	1.0
8	250	M	0.5	1.0
9	250	M	0.5	3.0
10	500	K & M (Uncorrelated.)	0.1	1.0
11	500	K & M (-ve correlation)	0.1	1.0
12	500	K & M (Uncorrelated)	0.5	1.0
13	500	K & M (-ve correlation.)	0.5	1.0
14	500	K & M (+ve correlation)	0.5	1.0
15	500	K & M (+ve correlation)	0.5	3.0
16	500	K & M (-ve correlation) & Uncorrelated to S	0.5	1.0 & 1.0

Three simulations (Simulations 1-3) were performed to serve as homogenous base cases to which results of other simulations are compared. In these three simulations, a uniform initial distribution of biomass concentration 0.01 mg/l is assumed to exist throughout the aquifer. In addition, a uniform velocity of 0.5 m/day in the X-direction is assumed. No biotransformation activities are assumed in simulation 1; hence, a simple advective-dispersive transport problem is simulated. Biotransformation activities are simulated in simulations 2 and 3 using low and high microbial maximum growth rates ($\mu_{\max} = 0.1$ and 0.5 day^{-1} , respectively).

The effects of increasing the biotransformation rate on both Cr(VI) and biomass concentrations at $t = 10$ and 35 days are presented in Figure 8-1b; and as expected, increasing μ_{\max} in Simulation 3 decreases soluble Cr(VI) at both times. Figures 8-1c, d, e, and f present biomass concentrations for Simulations 2 and 3 at both times (10 and 35 days), respectively. As expected, increasing the bacterial maximum growth rate by a factor of five in Simulation 3 significantly increases the resident microbial biomass.

8.3. Physical Heterogeneity

Three different simulations are used to study the effects of physical heterogeneity (Simulations 4-6, Table 8-1) on the concentrations and spatial moments of both Cr(VI) plume and bacterial populations. In all three simulations, 500 realizations of hydraulic conductivity fields with variance of 1.0 are used to generate 500 velocity fields, which are then used in the transport model. In Simulation 4, biological activities are not simulated; whereas for Simulations 5 and 6 biological activities are taken into account with low and high microbial growth rates, respectively. Figures 8-2a and b compare the ensemble mean concentrations of Cr(VI) for Simulation 4 with those of Simulation 5 after 10 and 35 days, respectively. Both figures show the effects of microbial activity on reducing Cr(VI) concentrations at both times. These effects are similar to those obtained from the two homogenous simulations (1 and 2) [Figure 8-1b].

Studying the concentration distributions of Cr(IV) alone does not reveal the effects of physical heterogeneity on the total reduced mass of Cr(VI). For that reason, Table 8-2 is used to show the percentage of mass reduced to the initial mass of Cr(VI) at the end of each simulation. Looking at simulation 5, physical heterogeneity did not change the total mass of Cr(VI) reduced as compared to the homogenous case

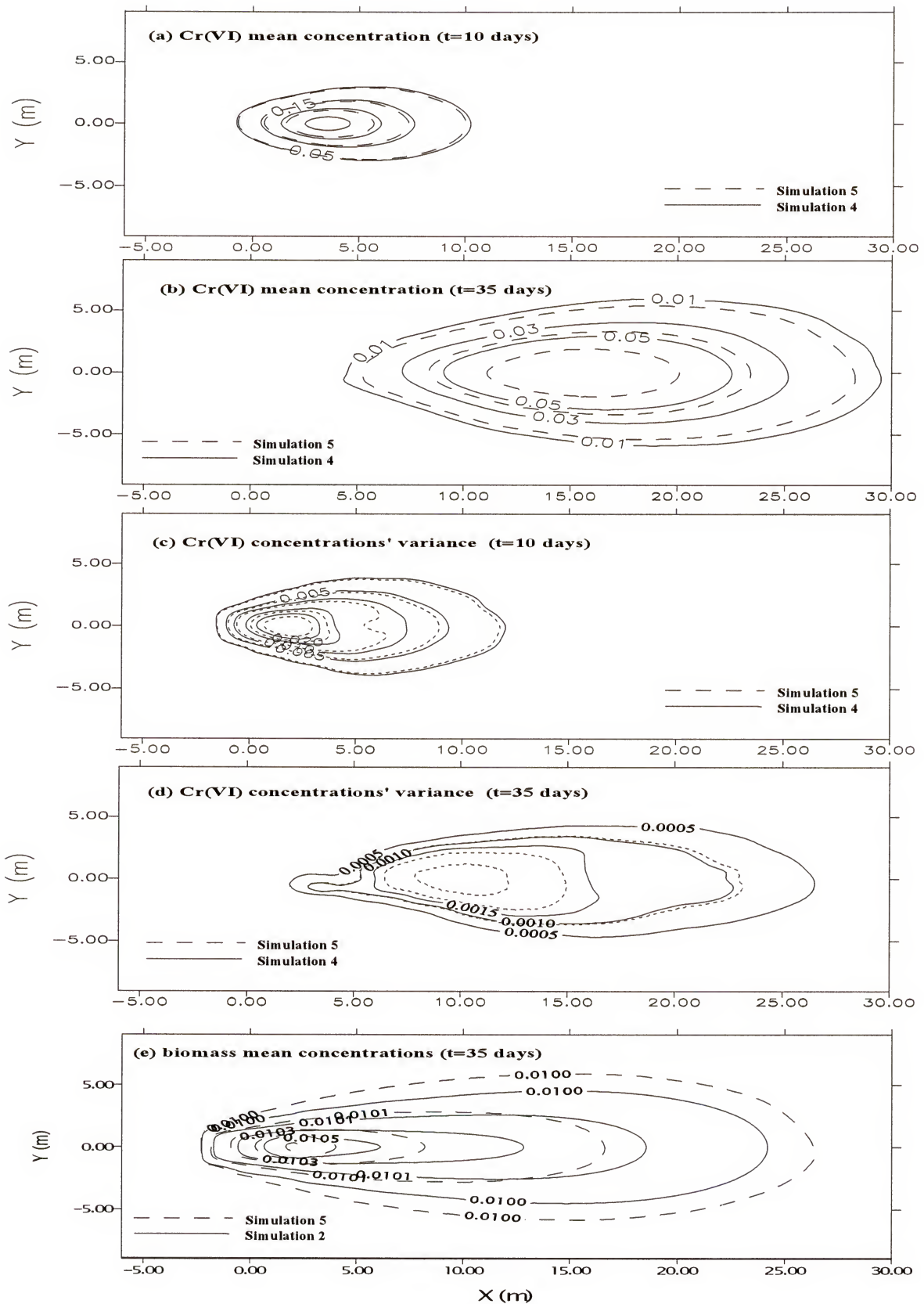


Figure 8-2 Comparison between Cr(VI) and biomass mean concentrations and variance for simulations 2, 4 and 5.

(Simulation 2); however, it induced a clear increase in dispersion in both longitudinal and transverse directions (compare the Cr(VI) plume in Figures 8-1b and 8-2b). Figures 8-2c and d present the uncertainty in the evaluated Cr(VI) mean concentrations for Simulations 4 and 5 after 10 and 35 days. Because biological activities decrease Cr(VI) concentrations, a consequent reduction in the concentration variances in Simulation 5 is observed compared to the homogenous case.

Table 8-2 Bioremediation efficiencies of the different simulations

Simulation	Bioremediation Efficiency
1	0.00
2	0.46
3	0.91
4	0.00
5	0.46
6	0.90
7	0.45
8	0.88
9	0.81
10	0.45
11	0.45
12	0.88
13	0.88
14	0.87
15	0.80
16	0.54

In Simulation 5, the increase in the hydrodynamic dispersion (created by physical heterogeneity) enhanced Cr(VI) transport which in turn stimulated the development of higher ensemble mean biomass concentrations further downgradient than obtained from the homogeneous case (Simulation 2) (Figure 8-2e). However, because the total growth in biomass is the same for both simulations (same total reduced mass of Cr(VI), Table 8-

2), lower peak of Cr(VI) concentrations are observed in simulation 5 as compared to simulation 2 (Figure 8-2e).

Figure 8-3a illustrates the spatial moments of Cr(VI) plumes from Simulations 1, 2, 4, and 5. Figure 8-3a(i) reveals that spatial variability in hydraulic conductivity did not change the total mass of Cr(VI) reduced. Similarly, Figure 8-3a(ii) shows that for the cases of uniform biological activity and physical heterogeneity, the centroid of Cr(VI) plume migrated at a constant velocity. Figures 8-3a(iv and vi) clearly illustrate that physical heterogeneity increases dispersion in both longitudinal and transverse directions; although the same figures do not reveal the effects of biotransformations on Cr(VI) concentration variance. This is because, as discussed in previous chapters, the second moments are normalized by the current Cr(VI) mass. However, when the initial Cr(VI) mass is used to normalize longitudinal and transverse second moments [Figures 8-3a(iii and v)], the effects of microbial activities become clearly evident. Hence, in Figures 8-3a(iii and v) the combined effects of physical heterogeneity with biotransformations are presented in the time rate of change in normalized variance of the mean concentration of the Cr(VI) plume. Furthermore, the same two figures indicate that the effect of biologically induced reduction is most evident in the second moment when physical heterogeneity is considered. Figures 8-3a(vii-x)] show that physical variability increases both skewness and peakness of the Cr(VI) concentration distribution at early times. However, both moments decrease more rapidly with time than in the homogenous cases.

Cr(VI) mass fluxes calculated at two sections (1 and 2, Figure 8-1a) located 5 and 10 m, respectively, downstream from the center of the initial Cr(VI) release are presented in Figure 8-3b(i) for Simulations 1, and 2. The same figure also shows the ensemble

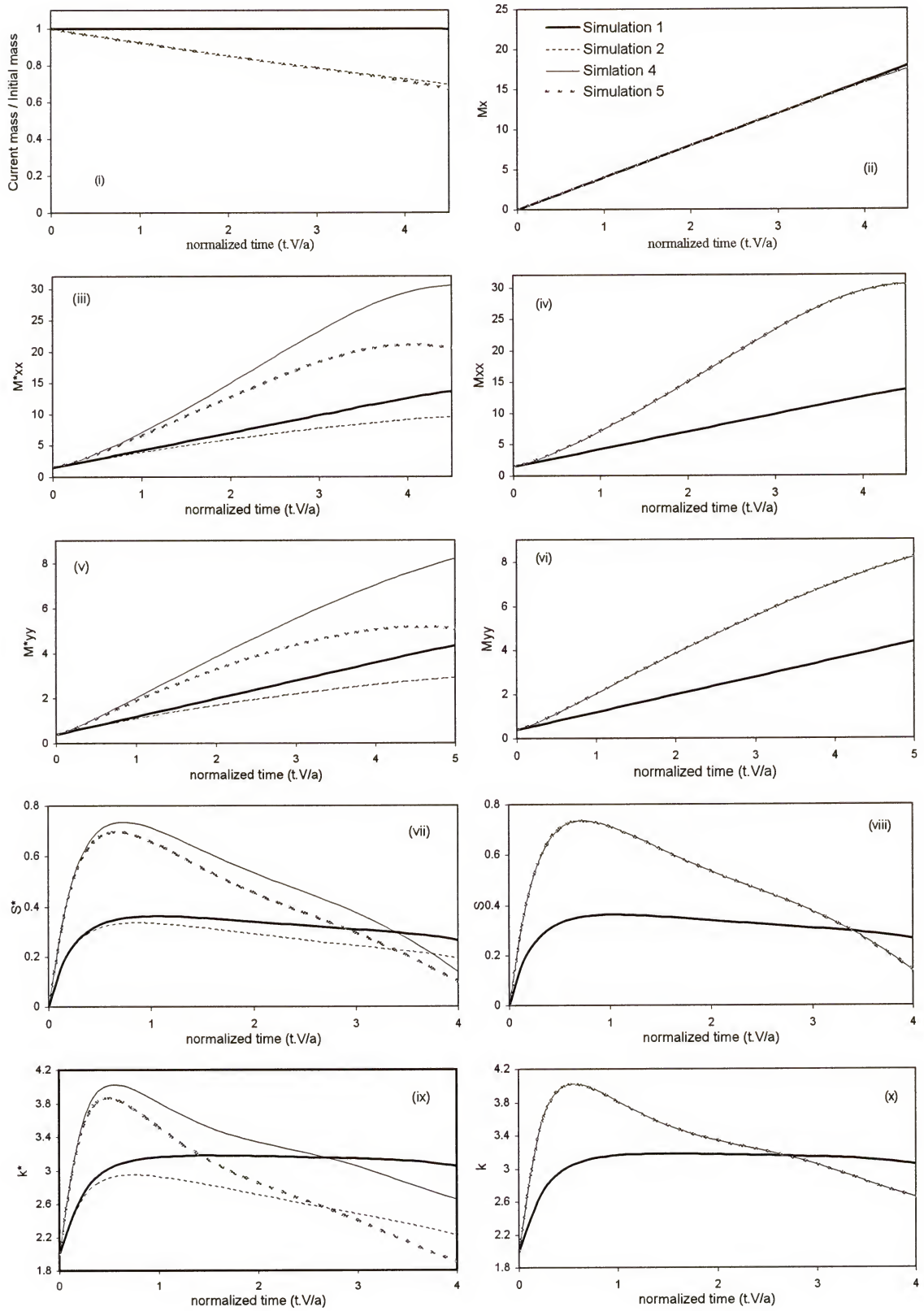


Figure 8-3a Spatial moments of Cr(VI) plume for simulations 1, 2, 4, and 5.

mean mass fluxes from Simulations 4 and 5 at the same two sections. As expected, cumulative mass flux across each section is less when Cr(VI) reduction is considered (Simulations 2 and 5). The same conclusions can also be drawn from Table 8-3 by comparing cumulative Cr(VI) mass traversing the two sections in Simulations 1 and 2, or 4 and 5. This table also shows Cr(VI) fluxes at section 2 being less than that at section 1 in simulations where biological activity exists. This conclusion could not be quantitatively deduced from viewing Figure 8-3b(i) alone.

Because physical heterogeneity increases dispersion in both directions, attenuation of peak mass fluxes at both sections is evident (compare Simulation 1 with 4 and 2 with 5) [Figure 8-3b(i)]; although, from Table 8-3 this type of heterogeneity has no effect on the cumulative mass flux (compare Simulations 2 and 5).

The peak of the mean mass flux at each section occurs approximately at the time when the centroid of the Cr(VI) plume is passing through the section. However, that is not the case with mass flux variance.

Clearly, there are two periods of high uncertainty in mass flux; the first occurs as the leading edge of the plume reaches the section, while the second occurs as the trailing edge traverses the same section. That explains the existence of two peaks in the mass flux variance curves [Figure 8-3b(ii)]. The uncertainty associated with the arriving of the leading or the trailing edge of the plume at a section depends on both the variability of the groundwater velocity. That is, more plumes (of the simulated realizations) arrive earlier at any section causing more variability, and therefore, the higher the peak of the flux variance. Therefore, at any section, because the leading edge arrives earlier than the trailing edge the uncertainty in mass flux is greater at the leading edge [Figure 3b(ii)].

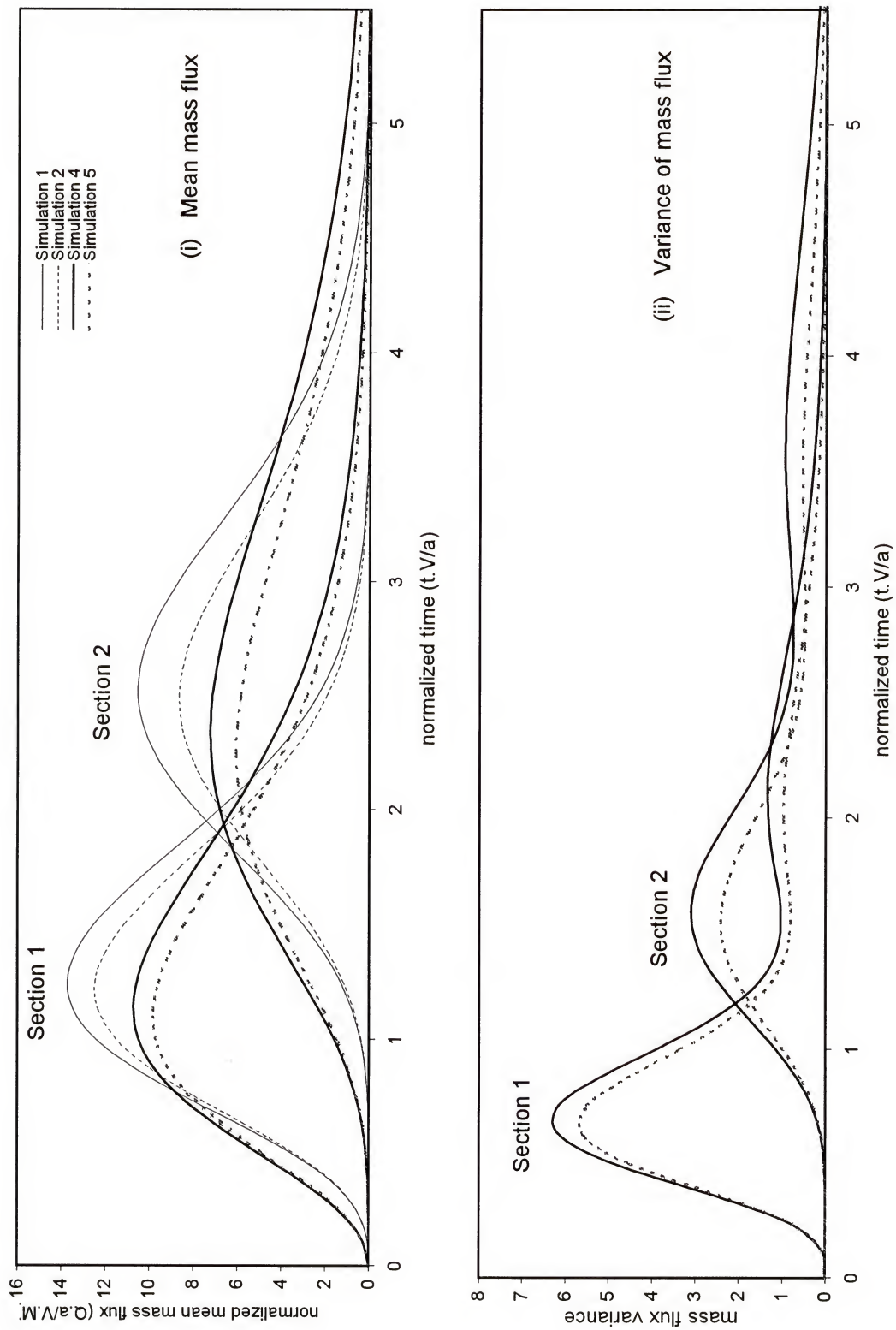


Figure 8-3b Mass fluxes of simulations 1, 2, 4 and 5.

For the same reason, the first peak of the mass flux uncertainty at any section is higher than that of other sections located further downgradient of the contaminant source [compare sections 1 and 2 in Figure 8-3b(ii)].

Table 8-3 Percentage of total Cr(VI) mass traversing sections 1 and 2.

Simulation	Section 1	Section 2
1	1.00	1.00
2	0.90	0.81
3	0.63	0.39
4	1.00	1.00
5	0.88	0.81
6	0.62	0.40
7	0.90	0.82
8	0.66	0.42
9	0.70	0.46
10	0.88	0.81
11	0.89	0.81
12	0.65	0.44
13	0.65	0.44
14	0.65	0.43
15	0.71	0.51
16	0.87	0.77

The presence of biotransformation decreases Cr(VI) concentrations between sections, which in turn decreases mass flux variance as the plume migrates downgradient. A closer look at Figure [8-3b(ii)] suggests a greater decrease in flux variance occurs at the trailing edge of the plume than at the leading edge. This occurs most likely because the trailing edge encounters more biotic activities than the leading edge, as more time is required for the trailing edge to reach each section.

The effects of physical heterogeneity on the ensemble mean concentrations of both Cr(VI) and biomass were studied via Simulation 5. In this simulation a low microbial maximum growth rate (0.1 day^{-1}) is used, which resulted in a bioremediation efficiency of only 46%. Increasing the microbial maximum growth rate itself might further amplify the effects of physical heterogeneity. To investigate this, Simulation 6 was conducted using a higher microbial growth rate of 0.5 day^{-1} (Table 8-1).

Figures 8-4(a and b) show that five fold increase of μ_{\max} reduces the ensemble mean of Cr(VI) concentrations dramatically at $t = 10$ and 35 days. This change in μ_{\max} also increased bioremediation efficiency to 90% (Table 8-2). Simultaneously, the ensemble Cr(VI) concentration variance dramatically decreased [Figures 8-4c and d].

Like Figure 8-2e, Figure 8-4e shows the increased spatial extent of microbial growth associated with physical heterogeneities. Despite that huge reduction in Cr(VI) mass for Simulation 6 [Figure 8-5a(i)], physical heterogeneity alone still has minor effect on the mass of Cr(VI) reduced (obtained from mean Cr(VI) plume) as compared to the homogenous case (Simulation 3). The same conclusion can also be drawn from Table 8-2 as the bioremediation efficiency of Simulation 6 (90%) is very close to that of Simulation 3 (91%). Therefore, it can be concluded that physical heterogeneity alone does not affect the estimation of the mass of Cr(VI) reduced (obtained from the mean plume) when uniform initial biomass and constant biological parameters are assumed and microbial transport is not considered. Increasing μ_{\max} dramatically decreases the Cr(VI) mass and, as a result, reduces all spatial moments normalized with respect to the initial Cr(VI) mass (M_{xx}^* , M_{yy}^* , s^* , and κ^*) [Figures 8-5a(iii, v, vii, and ix)]; this observation is even more evident when comparisons are made with Figure 8-3a.

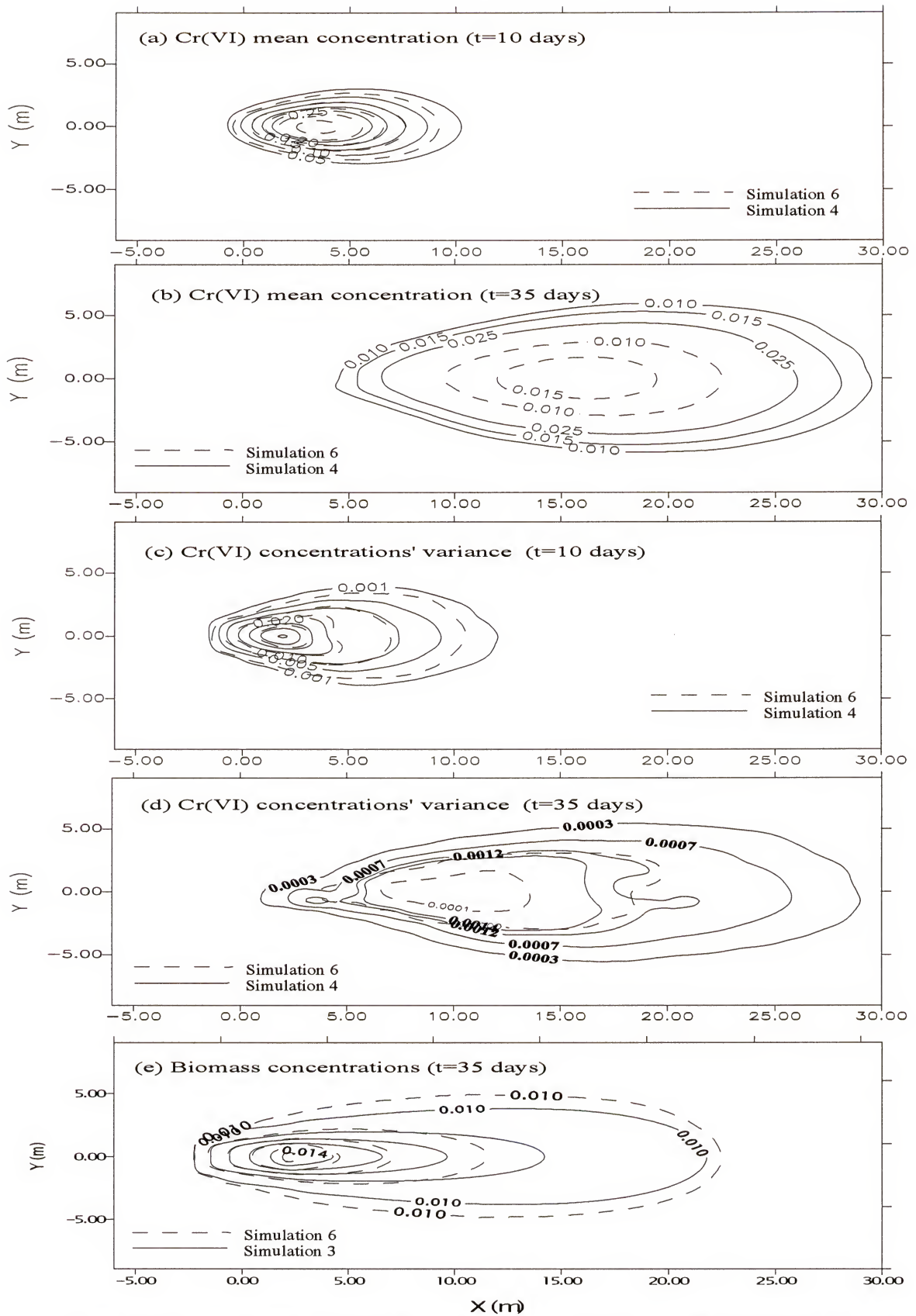


Figure 8-4 Comparison between Cr(VI) and Biomass mean concentrations and variance for simulations 3, 4 and 6.

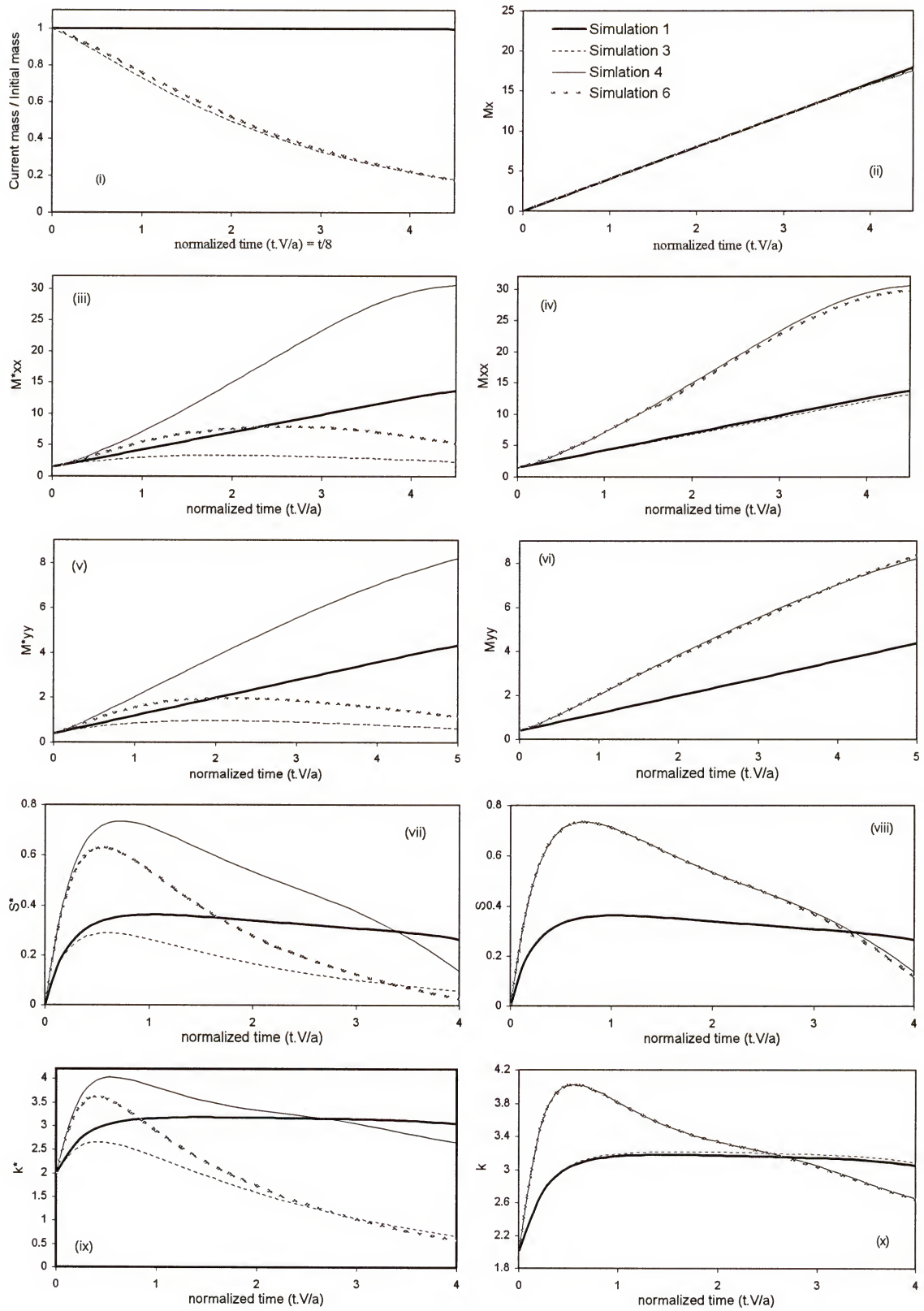


Figure 8-5a Spatial moments of Cr(VI) plume for simulations 1, 3, 4, and 6

Figure 8-5b illustrates the different spatial moments of biomass distributions from scenarios 3 and 6. Despite using higher μ_{\max} in both simulations, physical heterogeneities did not greatly affect the increase in total biomass at any time [Figure 8-5b(i)]. Figure 8-5b(ii) shows that at early times, the bacterial center of mass drifts upgradient from the center of the aquifer (its initial position) towards the position of initial Cr(VI) release (i.e., in the negative X-direction). However, as the Cr(VI) plume migrates downgradient (in the positive X-direction) the direction of drift reverses such that the biomass centroid trails the Cr(VI) plume.

The initial value of the second spatial moment is relatively high because biomass is uniformly distributed in the aquifer at that time [Figure 8-5b(iv)]. However, the same figure suggests that as microbes grow near the centroid of the Cr(VI) plume, biomass second spatial moments slightly decreases [Figure 8-5b(iv)]. The second moment of biomass concentrations normalized by the initial biomass increase with time because the biomass concentrations increase with time [Figure 8-5b(iii)].

The movement of the biomass centroid, as discussed earlier, explains the transient nature of skewness in the biomass distribution [Figures 8-5b(vii and viii)]. That is, as biomass increases with the Cr(VI) plume in the upgradient half of the aquifer, skewness increases. As the Cr(VI) plume migrates downgradient, bacterial concentrations increase there and skewness decreases. However, the increase in biomass is not large enough to change the peakness of the distribution [Figures 8-5b(ix and x)].

When the μ_{\max} is increased 5 times, a dramatic decrease of the mean mass fluxes across each of the two sections is noted [Figure 8-5c(i)] compared to simulations where a lower growth rate was used [Figure 8-3b(i)]. However, this effect is most evident at

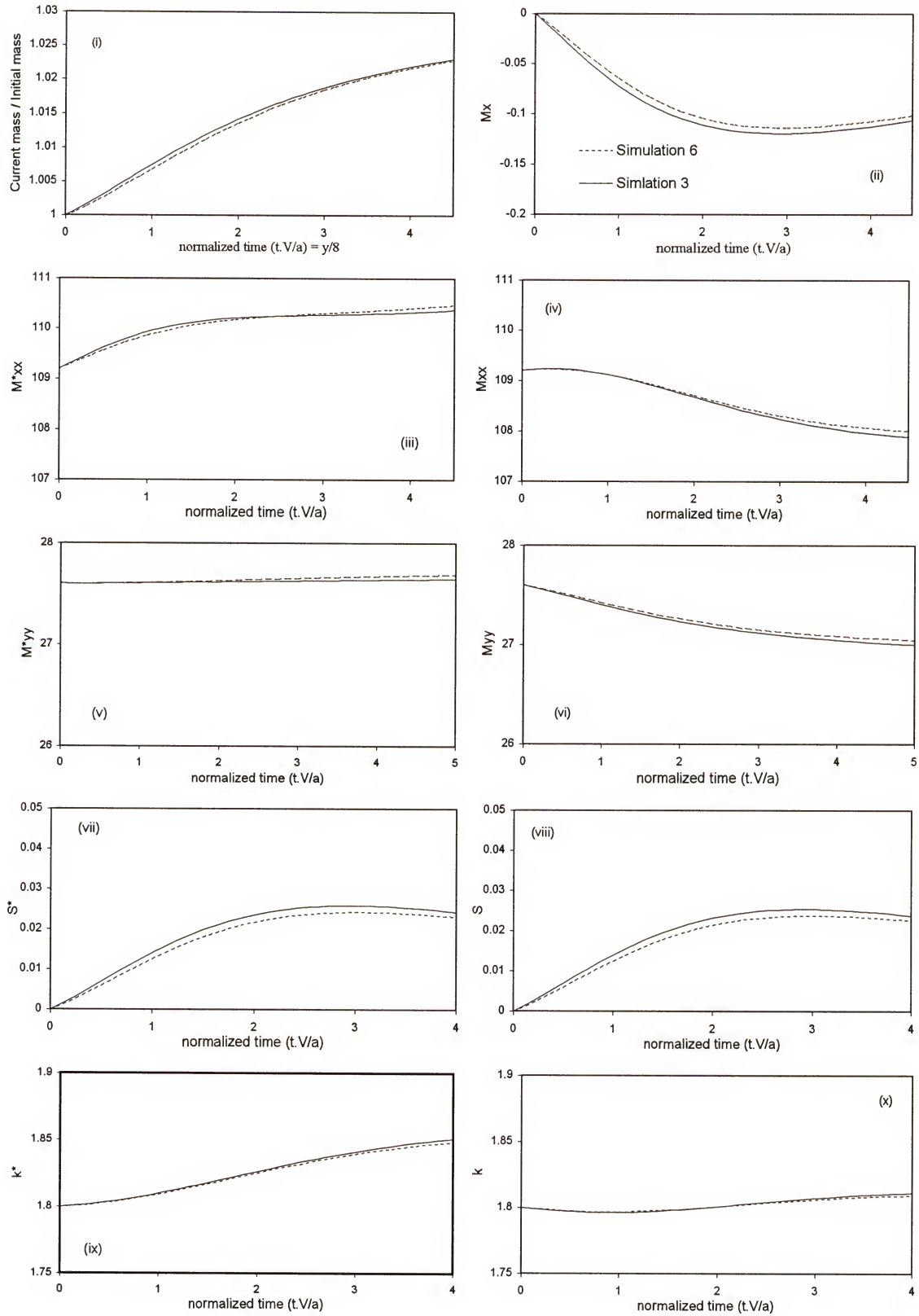


Figure 8-5b spatial moments of biomass distribution for simulations 3 and 6

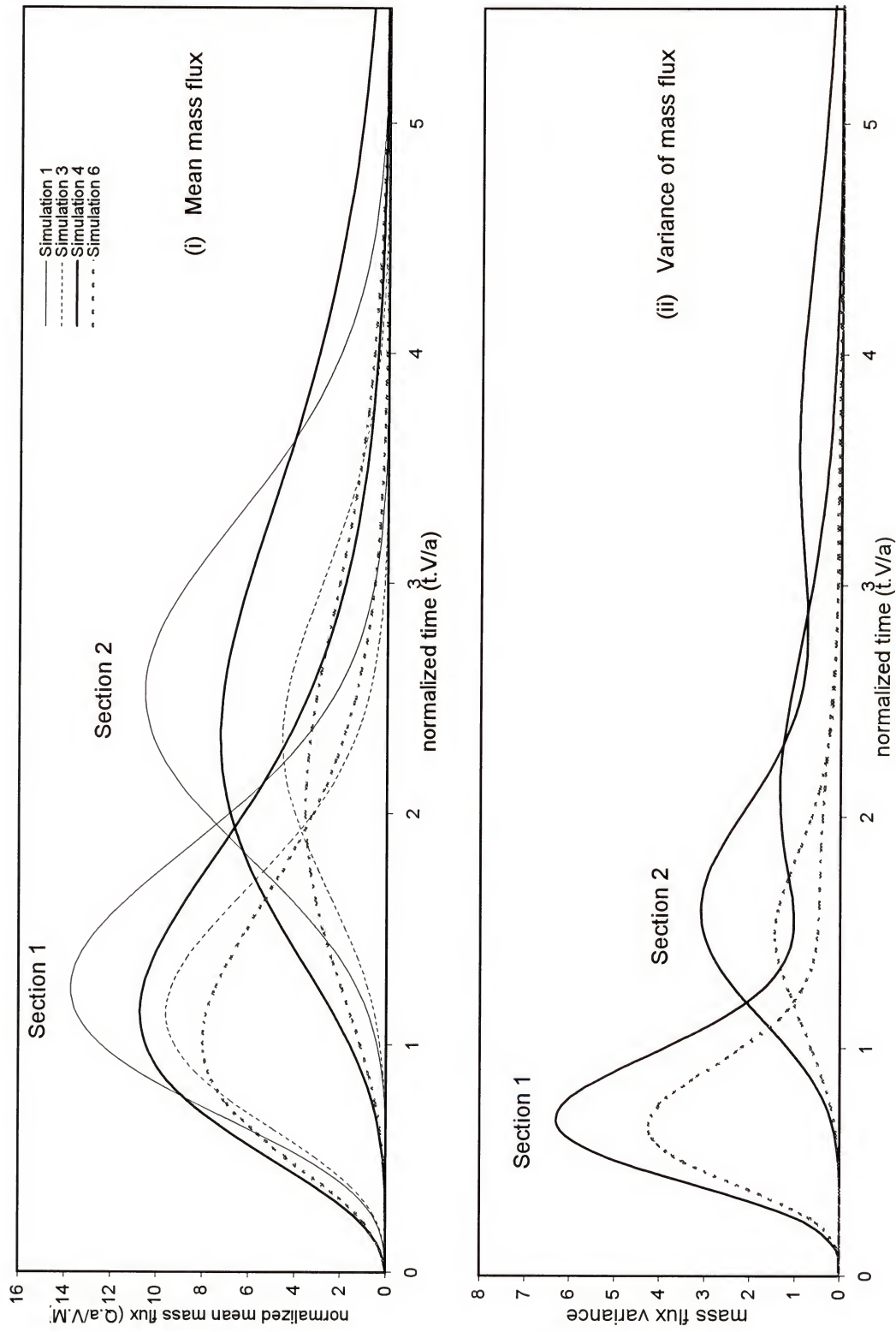


Figure 8-5c Mass fluxes of simulations 1, 3, 4 and 6.

section 2 before which Cr(VI) plume was exposed to more reduction than section 1. As expected, increasing growth rate decreases the Cr(VI) mass flux variance at both sections [Figure 8-5c(ii)]. Because the trailing edge of the Cr(VI) plume was exposed to more reduction in Simulation 6, a second peak in variance did not appear [Figure 8-5b(ii)].

In conclusion, regardless of the increase in bacterial growth rate, including physical heterogeneity (Simulation 6) did not produce different estimates of mean cumulative mass fluxes at each section compared to deterministic results (Simulation 3) [Table 8-3]. As long as uniform initial microbial distribution and constant biological parameters are assumed, physical heterogeneity only affects the physical properties (such as dispersion) of the plume, and has minor effects on mean biological activities.

8.4. Biological Heterogeneity

In this section, biological heterogeneity (presented by spatial distribution of initial biomass concentration) is the only variability considered. The effect of such heterogeneity is studied through three simulations (7-9, Table 8-1). In Simulation 7, low microbial maximum growth rate is used (0.1 day^{-1}), while a higher one is used in Simulation 8 ($\mu_{\max} = 0.5 \text{ day}^{-1}$). The spatial variance (σ^2) of the initial biomass distribution is assumed to equal 1.0 in both simulations; however, it is increased to 3 in the third simulation (see Simulation 9 in Table 8-1). It should be noted that the mean initial biomass is constant between the three simulations (7-9) and equals the total initial biomass assumed in the homogenous simulations (2 and 3).

Figure 8-6a shows the effects of spatially variable biomass on the Cr(VI) concentrations compared to the case of a non-reactive solute (Simulation 1). Figure 8-6b, suggests that for a low μ_{\max} , biological heterogeneity does not significantly alter the

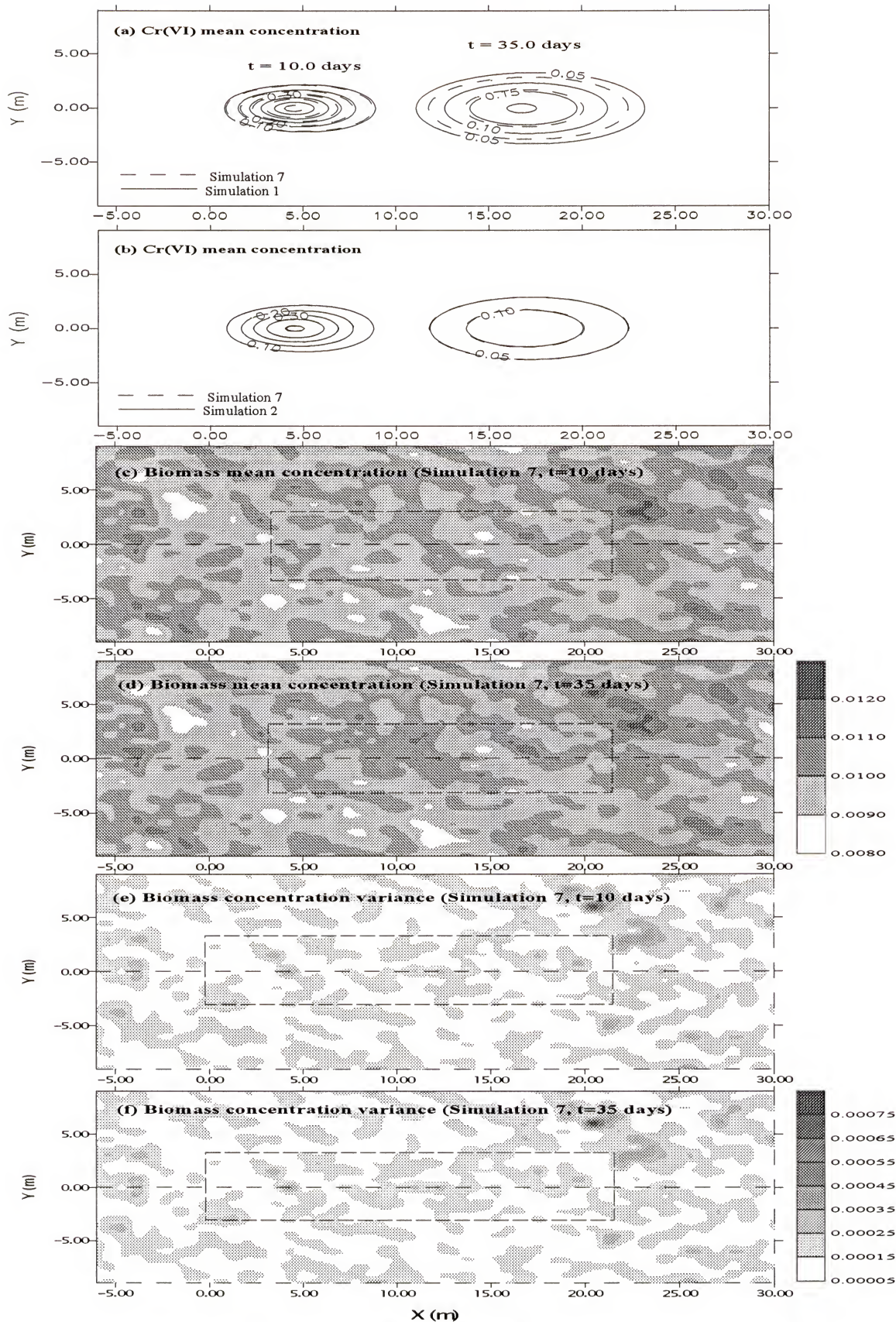


Figure 8-6 Comparison between Simulation 7 and deterministic cases.

reduction in Cr(VI) compared to that of the homogenous case (Simulation 2) at 10 and 35 days. That is also clear from Table 8-2 where values of the bioremediation efficiency of both simulations (2 and 7) are similar. In addition, because low microbial growth rate is assumed, minor increase in the ensemble mean biomass concentrations at $t = 35$ days is seen compared to that at $t = 10$ days [Figures 8-6c and d].

Associated with this small increase in the ensemble mean of biomass concentrations is a slight change in the variance [Figures 8-6e and f]. Because bacteria grow where the electron acceptor (Cr(VI)) exists, any increase in the mean or the variance of biomass concentrations is expected within the illustrated dashed boxes [Figures 8-6 (c, d, e, and f)], or within the region where the Cr(VI) plume migrates. Increasing μ_{\max} to 0.5 day^{-1} in Simulation 8 (Table 8-1) produces less Cr(VI) reduction than the corresponding homogeneous case of Simulation 3 [see Figures 8-7a and 8-2]. This reduction is associated with an increase in the bioremediation efficiency (Table 8-2). By comparing Simulation 8 to the homogenous case (Simulation 3), [Figure 8-7b], it becomes evident that the homogenous solution overestimates Cr(VI) mass reduced, and therefore, overestimates bioremediation efficiency (Table 8-2). This result suggests that homogenous modeling of systems may underestimate the time required to remediate an aquifer. In addition, increasing bacterial growth rate amplifies the differences between the homogenous and stochastic systems when biological variability is considered. Therefore, estimation of the microbial growth rate is crucial during the incipient stages of remediation when biological heterogeneity is considered. The higher the microbial growth rate the more noticeable the influence of the biological heterogeneity on nascent changes in Cr(VI) plume size, moments, and mass fluxes.

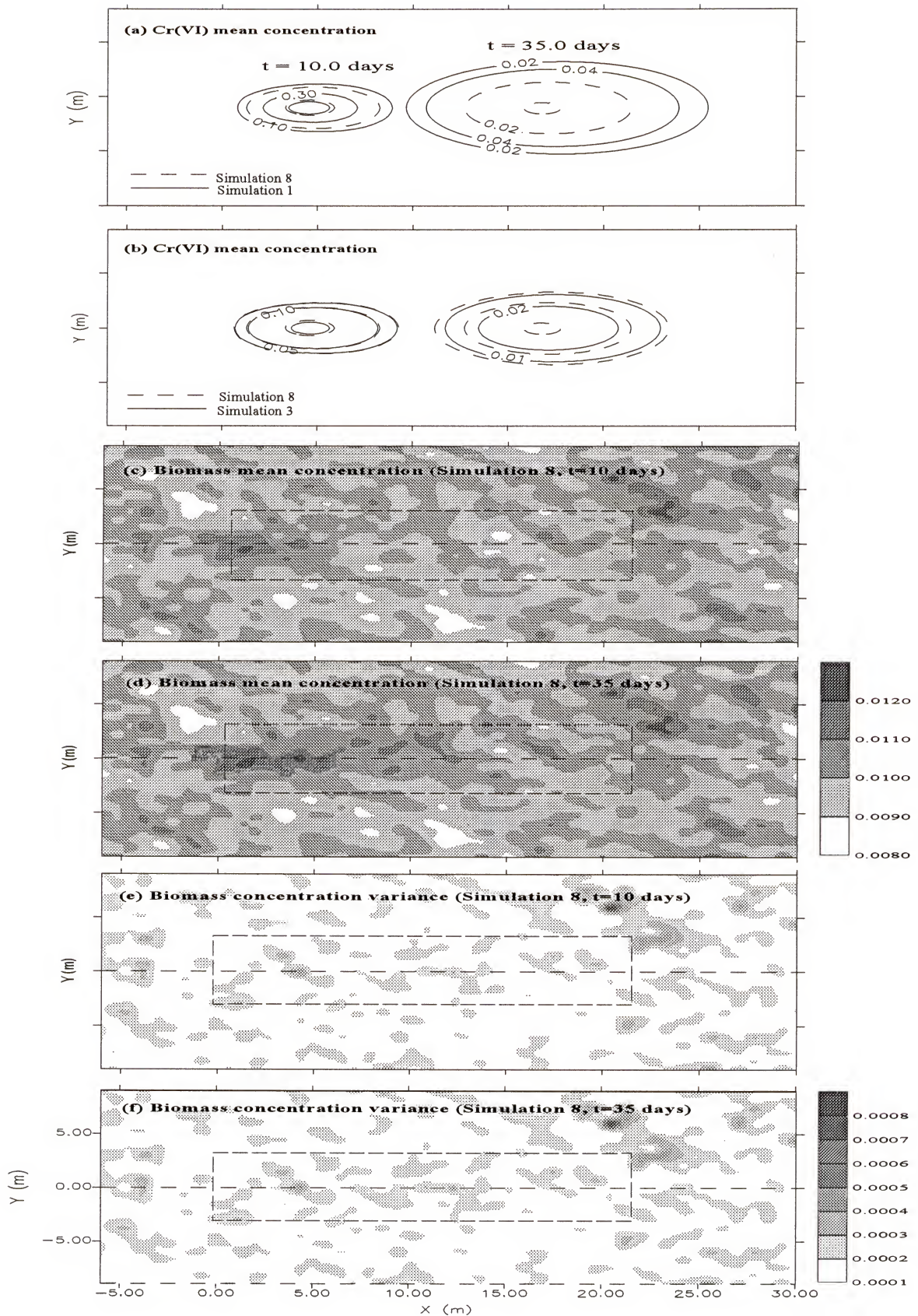


Figure 8-7 Comparison between Simulation 8 and deterministic cases (1 and 3).

Increasing the microbial maximum growth rate in Simulation 8 produced a distinctive increase in the mean biomass concentration within the Cr(VI) plume (dotted box) at $t = 35$ days, compared to that at $t = 10$ days [Figures 8-7c and d]. However, similar to Simulation 7 [Figure 8-6e and f] changes in local biomass concentrations variance in Simulation 8 are small [Figure 8-7e and f].

Increasing the variance of the initial biomass distribution (σ^2) in Simulation 9 leads to less Cr(VI) remediation than in either Simulations 3 or 8 [Figure 8-8a and b]. Table 8-2 indicates that increasing the value of (σ^2) results in a decrease in the estimated Cr(VI) attenuation efficiency. This occurs because increasing (σ^2) produces regions of extremely high and low biomass concentrations. As a result, Cr(VI) plume escapes attenuation as migrates through regions of low biomass concentrations.

Although both Simulations 8 and 9 were initiated with the same total initial volumetric biomass in the aquifer, Simulation 9 reflects the highest, as well as the lowest, bacterial concentrations, under the largest value of σ^2 . This is also clear by comparing biomass concentrations from both Simulations [compare Figures 8-7(c and d) with Figures 8-8(c and d)]. Similarly, Simulation 9 is characterized with the highest and lowest biomass concentration variances [compare Figures 8-7(e and f) with Figures 8-8(e and f)].

In general there is a reduction on attenuation efficiency as the variance of the initial biomass distribution is increased. Figure 8-9a presents the spatial moments of the Cr(VI) concentrations distribution. Figure 8-9a(i) emphasizes the point that was concluded from Table 8-2; that is the mass of Cr(VI) reduced in Simulation 9 is less than that in Simulations 3 and 8. For this reason, increasing biological heterogeneity increases

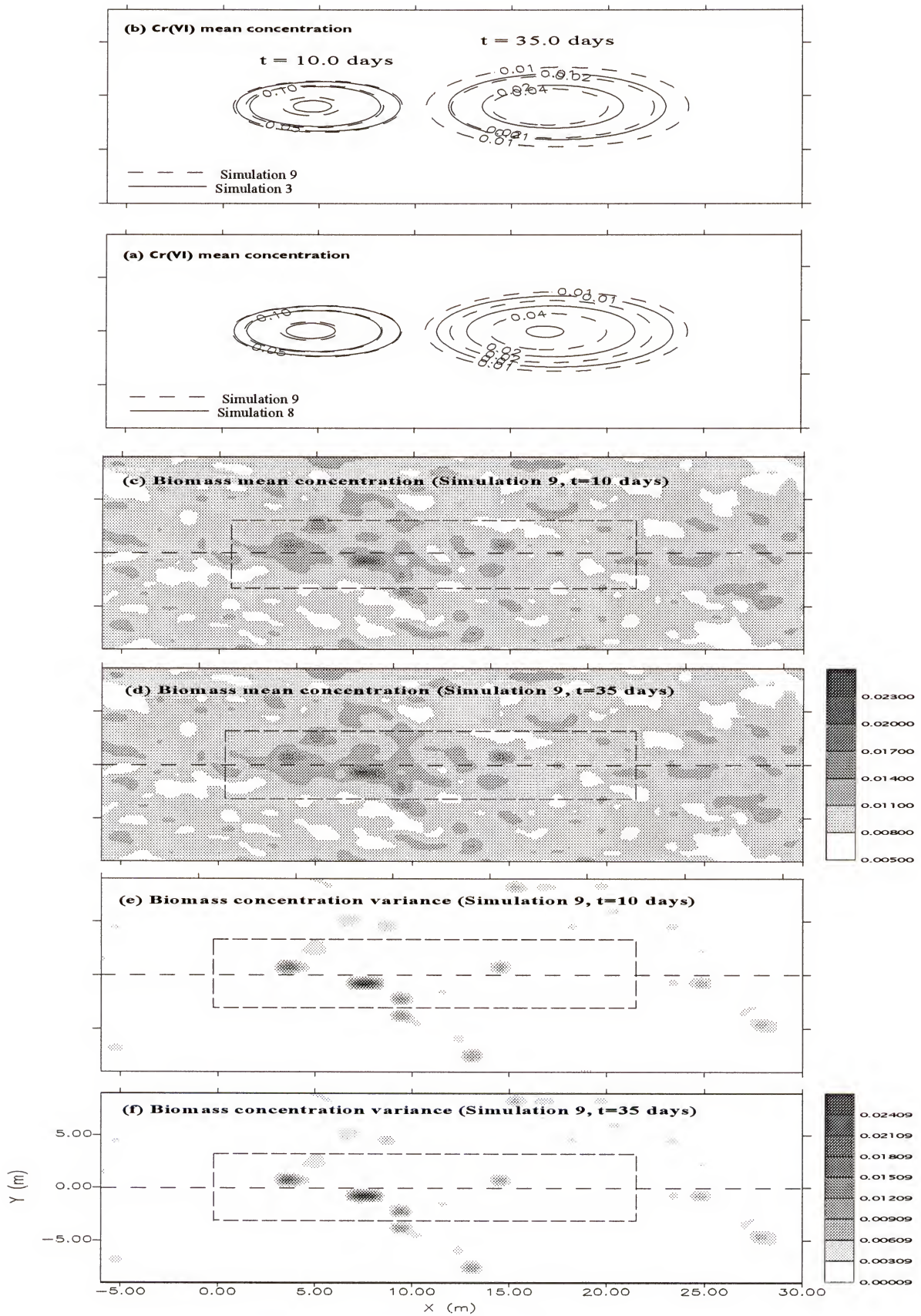


Figure 8-8 Comparison between Simulation 3, 8 and 9.

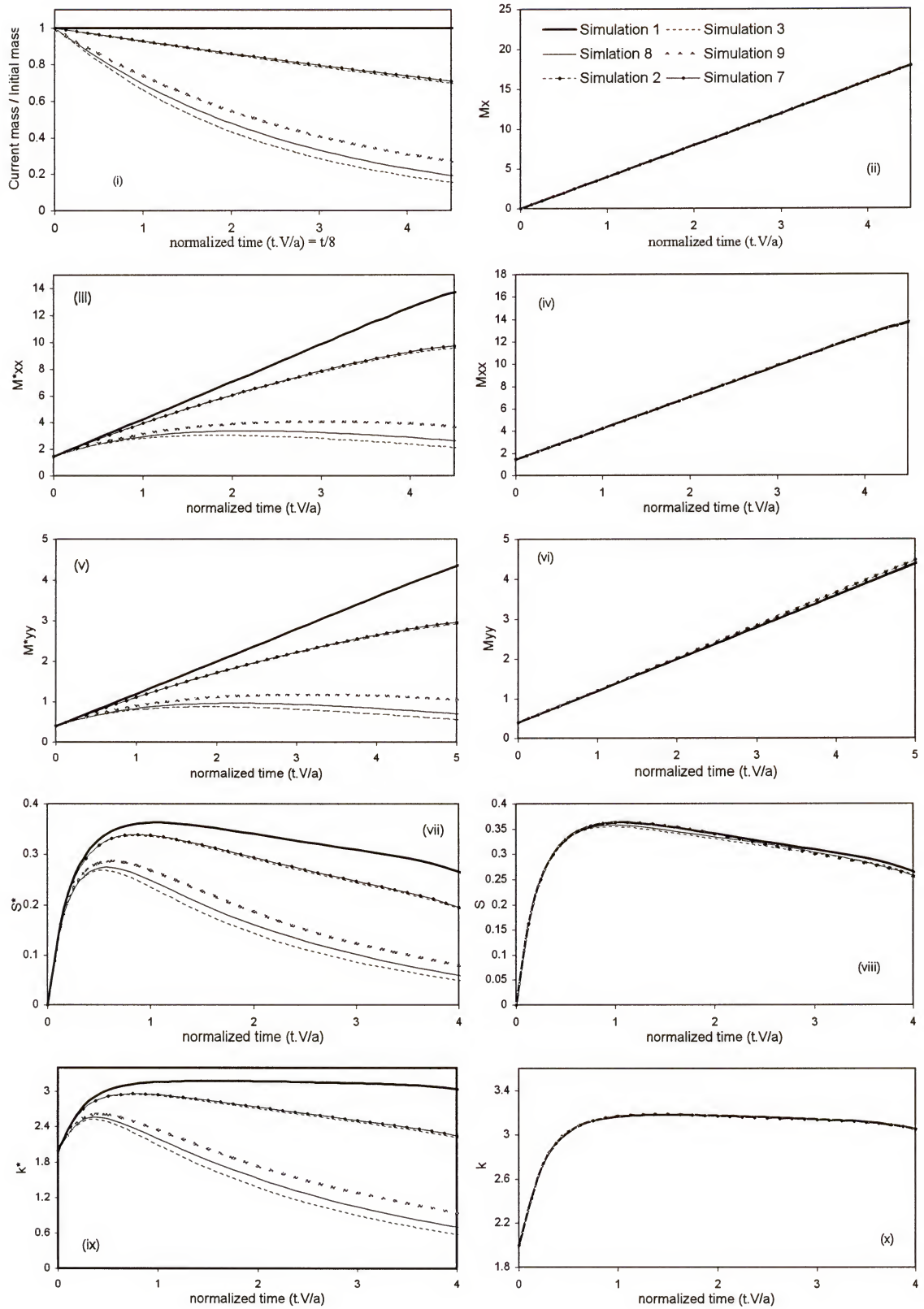


Figure 8-9a spatial moments of Cr(VI) plume for simulations 1, 2, 3, 7, 8, and 9.

all spatial moments normalized with the initial Cr(VI) biomass (M_{xx}^* , M_{yy}^* , s^* , and κ^*) when compared to the homogenous case [Simulations 3, 8 and 9; Figure 8-9a(iii, iv, vii, and ix)]. Furthermore, the same figures show that under low bacterial growth rates (Simulations 2 and 7), measurable spatial moments (of the mean plume) effects may not be observed. Finally, it is observed that when the initial biomass concentration variance is increased, biological heterogeneity has little effect on mean spatial moments normalized by the current Cr(VI) mass (M_{xx} , M_{yy} , s , and κ) [Figure 8-9a(iv, vi, viii, and x)].

Figure 8-9b compares the mass fluxes at sections 1 and 2 for all simulations where biological heterogeneity is considered (Simulations 7, 8, and 9). As expected, a low growth rate coupled with biological heterogeneity only slightly increases mass fluxes at both sections relative to the homogenous case (Simulations 2 and 7). However, when the growth rate is increased, fluxes differ significantly between Simulations 3 and 8 at both sections. Finally, for Simulation 9, increasing the initial biomass concentration variance (σ^2) leads to greater mass fluxes compared to Simulations 3 and 8.

From Table 8-3 it may be concluded that using a value of 1 for the variance in the initial biomass distribution (σ^2) with a low microbial growth rate produces estimations of the mass fluxes that are similar to the homogenous cases (Simulations 2 and 7). However, as β_{\max} increases the estimated flux from a homogenous system is less than that characterized with spatially variable distribution of biomass (Simulations 3 and 8). Increasing the variance in the initial biomass distribution (σ^2) (Simulation 9) also increases estimated mass fluxes compared to the homogenous case (Simulation 3) or to the less heterogeneous case (Simulation 8).

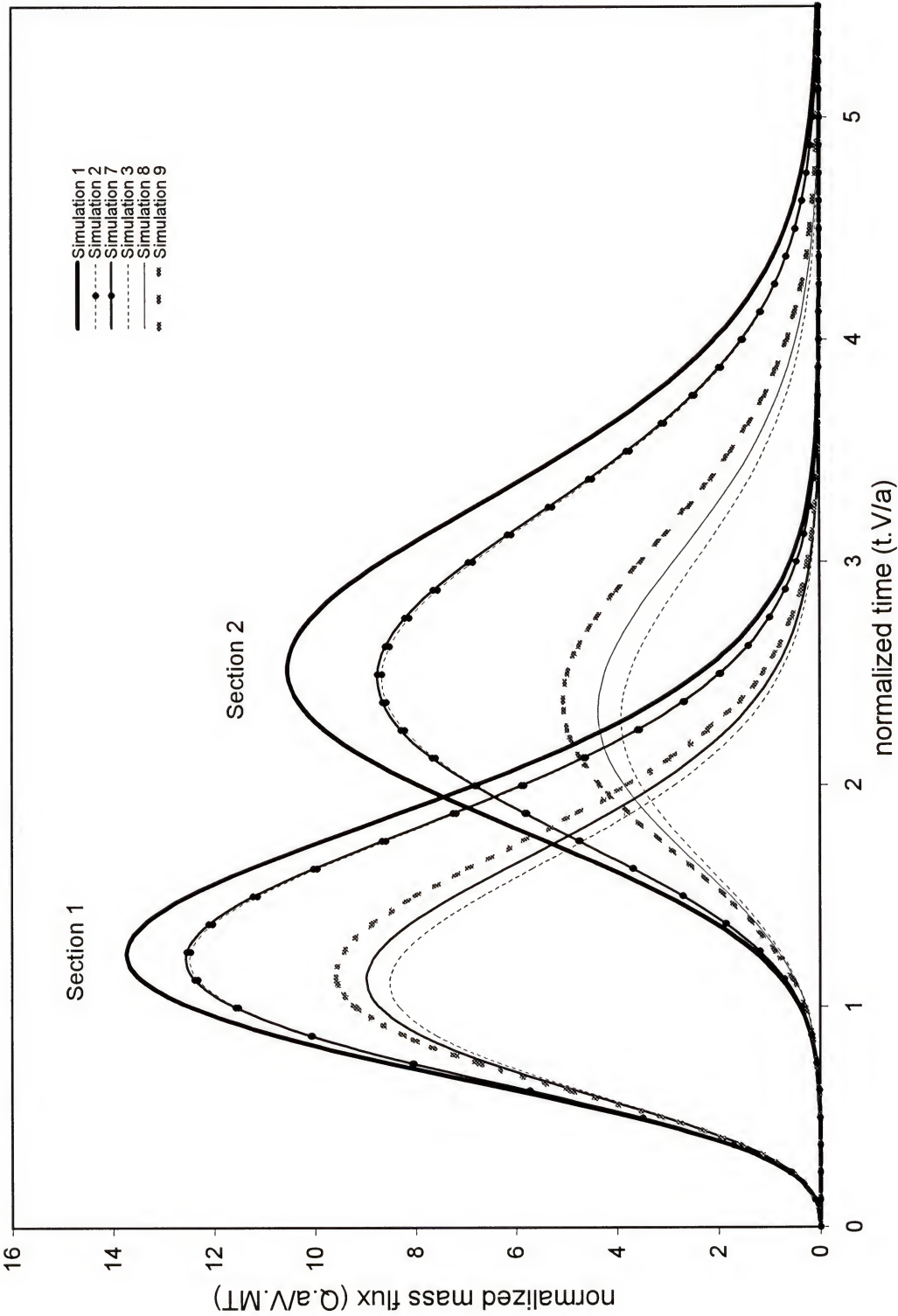


Figure 8-9b Mass fluxes of simulation 1, 2, 3, 7, 8, and 9.

8.5. Physical and Biological Variability

Correlation between both biological and physical heterogeneity is considered in this section where 6 simulations are discussed (Simulations 10-15; Table 8-1). Two of these simulations (10 and 11) are used to illustrate the effects of the negative correlation between the two heterogeneities using low bacterial growth rate, while a higher growth rate is used in Simulations 12 and 13 for the same purpose. The purpose of simulations 14 and 15 is to study the effects of a positive correlation between both heterogeneities. In Simulation 15, however, the impact of increasing the variance of the initial biomass concentration is considered. Simulation 16 the effects of spatial variability in the initial concentrations of an electron donor are examined. In this simulation, initial concentrations of the electron donor are assumed to be uncorrelated to either hydraulic conductivity or initial biomass concentrations; however, a negative correlation between the later two is assumed [Table 8-1].

Figure 8-10a(i and ii) shows the ensemble mean concentration of Cr(VI) at two time steps (10 and 35 days) for Simulations 10 and 11. The practical explanation of assuming negative correlation between both heterogeneities in Simulation 11 may be justified by the fact that a high groundwater velocity tends to wash out the attached bacteria, which are assumed to be responsible for Cr(VI) biotransformation. Therefore, low biological activities occur in high velocity areas and vice versa [Figures 8-10a(i and ii)].

Differences between the ensemble mean concentrations of both simulations (10 and 11) are minor at both time steps [Figure 8-10a(i and ii)]. This is probably due to using a low microbial growth rate (μ_{\max}); the same reason may also explain the slight

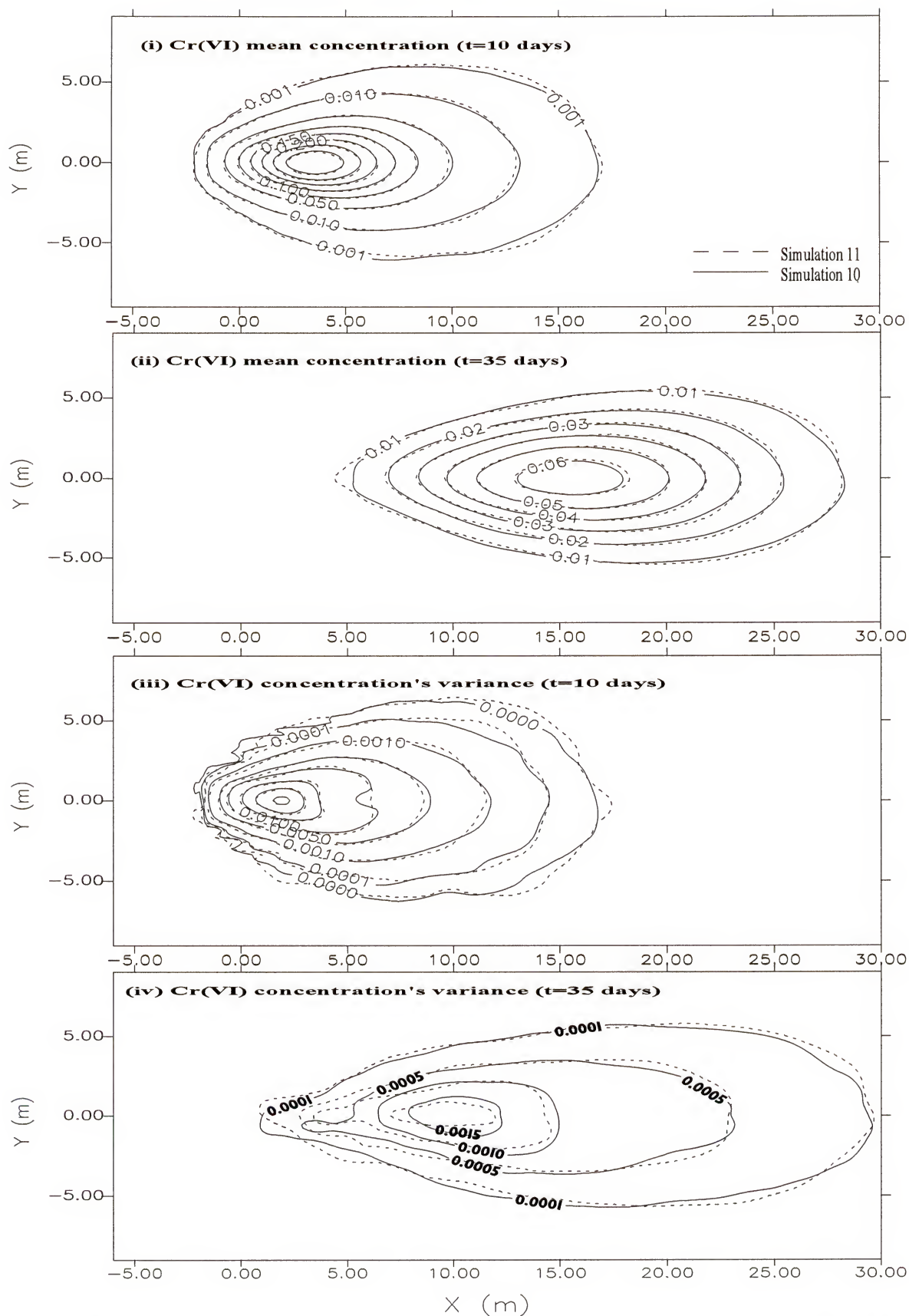


Figure 8-10(a) Comparison between concentration's mean and variance of Simulations 10 and 11.

differences between concentration variances obtained from the two simulations [Figure 8-10a(iii and ix)]. Differences between expected Cr(VI) concentrations and variances become clearer on the trailing edge of the plume [Figures 8-10a(iii-iv)]. This is most likely due to the negative correlation between the two heterogeneities, which places higher biological activity in zones of lower groundwater velocity.

Despite the clear increase in the ensemble mean concentrations of the microbial population at $t = 35$ days compared to $t = 10$ days [within the dotted box in Simulation 10; Figures 8-10b (i and ii)], slight differences in biomass are observed when compared to Simulation 11 at both time steps [compare Figures 8-10b (i with iii) and (ii with iv)]. In general, the microbial maximum growth rate was not high enough to reveal consequences of the negative correlation between both heterogeneities. Similarly, the same conclusion could be reached by comparing the uncertainty in mean biomass concentrations for the two simulations (10 and 11) at both time steps [Figure 8-10c].

Figure 8-11a compares spatial moments of the ensemble mean concentrations of Cr(VI) for Simulations 4, 5, 10 and 11. Figure 8-11a(i) suggests that any correlation between physical and biological heterogeneities has little effects on the total mass of Cr(VI) reduced compared to the cases where physical or biological heterogeneity is considered alone (Simulations 5 and 7). The same conclusion could also be drawn from Table 8-2, which further reveals that the reduced Cr(VI) mass estimated from all these simulations (5, 7, 10, and 11) equals that estimated using homogenous model (Simulation 2). Thus, physical heterogeneity, as well as biological heterogeneity under low microbial growth rates, does not significantly alter estimates of predicted moments of the contaminant plume.

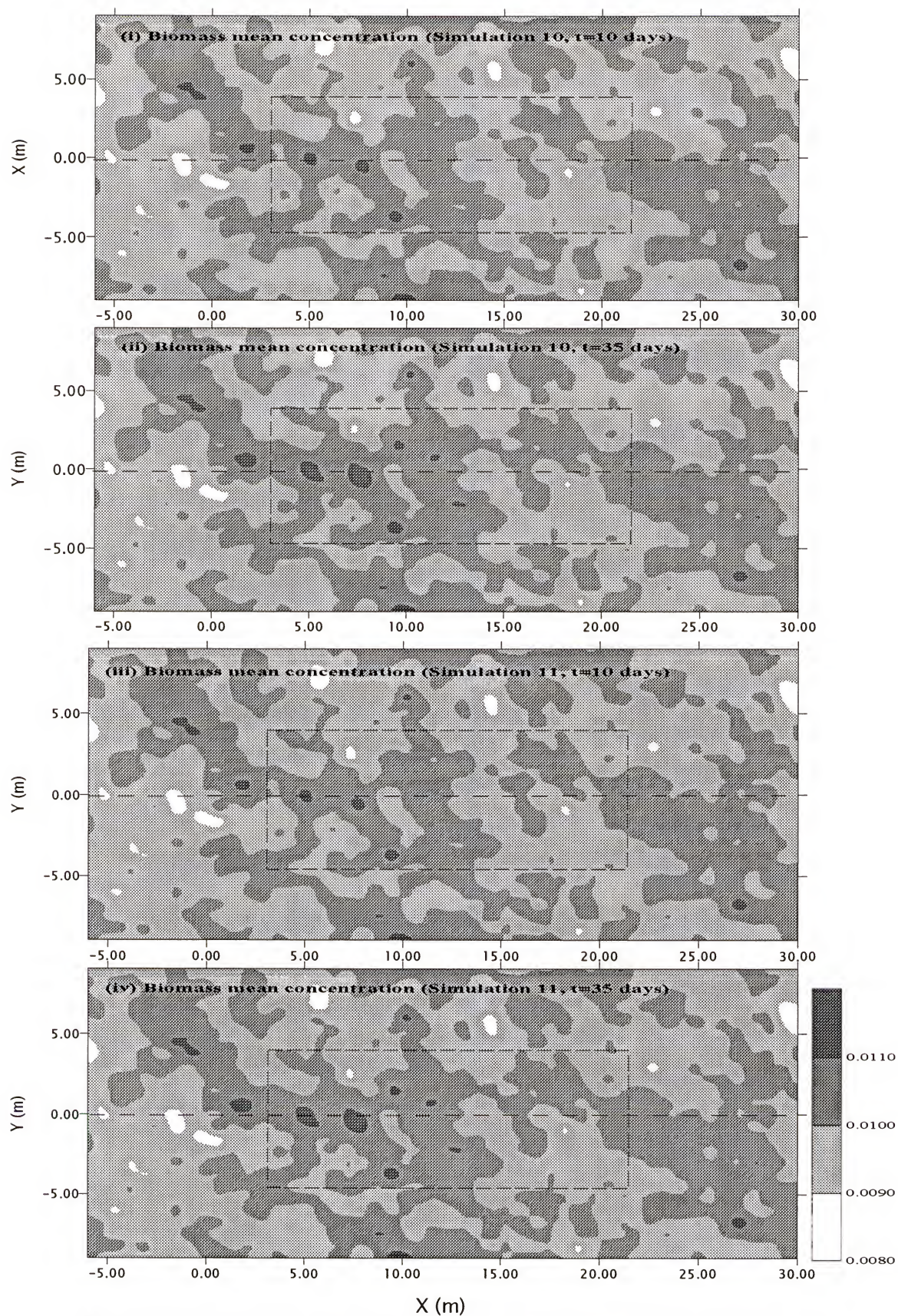


Figure 8-10(b) Comparison between biomass mean concentrations of Simulations 10 and 11.

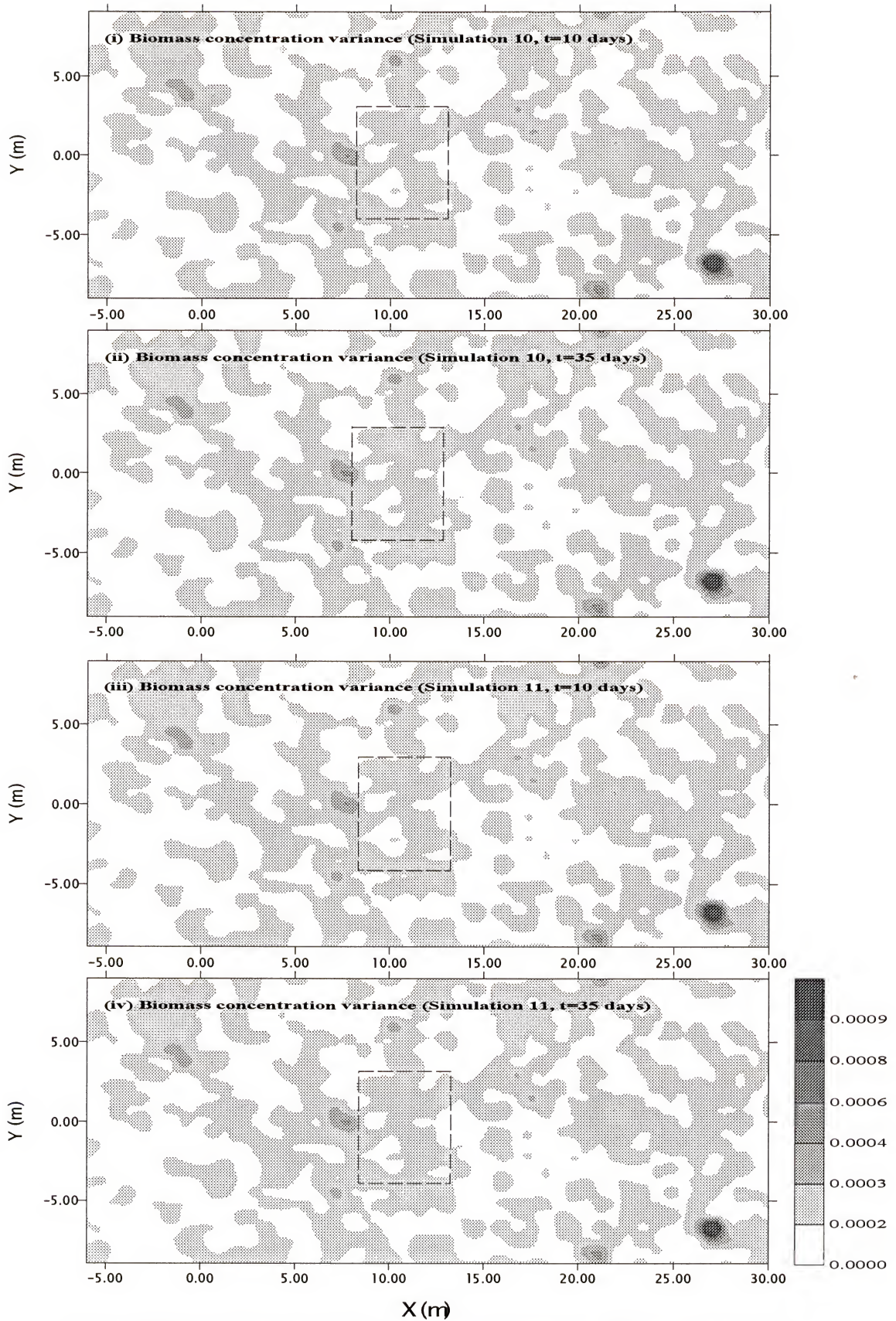


Figure 8-10(c) Comparison between biomass concentration's variance of Simulations 10 and 11.

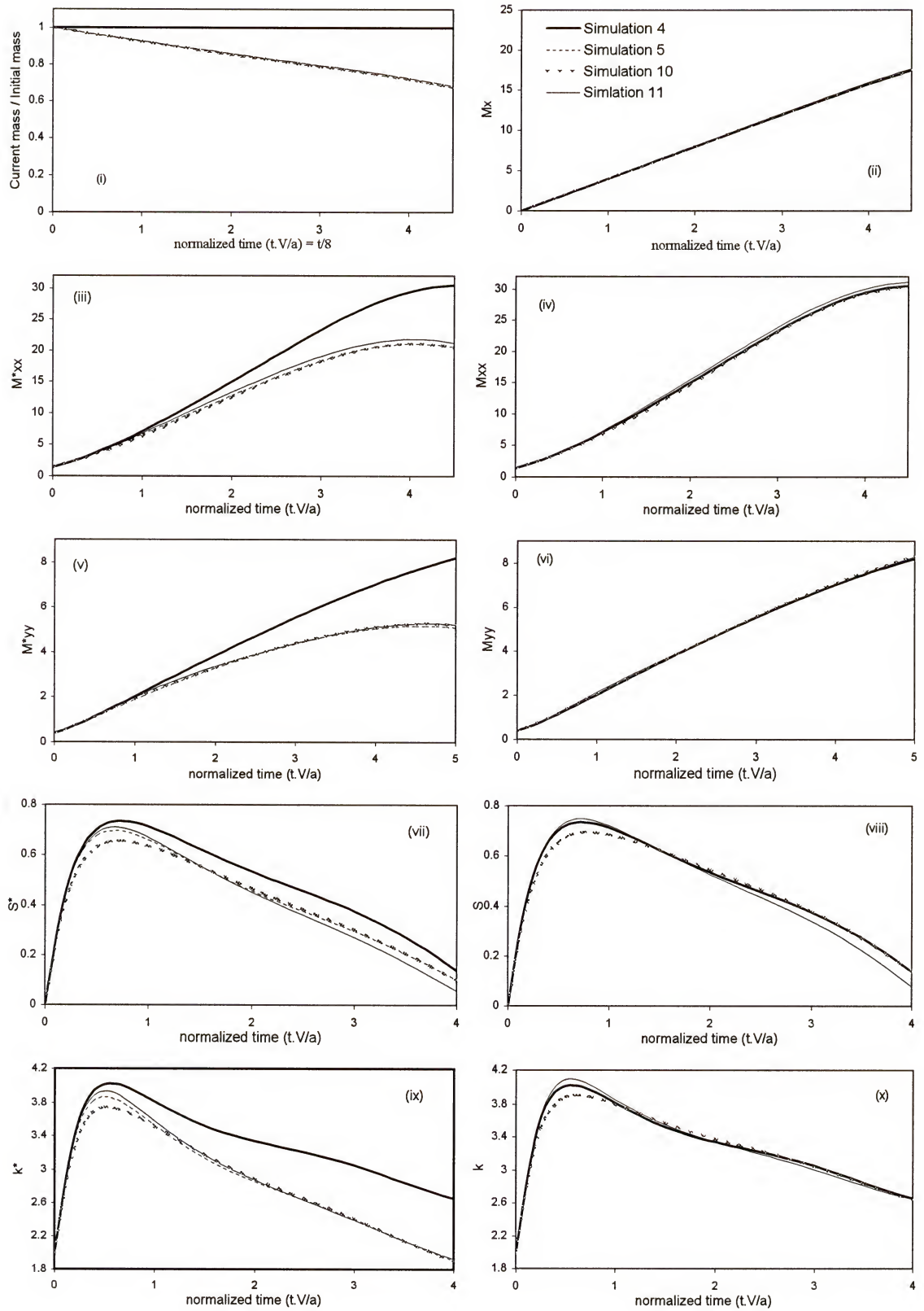


Figure 8-11a Spatial moments of Cr(VI) plume for simulations 4, 5, 10, and 11.

Longitudinal and transverse dispersion in Simulations 10 and 11 are the same as those estimated in Simulation 5, where only physical heterogeneity is considered [Figures 8-11a(iv and vi)]. On the other hand, in the case of “no correlation” (Simulation 10) minor differences exist in skewness and kurtosis [Figure 8-11a(vii and ix)] which are manifestations of differences in Cr(VI) concentrations on the trailing edge of the plume.

Minor differences between mass fluxes across sections 1 and 2 of all cases (Simulations 5, 10 and 11) are predicted [Figure 8-11b(i)]. However, the same figure indicates that when biological activities are considered in all three simulations (5, 10 and 11) lower fluxes are obtained compared to Simulation 4 (where no biotransformation activity is assumed). The same conclusion can be obtained from Table 8-3 by comparing the percentage of cumulative mass intercepted each section in these three simulations. On the other hand, Figure 8-11b(ii) suggests that when biological heterogeneity is assumed uncorrelated to physical heterogeneity, it slightly reduces the uncertainty in the evaluated mass fluxes at the leading edge of the plume (compare Simulations 5 and 10). This occurs because the range of contaminant fluxes is greater at the leading edge of the plume under negative correlation, where fast velocity zones exhibit less Cr(VI) reduction rates. However, assuming negative correlation between both heterogeneities increases the uncertainty in the estimation of the mass flux values (Figure 8-11b(ii); compare Simulations 10 and 11). The small differences in results between simulations 10 and 11 could be related to the use of a low microbial growth rate. To investigate this issue, microbial growth rate was increased in simulations 12 and 13.

Increasing μ_{\max} under an assumed negative correlation between both heterogeneities (Simulation 13) augments the effects of correlation on Cr(VI) ensemble

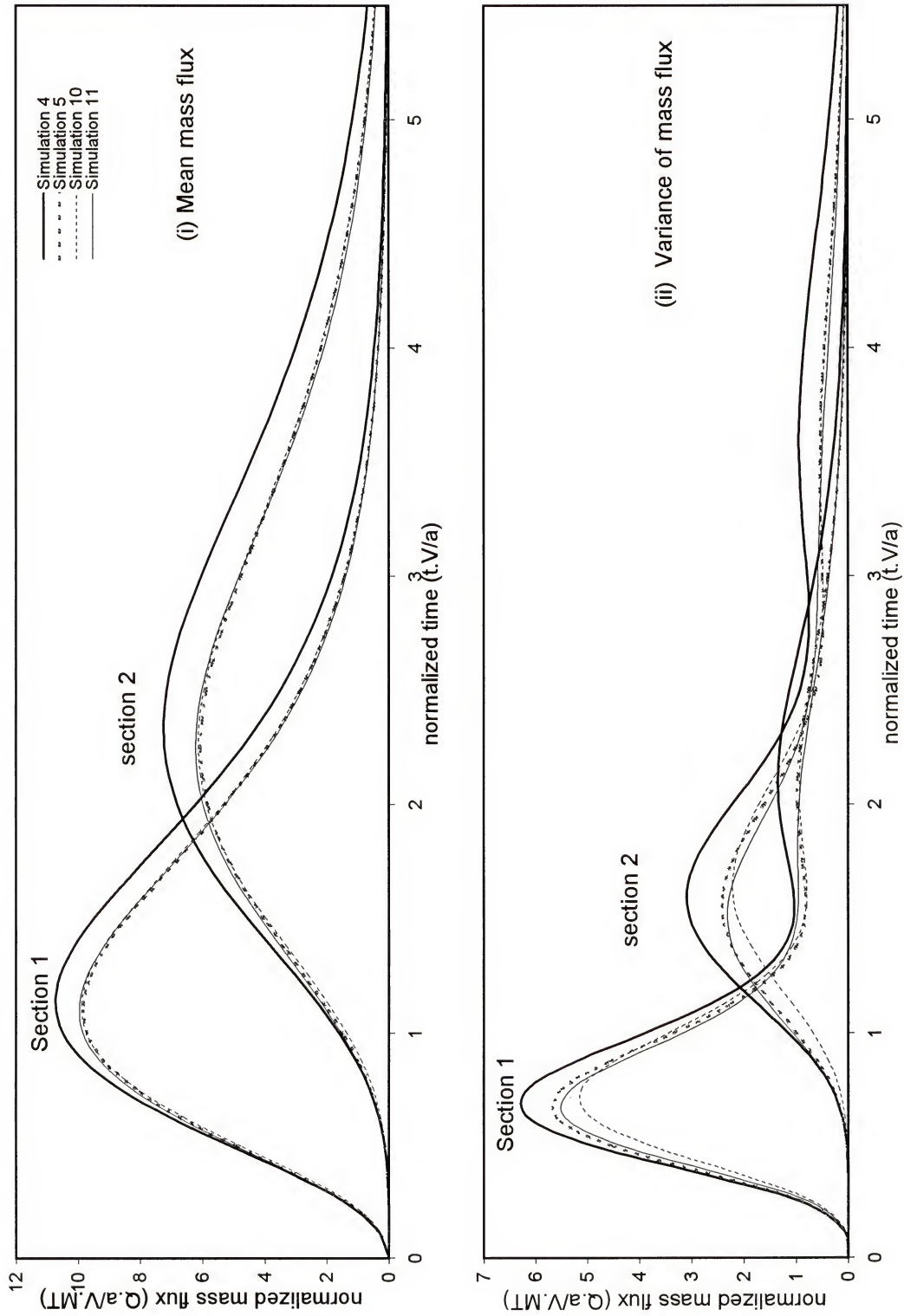


Figure 8-11b Mass fluxes of simulations 4, 5, 10, and 11.

mean concentrations, compared to the “no correlation” case (Simulation 12) [Figure 8-12a(i and ii)]. That is, it becomes more evident that in the high velocity zones (the leading edge of Cr(VI) plume), less Cr(VI) reduction is occurring in Simulation 13 than that in Simulation 12, and vice versa in low velocity zones (trailing edge of the plume) [Figures 8-12a(i and ii)]. Therefore, assuming a negative correlation between both heterogeneities can lead to elevated predictions of expected Cr(VI) concentrations at the leading edge of the plume and depressed predictions at the trailing edge. Similar effects on concentration variance are noted particularly at later times [Figures 8-12a(iii and iv)].

Due to the increase in the value of microbial maximum growth rate, higher mean biomass concentrations and variances are found at the two time steps in Simulations 12 and 13 compared to those in Simulations 10 and 11 [compare Figure 8-12b and c with 8-10b and c]. Furthermore, for the same reason, ensemble mean concentrations and variances of Simulations 12 and 13 at $t = 35$ days are greater than those at $t = 10$ days. Differences between variances in the two simulations at $t = 35$ days are more distinguished [Figure 8-12c(ii and iv)] than those of simulations 10 and 11. It should be mentioned that the same 500 realizations of initial biomass are used in simulations 12 and 13 and, therefore, the effect of considering negative or no correlation only appears in the hydraulic conductivity realizations. For that reason, values of the ensemble mean and variance of biomass concentrations are similar in the regions where Cr(VI) is not reduced (out of the dotted box) [Figures 8-12b and c].

Unlike Simulation 13, positive correlation between the two heterogeneities is assumed in Simulation 14 (Table 8-1). The practical reasoning of this assumption can be explained by the fact that solutes move more rapidly through high velocity regions and;

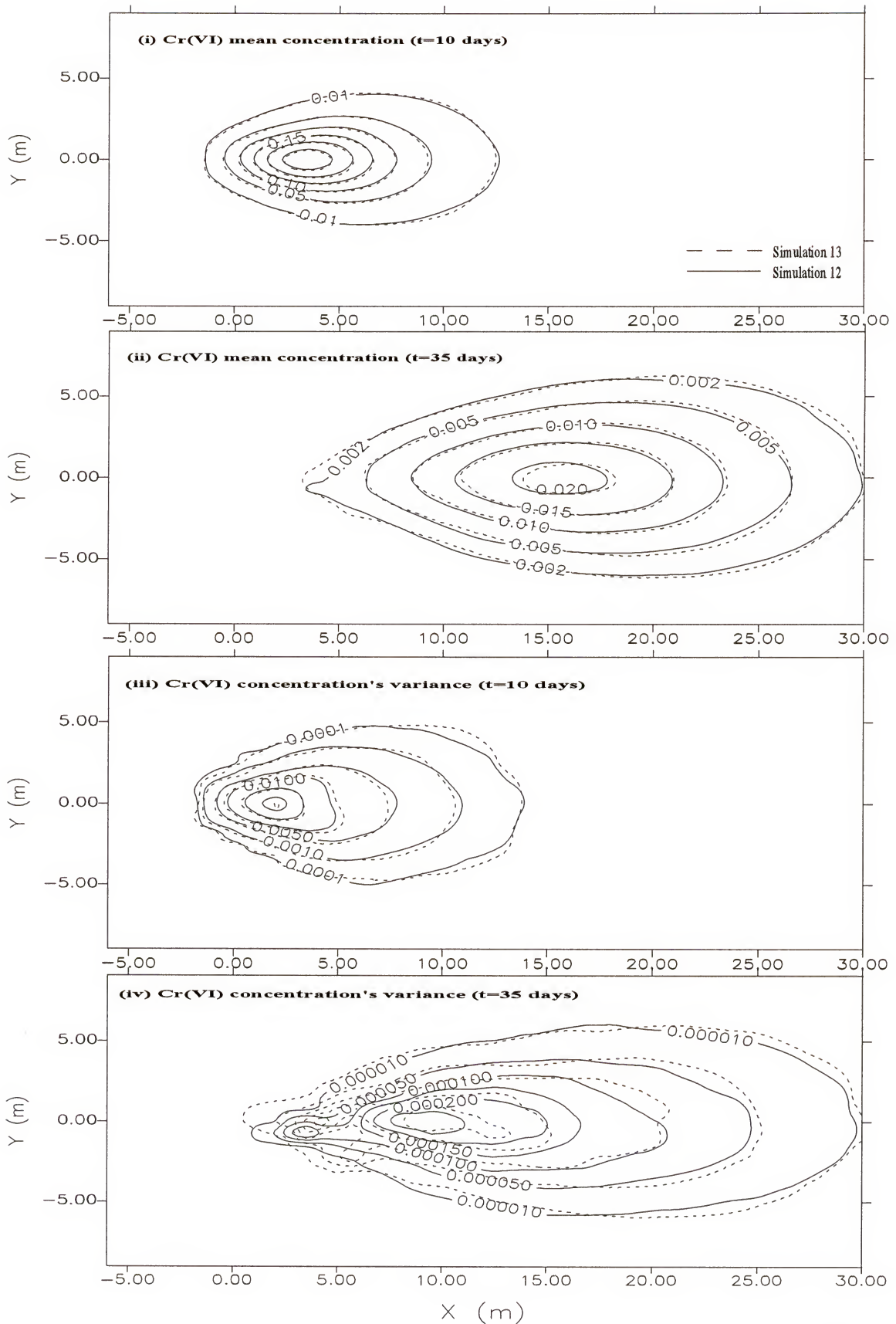


Figure 8-12(a) Comparison between concentration's mean and variance of Simulations 12 and 13.

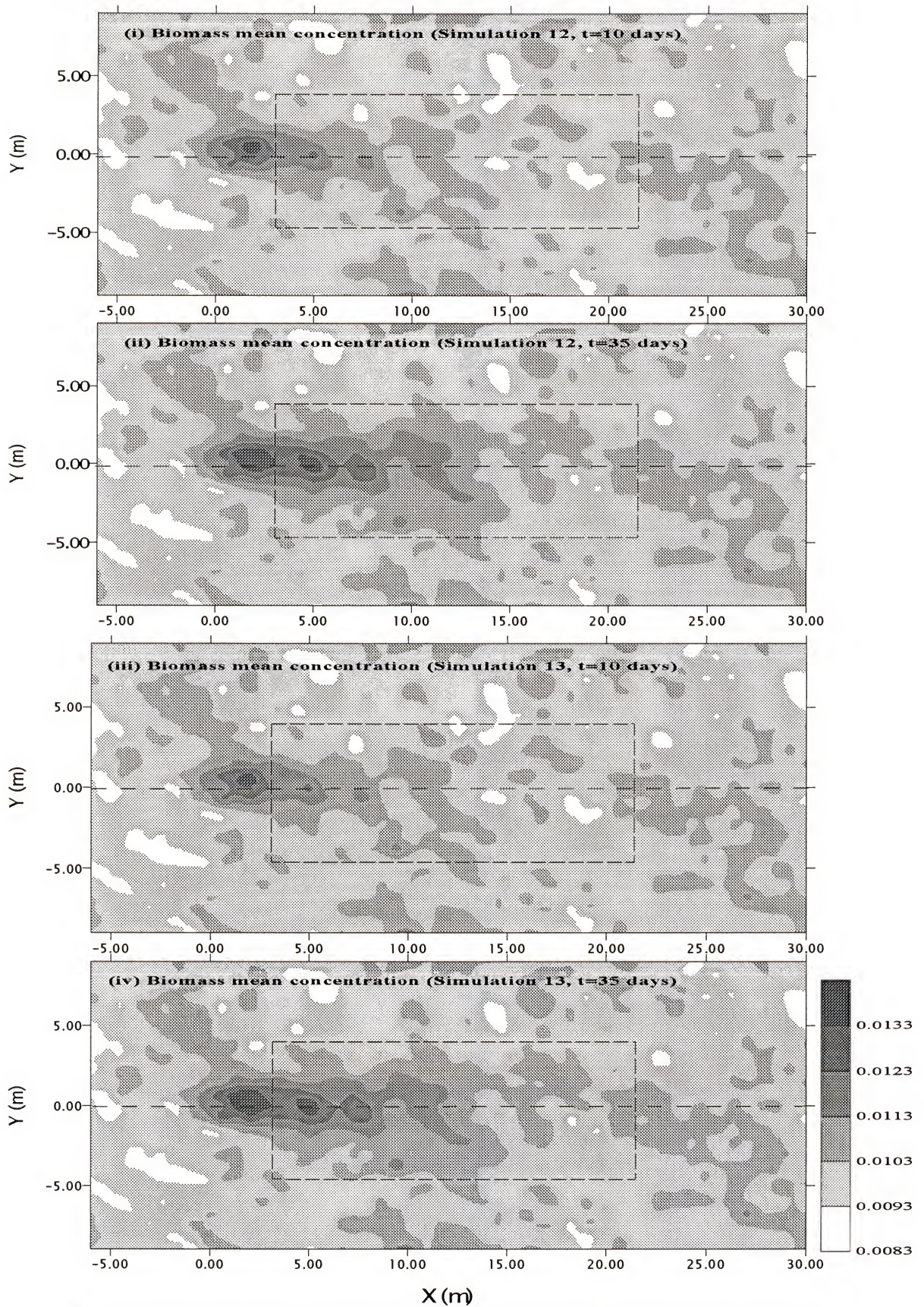


Figure 8-12(b) Comparison between biomass mean concentrations of Simulations 12 and 13.

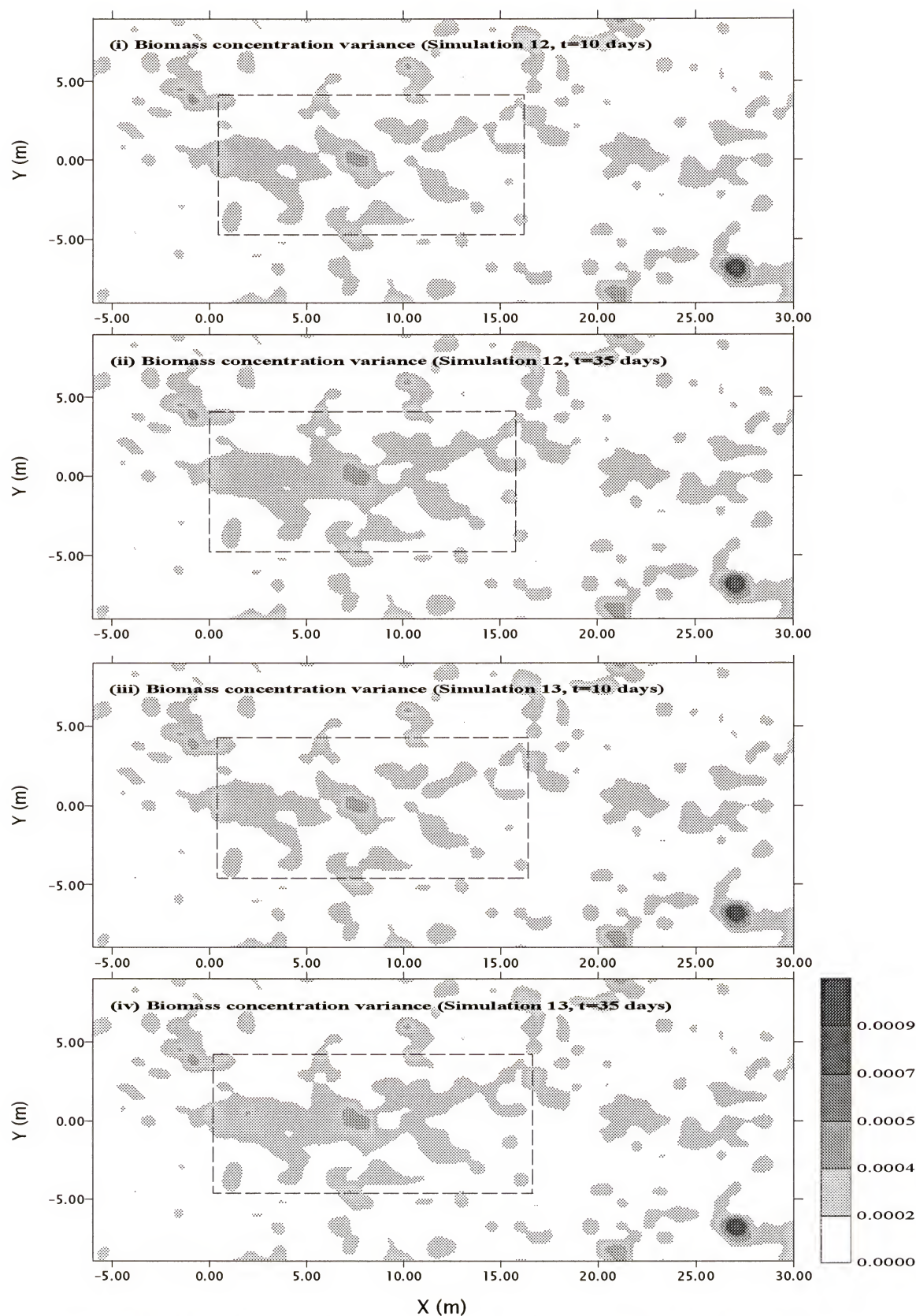


Figure 8-12(c) Comparison between biomass concentration's variance of Simulations 12 and 13.

therefore, nutrients are more available for microbial growth in these regions. This implies enhanced Cr(VI) reduction is expected to occur over high velocity regions. Therefore, the effect on the Cr(VI) ensemble mean concentrations is expected to be the opposite of that observed with Simulation 13 [Figure 8-13a(i and ii)]. That is, in Simulation 14 more biotransformations occur within high velocity regions (the leading edge of the Cr(VI) plume) compared to Simulation 12 and vice versa over low velocity regions (the trailing edge of the plume) [Figures 8-13a(i and ii)].

Similar effects on the concentration variance, as with concentration, are visible at both time steps [Figures 8-13a(iii and iv)]. However, effects of the correlation between physical and biological heterogeneities are clearer at $t = 35$ days.

The same hydraulic conductivity realizations were used in simulations 13 and 14 and therefore, the change in the correlation was only incorporated in the 500 realizations of the initial biomass distribution. For this reason, areas of high and low biomass concentrations (in the regions where no biotransformation occurs, i.e. outside of the of dotted box) are switched in Simulation 14 as compared to those in Simulation 13 [compare Figures 8-12b(iii) and 8-13c(i)]. It appears that regardless of the correlation between the two heterogeneities, which determine the initial distribution of biomass, it is the high bacterial growth rate that produces the distinctive bacterial growth pattern after 35 days compared to that at 10 days (within the dotted box) [Figure 8-13c(ii)].

When the variance of initial biomass concentration is increased from 1.0 (Simulation 14) to 3.0 (Simulation 15), no effect on the mean Cr(VI) concentrations is observed at 10 days [Figure 8-13b(i)]; however, by day 35 the effects are clearly evident. As the initial biomass concentration variance is increased, there is less likelihood that

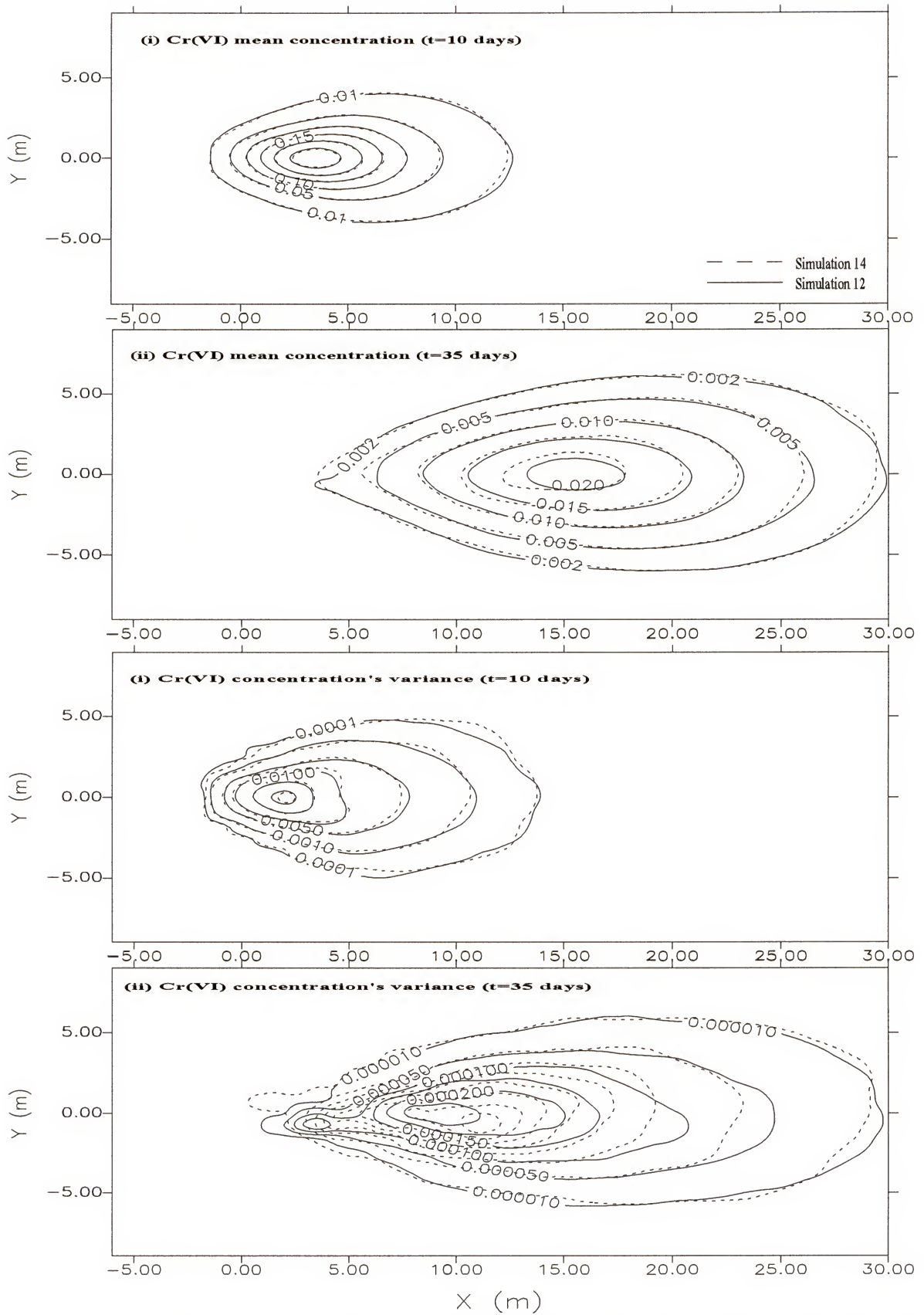


Figure 8-13(a) Comparison between concentration's mean and variance of Simulations 12 and 14.

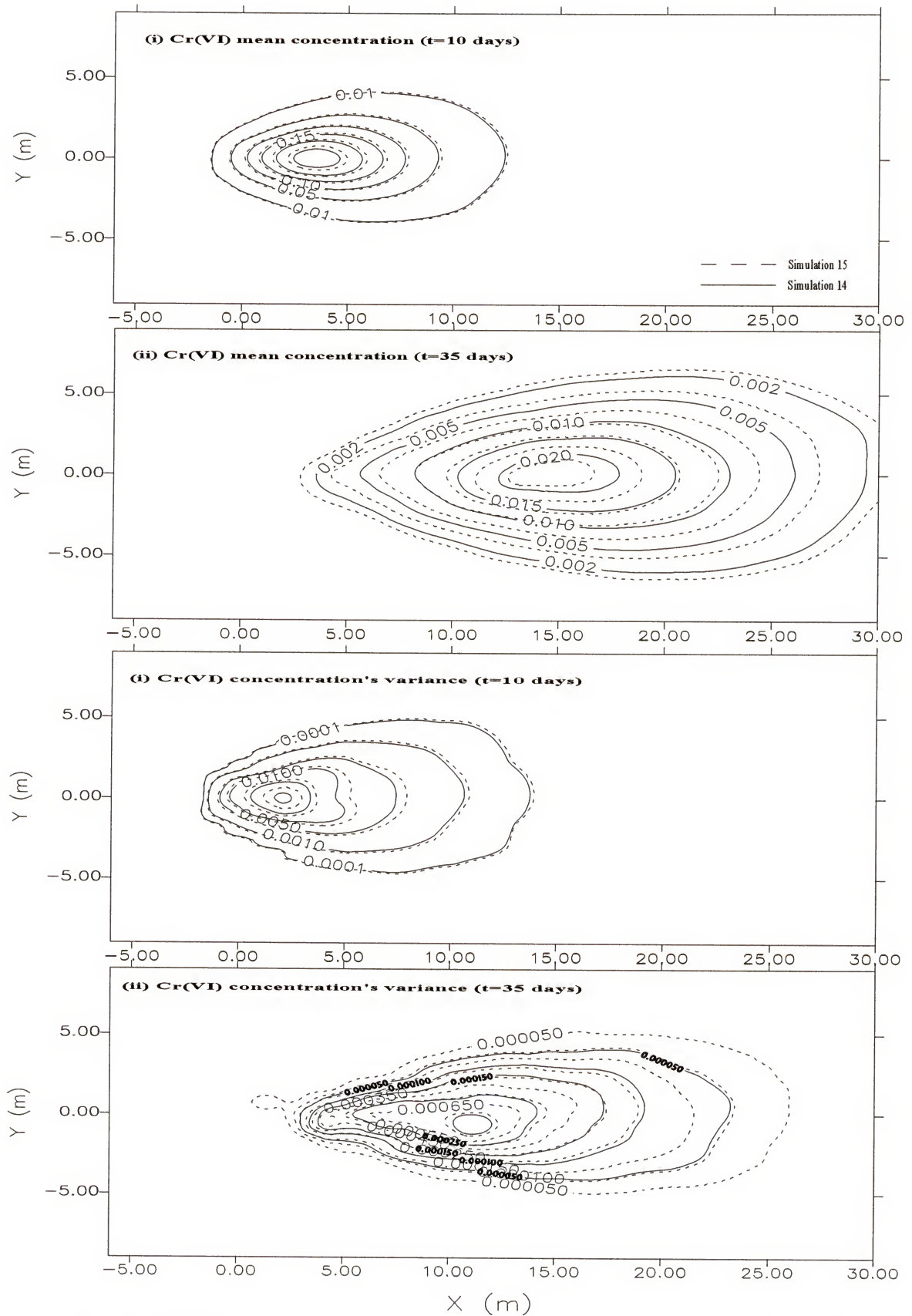


Figure 8-13(b) Comparison between concentration's mean and variance of Simulations 14 and 15.

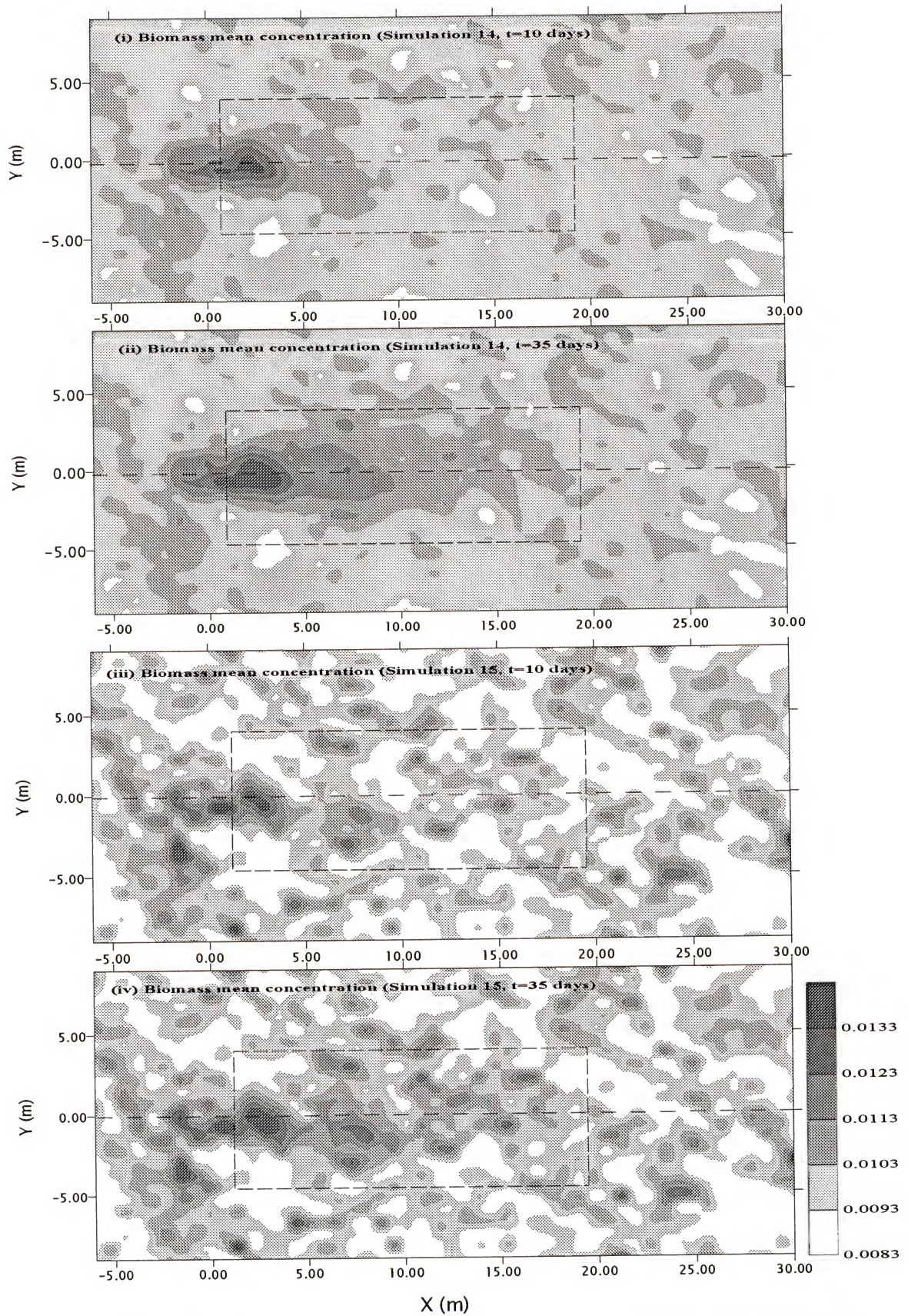


Figure 8-13(c) Comparison between biomass mean concentrations of Simulations 14 and 15.

Cr(VI) plume intersects with zones of high biomass concentrations; consequently, there is greater likelihood that Cr(VI) plume will escape attenuation [Figure 8-13b(ii)]. As a result, Simulation 15 predicts higher ensemble mean Cr(VI) concentrations in the system [Figure 8-13b(ii)]. Uncertainties in the Cr(VI) mean concentration also increased for the same reason, particularly at later travel times [Figure 8-13b(iii and iv)].

It is also clear that when the variance in the initial biomass concentration was increased (Simulation 15), the spatial variability in mean biomass concentration [Figure 8-13c(iii and iv)] and the biomass concentration variance [Figure 8-13d(iii and iv)] increased compared to those of Simulation 14 [Figures 8-13c(i and ii) and 8-13d(i and ii), respectively].

Spatial moments of Cr(VI) are more sensitive to changes in the initial biomass concentration variance than that of the nature of the correlation (positive or negative). For example, the total reduced mass of Cr(VI) estimated via Simulations 12, 13, and 14 (obtained from the mean plume) is almost the same [Table 8-2 and Figure 8-14a(i)]. However, the same table indicates that Simulation 15 estimates lower Cr(VI) mass reduced (or bioremediation efficiency) compared to any of simulations 12-14. The change in the correlation between the two heterogeneities as well as the change in the variance of the biomass initial concentrations produced minor effects on spatial moments of the Cr(VI) plume normalized by current mass [Figure 8-14a(ii, iv, vi, viii, and x)]. However, due to microbial mediated reduction in Cr(VI) concentrations caused by biotransformations, differences are evident among spatial moments of simulations 12-14, normalized with respect to the initial mass, [Figure 8-14a(i, iii, v, vii, ix)].

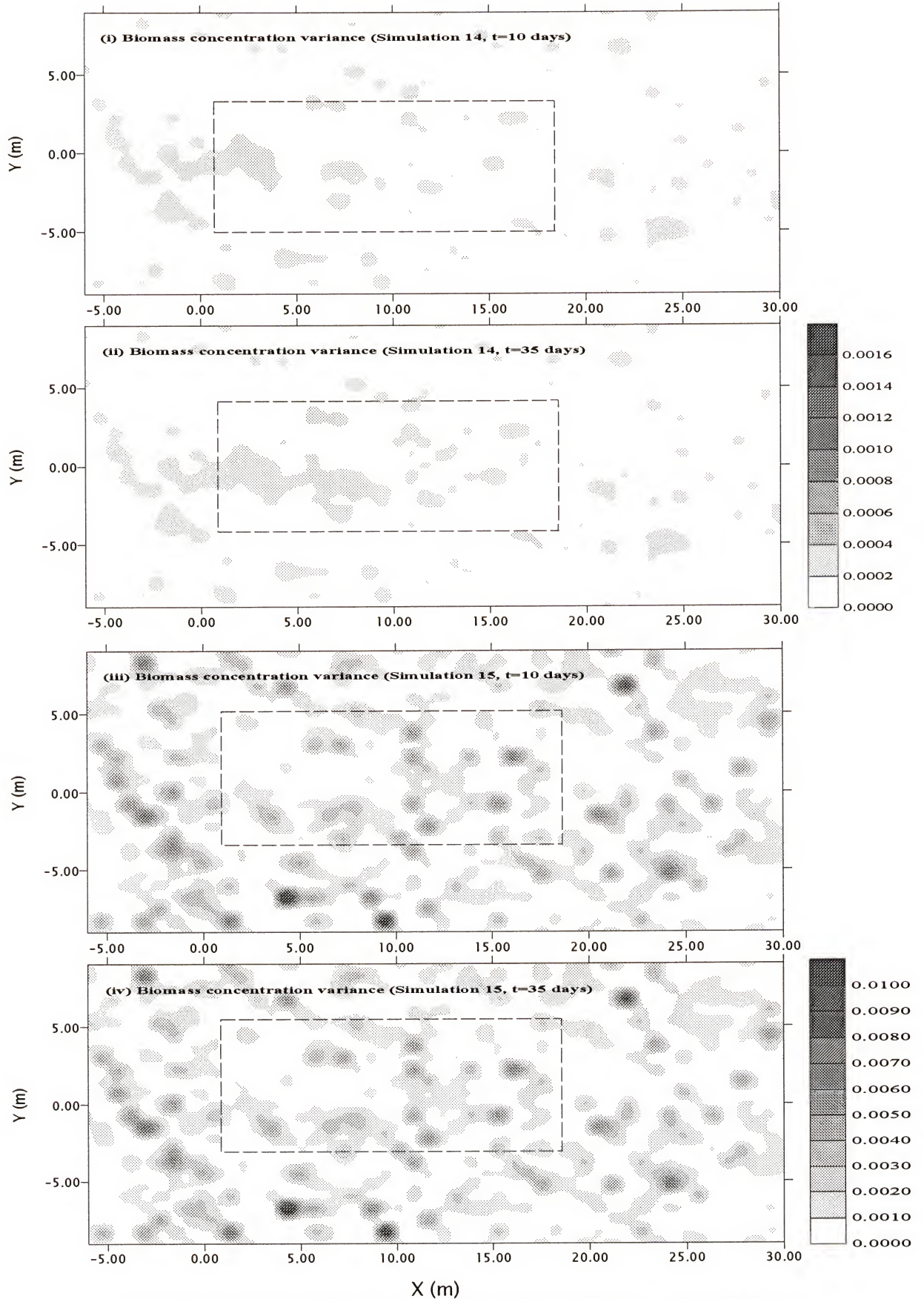


Figure 8-13(d) Comparison between biomass concentration's variance of Simulations 14 and 15.

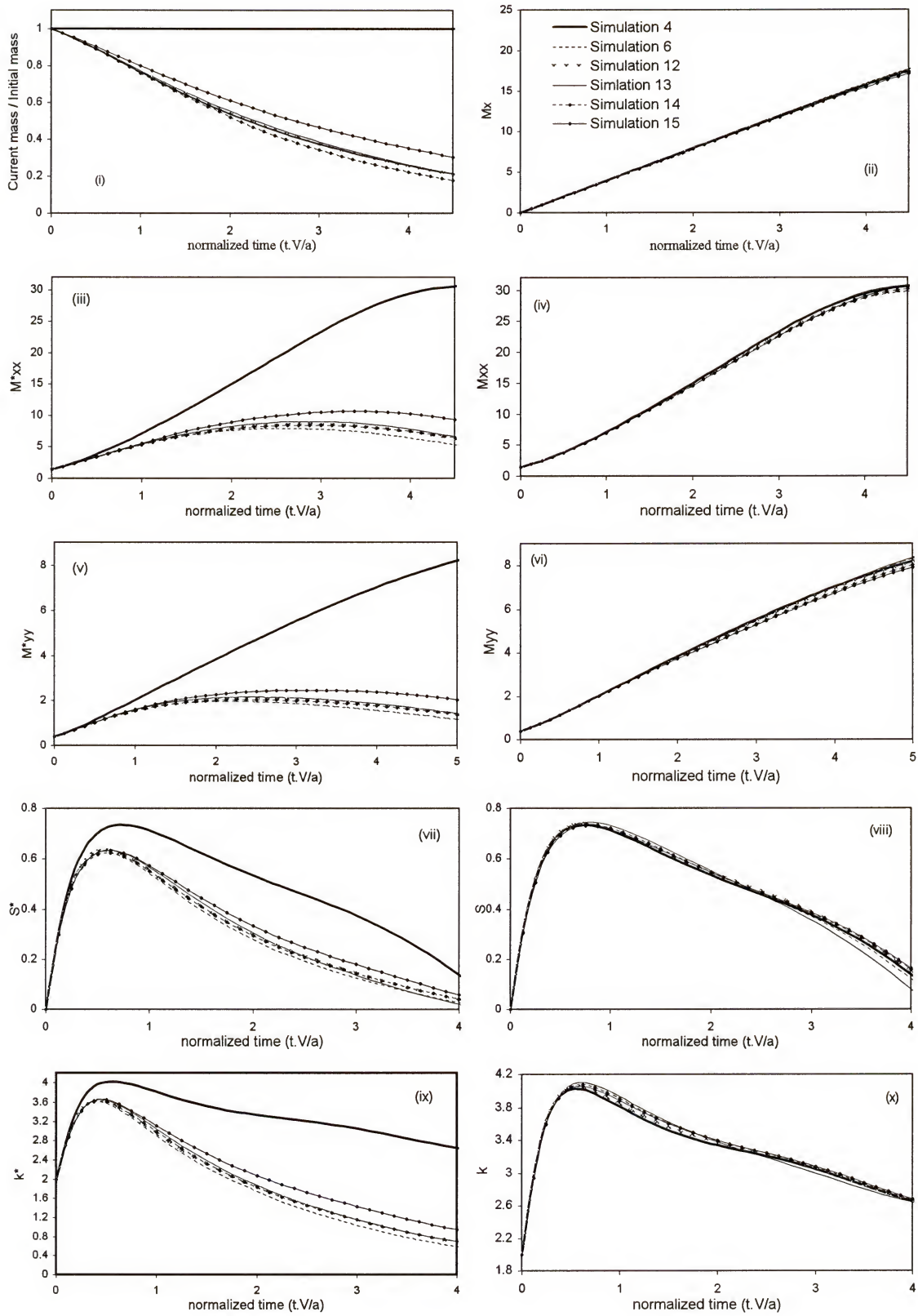


Figure 8-14a Spatial moments of Cr(VI) plume for simulations 4, 6, 12, 13, 14, 15

In Simulation 15 less biomass was generated than that in Simulation 14 [Figure 8-14b(i)]; this is coupled to the fact that less Cr(VI) was reduced in Simulations 15 than that in Simulation 14 [Figure 8-14a(i)].

Clear effects of both the type of the correlation between the physical and biological heterogeneities (positive, negative, or no correlation) and the variance of the initial biomass are noted on spatial moments of the ensemble mean of biomass concentrations. When the correlation between the physical and biological heterogeneities was changed from negative correlation (Simulation 13) to positive correlation (Simulation 14), the initial position of the bacterial center of mass changed accordingly from 0.07 to -0.07 (referenced to the center of the aquifer) [Figure 8-14b(ii)]. However, because all other parameters are preserved between simulations, the transient change in first moment in both simulations followed the same pattern. In addition, when the variance in the initial biomass concentration is increased to 3.0 (Simulation 15), the initial value of the first moment is also decreased (-0.14 m) compared to Simulation 14 (-0.07 m) [Figure 8-14b(ii)].

Similar observations are also noted in all other spatial moments; i.e. curves of the different spatial moments of negative and positive correlations are on opposite sides of that of Simulation 6, where biological heterogeneity was ignored [Figure 8-14b]. Finally, as the initial biomass variance is increased (Simulation 15), spatial moments are increased, or decreased, in a direction consistent with that of Simulation 14 with respect to the homogenous case [Figure 8-14b].

Figure 8-14c shows comparison between mass flux mean and variance for Simulations 12, 13, 14, 15, and 6 (when biological variability was ignored).

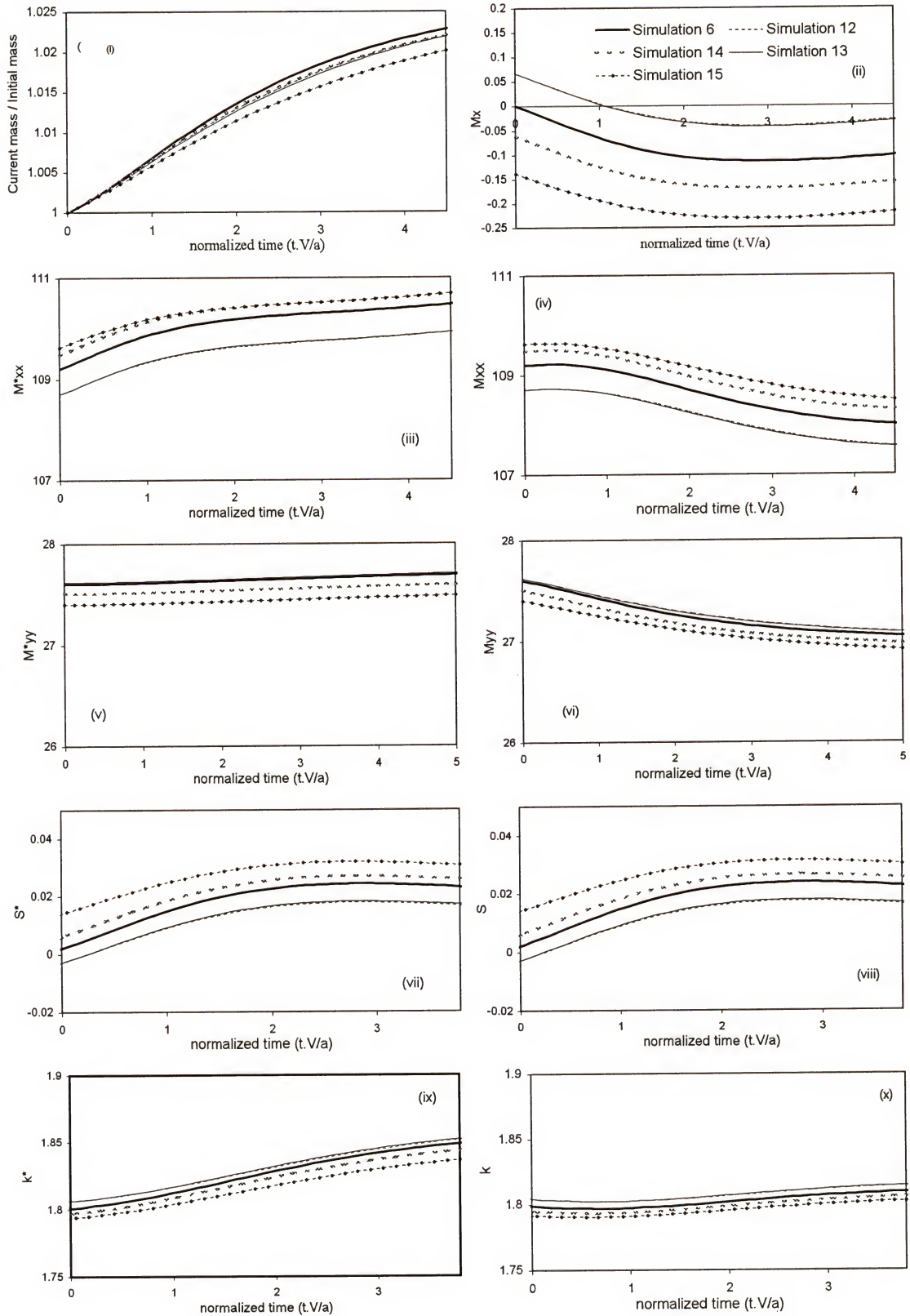


Figure 8-14b Biomass distribution spatial moments of simulations 6,12,13,14,15

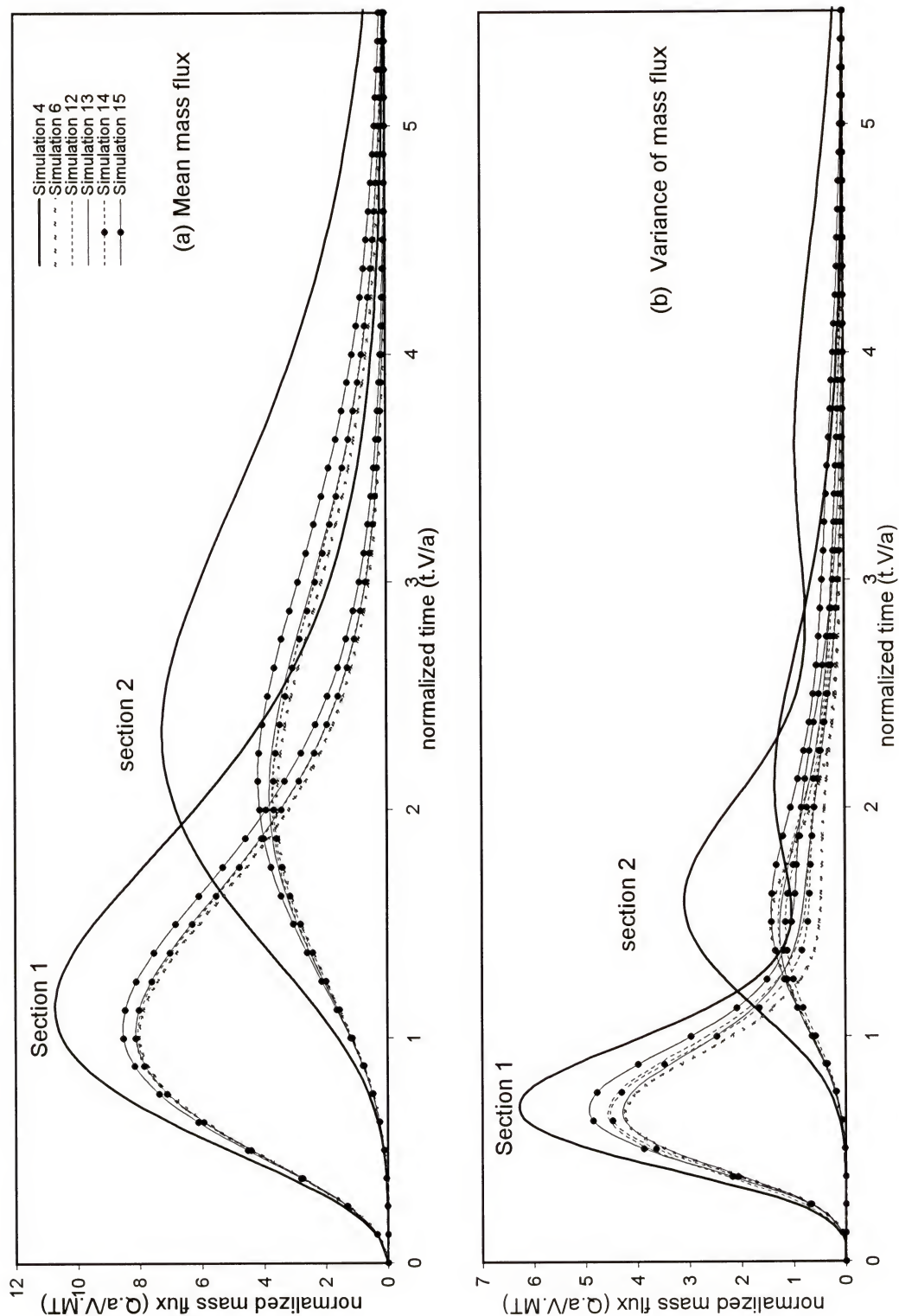


Figure 8-14c Mass fluxes of simulations 4, 6, 12, and 13, 14, 15.

Ignoring biological variability produces lower estimates of the mean mass fluxes compared to all other cases when biological variability was considered [Figure 8-14c(i)]. Therefore, less uncertainties in these values is predicted in this case [Figure 8-14c(ii)]. However, all other Simulations, except for Simulation 15, imply that using unit spatial variance of the initial biomass is not enough to demonstrate the effects of biological variability on the calculations of the mean mass fluxes. However, when this value was increased to 3 in Simulation 15 a relatively distinctive increase in the mass flux and the associated variance are observed at the two sections [Figure 8-14c(i)]. Similar conclusions can be obtained from Table 8-3.

8.6. Electron Donor Variability

In all previous simulations it was assumed that there was an abundance of electron donors and/or nutrients, required for Cr(VI) biotransformation. However, this is not likely to be the case in many real world situations, as the availability of these solutes in the aquifer is often a limiting factor with natural attenuation. In this final simulation (Simulation 16, Table 8-1) variability in the concentrations of the electron donor is assumed in addition to the physical and biological variability. Unit variances in the hydraulic conductivity, initial biomass concentrations, and initial electron donor concentrations are assumed in this simulation.

For Simulation 16 the availability of both Cr(VI), as electron acceptor, and the electron donor are assumed to be crucial for the biotransformation process. This assumption places additional constraints on Cr(VI) reduction to occur. Comparing simulations 13 and 16 it is the case that despite using the same growth rate in both simulations, the variability in the electron donor (Simulation 16) reduces the microbial growth in the aquifer at both time steps [Figure 8-15 a and b].

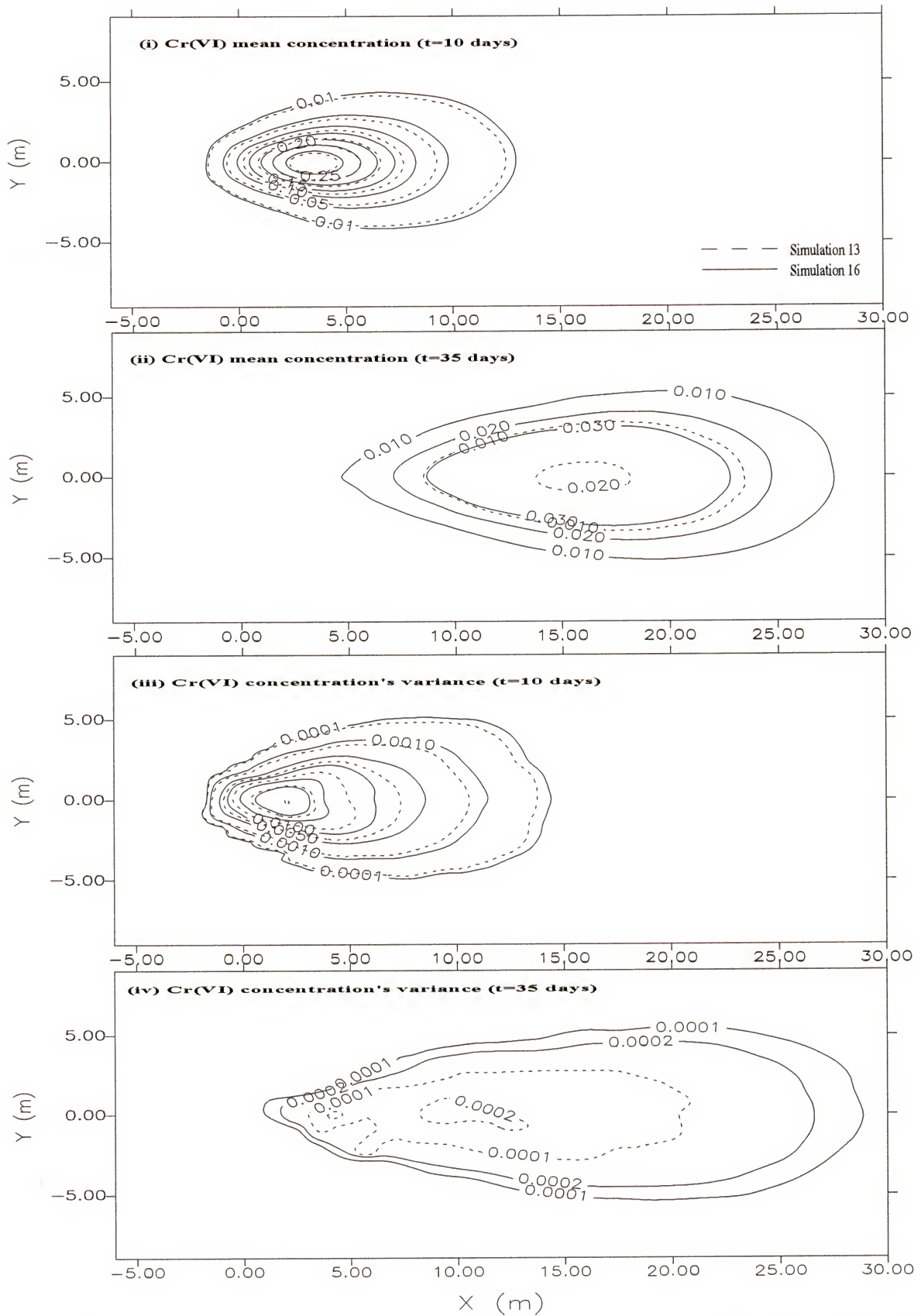


Figure 8-15(a) Comparison between concentration's mean and variance of Simulations 13 and 16.

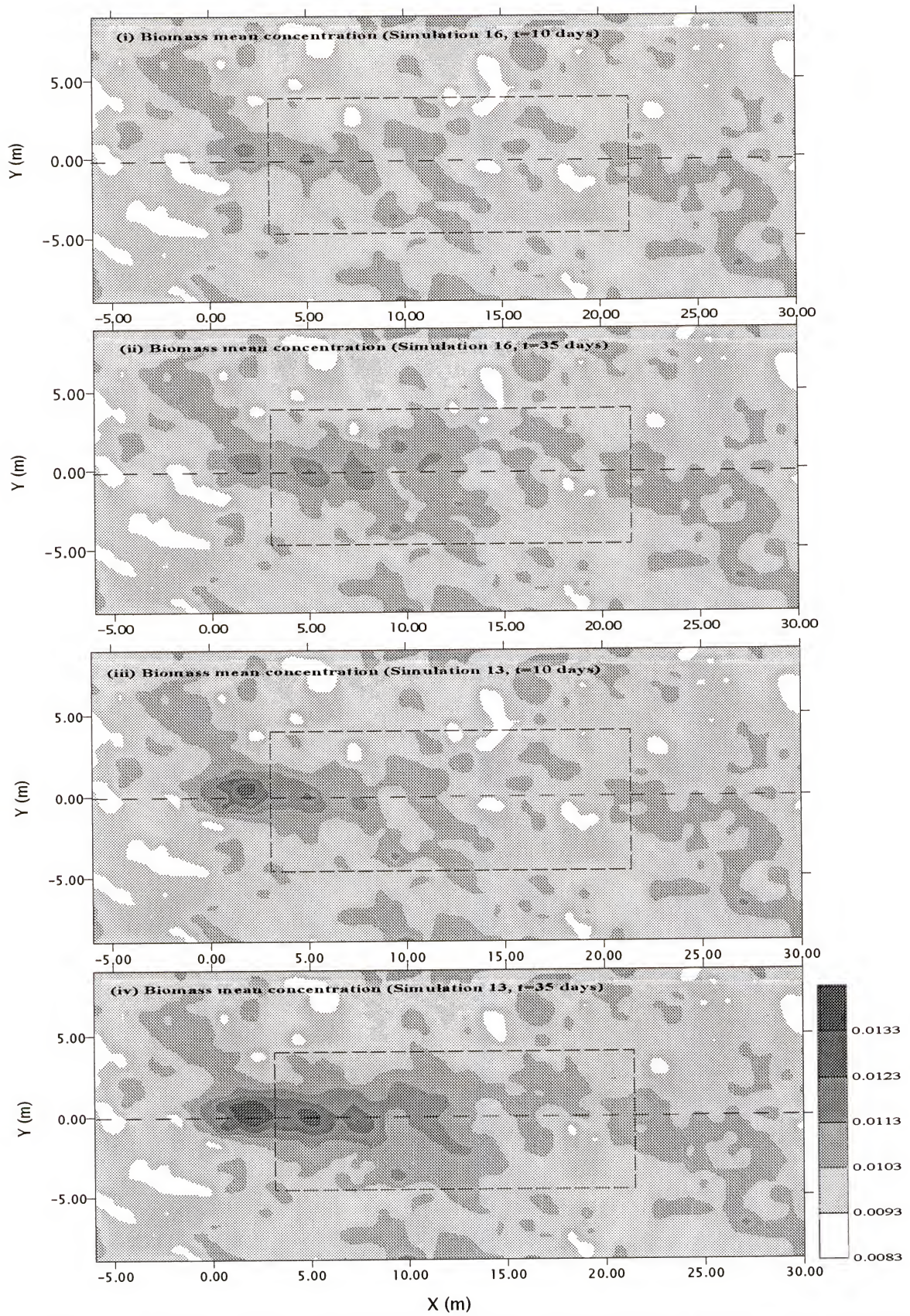


Figure 8-15(b) Comparison between biomass mean concentrations of Simulations 13 and 16.

As a result, there are higher ensemble mean Cr(VI) concentrations in Simulation 16 than in Simulation 13 [Figure 8-15a(i and ii)]. In addition, the spatial variability of the initial electron donor concentrations has increased the uncertainty in the estimated Cr(VI) concentrations [Figure 8-15a(iii and iv)]. The reduction in the ensemble mean of biomass concentration in the aquifer for Simulation 16 compared to Simulation 13 is accompanied with a reduction in the variance [Figure 8-15c].

More than a 30% reduction in the attenuation efficiency (total biotransformed Cr(VI) mass in the aquifer) is seen with Simulation 16 as compared to Simulation 13 (Table 8-2). However, despite this fact, no effect is observed on the first moment or the higher moments based on current plume mass [Figure 8-16a(ii, iv, vi, viii, x)]. Like biological variability, electron donor variability does not affect the dispersion of the ensemble mean concentration of Cr(VI). However, this was not the case when initial mass is used to normalize moments. Clear increases are seen with second, third and fourth moments as compared to simulations 6 and 13 [Figure 8-16a(iii, v, vii, and ix)]. Less microbial growth in scenario 16 is evident from the spatial biomass moments as compared to the other simulations [Figure 8-16b(i)]. Although the initial position of the biomass centroid is the same between Simulations 13 and 16 [Figure 8-16b(ii)], the transient shift of the centroid in simulation 16 is significantly less than that of simulations 6 and 13 [Figure 8-16b(ii)]. Similarly, a decrease in most of the spatial moments of the biomass mean concentration is observed [Figure 8-16b]. Finally, ignoring variability in the electron donor initial concentration can lead to an underestimation of the mean mass flux and the uncertainty associated with that flux [Figure 8-16c and Table 8-3].

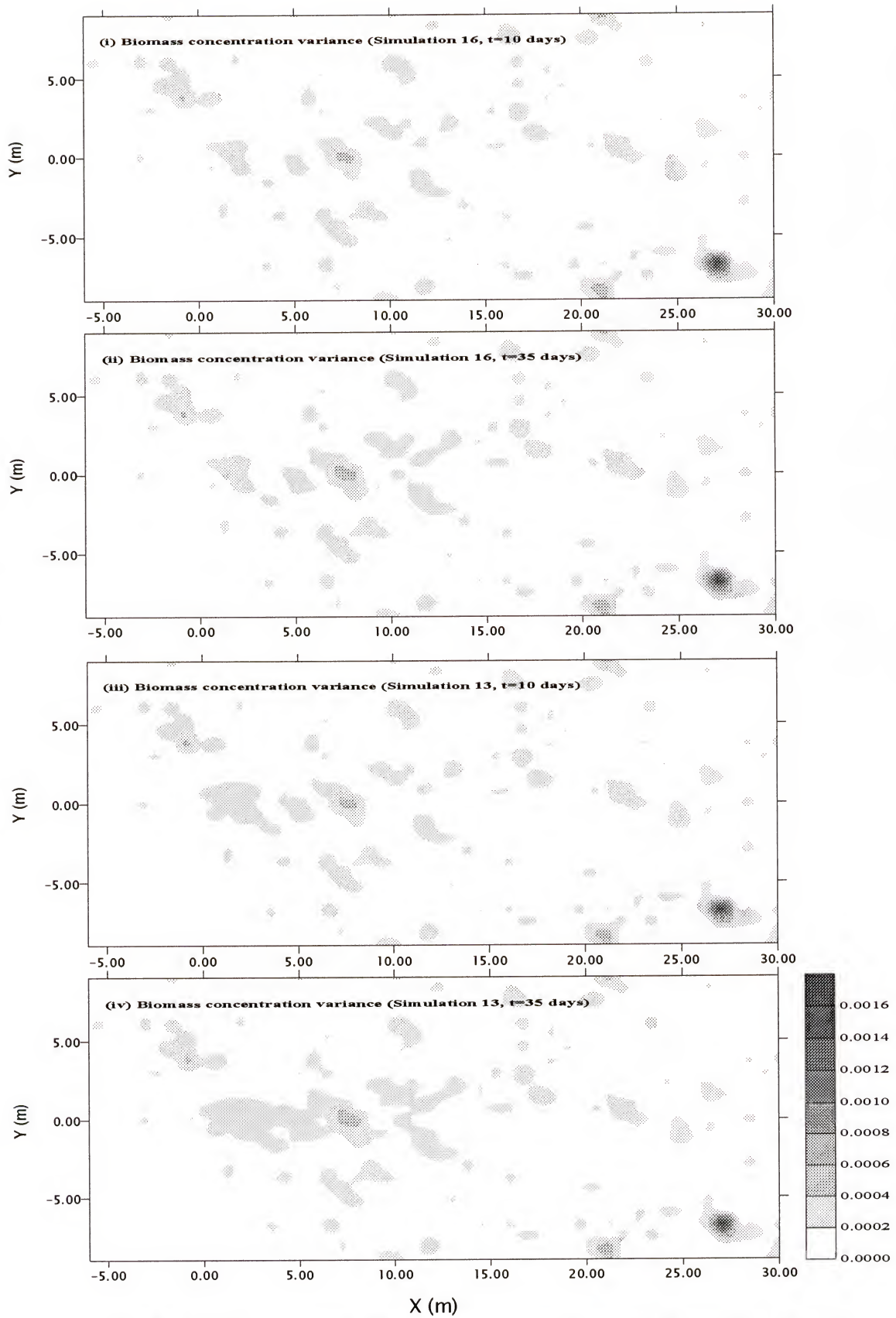


Figure 8-15(c) Comparison between biomass concentration's variance of Simulations 13 and 16.

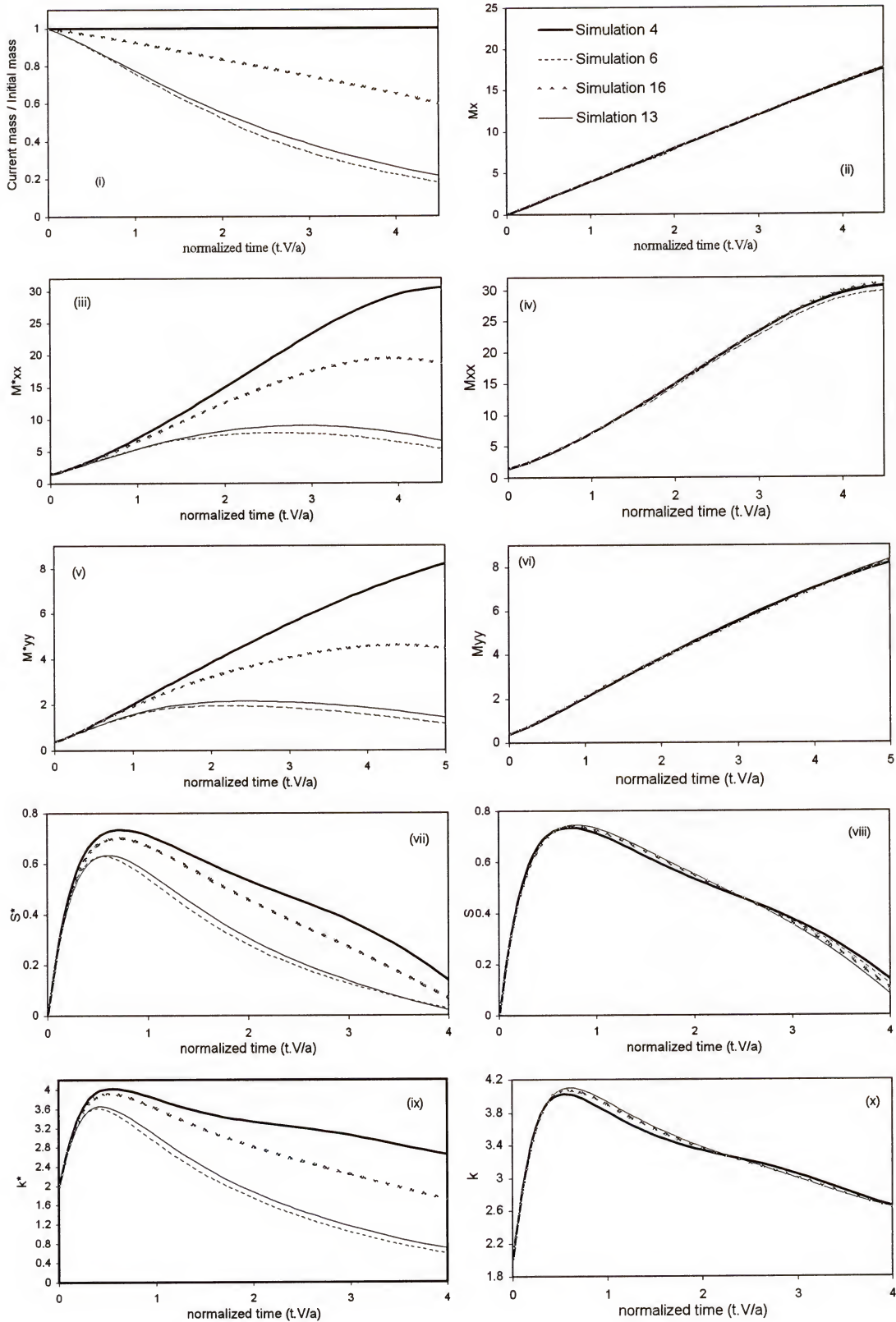


Figure 8-16a Spatial moments of Cr(VI) plume for simulations 4, 6, 13, and 16

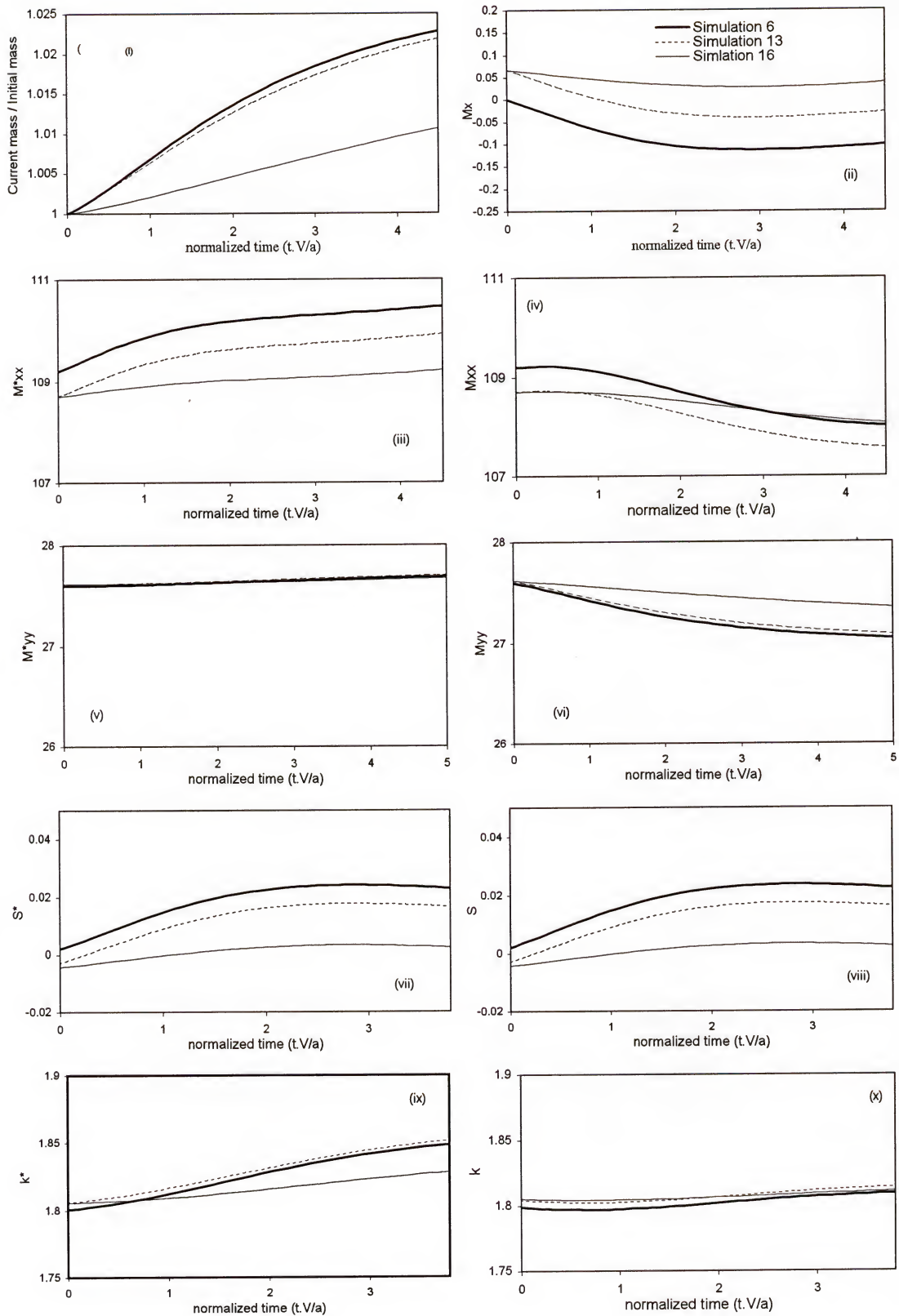


Figure 8-16b Biomass distribution spatial moments of simulations 6, 13, and 16

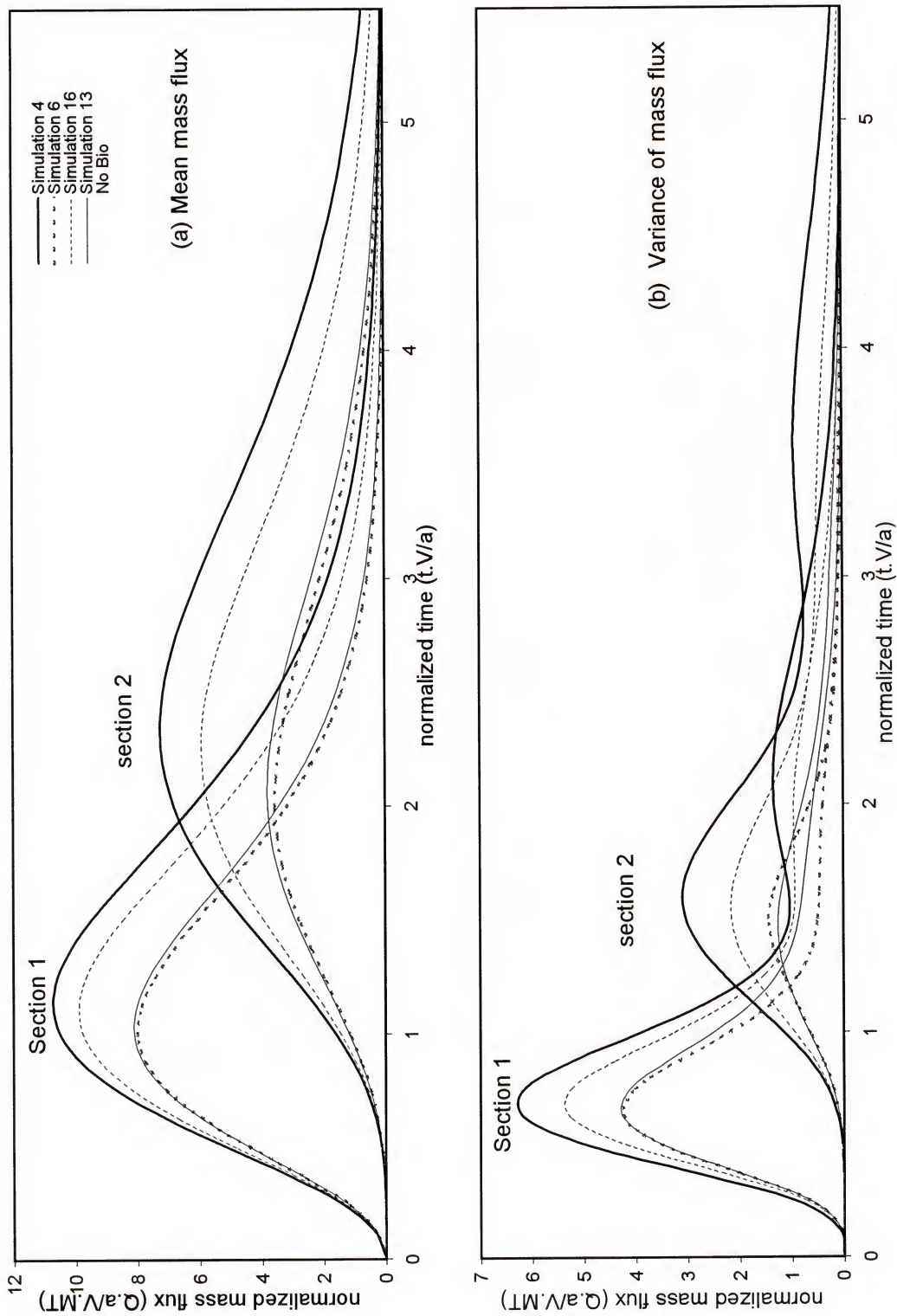


Figure 8-16c Mass fluxes of simulations 4, 6, 13, and 16.

CHAPTER 9

SUMMARY, CONCLUSIONS AND RECOMENDATIONS

9.1. Summary and Conclusions

In this dissertation, a three-dimensional finite element model, METABIOTRANS was developed for simulating the transport and biotransformation of metals in saturated groundwater. The model simulates steady-state groundwater flow in saturated porous media, transient transport of multiple solutes (i.e., metals, hydrocarbons) in heterogeneous/anisotropic porous media, sorption of dissolved constituents, microbially-mediated redox reactions between multiple electron donors and acceptors, and growth of multiple bacterial species coupled to redox reactions.

METABIOTRANS uses Michaelis-Menten kinetics relationships to describe the reduction of available electron acceptors, the consumption of electron donors, and the growth of microbial biomass. These relationships were modified to incorporate two different mechanisms of microbial growth inhibition. The first mechanism evolves from a competition for the most desired electron acceptor in the aquifer; while the other inhibition mechanism reflects the toxicity of the metal itself on bacterial species.

Chapter two reviewed the literature on the biological mechanisms and mathematical modeling of Cr(VI) reduction. Findings from the literature were used in chapter three to develop a system of non-linear ODE's that describe biologically-mediated Cr(VI) reduction in batch reactors.

The focus of chapter three was to investigate numerical solutions to systems of coupled non-linear biological reaction ODEs. Four methods were evaluated including (1) the Quasi-steady-state-approximation (QSSA), (2) the Finite difference method (FDM), (3) the Taylor expansion series approximation, and (4) the Fourth-order Runge-Kutta method (RKM). Solutions from each method were compared to those of analytical solutions and another numerical model (BIOKEMOD). Both the QSSA and the FDM produced good solutions compared to those of the analytical solution and the RKM; however, the QSSA showed slightly better agreement with the RKM than the FDM. The Taylor series expansion, on the other hand, delivered inaccurate results.

The QSSA was easily implemented to solve the coupled biological ODE's and it proved to be a robust solution method. For these reasons, it was selected to model experimental data of Cr(VI) reduction batch experiments. The QSSA method delivered excellent simulations of the Cr(VI) reduction compared to the laboratory observations. The strong agreement between QSSA results and those of RKM, BIOKEMOD, analytical solution, and laboratory data suggests that QSSA can be used with more complicated cases when more than one substrate is being utilized in batch culture experiments. Furthermore, QSSA can be easily implemented to solve systems of nonlinear biological reaction ODEs derived from a system of subsurface transport equations.

In chapter four, the system of non-linear ODE's that describe biologically-mediated Cr(VI) reduction (presented in chapter three) was combined with the subsurface transport equation obtaining a system of coupled non-linear PDE's that represent Cr(VI) transport and biotransformation in saturated porous media. The conceptual basis, assumptions, and numerical methods used in the development of METABIOTRANS to

solve such PDE's were also introduced. A time splitting algorithm (TSA), previously used by Wheeler et al. (1987), Dawson et al. (1987), and Chiang et al. (1991), was employed to solve the system of PDE's. Pertinent steps of the solution algorithm were as follows: 1) the steady-state saturated groundwater equation is solved to obtain accurate Darcy velocities in each element; 2) biological terms associated with each constituent transport equation are excised to produce a system of nonlinear couple biological ODE's and a system of uncoupled advection-dispersion equations (ADE's); 3) the system of ADE's is solved first using concentrations obtained from the previous time step as initial conditions; 4) the system of coupled biological ODE's and a system of microbial growth equations are then solved using the fourth-order Runge Kutta method and initial concentrations obtained from the ADE's in step 3; and 5) Steps (3) and (4) are repeated N times where $N \times \Delta t = \text{total simulation time}$.

In chapter five, METABIOTRANS was verified using analytical solutions to eleven problems. These problems were employed to evaluate the model performance under different groundwater flow, transport, and boundary conditions for one, two, and three-dimensional problems. Results of the validation study suggest METABIOTRANS is capable of simulating the transport of multi-solutes in heterogeneous/anisotropic saturated aquifers as influenced by advection, dispersion, sorption and biodegradation/biotransformation under different modeling conditions.

Once the model was verified, it was used to study three important aspects of remediating sites contaminated with Cr(VI). The first aspect was the relative impact of various biological parameters on the natural attenuation of Cr(VI) in the subsurface. The second aspect was the effects of nutrients and electron donor availability on the in situ

active remediation of Cr(VI) contaminated groundwater. The final aspect of interest was to investigate effects of both physical and biological heterogeneities on the natural attenuation of Cr(VI).

The focus of chapter six was a sensitivity analysis performed with each of the single-valued biological parameters (such as μ_{\max} , K_a , B , and K_i) to assess their effects on natural attenuation of Cr(VI) and the growth of the metal-reducing bacteria. Two examples were presented; the first of which was a two-dimensional problem, while the second was three-dimensional. Ten different model runs were used in each example to elucidate the significance of each biological parameter.

Increasing the maximum microbial growth rate (μ_{\max}) increased the rate of Cr(VI) reduction and, therefore, reduced the time required for natural attenuation. Changing this parameter did not alter the transient behavior of first and second spatial moments of the Cr(VI) plume normalized with respect to the current mass. Bacterial biomass distribution was quite sensitive to a change in μ_{\max} . For example, an increase in μ_{\max} by a factor of four caused a 300% increase in the biomass after 60 days. Increasing the microbial growth rate produced a shift in the biomass centroid towards the location of the initial Cr(VI) release and, as a result, increased the skewness of the microbial distribution. The variance and the peakness of the biomass distributions were not sensitive to perturbation in the microbial growth rate.

Perturbing the Cr(VI) half saturation coefficient (K_c) produced the opposite effect of the microbial growth rate when K_c was much greater than the local Cr(VI) concentration. As K_c approached the magnitude of local Cr(VI) concentrations the effect

of the half saturation coefficient was largely dependent on metal concentrations and the inhibition factor.

In general, both metal and bacterial concentrations were not extremely sensitive to variations in the inhibition factor (K_i) as compared to the other investigated parameters. However, an order of magnitude variation in its value produced a significant change in the biomass distribution. The inhibition factor forced bacteria to grow more uniformly in the aquifer. Therefore, minor changes were observed in the in centroid and skewness of microbial biomass distribution. In addition, unlike other parameters, reducing the inhibition factor slightly changed the contaminant variance in both longitudinal and transverse directions.

Increasing the microbial death coefficient (B) decreased the rate of biomass accumulation in the aquifer and, therefore, less Cr(VI) was reduced. Thus, B affected the size of the Cr(VI) plume; and therefore, the second, third, and fourth moments (normalized by the initial Cr(VI) mass) of the Cr(VI) plume. Unlike the maximum growth rate coefficient, the microbial death coefficient equally affects all bacteria in the aquifer independent of the Cr(VI) concentration. Because of this, no effect was observed on the biomass distribution variance, skewness, or kurtosis.

Finally, in chapter six, the effects of all these parameters on the contaminant mass flux were investigated. Mass flux was most sensitive to variations in μ_{\max} and K_c and least sensitive to K_i and B . Hence, measuring fluxes could be one way of estimating the growth and half saturation coefficients.

In chapter 7, remediation of the Cr(VI) plume was studied through 36 different scenarios. These scenarios were designed to investigate the effects on remediation

produced by modifying the number and position of wells and the nutrient and electron donor injection rates. This chapter also examined the sensitivity of remediation scenarios to the inhibition induced by elevated nutrient and electron donor concentrations.

With respect to well position, placing the nutrient and electron donor injection wells near the location of the initial contaminant release did not produce efficient remediation. Furthermore, treatment wells should not be situated an excessive distance downgradient the point of Cr(VI) release, as treatment of a much larger plume could become problematic. Placing injection well(s) a moderate longitudinal distance downstream of the initial contaminant release (5 m in the simulations presented in this study) produced the highest efficiencies of Cr(VI) reduction.

Increasing the number of wells and injection rates clearly had a direct effect of increasing Cr(VI) reduction in the aquifer. In general, line sources produced the highest levels of Cr(VI) transformation. This is not to say that this injection pattern made the most efficient use of electron donors and nutrients. Consider for example case two where the efficacy of three wells (injecting a total of 15 mg/l/day) was comparable to that obtained using a line source (injecting 40 mg/l/day). This example clearly indicates that more nutrient mass was injected than could be effectively used. Hence, it appears there is need for coupling METABIOTRANS to an optimization algorithm for the purpose of identifying an optimal remediation design that considers not just the physical/biological processes currently presented in the model but also the effective delivery of required nutrients and electron donors.

Finally, in Chapter seven it was shown that it is important to accurately characterize the microbial species (or consortium) responsible for metal reduction.

Inaccurate determination of constituent inhibition factors for Cr(VI), nutrients, or electron donors could undermine efforts to bring about effective remediation. For example, if added electron donors or nutrients induce growth inhibition at low levels, use of multiple-properly-spaced wells with lower injection rates is the preferred alternative to a single well where maintaining constituent concentrations below toxic levels is more difficult.

In chapter 8, METABIOTRANS was used, in a Monte Carlo scheme, to evaluate the effects of both physical (hydraulic conductivity) and biological (initial biomass concentrations) heterogeneities on metal biotransformations in the subsurface. In addition, effects of a correlation between both heterogeneities were also addressed. Four general cases were investigated. In the first case, only physical heterogeneity was considered. Biological heterogeneity was examined next; and then for the third case, the effects of both heterogeneities were studied as spatially correlated processes. Finally, in case four, variability in electron donor concentrations was investigated. Within each case, a sensitivity analysis was performed involving other parameters such as the microbial maximum growth rate and the initial biomass concentration variance (σ^2) in the aquifer.

Physical heterogeneity alone did not affect the estimation of the mass of Cr(VI) reduced (compared to the deterministic case) as long as uniform initial biomass and constant biological parameters were assumed. As expected, physical heterogeneity increased dispersion in both longitudinal and transverse directions and the skewness and the peakness of metal concentration distributions normalized with the current Cr(VI) mass; nonetheless, these changes were indistinguishable between reactive metal and non-reactive constituents. For moments normalized by the initial Cr(VI) mass, effects of biological activity on contaminant distributions were not obscured. For example, it was

evident from the second moments that Cr(VI) concentrations variances decreased with respect to a non-reactive contaminant; and increasing the microbial maximum growth rate magnified such differences. Finally, the increase in the hydrodynamic dispersion (created by physical heterogeneity) enhanced Cr(VI) transport which in turn encouraged greater than expected microbial growth such that higher ensemble mean biomass concentrations appeared further down-gradient than simulated with a homogeneous aquifer.

Physical heterogeneity had no effect on the cumulative mass flux, although, peak mass fluxes were attenuated due to increased dispersion. Two periods of high uncertainty in mass flux were observed; the first occurred as the leading edge of the plume approached the section, while the other occurred as the trailing edge traversed the same section. Biotransformation decreased Cr(VI) concentrations between sections, which in turn decreased the cumulate mass flux and the flux variance. For the same reason, a greater decrease in the flux variance was observed at the trailing edge of the plume than at the leading edge.

Biological variability alone did not change the reduction in Cr(VI) mass compared to that of the homogeneous case when a low growth rate was used. However, when higher microbial maximum growth rate is used, it the homogeneous case overestimates the biotransformed mass of Cr(VI) and therefore, underestimates the time required to remediate an aquifer. Thus, for remediation scenarios characterized with low microbial growth rates, a homogeneous assumption could be used to obtain an acceptable approximation of the required remediation time. The higher the microbial growth rate the

more noticeable the influence of the biological heterogeneity on changes in Cr(VI) plume size, moments, and mass fluxes.

Increasing the spatial variance of the initial biomass distribution resulted in a decrease in the estimated bioremediation efficiency. An increased biomass variance produces regions of extremely high and low biomass concentrations; as a result, opportunities increase for less efficient interception with the Cr(VI) plume and microbial reduction of Cr(VI).

Increasing biological heterogeneity increases all spatial moments normalized by the initial Cr(VI) mass when compared to the homogeneous case. Little if any effect was observed with moments normalized by the current Cr(VI) mass.

When negative correlation between physical and biological heterogeneities was considered, higher biological activity was expected in zones of lower groundwater velocity and vice versa. Thus, a negative correlation lead to expected Cr(VI) concentrations at the leading edge that were higher than those for the case of zero correlation; and the opposite was simulated at the trailing edge of the plume. Finally, increasing the microbial growth rate augmented differences simulated between the two cases.

When a positive correlation was considered, enhanced Cr(VI) reduction is predicted over the high velocity regions. Effects on the ensemble mean concentrations of Cr(VI) are opposite to those observed with a negative correlation.

Increasing the variance of initial biomass concentration from 1.0 to 3.0 (assuming positive correlation), decreased effectiveness of the natural attenuation of Cr(VI). In addition, uncertainties in the mean Cr(VI) concentration increased.

When the correlation between the physical and biological heterogeneities was changed from negative to positive, the initial position of the bacterial center of mass changed accordingly from 0.07 to -0.07 meters (referenced to the center of the aquifer). This occurred because random generations of biomass distributions were derived from a common spatial distribution of hydraulic conductivities, which exhibited slightly higher conductivities in the upgradient half of the flow domain. Because all other parameters were preserved between simulations, the trajectory of the first moment followed parallel paths. This means that the correlation between physical and biological heterogeneities does not affect the trajectory of the biomass centroid. Similar effects were also seen in other spatial moments (i.e. curves of the different spatial moments of negative and positive correlations were on opposite sides of that of the simulation where biological heterogeneity was ignored). The effect of changing the variance of the initial biomass concentration is more crucial than that of the type of the correlation itself (positive or negative) on the spatial moments of both Cr(VI) plume and biomass distribution.

Using a unit spatial variance of the initial biomass was not enough to visualize the importance of the correlation to predicting the mean mass fluxes. For example, when the variance was increased to three there was a distinctive increase in the expected mass flux and mass flux variance.

Variability in the initial concentrations of electron donor reduced microbial growth; and it increased the uncertainty in estimated Cr(VI) concentrations. For the conducted simulations, there was at least a 30% reduction in the biotransformation efficiency (total biotransformed Cr(VI) mass in the aquifer). Like biological variability, electron donor variability does not affect the dispersion of the ensemble mean

concentration of Cr(VI). However, this was not the case when Cr(VI) initial mass is used to normalize moments. Clear increases were seen with second, third and fourth moments. On the other hand, a decrease in spatial moments of the biomass mean concentration is observed. Finally, ignoring variability in the electron donor initial concentration can lead to an underestimation of the mean mass flux and the uncertainty associated with that flux.

9.2. Recommendations for Future Work

METABIOTRANS was used in this dissertation to study three important aspects concerning the fate and transport of Cr(VI) in the subsurface environment. The first aspect investigated the relative impact of various biological parameters on the natural attenuation of Cr(VI). The second examined the effects of nutrients and electron donor availability on active in situ remediation of Cr(VI) contaminated groundwater. The final aspect of interest explored was the effects of both physical and biological heterogeneities on the natural attenuation of Cr(VI). Future research based on the current work could take several directions including:

- 1) An enhancement of METABIOTRANS to describe the transport of bacteria. This line of research would ascertain the importance and dynamics of bacterial transport in remediation.
- 2) An enhancement of METABIOTRANS to simulate complex geo-chemical processes (such as precipitation). The natural oxidation of reduced metals could once again mobilize metals that were previously insoluble and stationary.
- 3) Developing scaling relationships between spatial moments of both the contaminant plume and the bacterial population for the purpose of designing

field-scale tests for estimating field scale biological parameters. Using such parameters could be of practical value in remediation.

- 4) Coupling METABIOTRANS to an optimization model for the purpose of identifying cost effective remediation schemes.
- 5) Studying spatial variability effects of more than one microbial species and electron donors on Cr(VI) and biomass distributions.

APPENDIX ANALYTICAL SOLUTION OF REACTION ODE's

In order to obtain the analytical solution of the four governing equations (3-7 through 3-10), the microorganisms' death rate (B) is assumed to be zero. By combining equations (3-7 and 3-10), (3-8 and 3-10), (3-9 and 3-10), and by integrating we obtain:

$$M = M_o + Y_s S_o - Y_s S \quad (A1)$$

$$N = N_o + \frac{Y_s}{Y_n} S - \frac{Y_s}{Y_n} S_o \quad (A2)$$

$$A = A_o + \frac{Y_s}{Y_a} S - \frac{Y_s}{Y_a} S_o \quad (A3)$$

Where S_o , A_o , N_o , and M_o are the initial values of the Substrate, electron acceptor, nutrient, and microbial species. By defining the following constants:

$$C_o = \frac{M_o}{Y_s} + S_o \quad (A4)$$

$$C1 = \frac{Y_n}{Y_s} N_o - S_o \quad (A5)$$

$$C2 = \frac{Y_n}{Y_s} N_o + \frac{Y_n}{Y_s} K_n - S_o \quad (A6)$$

$$C3 = \frac{Y_a}{Y_s} A_o - S_o \quad (A7)$$

$$C4 = \frac{Y_a}{Y_s} A_o + \frac{Y_a}{Y_s} K_a - S_o \quad (A8)$$

and by substituting equations A1 through A8 into equation 10 the following equation is obtained:

$$\frac{dS}{dt} = -\mu_{\max} \left(\frac{S}{K_s + S} \right) \left(\frac{S + C1}{S + C2} \right) \left(\frac{S + C3}{S + C4} \right) (C_o - S) \quad (A9)$$

Integrating (A9) by partial fractions an expression for S is obtained:

$$\left(\frac{S}{S_o} \right)^d \left(S - S_o + \frac{Y_n}{Y_s} N_o \right)^f \left(\frac{Y_n}{Y_s} N_o \right)^{-f} \left(S - S_o + \frac{Y_a}{Y_s} A_o \right)^g \left(\frac{Y_a}{Y_s} A_o \right)^{-g} \left(S_o - S + \frac{M_o}{Y_s} \right)^h \left(\frac{M_o}{Y_s} \right)^{-h} = e^{-t} \quad (A10)$$

where

$$d = \frac{1}{\mu_{\max}} \left(\frac{K_s C2 C4}{C_o C1 C3} \right) \quad (A11)$$

$$f = \frac{1}{\mu_{\max}} \left(\frac{(K_s - C1)(C2 - C1)(C4 - C1)}{-C1(C3 - C1)(C_o + C1)} \right) \quad (A12)$$

$$g = \frac{1}{\mu_{\max}} \left(\frac{(K_s - C3)(C2 - C3)(C4 - C3)}{-C3(C1 - C3)(C_o + C3)} \right) \quad (A13)$$

$$h = \frac{1}{\mu_{\max}} \left(\frac{(K_s + C_o)(C2 + C_o)(C4 + C_o)}{C_o(C_o + C1)(C_o + C3)} \right) \quad (A14)$$

The Newton-Raphson iteration method is used to solve the non-linear equation A10 to obtain the values of S at any time t. With S known, equations A1, A2 and A3 can be used to find M, N, and A respectively.

LIST OF REFERENCES

- Balkwill, D. L. and Ghiorse, W. C., Characterization of subsurface bacteria associated with two shallow aquifers in Oklahoma. *Appl. Environ. Microbiology*, 3(50), 580-588, 1985.
- Baker, J. H., Relationship between microbial activity of stream sediments determined by three different methods and abiotic variables, *Microbial Ecol.*, 12, 193-203, 1986.
- Bedient, P. B., Rifai, H. S., and Newell, C. J., *Groundwater Contamination: Transport and Remediation*. PTR Prentice-Hall, Inc., Englewood Cliffs, New Jersey, 1994.
- Beeman, R. E. and Suflita, J. M., Microbial ecology of shallow unconfined groundwater aquifer polluted by municipal landfill leachate. *Microbial Ecology*, 14, 39-54, 1987.
- Bellin, A., A. Rinaldo, W. J. P. Bosma, S. E. A. T. M. van der Zee, Y. Rubin, Linear equilibrium adsorbing solute transport in physically and chemically heterogeneous porous formations, 1, Analytical solutions, *Water Resour. Res.*, 29(12) 4019-4030 1993.
- Bollag, J. M., and Bollag, W. B., Soil contamination and the feasibility of biological remediation. In *Bioremediation: science and applications*, Skipper, H. D., and Turco, R. F., Eds, Madison, Wis., Soil Science Society of America, 1-31, 1995.
- Bopp, L. H., Chakrabarty, A. M., and Ehrlich, H. L., Chromate resistance plasmid in *Pseudomonas fluorescens*. *J. Bacteriol.*, 155(3), 1105-1109, 1983.
- Borden, R. C., and Bedient, P. B., Transport of dissolved hydrocarbon influenced by oxygen-limited biodegradation 1. Theoretical development. *Water Res. Res.* 22, 1973, 1986.
- Bosma, T. N. P., Schnoor, J. L., Schirra, G., and Zehnder, A. J. B., Simulation model for biotransformation of xenobiotics and chemotaxis in soil columns. *J. Cont. Hyd.*, 2, 225-236, 1988.
- Bull, A. T., *Microbial growth: in companion to biochemistry*. Bull, A. T., Lagnado, J. R., Thomas, J. O., and Tipton, K. F., Eds., Longmans, London, p. 415, 1974.

Burr, D. T., E. A. Sudicky, R. L. Naff, Nonreactive and reactive solute transport in three-dimensional heterogeneous porous media: Mean displacement, plume spreading, and uncertainty, *Water Resour. Res.*, 30(3) 791-815 1994.

Celia M. A., Kindred, J. S., and Herrera, I. Contaminant transport and biodegradation: 1. A numerical model for reactive transport in porous media. *Water Res. Res.*, 25(6), 1141-1148, 1989.

Chapelle, F. H., McMahon, P. B., Bubreovsky, N. M., Fuji, R. F., Oaksford, E. T., and Vroblesky, D. A., Deducing the distribution of the terminal electron-accepting in hydrologically diverse groundwater system. *Water Res. Res.*, 31, 359-371, 1995.

Chen, Y., Abriola, L.M., Alvarez, P. J. J., Anid, P. J., and Vogel, T. M., Modeling transport and biodegradation of benzene and toluene in sandy aquifer material: comparisons with experimental measurements. *Water Res. Res.*, 28(7), 1833-1847, 1992.

Chen, J. M. and Hao, O. J., Environmental factors and modeling in microbial chromium(VI) reduction. *Water Environ. Res.*, 68(7), 1156, 1996.

Chiang, C. Y., Dawson. C. N., and Wheeler, M. F., Modeling of in-situ bioremediation of organic compounds in groundwater, Technical report. *Trans. in porous media*, 6, 667-702, 1991.

Chiang C. Y., Wheeler, M. F., and Bedient P. B., A modified method of characteristics technique and mixed finite elements method for simulation of groundwater solute transport. *Water Res. Res.*, 25, 1541-1549, 1989.

Coleman, R. N., and Padran, J. H., Biofilm concentration of chromium. *Environ. Tech.*, 12, 1079, 1991.

Cvetkovic, V.D., and A. M. Shapiro, Mass arrival of sorptive solute in heterogeneous porous media, *Water Res. Res.*, 26(9), 2057-2067, 1990.

Cvetkovic, V. D., G. Dagan, and H. Cheng, Contaminant transport in aquifers with spatially variable hydraulic and sorption properties, *Proc. R. Soc. London, Ser. A*, 454, 2173-2207, 1998.

Dagan, G., Solute transport in heterogeneous porous formations, *J. Fluid Mech.*, 145, 151-177, 1984.

Dagan, G., Time-dependent macrodispersion for solute transport in anisotropic heterogeneous aquifers, *Water Res. Res.*, 24(9), 1491-1500, 1988.

Dagan G., and V. D. Cvetkovic, Spatial moments of a kinetically sorbing solute plume in a heterogeneous aquifer, *Water Res. Res.*, 29(12), 4053-4061, 1993.

Dawson, C. N., Wheeler, M. F., and Bedient, P. B., Numerical modeling of subsurface contaminant transport with biodegradation kinetics. Proceedings of National Water Wells meeting, Houston, Texas, 329, 1987.

Dawson, C. N., Wheeler, M. F., Nguyen, T. M., and Poole, S. W., Simulation of hydrocarbon biodegradation in groundwater. CRAY Channels 8, 3, p. 14, 1986.

Dawson, C. N., Wheeler, M. F., Nguyen, T. M., and Poole, S. W., Simulation of subsurface contaminant transport with biodegradation kinetics. Proceedings of Third International Symposium on Science and Engineering on CRAY supercomputers, Mendota Heights, Minnesota, p. 75, 1987.

De Blanc, P. C., Sepehrnoori, K., Speitel, G. E., and McKinney, D. C., Investigation of numerical solution techniques for biodegradation equations in a groundwater flow model. Inter. Conf. Comp. Meth. Water Res., CMWR, v1, 161-168, 1996.

DeFilippi, L., New process cleans contaminated groundwater. Water Eng. Manage., 141(3), 16, 1994.

Douglas, J. Jr. and Russel, T. F., Numerical methods of convection-dominated diffusion problems based on combining the method of characteristics with finite elements or finite difference procedures, SIAM J. Num. Anal. 19, p. 871, 1982.

Eary, L.E., and Rai, D., Kinetics of chromium(III) oxidation to chromium(VI) by reaction with manganese dioxide. Environ. Sci. Technol., 21, 1187, 1987.

Eary, L.E., and Rai, D., Chromate removal from aqueous waste by reduction with ferrous iron. Environ. Sci. Tech., 22, 972-977, 1988.

Frankenberger, W. T. and Losi, M. E., Applications of bioremediation in the cleanup of heavy metals and Metalloids. In Bioremediation: science and applications, Skipper, H. D., and Turco, R. F., Eds, Madison, Wis., Soil Science Society of America, 173-210, 1995.

Frind, E. O., Duynisveld, W. H. M., Strebel, O., and Boettcher, J., Modeling of multicomponent transport with microbial transformation in groundwater: the Furhberg case. Water Res. Res., 26, 1707-1719, 1990.

Fujie, K., Tsuchida, T., Urano, K., and Ohtake, H., development of bioreactor system for the treatment of chromate wastewater using *Enterobacter cloacae* HO1. Water Sci. Technol., 30(3), 235, 1994.

Garabedian, S. P., L. W. Gelhar, and M. A. Celia, Large-scale dispersive transport in aquifers: Field experiment and reactive transport theory, Ralph M. Parsons Lab. Rep. 315, Dep. of Civil Eng., Mass Inst. Of Technol., Cambridge, 1988.

Gear C. W., Numerical initial value problems in ordinary differential equations. Prentice-Hall, New Jersey, 1971.

Gelhar, L. W., and C. L. Axness, Three-dimensional stochastic analysis of macrodispersion in aquifers. *Water Res. Res.*, 19(1), 161-180, 1983.

Gelhar, L.W., A. L. Gutjahr, and R. L. Naff, Stochastic analysis of macrodispersion in a stratified aquifer, *Water Res. Res.*, 15(6), 1487-1397, 1979.

Ghiorse, W. C., and Balkwill, D. L., Enumeration and morphological characterization of bacteria indigenous to subsurface environments. *Develop. Ind. Microbiol.*, 34, 313-335, 1983.

Ghosh, S. and Bupp, S., Simulation of biological uptake of heavy metals. *Water Sci. Technol.*, 26(1/2), 227, 1992.

Gorby, Y. A., Amonette, J. E., and Fruchter, J. S., Remediation of contaminated subsurface materials by a metal-reducing bacterium. In *in-situ remediation: Scientific basis for current and future technologies*, Thirty Third Hanford Symposium on Health and the Environment, Glendon, W., and Richard, N., Eds., p. 233-247, November 7-11, 1994.

Gvozdyak, P. I., Mogilavich, N. F., Rylskii, A. F., and Grishchenko, N. I., Reduction of hexavalent chromium by collection strains of bacteria. *Mikrobiologiya*, 55(6), 962, 1986.

Hao, O. J., Huang, L, Chen, J. M., and Buglass, R. L., Effects of metal additions on sulfate reduction activity in wastewaters. *Toxicol. Environ. Chem.*, 46(2), 197, 1994.

Harvey, R. W., George, L.H., Smith, R. L., LeBlanc, D. R., Garabedian, and Howes, B. L., Transport of bacteria through a contaminated freshwater aquifer. USGS Open File Rep., p. 87-109, B31-B33, 1987.

Harvey, R. W., Smith R. L., and George, L. G., Effect of organic contaminant upon microbial distribution and heterotrophic uptake in a Cape Cod, Mass. aquifer. *Appl. Environ. Microbiol.*, 48, 1197-1201, 1984.

Hass, C. N. and Polprasert, C., Biological sulfide prestripping for metal and COD removal. *Water Environ. Res.* 65(5), 645, 1993.

Hassan, A. E., J. H. Cushman, and J. W. Delleur, Monte Carlo studies of flow and transport in fractal conductivity fields: Comparison with stochastic perturbation theory, *Water Res. Res.*, 33(11), 2519-2534, 1997.

Hassan, A. E., J. H. Cushman, and J. W. Delleur, A Monte Carlo assessment of Eulerian flow and transport perturbation models, *Water Resour. Res.*, 34(5), 1143-1163, 1998.

Hertel, O., Berkowicz, R., Christensen J., and Hov, Ø., Test of two numerical schemes for use in atmospheric transport-chemistry models. *Atmos. Environ.*, 27A(16), 2591-2611, 1993.

Hesstvedt, E., Hov, Ø., and Isaksen, I. S. A. Quasi steady-state approximation in air pollution modeling: comparison of two numerical schemes for oxidant predictions. *International Journal of Chemical Kinetics*, 10, 971-994, 1978.

Hewson, Thomas. Simulation of leachate movement in the areal plane- A finite element approach: Princeton University, B.S. thesis, 150 p, 1976.

Horitsu, H., Nishita, H., Kato, H., and Tomoyeda, M., Isolation of potassium chromate tolerant bacterium and chromate uptake by the bacterium. *Agric. Biol. Chem.*, 42(11), 2037, 1978.

Horitsu, H., Tuto, S., Miyazawa, Y., Ogal, S., and Kawai, K., Enzymatic reduction of hexavalent chromium tolerant pseudomonas ambigua G-1. *Agric. Biol. Chem.* 51(12), 2417, 1987.

Hu, B. X., F. W. Deng , and J. H. Cushman, Non-local reactive transport with physical and chemical heterogeneity: Linear nonequilibrium sorption with random K_d , *Water Res. Res.* 31(9), 2239-2252, 1995.

Hu, B. X., J. H. Cushman, F.-W. Deng, Nonlocal reactive transport with physical, chemical, and biological heterogeneity, *Adv. Water Resour.*, 20(5-6) 293-308 1997.

Ishibashi, Y., Cervantes, C., and Silver, S., Chromium reduction in pseudomonas putida. *Appl. Environ. Microbiol.*, 56(7), 2268, 1990.

James, B. R., and Bartlett, R. J. *J. Environ. Qual.*, 12(2), 169-172, 173-176, 177-181, 1983.

Kim, S., and Corapcioglu, M. Y., A kinetic approach to modeling mobile bacteria-facilitated groundwater contaminant transport. *Water Res. Res.*, 32, 321, 1996.

Kindred, J. S. and Celia, M. A., Contaminant transport and biodegradation 2. Conceptual model and test simulation, *Water Res. Res.* 25, 1149-1159, 1989.

Kinzelbach, W., Schafer, W., and Herzer, J., Numerical modeling of natural and enhanced denitrification process in aquifers. *Water Res. Res.*, 27, 1123-1135, 1991.

Konikow, L. F., and Bredehoeft, J. D., Computer model for 2-D solute transport and dispersion in groundwater. Automated data processing and computations. *Techniques of Water Resources Investigation of the United States Geological Survey*, Washington, DC, 1978.

Kormi, K., Rivas, A., Toda, K., and Ohtake, H., biological removal of toxic chromium using an *Enterobacter cloacae* strain that reduces chromate under anaerobic conditions. *Biotechnol. Bioeng.*, 35(4), 951, 1990a.

Kormi, K., Toda, K., and Ohtake, H., Effects of oxygen stress on chromate reduction in *Enterobacter cloacae* strain HO1. *J. Ferment. Bioeng.*, 69(1), 67, 1990b.

Kormi, K., Wong, P., and Ohtake, H., Factors affecting chromate reduction in *Enterobacter cloacae* strain HO1. *Appl. Microbiol. Biotechnol.*, 33(4), 567, 1989.

Llovera, S., Boner, R., Simon-Pujol, M. D., and Congregado, F., Chromate reduction by resting cells of *Agrobacterium radiobacter* EPS-916. *Appl. Environ. Microbiol.*, 59(10), 3516, 1993.

Losi, M. E., Amrhein, C., and Frankenberger, W. T., Jr., Bioremediation of chromate contaminated groundwater by reduction and precipitation in surface soils. *J. Environ. Qual.*, 23(8), 1141, 1994a.

Losi, M. E., Amrhein, C., and Frankenberger, W. T., Jr., Environmental biochemistry of chromium. *Rev. Environ. Contamination Toxicol.*, 136, 91, 1994b.

Lovely, D. R., Dissimilatory Fe(II) and Mn(IV) reduction. *Microbiol. Rev.*, 55, 259-287, 1991.

Lovely, D. R., Dissimilatory metal reduction. *Annu. Rev. Microbiol.*, 47, 263, 1993.

Lovely, D. R., Bioremediation of organic and metal contaminants with dissimilatory metal reduction. *J. Ind. Microbiol.*, 14, 85, 1995.

Lovely, D. R., and Chapelle, F. H., Deep subsurface microbial processes. *Rev. Geophys.*, 33, 365-381, 1995.

Lovely, D. R., and Phillips, E. J. P., Reduction of chromate by *Desulfovibrio vulgaris* and its C(3) cytochrome. *Appl. Environ. Microbiol.*, 60(2), 726, 1994.

Luli, G. W., Talnagi, J. W., Strohl, W. R., and Pfister, R. M., Hexavalent chromium resistant bacteria isolated from river sediments. *Appl. Environ. Microbiol.*, 46(4), 846, 1983.

Lynch, J. M., and Poole, N. J., Eds, *Microbial Ecology: A Conceptual Approach*. Wiley, N.Y., 1979.

MacQuarrie, K. T. B., Sudicky, E. A., and Frind, E. O., Simulation of biodegradable organic contaminants in groundwater 1. Numerical foemulation in principal directions. *Water Res. Res.*, 26(2), 207, 1990.

Malone, D. R., Kao, C., and Borden, R. C., Dissolution and bioremediation of non-aqueous phase hydrocarbons: model development and laboratory evaluation. *Water Res. Res.*, 29(7), 2203-2213, 1993.

Mathur, R., Young, J. O., Schere, K. L., and Gipson, G. L., A comparison of numerical techniques for solution of atmospheric kinetic equations. *Atmos. Environ.*, 32(9), 1535-1553, 1998.

McInerney, M. J., Leon, N., Worrell, V. E., and Coates, J. D., Development of techniques for the bioremediation of chromium-contaminated soil and groundwater. EPA/600/R-95/076, Office of Research and Development, U.S.EPA, Washington, DC, 1995.

Miralles-Wilhelem, F., L. W. Gelhar, and V. Kapoor, Stochastic analysis of oxygen-limited biodegradation in three-dimensionally heterogeneous aquifers, *Water Res. Res.*, 33(6), 1251-1263, 1997.

Molz, F. J., Widdowson, M. A., and Benefield, L. D., Simulation of microbial growth dynamics coupled to nutrient and oxygen transport in porous media. *Water Res. Res.*, 22, 1207-1216, 1986.

Monod, J., *Recherché Sur la Croissance des Cultures Bacteriennes*. Herman & Cie, Paris, 1942.

Nieboer, E. and Jusys, A. A., Biologic chemistry of chromium. In chromium in natural and human environments, Nriagu, F. O. and Nieboer, E., Eds., John Wiley, New York, p. 21, 1988.

Odman M. T., Kumar, N., and Russel, A. G., Technical note: A comparison of fast chemical kinetic solvers for air quality modeling. *Atmos. Environ.*, 26A(9), 1783-1789, 1992.

Ohtake, H., Fuji, E., and Toda, K., Bacterial reduction of hexavalent chromium: kinetic aspects of chromate reduction by *Enterobacter cloacae* HO1. *Biocatalysis*, 4(2), 227, 1990b.

Ohtake, H., Fuji, E., and Toda, K., Reduction of toxic chromate in an industrial effluent by use of a chromate-reusing strain of *Enterobacter cloacae*. *Environ. Tech.*, 11(6), 663, 1990c.

Ohtake, H., Fuji, E., and Toda, K., A survey of effective electron donors for reduction of toxic hexavalent chromium by *Enterobacter cloacae* strain HO1. *J. Gen. Appl. Microbiol.*, 36(3), 203, 1990d.

Ohtake, H., and Hardoyo, J. K., New biological method for detoxification and removal of hexavalent chromium. *Water Sci. Tech.*, 25(11), 395, 1992.

Ohtake, H., Komori, K., Cervantes, C., and Toda, K., Chromate-resistance in a chromate reducing strain of *Enterobacter cloacae*. FEMS Microbiol. Lett. 67(1/2), 85, 1990a.

Ohtake, H., and Silver, S., Bacterial detoxification of toxic chromate. In Biological Degradation and Biotransformation of Toxic Chemicals, G. R. Chaudhry, Eds., Portland, Oregon, p. 403, 1994.

Palmer, C. D., Fish, W., and Kelly, J. F., Inorganic contaminants: Recognizing the problem. Proceedings of the Second National Outdoor Action Conference on Aquifer Restoration, Groundwater Monitoring, and Geophysical Methods., p. 555-579, 1988.

Parlange, J. Y., Starr, J. L., Barry, D. A. and Braddock, R. D. Some approximate solutions of the transport equation with irreversible reactions: Soil Science Society of America Journal, v. 137, no. 6, p. 434-442, 1984.

Puls, R. W., Clark, D. A., Paul, C. J., and Vardy, J., Transport and transformation of hexavalent chromium through soils and into groundwater. J. Soil Cont., 3(2), 203, 1994.

Rifai, H. S., Numerical techniques for modeling in-situ bioremediation and biodegradation of organic contaminants in groundwater, Ph.D. Thesis, Rice University, 1989.

Reily, R. G., and Zachara, J. M., Chemical contaminants on DOE lands and selection of contaminant mixtures for subsurface science research. DOE/ER-0547T U.S. Department of Energy, Washington DC., 1992.

Ritman, B. E. and McCarty, P. L., Model of steady state biofilm kinetics. Biotech. Bioeng., 22, 2343, 1980.

Romanenko, V. I. and Koren'kov, V. N., A pure culture of bacteria utilizing chromates and dichromates as hydrogen acceptors in growth under anaerobic conditions. Mikrobiologiya, 46(3), 414-417, 1977.

Romanenko, V. I., Kusnestove, S. I., and Koren'kov, V. N., Method for biological purification of wastewater. USSR Patent SU 521, 234, 1976.

Russell, T. F., Time splitting along characteristics with incomplete iteration for a Galerkin approximation of miscible displacement in porous media. SIAM J. Num. Anal., 22, 970, 1985.

Russell, T. F., Wheeler, M. F., and Chiang, C. Y., Large-scale simulation of miscible displacement. Proceedings of SEG/SIAM/SPE Conference on mathematical and Computational Methods in Seismic Exploration and Reservoir Modeling, W. E., Fitzgibbon, Ed., Society of Industrial and Applied mathematics, Philadelphia, p. 85, 1986.

Schafer, W., and W. Kinzelbach, Numerical investigations into the effects of aquifer heterogeneity on in-situ bioremediation, in *In-Situ and On-Site Bioreclamation*, pp. 196–225, Batelle Mem. Inst., Co-lumbus, Ohio, 1991.

Scholl, M. A., Effects of heterogeneity in aquifer permeability and biomass on biodegradation rate calculations-results from numerical simulations. *Ground Water*, 38(5), 702-712, 2000.

Shen, H., Pritchard, P. H., and Sewell, G. W., Microbial reduction of Cr(VI) during anaerobic degradation of benzoate. *Environ. Sci. Technol.*, 30, 1667-1674, 1996.

Shen, H., and Wang, Y. T., Biological reduction of chromium by E. Coli. *J. Environ. Eng. Am. Soc. Civil Eng.*, 120(3), 560, 1994a.

Shen, H., and Wang, Y. T., Modeling hexavalent chromium reduction in E. Coli 33456. *Biotechnol. Bioeng.*, 43(4), 293, 1994b.

Shen, H., and Wang, Y. T., Simultaneous chromium reduction and phenol degradation in a coculture of E. Coli ATCC 33456 and P. putida DMP-1. *Appl. Environ. Microbiol.*, 61, 2745, 1995.

Smith, L. A., Alleman, B. C., and Copley-Graves, L., Biological treatment options. In *Engineering Technology for Bioremediation of Metals*, Means, J. L. and Hinchee, R. E., Eds., CRC Press, Boca Raton, Fl, p.1, 1994.

Suflita, J.M., Microbiological Principles Influencing the Bioremediation of Aquifers. In *Transport and Fate of Contaminants in the Subsurface*, EPA/625/4-89/019, Robert S. Kerr Environmental research laboratory, U.S. EPA, Ada, OK, p. 85-99, 1989.

Suzuki, T., Miyata, N., and Horitsu, H., NAD(P)H-dependent chromium (VI) reductase of pseudomonas ambigua G-1: a Cr(VI) intermediate is formed during the reduction of Cr(VI) to Cr(III). *J. Bacteriol.*, 174(16), 5340, 1992.

Taylor, S. W., and P. R. Jaffe, Enhanced in situ biodegradation and aquifer permeability reduction, *J. Environ. Eng. N. Y.*, 117(1), 25–46, 1990.

Tracy, J. C., Erikson, L. E., and Davis L. C., Rate limited degradation of hazardous organic contaminant in the root zone of a soil. *Proc. 86th Annu. Meet. Exhib.*, Denver, Co, p. 93, June 1993.

Tracy, J. C., Ramireddy, H., Erikson, L. E., and Davis L. C., Effect of climatological variability on the performance of vegetative systems in remediation contaminated soils. *Proc. 87th Annu. Meet. Exhib.*, Denver, Co, p. 94, June 1994.

Valocchi, A. J., Spatial moments analysis of the transport of kinetically adsorbing solutes through stratified aquifers, *Water Res. Res.*, 25(2) 273-279, 1989.

Wang, P-C., Mori, T., Komori, K., Sasatsu, M., Toda, K., and Ohtake, H., Isolation and characterization of an *Enterobacter cloacae* strain that reduces hexavalent chromium under anaerobic conditions. *Appl. Environ. Microbiol.*, 55(7), 1665, 1989.

Wheeler, M. F., and Dawson, C. N., An operator splitting method for advection-dispersion-reaction problems. *MAFELAP proceedings VI*, J. A., Whiteman, Ed., Academic Press, p. 463, 1988.

Wheeler, M. F., Dawson, C. N., Bedient, P. B., Chiang, C. Y., Borden, R. C., and Rifai, H. S., Numerical Simulation of microbial biodegradation of hydrocarbons in groundwater. *Proceedings AGWSE/IGWMCH Conference on Solving Groundwater problems with Models*, National Water Wells Association, p. 92, 1987.

Widdowson, M. A., Molz, F. J., and Benefield, L. D., A numerical transport model for oxygen and nitrate-based respiration linked to substrate and nutrient availability in porous media. *Water Res. Res.*, 24, 1553-1565, 1988.

Widdowson, M. A., Molz, F. J., and Benefield, L. D., Development and application of a model for simulating microbial growth dynamics coupled to nutrient and oxygen transport in porous media. *Proceedings AGWSE/IGWMCH Conference on Solving Groundwater problems with Models*, National Water Wells Association, p. 28, 1987.

Wilson, L. T., McNabb, J. F., Balkwill, D. L., and Ghiores, W. C., Enumeration and characterization of bacteria indigenous to the shallow water table aquifer. *Ground Water*, 2, 134-142, 1983.

Wood, B. D., Dawson, C. N., Szecsody, J. E., and Streile, G. P., Modeling contaminant transport and biodegradation in layered porous media system. *Water Res. Res.*, 30(6), 1833-1845, 1994.

Wood, B. D., Ginn, T. R., and Dawson, C. N., Effects of microbial metabolic lag in contaminant transport and biodegradation modeling in a layered porous media system. *Water Res. Res.*, 31, 553-563, 1995.

Wood, J. M. and Wang, H. K., Microbial resistance to heavy metals. *Environ. Sci. Technol.*, 7, 47-50, 1983.

Yamamoto, K., Kato, J., Yano, T., and Ohtake, H., Kinetics and Modeling of hexavalent chromium reduction in *Enterobacter cloacae*. *Biotechnol. Bioeng.*, 41(1), 129, 1993.

Yeh, G. T., and Tripathi, V. S., *HYDROGEOCHEM: A coupled model of hydrologic transport and geochemical equilibrium in reactive multicomponent systems*. ORNL-6371, Oak Ridge National Laboratory, Environmental Science Division, 1991.

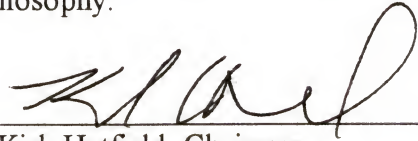
Zachara, J. M., Ainsworth, C. C., Cowan, C. E., and Resch, C. T., Adsorption of chromate by subsurface soil horizons. *Soil Sci. Soc. Am. J.*, 53(2), 418, 1989.

BIOGRAPHICAL SKETCH

Mohamed Mostafa A. Mohamed was born in Cairo, Egypt, in 1972. In the summer of 1994 he received B.Sc. degree in civil engineering from Cairo University. Immediately after his graduation he was appointed as a teaching and research assistant in the same department. He started his work towards a M.Sc. in hydrology in fall 1994. He used numerical techniques to simulate seawater intrusion in the Nile Delta aquifer during his studies for the M.Sc. degree, which he earned in spring 1997. From January 1995 till March 1996 he joined the Egyptian army as a civil engineer. In March 1996 he worked as an environmental engineer in one of the leading design offices in Egypt. He participated in the design of many significant infrastructure projects in Egypt. In March 1997 he became a Chief Engineer in the same office. At that time his experience was extended to several projects in Africa.

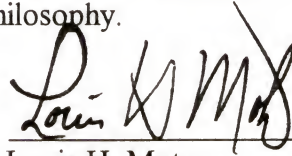
In the fall of 1997 he was admitted in the Civil Engineering Department, University of Florida, as a Ph.D. candidate. During his studies at the University of Florida he received several teaching and research assistantship rewards from the Civil Engineering Department. In summer 2000, he joined the Desert Research Institute as a research intern. During this period he worked within an interdisciplinary program with many scientists from different fields of earth science. His main task was to evaluate and develop numerical models to describe groundwater transport phenomena. After graduation, Mr. Mohamed will teach at the Civil Engineering Department at Cairo University, Egypt.

I certify that I have read this study and that in my opinion it conforms to acceptable standards of scholarly presentation and is fully adequate, in scope and quality, as a dissertation for the degree of Doctor of Philosophy.



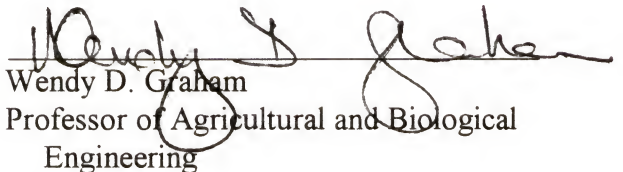
Kirk Hatfield, Chairman
Associate Professor of Civil and Coastal
Engineering

I certify that I have read this study and that in my opinion it conforms to acceptable standards of scholarly presentation and is fully adequate, in scope and quality, as a dissertation for the degree of Doctor of Philosophy.



Louis H. Motz
Associate Professor of Civil and Coastal
Engineering

I certify that I have read this study and that in my opinion it conforms to acceptable standards of scholarly presentation and is fully adequate, in scope and quality, as a dissertation for the degree of Doctor of Philosophy.




Wendy D. Graham
Professor of Agricultural and Biological
Engineering

I certify that I have read this study and that in my opinion it conforms to acceptable standards of scholarly presentation and is fully adequate, in scope and quality, as a dissertation for the degree of Doctor of Philosophy.



Michael D. Annable
Associate Professor of Environmental
Engineering Sciences


I certify that I have read this study and that in my opinion it conforms to acceptable standards of scholarly presentation and is fully adequate, in scope and quality, as a dissertation for the degree of Doctor of Philosophy.



Jennifer M. Jacobs
Assistant Professor of Civil and Coastal
Engineering

This dissertation was submitted to the Graduate Faculty of the College of Engineering and to the Graduate School and was accepted as partial fulfillment of the requirements for the degree of Doctor of Philosophy.

August 2001



Pramod Khargonekar
Dean, College of Engineering

Winfred Phillips
Dean, Graduate School